Block Copolymer Nanoparticles Prepared by RAFT Aqueous Polymerisation

Charlotte Jade Mable

Department of Chemistry

The University of Sheffield

Submitted to the University of Sheffield in fulfilment of the requirements for the award of Doctor of Philosophy

September 2017

Declaration

The work described in this Thesis was carried out at the University of Sheffield under the supervision of Professor Steven P. Armes FRS between October 2013 and September 2017 and has not been submitted, either wholly or in part, for this or any other degree. All the work is the original work of the author, except where acknowledged by references.

Signature:…….

Charlotte Jade Mable September 2017

Acknowledgements

I am extremely lucky to have received help and support from lots of people during my PhD studies. First and foremost, a huge thank you goes to my supervisor Steve Armes, for giving me the opportunity to work in your group, for your support, enthusiasm and advice. Thanks for taking a chance five and a half years ago when I stuck my head in your office asking for a summer project! I'd also like to thank you for giving me the chance to travel to some great places for conferences and SAXS trips. I would also like to thank the ERC for funding my PhD studies.

Much of the work in this thesis would not have been possible without the help of Sasha Mykhaylyk (a.k.a the SAXS machine) and his protégé Matt Derry. Thank you Sasha for providing SAXS models, and both of you for an unlimited supply of help and knowledge over friendly cups of tea. I also thank the other members of the SAXS team, Nick W, Lee, and Lizzy for making those long, long night shifts much more fun. We had some good times, going for steak, going skiing and breaking rental car rear windows with snowboards!!

It has been a privilege to work with an amazing bunch of fun, helpful and friendly chemists in the Armes group. My PhD has been a (mostly) enjoyable experience, and you have all helped me to keep my sense of humour despite renovating a house, planning a wedding, getting married, renovating another house and having a baby whilst doing my PhD! A huge thank you goes to Kate, my work wife. You introduced me to polymer chemistry and taught me the ropes, but most importantly you have been my rock! We have too many memories to list here, but one of my favourites involves a large spanner…we will leave that there. Another very special lady is Amy Cockram, you have been a terrific friend since the first day of our summer projects, at the beginning of our Armes group journeys. Thank you Vicki for always being there with amazing cake and to the MChem students I helped supervise (Rheanna, Reb and Dan) for being lovely. Thank you to Irene, for sharing my enthusiasm in biology and baby clothes! Thank you to Mark, Nick P, Yin, Joe, Liam, Greg, Fiona, Sarah B, Sarah C, Dave, Matt R, Craig, Deborah, Shannon, Ollie, Eric, Darren, Simon, Birte, Froso, Mona, Vince and Jeppe and all of the past and present Armes group members for the great memories and for providing a supportive working environment.

The department would definitely not be the same without the accounts ladies, Denise and Louise, who know everything finance related and can never do enough to help you. I'd like to say thank you to Svet Tzokov and Chris Hill for all of the TEM technical help and grid prep, and Sue Bradshaw and Sandra Marshall for answering numerous NMR questions. Thanks to Beulah for the Cryo-TEM images.

Thanks to Babslarr for the regular laughs over cups of tea (Yorkshire of course) and Kat for the St Thomas road memories. Thanks to my undergraduate friends who made my first four years in Sheffield enjoyable: Kate, Ammeh M, Eeejj, Hevlar, Scotty, Tracy, Harini and last but certainly not least Bryony (always a friendly face in the department).

I would like to thank my entire family for supporting me over the years. In particular my Mum, thanks for always listening to my dilemmas and being so supportive in every way, but most of all for being my best friend. A special thank you to my Dad, for your patience with all the Maths help in the early days. My sisters, Alice and Emily, are amazing and have always provided me with a giggle. My grandparents have always shown an interest in my PhD research regardless of whether they understand.

I'm especially grateful for being given the opportunity to work in the Armes group because it is where I met and fell in love with my husband. Andrew, you have been there every step of the way and I know you always will be. Thank you for your friendship, love, support, encouragement and for all the proof-reading. None of what I have achieved during my PhD studies would have been possible without you. I'd love to wholly dedicate this thesis to you, but as you have probably guessed, our daughter has squeezed her way in again, its not 'just the two of us' anymore! My little Jodie Deryn Morse, although you have not helped with this thesis in the slightest (quite the opposite actually), you are my world. I dedicate this thesis to both of you.

Publications

Primary publications resulting from work in this thesis:

"Framboidal ABC Triblock Copolymer Vesicles: A New Class of Efficient Pickering Emulsifier" C. J. Mable, N. J. Warren, K. L. Thompson, O. O. Mykhaylyk and S. P. Armes, *Chemical Science*, **2015**, *6*, 6179–6188.

"Loading of Silica Nanoparticles in Block Copolymer Vesicles During Polymerization-Induced Self-Assembly: Encapsulation Efficiency and Thermally Triggered Release" C. J. Mable, R. R. Gibson, S. Prevost, B. E. McKenzie, O. O. Mykhaylyk and S. P. Armes, *Journal of the American Chemical Society*, **2015**, *137*, 16098-16108.

"ABC Triblock Copolymer Worms: Synthesis, Characterization and Evaluation as Pickering emulsifiers for Millimetre-Sized Droplets" C. J. Mable, K. L. Thompson, M. J. Derry, O. O. Mykhaylyk, B. P. Binks and S. P. Armes, *Macromolecules*, **2016**, *49 (20)*, 7897–7907.

"Time-Resolved SAXS Studies of the Kinetics of Thermally Triggered Release of Encapsulated Silica Nanoparticles from Block Copolymer Vesicles" C. J. Mable, M. J. Derry, K. L. Thompson, L. A. Fielding, O. O. Mykhaylyk and S. P. Armes, *Macromolecules*, **2017**, *50 (11)*, 4465–4473.

Primary publications resulting from work conducted on other projects:

"Synthesis and pH-Responsive Behaviour of Framboidal ABC Triblock Copolymer Vesicles in Aqueous Solution" C. J. Mable, L. A. Fielding, M. J. Derry, O. O. Mykhaylyk, P. Chambon and S. P. Armes *(manuscript in preparation)*

"Sterile PISA Synthesis of Biomimetic pH-Responsive Framboidal Vesicles for Targeting Triple-Negative Breast Cancer Cells" C. J. Mable, I. Canton, O. O. Mykhaylyk, B. Ustbas, P. Chambon, E. Themistou and S. P. Armes *(manuscript in preparation)*

Publications resulting from work conducted on other projects:

"Are block copolymer worms more effective Pickering emulsifiers than block copolymer spheres?" K. L. Thompson, C. J. Mable, A. Cockram, N. J. Warren, V. J. Cunningham, E. R. Jones, R. Verber and S. P. Armes, *Soft Matter*, 2014, *10*, 8615-8626.

"Preparation of Pickering Double Emulsions Using Block Copolymer Worms" K. L. Thompson, C. J. Mable, J. A. Lane, M. J. Derry, L. A. Fielding and S. P. Armes, *Langmuir*, 2015, *31*, 4137-4144.

"In situ small-angle X-ray scattering studies of sterically-stabilised diblock copolymer nanoparticles formed during polymerisation-induced self-assembly in non-polar media" M. J. Derry, L. A. Fielding, N. J. Warren, C. J. Mable, A. J. Smith, O. O. Mykhaylyk and S. P. Armes, *Chemical Science*, 2016, *7*, 5078-5090.

"Directed Assembly of Soft Anisotropic Nanoparticles by Colloid Electrospinning" S. Jiang, C. J. Mable, S. P. Armes, D. Crespy, *Macromolecular Rapid Communications*, 2016, 37 (*19)*, 1598-1602.

"Giant Pickering Droplets: Effect of Nanoparticle Size and Morphology on Stability" V. J. Cunningham, E. C. Giakoumatos, P. M. Ireland, C. J. Mable, S. P. Armes and E. J. Wanless, *Langmuir*, 2017, *33 (31)*, 7669–7679.

"Using Dynamic Covalent Chemistry To Drive Morphological Transitions: Controlled Release of Encapsulated Nanoparticles from Block Copolymer Vesicles" R. Deng, M. J. Derry, C. J. Mable, Y. Ning and S. P. Armes, *Journal of the American Chemical Society*, 2017, *139 (22)*, 7616–7623.

"Bespoke Diblock Copolymer Nanoparticles Enable Production of Relatively Stable Oil-in-Water Pickering Nanoemulsions" K. L. Thompson, N. Cinotti, E. R. Jones, C. J. Mable, P. W. Fowler and S. P. Armes *(manuscript submitted)*

Oral presentations at conferences:

"Framboidal ABC Triblock Copolymer Vesicles: A New Class of Efficient Pickering Emulsifier" American Chemical Society National Meeting and Exposition, 16th-20th August 2014, Boston, USA.

"pH-Responsive Framboidal Vesicles Prepared using Polymerisation-Induced Self-Assembly via RAFT Aqueous Dispersion Polymerisation" American Chemical Society National Meeting and Exposition, 16th-20th August 2014, Boston, USA.

"Framboidal Vesicles as Pickering Emulsifiers and Virus-Mimics" Armes Festival 500, 30th-31st July 2015, Sheffield, UK.

"Encapsulation of Silica Nanoparticles Within Block Copolymer Vesicles and Their Subsequent Release" Soft Matter Analytical Laboratory Opening, 7th October 2016, Sheffield, UK.

Poster presentations at conferences:

"Framboidal Triblock Copolymer Vesicles: A New Class of Efficient Pickering Emulsifier" Macro Group Young Researchers Meeting, 24th-25th July 2014, Durham, UK.

"Framboidal Triblock Copolymer Vesicles: A New Class of Efficient Pickering Emulsifier" American Chemical Society National Meeting and Exposition, 10th-14th August 2014, San Fransisco, USA.

"pH-Responsive Framboidal Vesicles Prepared using Polymerisation-Induced Self-Assembly via RAFT Aqueous Dispersion Polymerisation" American Chemical Society National Meeting and Exposition, 10th-14th August 2014, San Fransisco, USA.

"Framboidal Triblock Copolymer Vesicles: A New Class of Efficient Pickering Emulsifier" Sheffield Colloid Network International Symposium, 6th May 2015, Sheffield, UK.

"Framboidal Triblock Copolymer Vesicles: A New Class of Efficient Pickering Emulsifier" Armes Festival 500, 30th-31st July 2015, Sheffield, UK.

"Framboidal Triblock Copolymer Vesicles: A New Class of Efficient Pickering Emulsifier" The Polymer Conference, 10th-14th July 2016, Warwick, UK.

Abstract

This thesis describes the reversible addition-fragmentation chain transfer (RAFT) polymerisation of block copolymer nanoparticles in water. Firstly, a water-soluble poly(glycerol monomethacrylate) (PGMA) macromolecular chain-transfer agent (macro-CTA) was synthesised via RAFT solution polymerisation in ethanol. The PGMA macro-CTA is then chain-extended with 2-hydroxypropyl methacrylate (HPMA) via RAFT aqueous dispersion polymerisation. Polymerisation-induced self-assembly (PISA) occurs under these conditions, where the miscible HPMA monomer polymerises to form an insoluble poly (2-hydroxypropyl methacrylate) block, thus driving in situ formation of spheres, worms or vesicles. These PGMA-PHPMA diblock copolymers are then chain-extended with benzyl methacrylate (BzMA) via 'seeded' RAFT aqueous emulsion polymerisation to prepare PGMA-PHPMA-PBzMA triblock copolymers. In Chapter Two, a series of model framboidal PGMA-PHPMA-PBzMA triblock copolymer vesicles are synthesised with excellent control over surface roughness. Transmission electron microscopy (TEM) and small-angle X-ray scattering (SAXS) were utilised to characterise these nanoparticles, which were subsequently used to stabilise *n*-dodecane emulsion droplets in water. The adsorption efficiency, A_{eff}, of the nanoparticles at the *n*-dodecane/water interface was determined as a function of increasing vesicle surface roughness using a turbidimetry assay. A strong correlation between surface roughness and A_{eff} was observed, with A_{eff} increasing from 36 % up to 94 %. This is a significant improvement in Pickering emulsifier efficiency compared to that reported previously for similar vesicles with smooth surfaces. In Chapter Three, a series of PGMA-PHPMA-PBzMA triblock copolymer worms and spheres are synthesised. For certain block compositions, highly anisotropic worm-like particles are obtained, which are characterised by SAXS and TEM. The design rules for accessing higher order morphologies (*i.e.* worms or vesicles) are briefly explored. Surprisingly, vesicular morphologies cannot be accessed by targeting longer PBzMA blocks – instead only spherical nanoparticles are formed. SAXS is used to rationalise these counter-intuitive observations, which are best explained by considering subtle changes in the relative enthalpic incompatibilities between the three blocks during the growth of the PBzMA block. Finally, these PGMA-PHPMA-PBzMA worms are evaluated as Pickering emulsifiers for the stabilisation of oil-in-water emulsions. *Millimetre-sized* oil droplets were obtained using low-shear homogenisation (hand-shaking) in the presence of 20 % vol. *n*-dodecane. In contrast, control experiments performed using PGMA-PHPMA diblock copolymer worms indicated that these more delicate nanostructures did not survive even these mild conditions. In the latter two experimental Chapters of this thesis, PISA is used to design block copolymer nanoparticles as potential drug delivery vehicles. Thus, PGMA-PHPMA diblock copolymer vesicles are prepared in the presence of varying amounts of silica nanoparticles of approximately 18 nm diameter. After centrifugal purification to remove excess non-encapsulated silica nanoparticles, analysis confirms encapsulation of up to hundreds of silica nanoparticles per vesicle. Silica is a model payload: it has high electron contrast compared to the copolymer and its thermal stability enables quantification of the loading efficiency via thermogravimetric analysis. Encapsulation efficiencies can be obtained using disk centrifuge photosedimentometry, since the vesicle density increases at higher silica loadings while the mean vesicle diameter remains essentially unchanged. SAXS is used to confirm silica encapsulation, because a structure factor is observed at $q \sim 0.25$ nm^{-1}. A new two-population model provides satisfactory data fits to the SAXS patterns and allows the mean silica volume fraction within the vesicles to be determined. These silica-loaded vesicles constitute a useful model system for understanding the encapsulation of globular proteins, enzymes or antibodies within block copolymer vesicles for potential biomedical applications. They may also serve as an active payload for self-healing hydrogels or repair of biological tissue. Finally, by targeting a relatively short PHPMA block, PGMA-PHPMA vesicles can be obtained that lie close to the worm-vesicle phase boundary, rendering them thermo-responsive. The thermo-responsive nature of these vesicles enables thermally-triggered release of the encapsulated silica nanoparticles simply by cooling to 0-10^{o}C, which induces a morphological transition. TEM studies confirm the change in diblock copolymer morphology and also enables direct visualisation of the released silica nanoparticles. Time-resolved small angle X-ray scattering is used to quantify the extent of silica release over time. For these experiments, the purified silica-loaded vesicles were cooled to 0^{o}C for 30 min and SAXS patterns were collected every 15 s. For PGMA-PHPMA vesicles synthesised in the absence of silica nanoparticles, vesicles remained intact for 8 minutes before a vesicle-to-worm transition occurs. Thereafter, a worm-to-sphere transition occurs after 12 min at 0^{o}C. For lower silica loadings, cooling induces a vesicle-to-sphere transition with subsequent nanoparticle release. For higher silica loadings, cooling to 0^{o}C for 30 min only leads to perforation of the vesicle membranes, but silica nanoparticles are still released through the pores. For vesicles prepared in the presence of 30 % w/w silica, a new SAXS model has been developed to determine both the mean volume fraction of encapsulated silica remaining within the vesicles and also the scattering length density of the vesicle. Satisfactory data fits to the experimental SAXS patterns were obtained using this model. These results indicate that 68 % of the encapsulated silica is released from the vesicles after being held at 0^{o}C for 30 min.

List of Abbreviations

a_0	cross-sectional area of the hydrophilic block
ACVA	4, 4'-azobis-4-cyanopentanoic acid
A_{eff}	adsorption efficiency
BzMA	benzyl methacrylate
c_1	copolymer volume fraction
c_2	silica nanoparticle volume fraction
$C_{copolymer}$	copolymer volume fraction
CPDB	2-cyano-2-propyl benzodithioate
C_{rel}	volume fraction of released silica
cryo-TEM	cryogenic transmission electron microscopy
C_{SiO_2}	silica volume fraction
$D_{4/3}$	volume-average diameter
DCP	disc centrifuge photosedimentometry
D_h	hydrodynamic diameter
DLS	dynamic light scattering
DMF	dimethylformamide
DMSO	dimethylsulfoxide
DP	number-average degree of polymerisation
D_s	SAXS-derived mean sphere diameter
D_v	SAXS-derived mean vesicle diameter
D_w	weight-average diameter
EE_{DCP}	DCP-derived encapsulation efficiency
EGDMA	ethylene glycol dimethacrylate
ESRF	European Synchrotron Radiation Facility
f_{PY}	effective volume fraction
GMA	glycerol monomethacrylate
GPC	gel permeation chromatography
HPLC	high performance liquid chromatography
HPMA	2-hydroxypropyl methacrylate
l_c	length of the hydrophobic block
LE_{TGA}	TGA-derived silica loading efficiency
L_k	mean worm Kuhn length
L_w	mean worm contour length
macro-CTA	macromolecular chain transfer agent
M_n	number-average molecular weight
M_w	weight-average molecular weight
MWD	molecular weight distribution

M_w/M_n	dispersity
η	volume fraction of PHPMA block within the core domain
N_{agg}	aggregation number
NMR	nuclear magnetic resonance
N_{sv}	number of silica nanoparticles encapsulated per vesicle
o/w	oil-in-water
OM	optical microscopy
P	packing parameter
PBzMA	poly(benzyl methacrylate)
PDI	polydispersity index
p_{eff}	DCP-derived effective vesicle density
PEG	poly(ethylene glycol)
PETTC	4-cyano-4-(2-phenylethanesulfanylthiocarbonyl)sulfanyl-pentanoic acid
PGMA	poly(glycerol monomethacrylate)
PHPMA	poly(2-hydroxypropyl methacrylate)
PISA	polymerisation-induced self-assembly
PPG-TDI	tolylene 2,4-diisocyanate-terminated poly(propylene glycol)
q	scattering vector
RAFT	reversible addition-fragmentation chain transfer
R_{in}	radius of the vesicle lumen
R_g	radius of gyration
R_m	radius from the centre of the vesicle to the middle of the membrane
R_{out}	outer radius of the vesicle membrane
R_{PY}	Percus-Yevick correlation radius of densely packed spheres
R_s	sphere core radius
R_{sw}	radius of the worm core cross section
R_v	SAXS-derived vesicle radius
SAXS	small-angle x-ray scattering
SEM	scanning electron microscopy
TEM	transmission electron microscopy
T_g	glass transition temperature
TGA	thermogravimetric analysis
T_m	vesicle membrane thickness
UV-vis	ultraviolet visible
v	volume of the hydrophobic block
V_c	volume of the corona block
V_{co}	volume of the core-forming block
V_{in}	volume of the vesicle lumen

V_m	volume of the membrane-forming block
V_{out}	volume of the vesicle
V_{sl}	volume of the vesicle lumen occupied by silica nanoparticles
W_w	mean worm width
x_{sol}	volume fraction of solvent within the core domain

Contents

Chapter One - Introduction

Introduction

A polymer is a long-chain molecule comprising a series of covalently-bonded repeat units called monomers. Vinyl monomers are the focus of this thesis. Linear polymers are formed when monofunctional vinyl monomers are used.[1] A polymer containing two or more different monomers is known as a copolymer. Statistical, alternating and block copolymers are common examples of linear polymers. Linear block copolymers, specifically AB diblock and ABC triblock copolymers (see Figure 1.1), are of particular interest in this thesis.

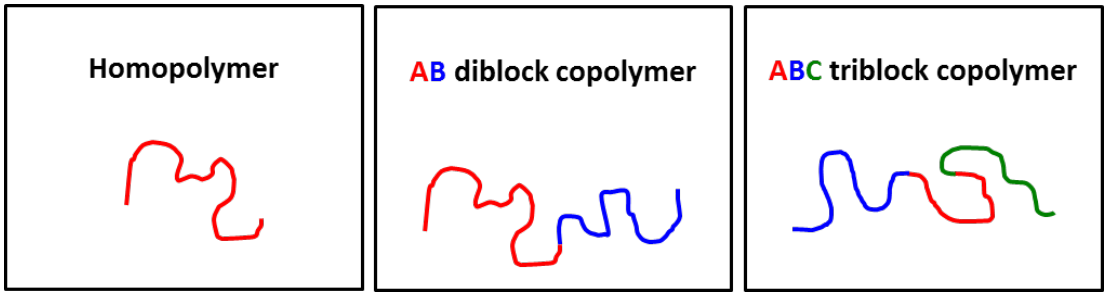

Figure 1.1. Schematic illustration of the linear block copolymers used in this thesis,[2, 3] where A (red), B (blue) and C (green) represent different vinyl monomers.

Polymerisation Techniques

Free Radical Polymerisation

This is a type of chain growth polymerisation. It is applicable to a wide range of functional vinyl monomers and this chemistry can be conducted under various physical conditions (solution, emulsion, dispersion, suspension etc.). There are four key steps to free radical polymerisation: initiator decomposition, chain initiation, propagation and termination. A typical free radical polymerisation reaction scheme is shown in Figure 1.2.

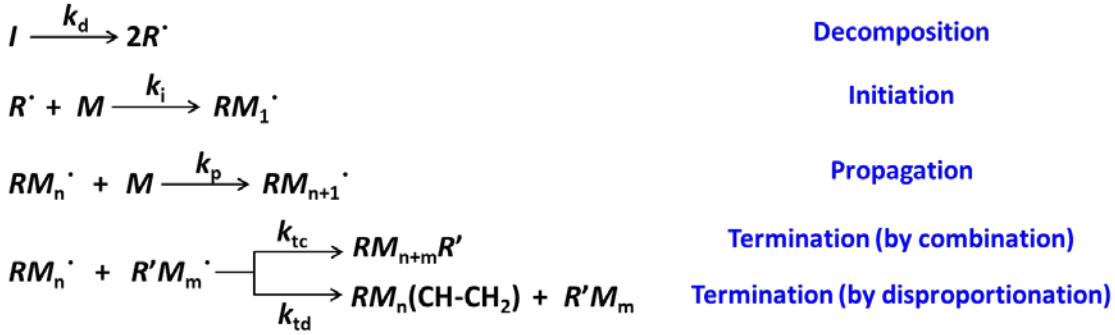

Figure 1.2. Free radical polymerisation reaction mechanism showing initiator decomposition, monomer initiation, chain propagation and chain termination steps, where *I* = initiator, *R* = radical, *M* = monomer, H = hydrogen, n and m are the mean degrees of polymerisation.

The formation of primary free radicals (*R*•) is usually achieved by thermal decomposition of the initiator (*I*) via homolytic dissociation of a covalent bond in the initiating species (see Figure 1.3). Common free radical initiators that undergo homolytic scission via thermolysis contain either azo (-N=N-) or peroxide (O-O-) groups.

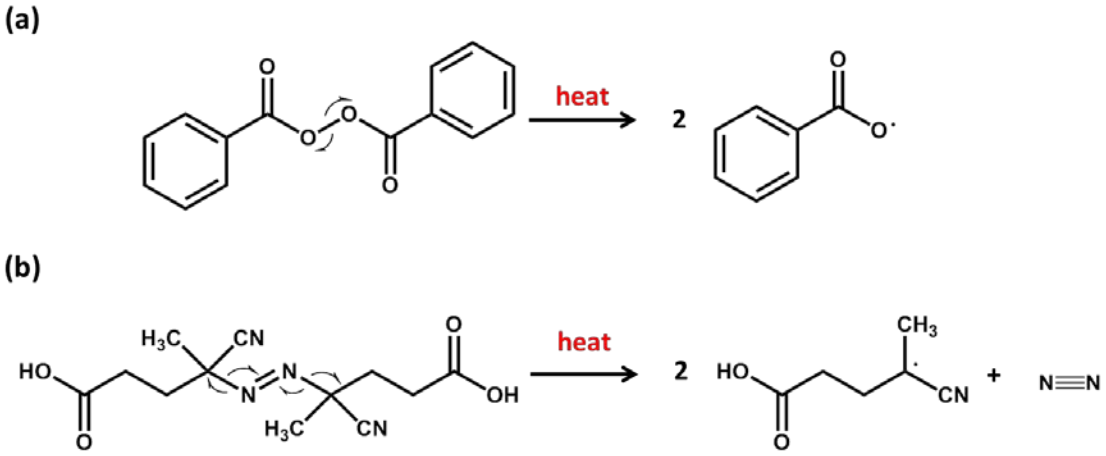

Figure 1.3. Reaction mechanism for the thermal decomposition of two common free radical initiators: (a) benzoyl peroxide and (b) 4,4'-azobis-4-cyanopentanoic acid. These reagents undergo homolytic cleavage on heating to generate primary radical species.

Initiation then occurs when a primary free radical (*R*•) reacts with a vinyl monomer (*M*) to produce a chain-initiating radial (RM_1•). It is this initiation step (specifically initiator decomposition) which is the rate-determining step for free radical polymerisation (see below for a more detailed kinetics discussion). Successive monomer additions then occur during propagation, until chain termination occurs. Termination of the chain can occur in one of two ways, either by combination or disproportionation. This is one reason why free radical polymerisation forms polymers that are relatively polydisperse. If termination occurs by combination, two radical chains combine to form a single bond and the resulting polymer has a molecular weight equal to the sum of the two original polymer radicals (producing $RM_{n+m}R'$). Alternatively, termination by disproportionation may occur, whereby a hydrogen atom is transferred from one polymer chain to another, resulting in a terminal vinyl group on one chain and a hydrogen-capped chain (producing $RM_n(CH{=}CH_2) + R'M_m$).

The rate of polymerisation is the rate at which monomer is consumed. Monomer consumption occurs in both the initiation and propagation steps. However, monomer consumption during initiation is negligible relative to that consumed during the

propagation step. Therefore, the rate of polymerisation can be approximated to the rate of propagation:

$$-\frac{d[M]}{dt} \approx R_p = k_p [RM_n^{\bullet}] [M] \qquad (1.1)$$

where $[M]$ is the monomer concentration, k_p is the rate constant of propagation, R_p is the rate of propagation and $[RM_n\bullet]$ is the polymer radical concentration. It is assumed that the rate of initiation (R_i) is equal to the overall rate of radical termination by combination and disproportionation (R_t, where $R_t = R_{tc}$ and R_{td}). Therefore, the concentration of polymer radicals, $[RM_n\bullet]$, is constant throughout the polymerisation. Consequently, the rate of change of radical concentration is effectively zero (this is the so-called steady-state approximation). This can be expressed as:

$$-\frac{d[RM_n^{\bullet}]}{dt} = R_i - R_t = 0 \qquad (1.2)$$

If we then substitute into this rate equation for the overall rate of termination by combination and disproportionation, we obtain Equation 1.3:

$$R_i - 2\, k_t [RM_n^{\bullet}] [RM_n^{\bullet}] = 0 \qquad (1.3)$$

Combining Equation 1.2 and Equation 1.3, we obtain an expression for the overall rate of initiation or termination (Equation 1.4):

$$R_i = R_t = 2\, k_t [RM_n^{\bullet}]^2 \qquad (1.4)$$

where k_t is the overall rate constant for radical termination (i.e. $k_t = k_{tc}+k_{td}$). The numerical factor of two arises because two polymer radicals are destroyed in each termination event. Equation 1.4 can be rearranged in terms of $[RM_n\bullet]$ and substituted into Equation 1.1 to give Equation 1.5:

$$R_p = k_p [M] \left(\frac{R_i}{2 k_t}\right)^{1/2} \quad (1.5)$$

Thus, the rate of propagation, R_p, has a square-root dependence on the initiation rate, R_i. As discussed earlier, initiation consists of two steps: (i) generation of primary radicals by dissociation of the initiator (commonly by thermolysis), followed by (ii) the addition of one monomer unit to generate the secondary radical adduct. The first step is much slower than the latter. Therefore, initiator decomposition is considered the rate-determining step for initiation, see Equation 1.6:

$$R_i = R_d = 2 f k_d [I] \quad (1.6)$$

where R_i is the rate of initiation, R_d is the rate of decomposition, f is the initiator efficiency, k_d is the rate constant for initiator decomposition and [I] is the initiator concentration. The initiator efficiency is defined as the fraction of radicals produced that go on to initiate polymer chains. Equation 1.6 can now be substituted into Equation 1.5 to give the rate equation for free radical chain polymerisation:

$$R_p = k_p [M] \left(\frac{f k_d [I]}{k_t}\right)^{1/2} \quad (1.7)$$

Equation 1.7 shows that the rate of free radical polymerisation depends on the square root of the initiator concentration and is first order with respect to monomer concentration.

As discussed above, in a free radical polymerisation, the rate of initiation is significantly slower than the rate of propagation ($R_i < R_p$).[4] Consequently, once initiation does occur, high molecular weight polymers are formed relatively quickly, making it difficult to control the molecular weight distribution of the resulting polymer. Moreover, if initiation continues to occur under monomer-starved conditions, the resulting polymer chains will be much shorter than those chains initiated at the beginning of the reaction.

Dispersion Polymerisation

Dispersion polymerisation was developed by researchers at both ICI[5] and Rohm & Haas[6] in the early 1960s as a method of producing near-monodisperse particles in the range of 0.1 to 15 μm.[7] In conventional free radical dispersion polymerisations, the continuous phase is a good solvent for the monomer, free radical initiator and steric stabiliser, but a non-solvent for the growing polymer chains. Therefore, the reaction mixture is initially homogeneous but becomes heterogeneous as the polymerisation progresses. Short polymer chains (oligomers) are formed and grow to a certain critical chain length, whereby nucleation occurs and the polymer chains precipitate from solution, leading to the formation of primary particles.[8] These primary particles are swollen by the polymerisation medium and/or the monomer. As a result, polymerisation progresses within the individual particles, leading to the formation of colloidally stable spherical polymer latex particles.[9] The steric stabiliser is used to prevent macroscopic precipitation. In the absence of this steric stabiliser, the polymer chains would simply precipitate from solution. The steric stabiliser must have two distinct properties: (i) it must contain at least one segment with an affinity for the polymer particle surface and (ii) it must contain a segment that is soluble in the chosen solvent.[8]

Emulsion Polymerisation

Emulsion polymerisation was established at the Goodyear Tyre and Rubber Company in the 1920s.[10] It produces a free-flowing aqueous dispersion of latex particles from which the polymer can be readily separated if required.[11] A typical free radical emulsion polymerisation comprises a water-immiscible monomer, a surfactant, a solvent-soluble free-radical initiator and water.[12] As the monomer is not soluble in the continuous phase, emulsion polymerisation is heterogeneous from the outset. However, the initiator and stabiliser are soluble in the continuous phase. The monomer has relatively low water solubility but is dispersed in the continuous phase by the surfactant (the monomer is largely confined within the monomer droplets and surfactant micelles).

Emulsion polymerisation offers many advantages over other polymerisation techniques. The low viscosity and high heat capacity of water leads to efficient stirring and excellent heat dissipation, respectively. Water is also a cheap and

environmentally-friendly solvent. Emulsion polymerisation also allows high molecular weight polymers to be generated at high rates and to very high conversions, with the latex products often requiring little or no further processing. One disadvantage to conventional emulsion polymerisation is that a high level of surfactant is usually required in order to disperse the water-immiscible monomer in the form of emulsion droplets.

Living Anionic Polymerisation

Living anionic polymerisation has become a widely used method of polymerisation since the pioneering work of Szwarc and co-workers[13] in 1956 whereby the propagating species was a carbanion.[10] Thus, there is electrostatic repulsion between the growing anionic polymer chain-ends and hence living anionic polymerisations involve no intrinsic termination step. This allows the synthesis of narrow molecular weight distribution polymers with predictable target molecular weights, according to Equation 1.8, where the number-average molecular weight (M_n) is simply calculated by the mass of monomer divided by the number of moles of initiator.[14]

$$M_n\,(\mathrm{g\,mol^{-1}}) = \frac{M(\mathrm{g})}{I(\mathrm{mol})} \qquad (1.8)$$

The average number of structural units per polymer chain, otherwise known as the number-average degree of polymerisation (DP), can be targeted by adjusting the molar ratio of the monomer and initiator, as shown in Equation 1.9.

$$\mathrm{DP} = \frac{[M]}{[I]} \qquad (1.9)$$

In living anionic polymerisation, the rate of initiation is much faster than the rate of propagation ($k_i >> k_p$).[15] This ensures that all chains are initiated at the same time and subsequently grow uniformly. Thus the molecular weight increases linearly with conversion. This is in contrast to free radical polymerisation, whereby the molecular weight increases very quickly, then attains an approximately constant value (see Figure 1.4).

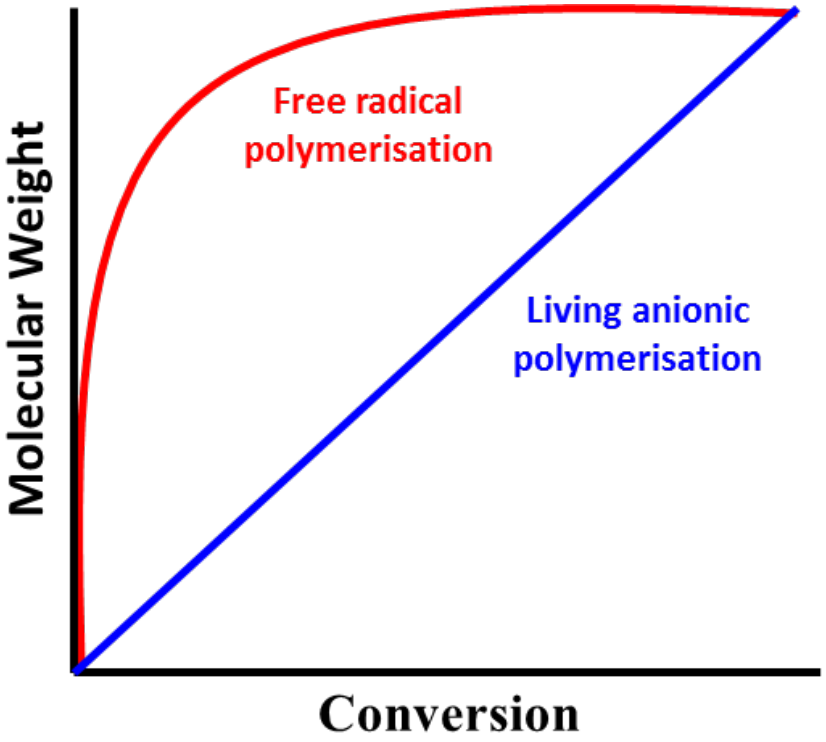

Figure 1.4. Molecular weight vs. conversion curves for living anionic polymerisation and free radical polymerisation.[16]

The monomer (and growing chain-ends) must be able to stabilise anionic charge. Hence suitable monomers for living anionic polymerisation include vinyl monomers (H_2C=CHX) with electron-withdrawing X groups (e.g. phenyl, cyano or ester functionalities). The choice of solvent is also important. Protic solvents such as water or ethanol react rapidly with the active anion species via proton abstraction and thus are unsuitable. For the same reason, any protic impurities in the monomer must be completely removed prior to polymerisation and all glassware must be thoroughly dried to remove traces of moisture.

Living anionic polymerisation enables synthesis of well-defined block copolymers by sequential monomer addition, along with functionalised chain-ends by selective termination with appropriate reagents such as dry carbon dioxide or ethylene oxide.[17] In their initial communication, Szwarc et al.[18] reported the synthesis of polyisoprene-polystyrene-polyisoprene (PI-PS-PI) triblock copolymers via sequential monomer addition. Although this is a good example of living polymerisation, PI-PS-PI is not a particularly useful material. In 1963, Holden and Milkovich[19] patented the synthesis of polystyrene-polybutadiene-polystyrene (PS-PB-PS) using an *n*-

butyllithium initiator in a hydrocarbon solvent. These triblock copolymers were commercialised by Shell Chemicals (now Kraton). Since the PS and PB blocks are enthalpically incompatible, they form microphase-separated structures in the solid state. The relatively short outer PS blocks have a high glass transition temperature (T_g) whereas the relatively long inner PB block has a low T_g. Hence these copolymers are useful as thermoplastic elastomers or gels.[18] Other applications for related PS-PB block copolymers include lubricants and diesel soot dispersants. BASF markets a range of PS-PB star diblock and star-tapered copolymers made by coupling four living PS-PB chains.[20, 21] With high PS and low PB content (known as *Styrolux*®), such materials are used as tough impact-resistant thermoplastics. In contrast, copolymers comprising low PS and high PB content (known as *Styroflex*®) produce highly flexible transparent wrapping material. Similarly, a PS-PI star diblock copolymer is produced by Phillips under the trade name *Solprene*®.[22] A similar product is marketed as a viscosity modifier (thickener) for engine oils by Kraton.[23]

However despite its impressive control over molecular weight distribution and copolymer architecture, the synthetic utility of anionic polymerisation is rather limited. This is because this technique is only suitable for a relatively small sub-set of vinyl monomers.

Controlled/Living Radical Polymerisation

Controlled/living radical polymerisation is a 'pseudo-living' technique. Such polymerisations are characterised by the suppression of chain termination relative to chain propagation. This is achieved by creating a rapid equilibrium between active and dormant chains. Active polymer radicals are reversibly deactivated to minimise the probability of premature termination. Although termination is reduced considerably, it is still present to some extent. Consequently, there has been some dispute over nomenclature. Hence the International Union of Pure and Applied Chemistry (IUPAC) has recommended using the term "reversible deactivation radical polymerisation" (RDRP).[15] Examples of RDRP include nitroxide-mediated polymerisation (NMP) and atom transfer radical polymerisation (ATRP). One of the most widely used types of RDRP is reversible addition-fragmentation chain transfer

(RAFT) polymerisation.[15, 24] This is the synthetic technique used in this thesis and will be discussed in detail later.

Block Copolymer Self-Assembly

Self-assembly occurs spontaneously and is a thermodynamically-driven process. The self-assembled structures are not held together by strong covalent or ionic bonds but by weaker van der Waals interactions, hydrogen bonding and screened electrostatic interactions.[25] This results in soft, flexible materials that can respond to changes in the solution pH or electrolyte concentration.

The assembly of amphiphilic AB diblock copolymers has been extensively researched.[26-29] Block copolymers can undergo self-assembly in the bulk[26, 30] as well as in solution.[31] In the former case, microphase separation is typically observed as a result of the enthalpic incompatibility between the blocks.[27] In solution, amphiphilic block copolymers can self-assemble to form various morphologies, including spherical micelles,[32] worm-like micelles[33] and vesicles.[34] Three parameters influence the final copolymer morphology: (1) the volume fraction f_A and f_B for the A and B blocks, where the total volume fraction must equal unity ($f_A + f_B = 1$); (2) the total DP (N) of the two blocks (where $N = DP_A + DP_B$); (3) the Flory-Huggins parameter, χ_{AB} (defined in Equation 1.10), which describes the incompatibility between the two blocks.[35-37]

$$\boldsymbol{\chi_{AB}} = \left(\frac{\mathbf{1}}{\boldsymbol{k_B T}}\right)\left[\boldsymbol{\varepsilon_{AB}} - \frac{\mathbf{1}}{\mathbf{2}}(\boldsymbol{\varepsilon_{AA}} + \boldsymbol{\varepsilon_{BB}})\right] \qquad (1.10)$$

Here k_B is the Boltzmann constant, T is the absolute temperature and ε_{AB}, ε_{AA} and ε_{BB} are the three interaction energies for the A and B blocks.[35] The Flory-Huggins parameter varies inversely with temperature and this parameter is positive when A-B interactions result in an increase in the overall energy. Combining the Flory-Huggins parameter (χ_{AB}) with the DP can give the degree of segregation (χN) between the two blocks. Comparing this to the block volume fraction allows prediction of the copolymer morphology formed for the AB diblock. When f_A is 0.5 (equal volume fractions of the A and B blocks) then lamellae are observed. At lower f_A values,

either spheres or worms are expected. Increasing f_A above 0.5 leads to inverted structures.[38]

In solution, the precise nanostructure that is formed depends on the hydrophilic/ hydrophobic balance of the copolymer, which changes the molecular curvature.[39] If the hydrophilic block is kept constant, and the length of the hydrophobic core-forming block is increased, the resulting reduction in curvature can lead to the formation of higher-order morphologies such as cylindrical (worm-like) micelles or vesicles (Figure 1.5).[39] The curvature is related to the packing parameter, *P*, which is defined in Equation 1.11:

$$P = \frac{a_0}{l_c v} \qquad (1.11)$$

where a_0 is the optimal area of the head-group (or the hydrophilic stabiliser block), l_c is the chain length of the hydrophobic core-forming block and *v* is the volume of the hydrophobic core-forming block.

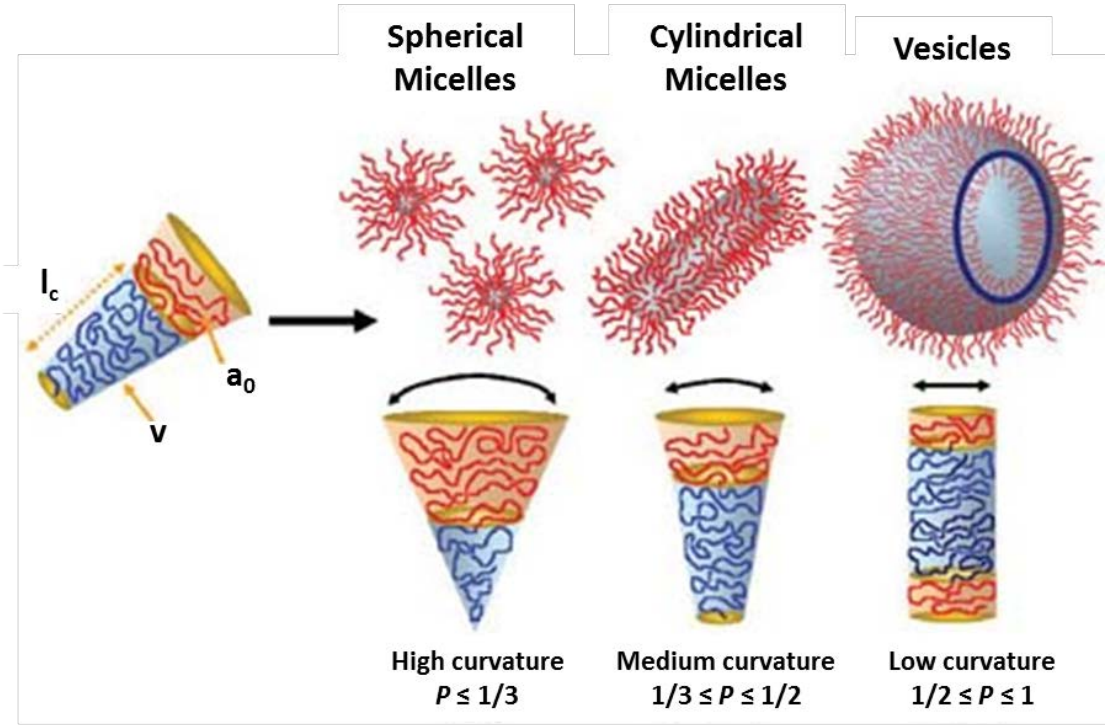

Figure 1.5. Self-assembly of an AB diblock copolymer into three different morphologies depending on the curvature of the copolymer in solution.[39] Cylindrical micelles are also known as worms. The packing parameter, *P*, depends on the optimal area of the hydrophilic group, a_0, the volume of the hydrophobic block, *v*, and the chain length of the hydrophobic block, l_c.

Such block copolymer nano-objects can be prepared using post-polymerisation processing techniques, such as rehydration of a copolymer film,[40] addition of a non-solvent for the membrane forming block,[41, 42] or by a temperature[42] or pH[43] trigger. Such processes are usually conducted in dilute solution (e.g. < 1 % w/w copolymer).

Over the past five years or so, polymerisation-induced self-assembly (PISA) has become established as a powerful tool for the rational design and efficient synthesis of a wide range of diblock copolymer nano-objects in either aqueous or non-aqueous media.[44-47] One advantage of this technique is that block copolymer nanoparticles can be prepared at copolymer concentrations of up to 25 % w/v solids.[48-52] PISA will be used throughout this thesis to prepare a wide range of block copolymer nano-objects.

Reversible Addition-Fragmentation Chain Transfer (RAFT) Polymerisation

Mechanism

RAFT is a type of controlled 'living' radical polymerisation that can produce well-defined block copolymers.[53] It was first reported by Rizzardo and co-workers[53] in 1998. RAFT polymerisation provides good control over the copolymer molecular weight, with narrow molecular weight distributions (M_w/M_n < 1.30) being routinely achievable.[54] The choice of RAFT chain transfer agent (CTA) is essential for a well-controlled polymerisation.[24] The generic chemical structures for a dithioester and trithiocarbonate RAFT CTA are shown in Figure 1.6.

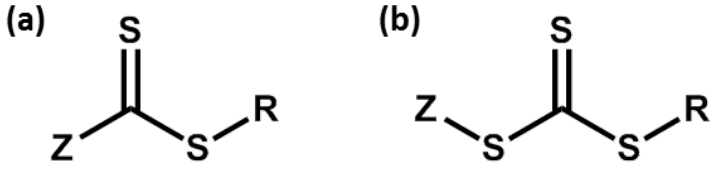

Figure 1.6. Generic chemical structures for (a) a dithioester and b) a trithiocarbonate RAFT chain transfer agent, where R is a good radical leaving group and Z is a good stabilising group.

The Z group activates the C=S bond towards radical addition and stabilises the transition state formed on addition of the propagating radical. The R group must be a good radical leaving group, but should also be capable of re-initiating polymerisation.[53] Like living polymerisation, the target DP does not depend on any rate constants or other kinetic parameters. Instead, the DP is simply given by the

monomer concentration divided by the RAFT CTA concentration, as shown in Equation 1.12.

$$\mathrm{DP} = \frac{[M]}{[\mathrm{CTA}]} \qquad (1.12)$$

The RAFT polymerisation mechanism[15, 24] is based on the same four steps already presented for free radical polymerisation, however the propagation step is different (see Figure 1.7). Initiation involves a conventional free radical initiator such as azo or peroxide compounds to generate radicals, which then react with multiple monomer units to generate polymer radicals (P_n•).

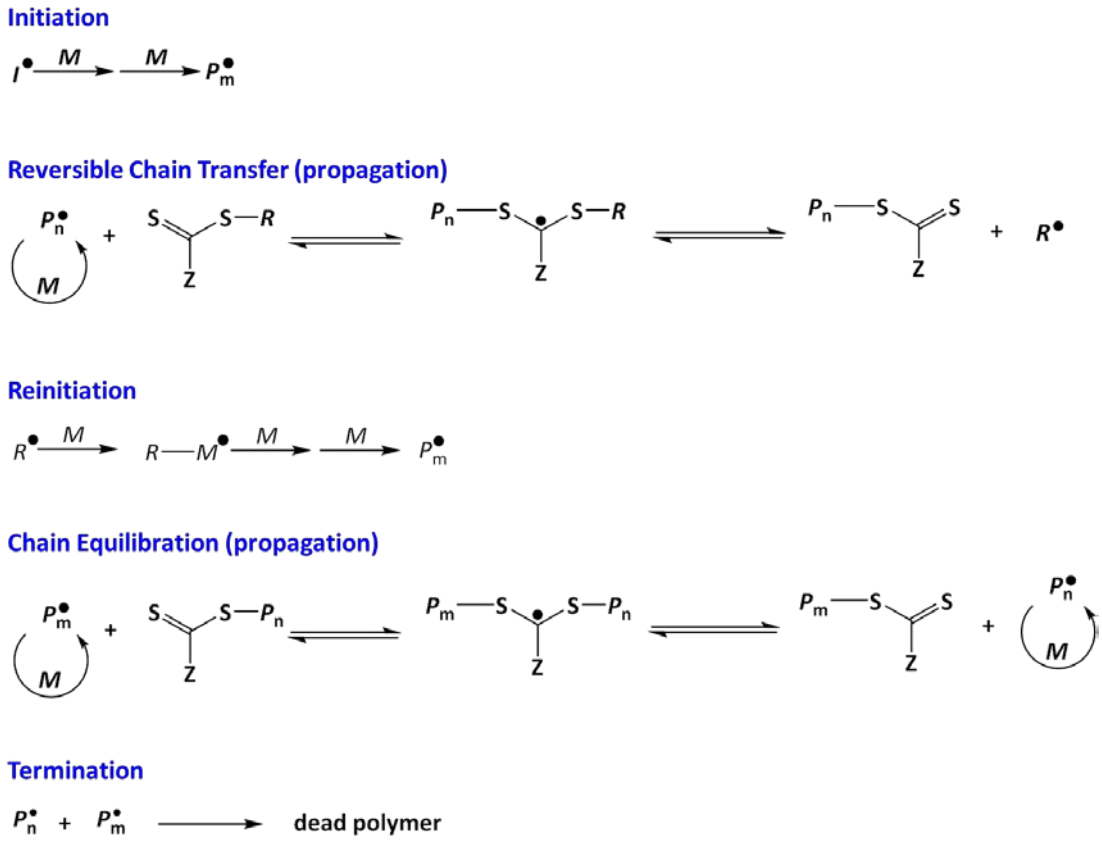

Figure 1.7. The postulated RAFT mechanism as outlined by Rizzardo et al,[55] where *I* = initiator, *M* = monomer, *P* = polymer and *R* = radical.

RAFT propagation has the additional kinetic steps of reversible chain transfer, reinitiation and chain equilibrium, as shown in Figure 1.7.[55] Reversible chain transfer involves a growing polymer radical reacting with the RAFT CTA, resulting in the removal of a radical (*R*•). This radical reinitiates the polymerisation, reacting with

monomer units to form a new polymer radical (P_m•), which then reversibly adds to the polymeric CTA produced in the reversible chain transfer step. This is the chain equilibrium step which enables controlled chain growth,[56] thus allowing specific molecular weights to be targeted and giving narrow molecular weight distributions. RAFT suppresses the rate of termination of polymer radicals relative to the rate of propagation, but some background termination is still present.[55] The probability of termination (and hence chain-end deactivation) increases under monomer-starved conditions. Therefore, these polymerisations are often quenched prior to complete conversion to allow the RAFT CTA to remain attached to the polymer chains for subsequent chain extension, if required. The 'living' nature of the RAFT mechanism is an important aspect which will be utilised in this project to design novel block copolymer nano-objects.

One disadvantage of RAFT polymerisation is that it produces intrinsically coloured and occasionally malodorous polymers, both of which are due to the sulfur-based RAFT CTA end-group.[57] However, removal of the RAFT end-group under controlled conditions after polymerisation can be achieved via aminolysis,[58] ozonolysis,[59] bond cleavage using radicals derived from addition of excess initiator,[60, 61] thermolysis,[62] addition of hydrogen peroxide[63] or light-mediated removal.[64]

RAFT Solution Polymerisation

One essential requirement for a solution polymerisation is that the monomer and the resulting polymer should be sufficiently soluble in the chosen solvent. RAFT solution polymerisations can be performed in many solvents, such as alcoholic media[65-67], *n*-alkanes[44, 68] and water.[69]

RAFT Aqueous Dispersion Polymerisation

One important difference between conventional dispersion polymerisation and RAFT dispersion polymerisation is that the steric stabiliser used in the latter technique is a solvent-soluble macro-CTA, previously synthesised by RAFT solution polymerisation. The solvent-miscible monomer polymerises from the macro-CTA to form oligomers. These oligomers are soluble in the solvent up to a certain critical DP. Thereafter, the growing polymer becomes insoluble in the solvent, causing

precipitation to form nascent diblock copolymer particles, which are stabilised by the solvent-soluble macro-CTA.

RAFT aqueous dispersion polymerisation requires chain extension of a water-soluble polymer with a water-miscible monomer that polymerises to form a water-insoluble polymer.[70] The use of aqueous media for RAFT polymerisations offers several advantages: water is cheap, non-toxic, non-flammable and has a high heat capacity. This means it is attractive on an industrial scale for both economic and environmental reasons.

The use of RAFT aqueous dispersion polymerisation for the synthesis of well-defined nanoparticles was first reported in 2010 by Li and Armes.[71] The prototype formulation was based on chain extension of a poly(glycerol monomethacrylate) (PGMA or G) macromolecular chain transfer agent (macro-CTA) using 2-hydroxypropyl methacrylate (HPMA); the chemical structures of these glycerol monomethacrylate (GMA) and HPMA monomers are shown in Figure 1.8.

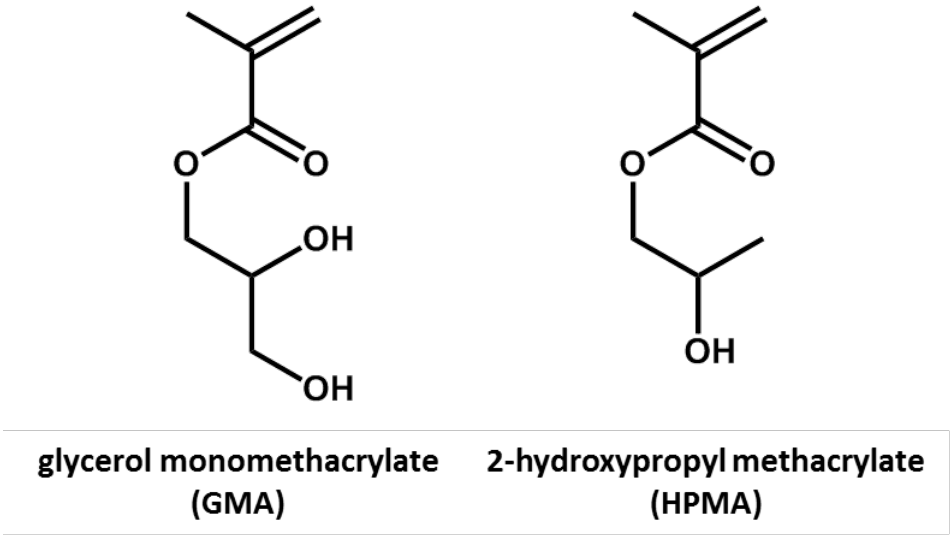

Figure 1.8. Chemical structures of glycerol monomethacrylate (GMA) and 2-hydroxypropyl methacrylate (HPMA). In each case only the major isomer is shown.[72]

The initial reaction solution is homogeneous since HPMA is water-miscible up to 10 % w/w at 70 ^{o}C.[73] As the RAFT polymerisation proceeds, the growing poly(2-hydroxypropyl methacrylate) (PHPMA or H) chains become water-insoluble. At this nucleation point *in situ* self-assembly occurs to form nanoparticles comprising a PHPMA core that are stabilised by the water-soluble PGMA chains. Since such self-assembly occurs as a result of the polymerisation, this process is called polymerisation-induced self-assembly (PISA). Two important parameters dictate the

final morphology of the copolymer: (i) the relative mean degree of polymerisation (DP) of the hydrophilic and hydrophobic blocks; (ii) the total solids concentration at which the PISA synthesis is conducted.[48] By systematically adjusting these parameters, a range of morphologies can be observed such as spherical micelles, worm-like micelles, and vesicles, plus various other, more transient, species such as branched worms, partially coalesced worms, nascent bilayers, "octopi" and "jellyfish".[49] Spherical micelles, worm-like micelles and vesicles can be reproducibly targeted for this versatile PGMA-PHPMA formulation following the construction of a predictive phase diagram, as shown in Figure 1.9.[50]

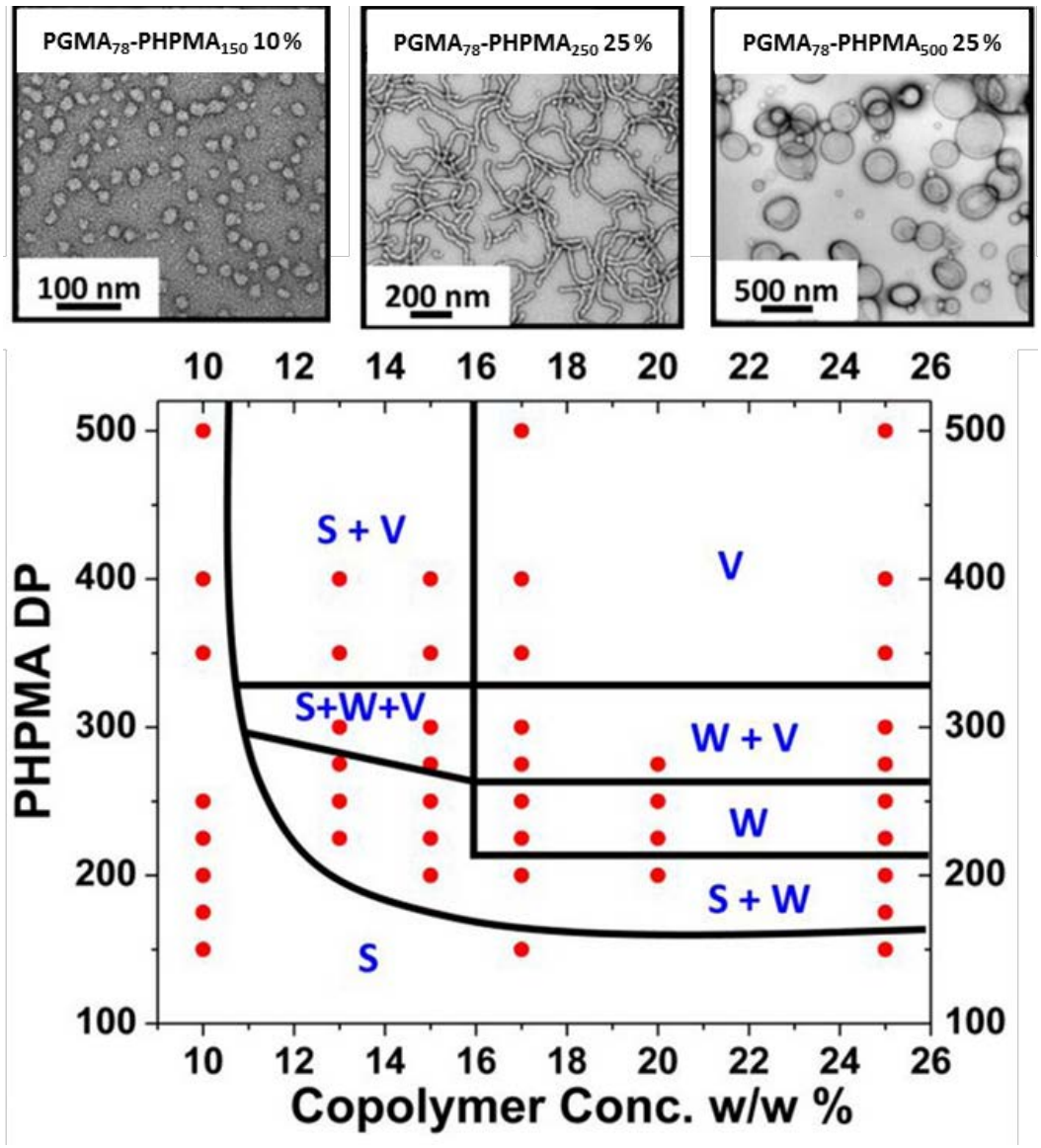

Figure 1.9. Phase diagram and selected transmission electron microscopy (TEM) images for a series of $PGMA_{78}$-$PHPMA_y$ diblock copolymers synthesised by RAFT aqueous dispersion polymerisation at concentrations ranging from 10 to 25 w/w % [S = spherical micelles, W = worms, and V = vesicles].[50]

However, higher order morphologies are not always achievable. Blanazs et al.[50] found that when a $PGMA_{112}$ stabiliser block was chain-extended with a sufficiently long PHPMA core-forming block, only spherical micelles were formed. The *in situ* evolution of morphology from spheres to worms or vesicles is most likely prevented as a result of more effective steric stabilisation, which impedes initial particle fusion. In order for higher order morphologies to be achieved, spherical micelles must first fuse together to form worms. If this sphere-to-worm transition cannot occur, the final morphology is simply kinetically-trapped spheres, regardless of the diblock copolymer asymmetry.

More recently, Warren et al.[52] tested the vesicular morphology to destruction. A series of $PGMA_{55}$-$PHPMA_y$ diblock copolymers were synthesised, with y ranging from 200 to 1000. DLS and SAXS studies indicated minimal change in the overall vesicle diameter when y = 400 to 800. However, the mean membrane thickness increased, hence the vesicle lumen must become smaller if the external vesicle dimensions remains constant (see Figure 1.10). Vesicle 'death' occurs when y exceeds 1000, which is thought to be due to greater steric congestion of the inner (vesicle lumen) stabiliser chains with increasing inner curvature.

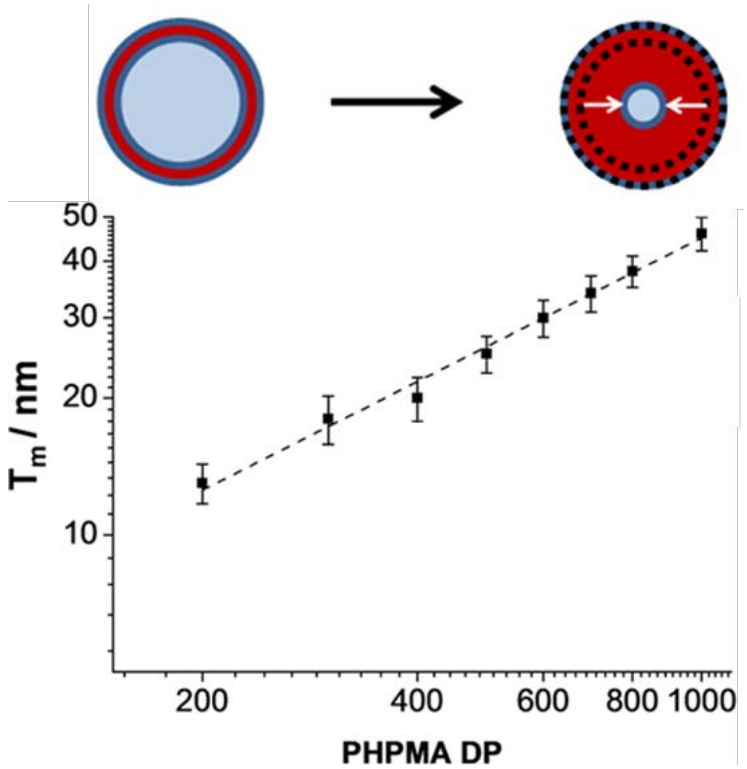

Figure 1.10. Evolution of vesicle membrane core thickness (T_m) with PHPMA DP (y) for a series of $PGMA_{55}$-$PHPMA_y$ block copolymer vesicles, measured using SAXS. The error bars in the SAXS data indicate the membrane polydispersity. Note: Figure adapted from Warren et al.[52]

RAFT Aqueous Emulsion Polymerisation

The main difference between conventional emulsion polymerisation and RAFT emulsion polymerisation is that there is no need for surfactant to be present in the latter technique. Instead, a polymeric surfactant is used, such as a hydrophilic macro-CTA. The water-immiscible monomer polymerises from the water-soluble macro-CTA, and the growing chains remain soluble in the reaction solution up to a critical DP. At this point, the hydrophobic oligomer becomes insoluble and self-assembles into micelles where the hydrophilic macro-CTA acts as a steric stabiliser for the nanoparticles. RAFT aqueous emulsion polymerisation offers some advantages over other controlled radical polymerisation techniques given its compatibility with a wide range of vinyl monomers, functional groups and experimental conditions. In contrast, RAFT aqueous dispersion polymerisation is only applicable to a rather limited set of vinyl monomers.[51]

RAFT aqueous emulsion polymerisation has been investigated in considerable detail in recent years. Hawkett et al. developed the first successful RAFT emulsion polymerisation formulation by chain extending a poly(acrylic acid) macro-CTA using *n*-butyl acrylate to form stable latex particles.[74-76] Furthermore, poly(acrylic acid)-poly(styrene)-poly(*n*-butyl acrylate) triblock copolymers were formed, leading to the formation of stable latexes.[77]

More recently, Charleux and co-workers studied a range of hydrophilic stabiliser blocks (acrylic,[78-80] methacrylic,[81] and acrylamide[82]) and hydrophobic core-forming blocks (*n*-butyl acrylate,[82] styrene,[81, 83, 84] methyl methacrylate,[85] and benzyl methacrylate[86]). Various formulations have been optimised to give high conversions, narrow molecular weight distributions and good control over the copolymer morphology. The first example of RAFT emulsion polymerisation to yield non-spherical nano-objects involved a poly(acrylic acid-*co*-ethylene oxide) methyl ether acrylate) macro-CTA.[81] This bifunctional water-soluble precursor was chain-extended using styrene to form a series of diblock copolymer nanoparticles.[81] PISA led to the formation of spheres, fibres (worms) or vesicles. Pure phases were achieved by replacing this acrylic macro-CTA with the equivalent methacrylic macro-CTA for the polymerisation of styrene.[87] An extensive review article summarising the development of RAFT emulsion polymerisation was published in 2012.[88]

A more recent study by Cunningham et al.[89] showed that a non-ionic water-soluble $PGMA_{51}$ macro-CTA (synthesised by RAFT solution polymerisation) could be chain-extended with benzyl methacrylate (BzMA) via RAFT aqueous emulsion polymerisation to form diblock copolymer nanoparticles. Despite exploring a wide range of variables such as the PGMA DP, PBzMA DP and copolymer concentration, only spherical morphologies could be obtained. It is still not understood why this is so often the case for such RAFT aqueous emulsion polymerisation formulations. It is postulated that diffusion of the water-immiscible BzMA monomer through the aqueous phase may occur too slowly on the time scale of the polymerisation to provide sufficient plasticisation of the growing PBzMA blocks. However, this hypothesis does not explain why Charleux et al. managed to achieve higher order morphologies using styrene as the core-forming block.[77, 82, 85]

Framboidal Nanoparticles

Various types of diblock copolymer nanoparticles can be readily synthesised via PISA using RAFT aqueous dispersion polymerisation. Chambon et al. showed that such formulations have sufficiently good living character to allow the production of well-defined ABC triblock copolymer vesicles via addition of a third comonomer.[90] Thus, addition of water-immiscible BzMA to a linear PGMA-PHPMA AB diblock copolymer vesicle precursor leads to novel framboidal ABC triblock copolymer vesicles via a seeded RAFT emulsion polymerisation mechanism. Here the BzMA is solubilised within the hydrophobic vesicular membrane and is polymerised therein. The chemical structure of these ABC triblock copolymer vesicles is shown in Figure 1.11, whereby the values of x and y are fixed for the AB diblock vesicle precursor, and z is systematically varied.

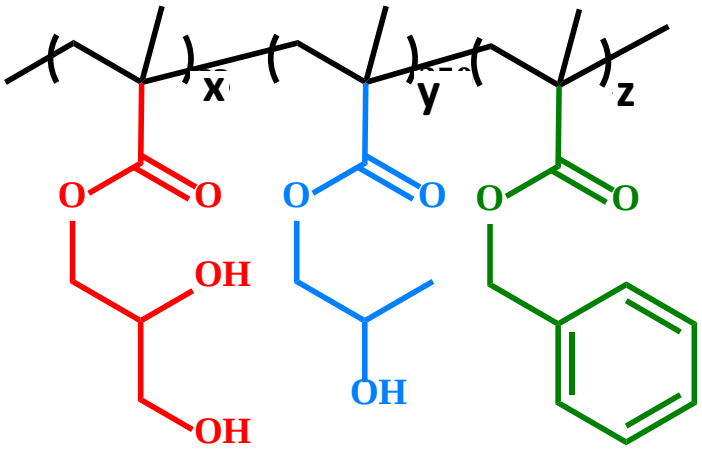

Figure 1.11. Chemical structure of a series of $PGMA_x$-$PHPMA_y$-$PBzMA_z$ triblock copolymers prepared by Chambon et al. whereby x = 58, y = 350 and z ranges from 200 to 400.[90]

As the BzMA polymerises, nano-scale phase separation within the hydrophobic vesicular membrane occurs, which is driven by enthalpic incompatibility between the PHPMA and the PBzMA blocks. This leads to the efficient production of framboidal (raspberry-like) ABC triblock copolymer vesicles. Transmission electron microscopy (TEM) studies reveal distinctive globules on the surface of the vesicles.

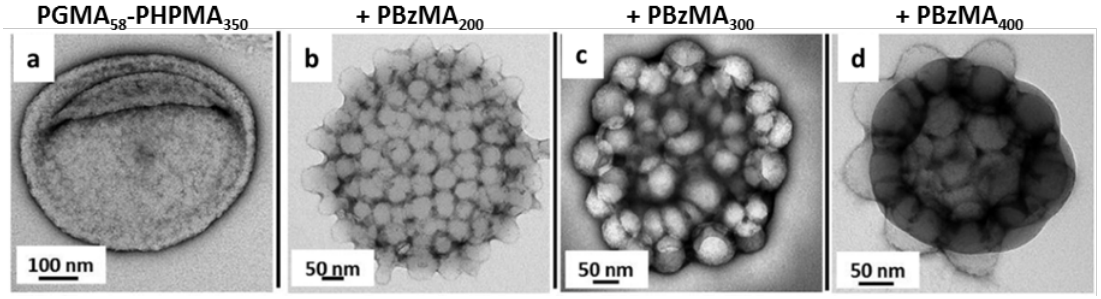

Figure 1.12. Representative transmission electron micrographs obtained for (a) linear diblock copolymer precursor vesicles and (b), (c) and (d) framboidal triblock copolymer vesicles.[90]

Chambon et al.[90] showed that the globule size (and consequently the surface roughness) can be tuned by varying the mean target degree of polymerisation of the PBzMA block (as shown in Figure 1.12). This suggests that the globules are mainly composed of PBzMA, which is the more hydrophobic of the two core-forming blocks.

Gel permeation chromatography (GPC) studies indicated unimodal traces for these framboidal ABC triblock copolymer vesicles with high blocking efficiencies being observed for the PGMA macro-CTA and the PGMA-PHPMA diblock precursor vesicles (see Figure 1.13). However, polydispersities of 1.21, 1.44 and 1.50 were obtained for target PBzMA DPs of 200, 300 and 400, respectively.[90] These molecular

weight distributions were somewhat broader than those expected for RAFT polymerisations (for which $M_w/M_n \leq 1.30$ is typical).[54] This problem is most likely due to the relatively low macro-CTA/initiator molar ratio of 2.0 used in these polymerisations, resulting in less control over the polymerisation.[55]

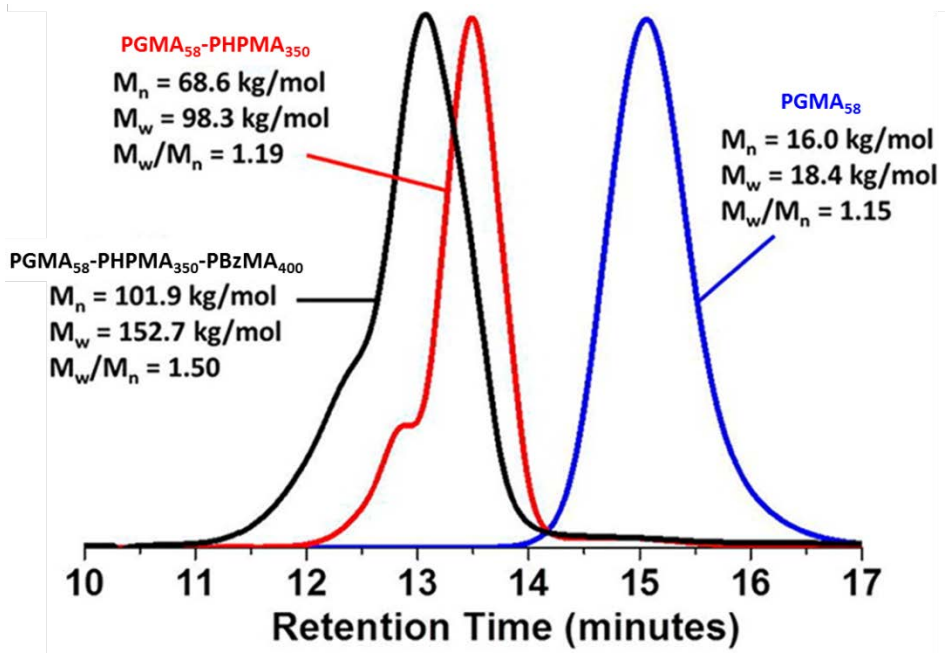

Figure 1.13. DMF GPC curves (vs poly(methyl methacrylate) standards) obtained for a $PGMA_{58}$ macro-CTA, $PGMA_{58}$–$PHPMA_{350}$ diblock copolymer precursor vesicles, and $PGMA_{58}$–$PHPMA_{350}$–$PBzMA_{400}$ triblock copolymer framboidal vesicles obtained via PISA.[90]

Block Copolymer Nanoparticles as Delivery Vehicles

Scope

Microcompartmentalisation is a fundamental prerequisite for life on Earth.[91-94] Microencapsulation is important for a large range of industrial formulations, such as orally-administered drugs,[95] agrochemicals[96, 97] and laundry products.[98, 99] In some cases it is essential for mutually incompatible components to be spatially separated. For example, if enzymes and bleach are mixed in liquid laundry products then enzyme denaturation occurs. In Nature, impermeable lipid membranes provide the physical separation required between components for many intracellular processes. Ideally, microencapsulation enables the controlled release of protected active components. For example, membrane proteins allow the selective diffusion of various chemical species in and out of cells.[100] Components may also be released via an external trigger such as pH and temperature.

Vesicles as Delivery Vehicles

Liposomes[101] and block copolymer vesicles[102-109] (or 'polymersomes') are some of the most widely used carriers in the development of drug delivery applications.[110-112] Typically, such hollow nanoparticles are loaded with water-soluble drugs,[113-115] oligonucleotides,[115-117] enzymes[118] or antibodies.[119] Hydrophobic components can also be loaded into the hydrophobic vesicle membrane. Block copolymer vesicle membranes have been shown to be more stable, and therefore more advantageous, than lipid membranes.[120] Furthermore, with block copolymer vesicles, the membrane properties can be easily tuned by varying the DP and nature of the hydrophobic block.

As discussed above, block copolymer vesicles can be prepared using post-polymerisation processing techniques, such as rehydration of a copolymer film,[40] addition of a non-solvent for the membrane forming block,[41, 42] or by a temperature[42] or pH[43] trigger. As discussed previously, block copolymer vesicles can also be prepared directly in water at high solids with no need for post-polymerisation processing via PISA.[49]

There are many reports of encapsulation of water-soluble molecules within vesicles, including fluorescent dyes and drugs.[41, 42, 107, 121-125] The incorporation of magnetic nanoparticles within block copolymer vesicle membranes has also been described, which may enable active targeting of tumors.[126]

Adams et al.[127] attempted encapsulation via post-polymerisation processing of diblock copolymers. Poly(ethylene oxide)-poly(N,N-diethylaminoethyl methacrylate) (PEO_{45}-$PDEAEMA_{81}$) diblock copolymers form vesicles after a switch from pH 2 to pH 11.[43] At pH 2, the PDEAEMA block is fully protonated and hydrophilic. As the pH increases, the PDEAEMA block becomes deprotonated and hence hydrophobic, causing aggregation of the block copolymer to form vesicles. In this study, riboflavin and rhodamine B dyes are solubilised at pH 2 and become encapsulated when the vesicles form during the pH switch. However, fluorescence studies indicated that no encapsulation occurs. The authors suggested that this was because the PEO_{45}-$PDEAEMA_{81}$ vesicles formed by an unusual mechanism when prepared by a pH switch. Cryo-TEM images indicated that this diblock copolymer first aggregates to form fractals, then spherical micelles, followed finally by vesicles (see Figure 1.14a). It was postulated that restructuring of the spherical micelles into

vesicles was faster than diffusion of the water-soluble dyes through the vesicle membrane into the lumen. Therefore, the dyes were essentially excluded during vesicle formation.

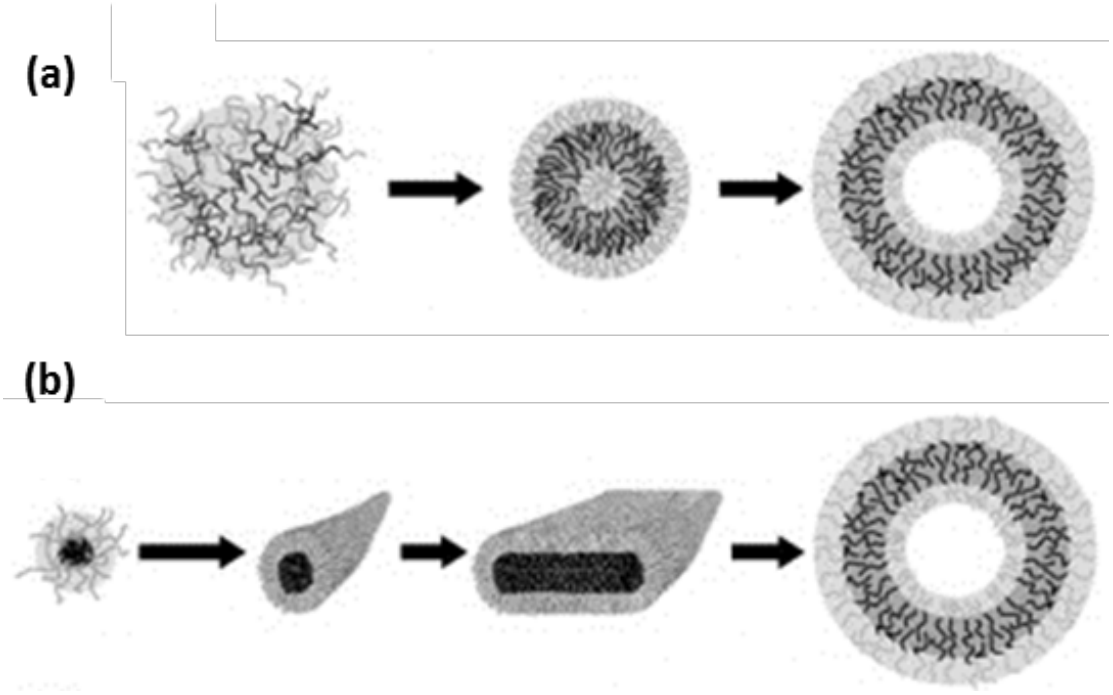

Figure 1.14. Schematic representation of two mechanisms of vesicle formation by block copolymers. (a) Fractals form small micelles, which grow to form larger micelles and then re-arrange to give vesicles. (b) Small micelles form worms, which then form bilayers and finally vesicles. Note: black corresponds to hydrophobic and grey to hydrophilic regions.[127]

However, Adams et al.[127] suggested that the generally accepted mechanisms of vesicle formation would be expected to lead to high encapsulation efficiencies. More specifically, if vesicles were formed from a sequence of spheres, worms and bilayers then the water-soluble component should not be excluded during vesicle formation (see Figure 1.14b).

Clearly, it would be beneficial to prepare loaded block copolymer vesicles directly via a one-step process (such as PISA), rather than relying on post-polymerisation processing techniques. The *in situ* encapsulation of a model hydrophobic dye (Nile Red) within poly(oligo(ethylene glycol) methacrylate)-poly(styrene) (POEGMA-PST) diblock copolymer vesicles using a PISA formulation in methanol was reported by Karagoz et al.[128] However, styrene monomer conversions of only 10% were obtained, so this formulation is of questionable utility. Moreover, this alcoholic PISA formulation has limited applicability for drug delivery. It was also not clear from the reported fluorescence spectroscopy data whether some (or all) of the dye was located

within the vesicle membrane, rather than the lumen. Additionally, encapsulation efficiencies of up to 120 % were claimed, which suggests either an experimental artifact or rather large systematic errors.

More recently, Tan et al.,[47] reported the successful in situ encapsulation of silica nanoparticles and Bovine Serum Albumin (BSA) within monomethoxy poly(ethylene glycol)-poly(2-hydroxypropyl methacrylate) (mPEG-PHPMA) diblock copolymer vesicles synthesised using a photoinitiated PISA formulation at 25°C (see Figure 1.15a). Silica nanoparticles were selected as a model encapsulant (see Figure 1.15b and Figure 1.15c). To examine whether proteins could be encapsulated without losing their biological activity they tested the BSA activity both before and after encapsulation was determined (see Figure 1.15d). Although this served as a promising strategy for preparing BSA-loaded thermosensitive vesicles via mild conditions (visible light, aqueous medium, and room temperature), the extent of encapsulation was not properly characterised so the encapsulation efficiency for this formulation is unknown.

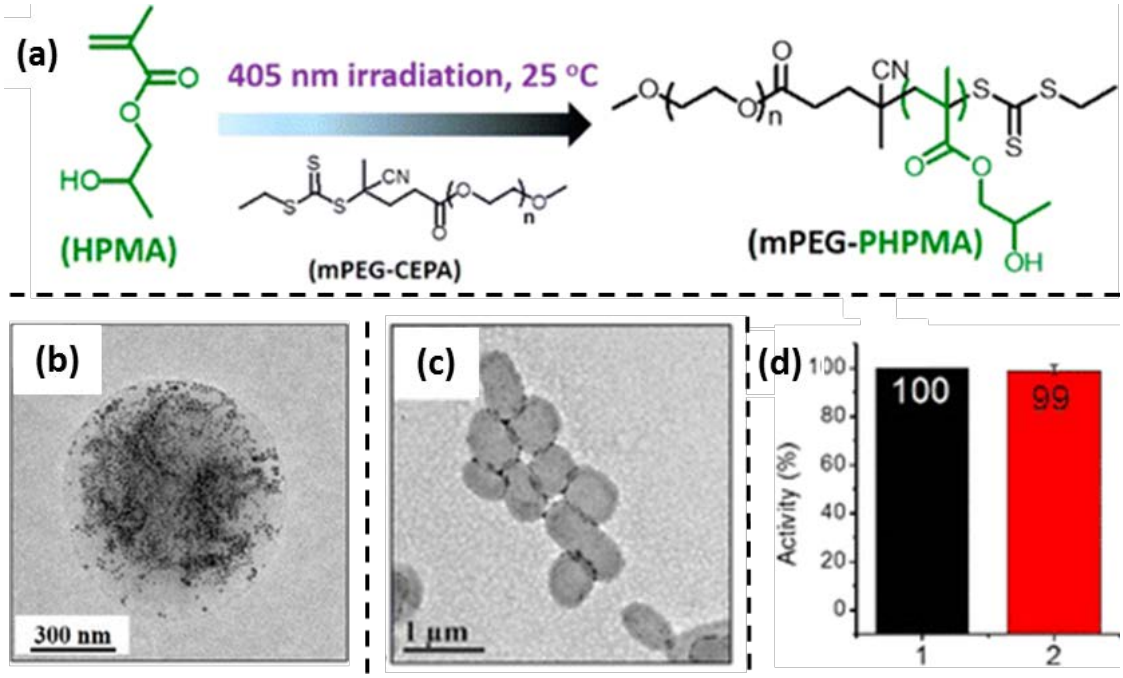

Figure 1.15. (a) Schematic for the preparation of PEG-PHPMA diblock copolymers which form various nano-objects via aqueous photo-PISA. (b) TEM image of purified $mPEG_{113}$-$PHPMA_{360}$ vesicles prepared by aqueous photo-PISA of HPMA in the presence of 3.0 g silica sol (30% solids concentration). (c) TEM image of $mPEG_{113}$-$PHPMA_{360}$ vesicles prepared by photo-PISA in the presence of BSA. (d) Activity of (1) native BSA and (2) BSA in the supernatant of the product prepared by photo-PISA. Figure adapted from Tan et al.[47]

Nanoparticles as Pickering Emulsifiers

Pickering Emulsions

Pickering[129] or Ramsden[130] emulsions comprise water or oil droplets stabilised by colloidal nanoparticles and have been recognised for more than a century. A wide range of nanoparticles such as silica sols[131,132] polystyrene latexes[133-136] or inorganic clays[137] have been shown to be effective Pickering emulsifiers. The nanoparticle wettability dictates the emulsion type. If the nanoparticles used for emulsification are hydrophobic, the contact angle will be greater than 90^o, thus the particle should preferentially sit in the oil phase thereby forming a water-in-oil emulsion. If the nanoparticles are hydrophilic, an oil-in-water emulsion will be formed because the contact angle will be less than 90^o (as shown in Figure 1.16).[138] The nanoparticles discussed in this thesis are hydrophilic as a result of the water-soluble PGMA stabiliser chains expressed at the surface of the nanoparticles, so oil-in-water emulsions are invariably formed.

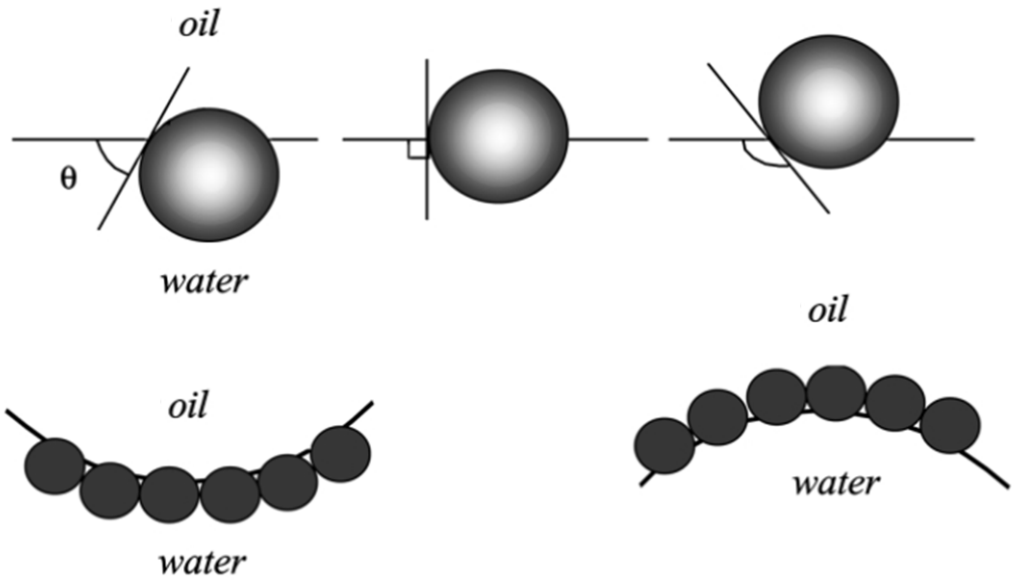

Figure 1.16. Position of a small spherical particle located at a planar oil-water interface for a contact angle (measured through the aqueous phase) less than 90^o (left), equal to 90^o (centre) and greater than 90^o (right).[138]

Once the nanoparticles are adsorbed to the oil/water interface, the energy, *E*, to detach the particles is given by Equation 1.13:[138]

$$E = \pi r^2 \gamma_{ow} (1 \pm \cos\theta)^2 \qquad (1.13)$$

where r is the particle radius, γ_{ow} is the surface tension at the oil/water interface and θ is the nanoparticle contact angle. The sign inside the bracket is negative for removal of the particle into the water phase, and positive for removal into the oil phase. Consequently, it costs less energy, and it is therefore easier for particles to detach into the water phase if $\theta < 90°$.[138] Similarly, if $\theta > 90°$ detachment into the oil phase is easier.

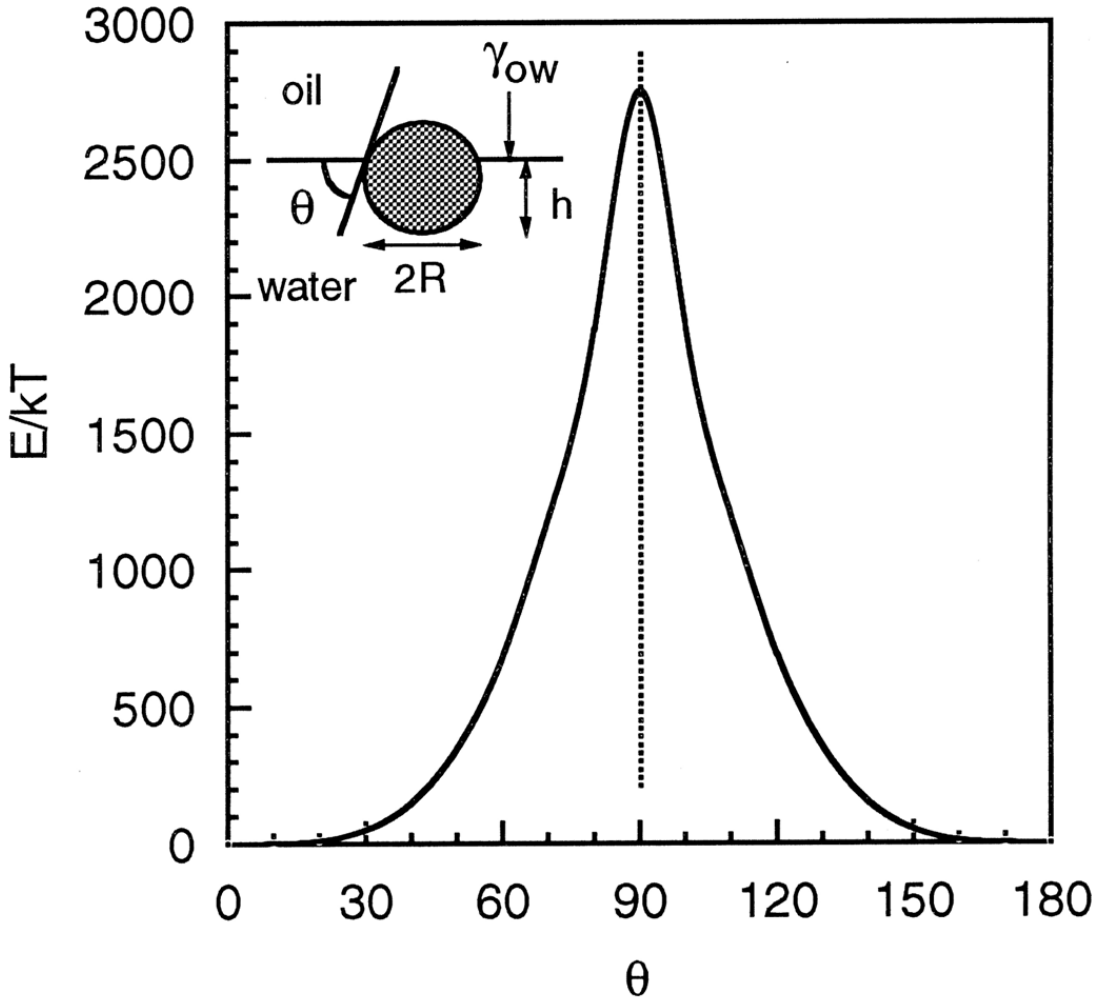

Figure 1.17. Variation in the energy of detachment, *E* (relative to kT), for a spherical particle of radius 10 nm with the particle contact angle, θ, at the toluene/water interface (assuming γ_{ow} = 0.036 N m^{-1}).[139]

Equation 1.13 shows that the energy of detachment of a particle adsorbed at the oil/water interface is strongly dependent on the three-phase contact angle, θ. Figure 1.17 illustrates this relationship for a particle of mean radius 10 nm adsorbed at the toluene/water interface.[139] The energy of detachment is greatest when $\theta = 90°$ and declines rapidly either side of this value. Therefore the most stable emulsions are

formed when θ is close to 90°, because the particles are held more strongly at the interface with a detachment energy of around 2750 kT.[139] However, larger/less stable emulsions are formed at both higher and lower values of θ. In fact, when the contact angle is less than 20° or greater than 160° the detachment energy is much lower (< 10 kT).[138] Hence, highly hydrophilic or hydrophobic nanoparticles typically do not act as effective Pickering emulsifiers.

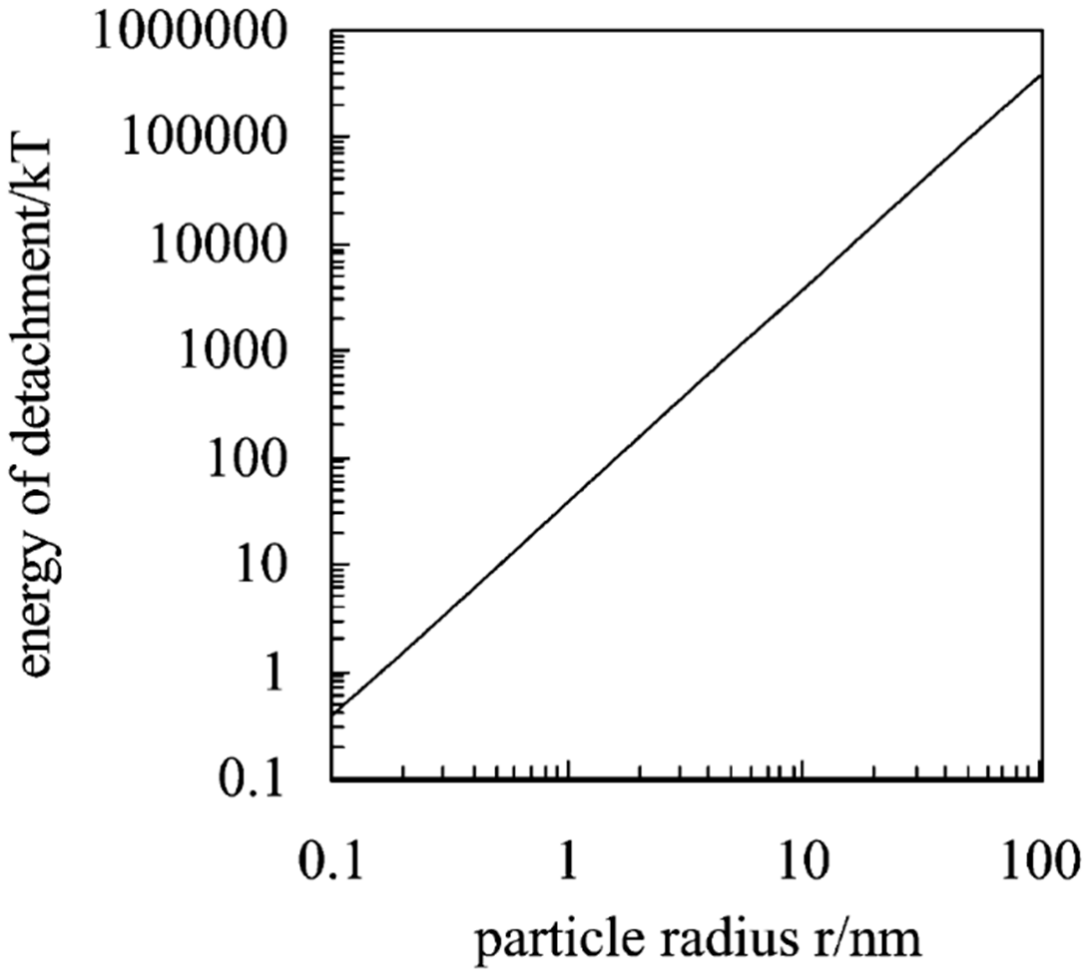

Figure 1.18. Variation of the theoretical detachment energy for spherical particles of differing radii exhibiting a contact angle of 90° at the *n*-alkane/water interface (γ_{ow} = 0.050 N m^{-1}) at 298 K.[138]

In addition to the contact angle, Equation 1.13 also shows that the detachment energy is proportional to the square of the particle radius. Figure 1.18 shows how the calculated detachment energy varies with mean radius for a particle adsorbed at the *n*-alkane/water interface with a contact angle of 90°. Particles of less than 1 nm radius have detachment energies similar to that of small-molecule surfactants (< 10 kT). In this case, only weak reversible adsorption is anticipated at the oil-water

interface. Hence such particles may not be very effective as Pickering emulsifiers. Clearly, very high detachment energies would be required to remove larger particles (e.g. > 10 nm radius) from the droplet interface, hence they can be considered to be irreversibly adsorbed.[138, 140]

This relatively high energy of particle attachment makes Pickering emulsions far more stable than surfactants, with the adsorbed particles providing a strong steric barrier to droplet coalescence.[138] This is because sufficiently large particles adsorb permanently at the oil/water interface, whereas surfactants are characterised by dynamic adsorption and desorption.[138, 141]

Improving Pickering Emulsion Stability

It has been proposed that modulating nanoparticle surface roughness can promote Pickering emulsion stability.[140, 142-144] This relationship has been demonstrated recently using cationic silica microparticles coated with anionic copolymers based on methacrylic acid and methyl methacrylate (Eudragit S-100) to stabilise the oil/water interface.[142] In a second study, rough carbon black nanoparticles were used to stabilise the water/*n*-octane interface.[145] The former study controls nanoparticle surface roughness by varying the extent of fusion of the nanoparticle coating by exposure to aqueous solutions containing either acetone or ethanol at various concentrations. Both contact angle hysteresis and emulsion stability measurements suggested that particle roughness improved the stability of the emulsions (see Figure 1.19). However, this only appears to be the case when wetting occurs homogeneously via the Wenzel regime[146], whereas the transition toward heterogeneous wetting (or Cassie–Baxter regime[147]) is associated with a loss of emulsion stability. Thus the wetting behaviour of nanoparticles is influenced by the amplitude and topography of the roughness features[148, 149] as well as by the specific surface chemistry.

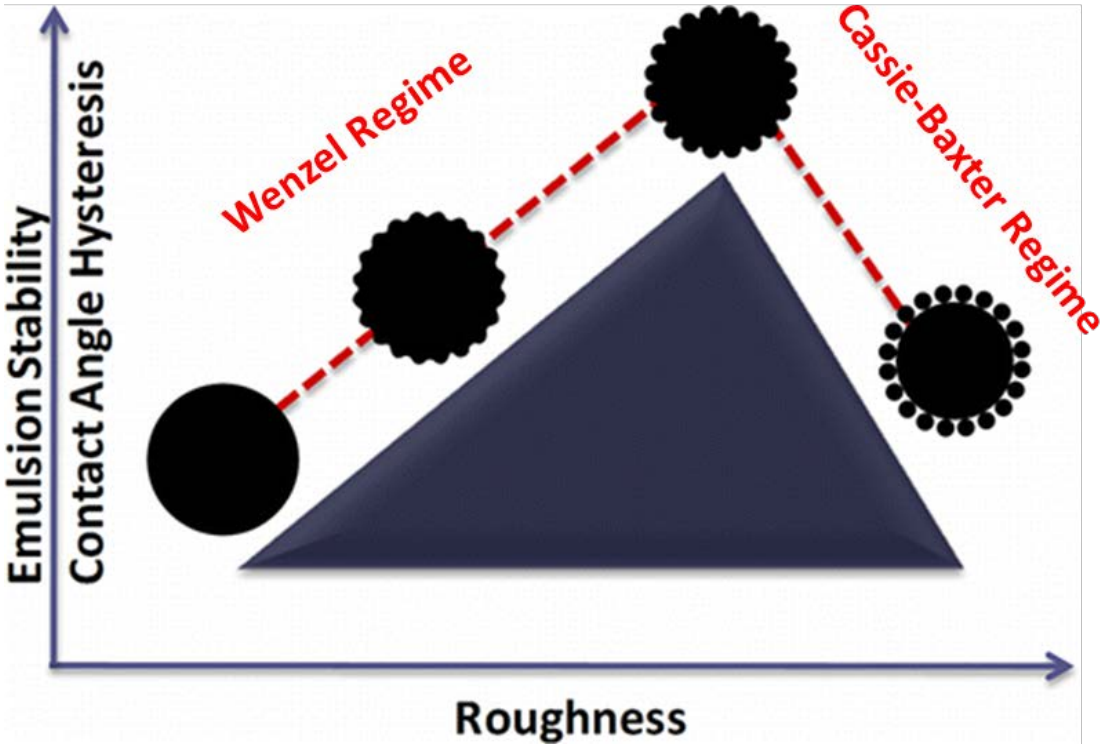

Figure 1.19. Schematic cartoon describing the relationship between surface topography/roughness and emulsion stability and contact angle hysteresis.[142] The Wenzel wetting regime is associated with improved emulsion stability via homogeneous wetting, whereas the Cassie-Baxter wetting regime is associated with a loss in emulsion stability due to heterogeneous wetting.

Block Copolymer Vesicles as Pickering Emulsifiers

The use of block copolymer vesicles as Pickering emulsifiers was reported by Thompson et al.[150] Linear $PGMA_{45}$-$PHPMA_{200}$ diblock copolymer vesicles did not survive the high-shear homogenisation conditions required for emulsification, and consequently adsorbed at the oil-water interface as individual amphiphilic diblock copolymer chains. In contrast, the use of ethylene glycol dimethacrylate (EGDMA) as a third comonomer cross-linked the vesicles and so rendered them stable towards high-shear homogenisation. TEM studies confirmed that linear $PGMA_{45}$-$PHPMA_{200}$ diblock copolymer vesicles had a smooth, featureless morphology, whereas the cross-linked $PGMA_{58}$-$PHPMA_{350}$-$PEGDMA_{20}$ triblock copolymer vesicles exhibited a nano-textured surface (see Figure 1.20).

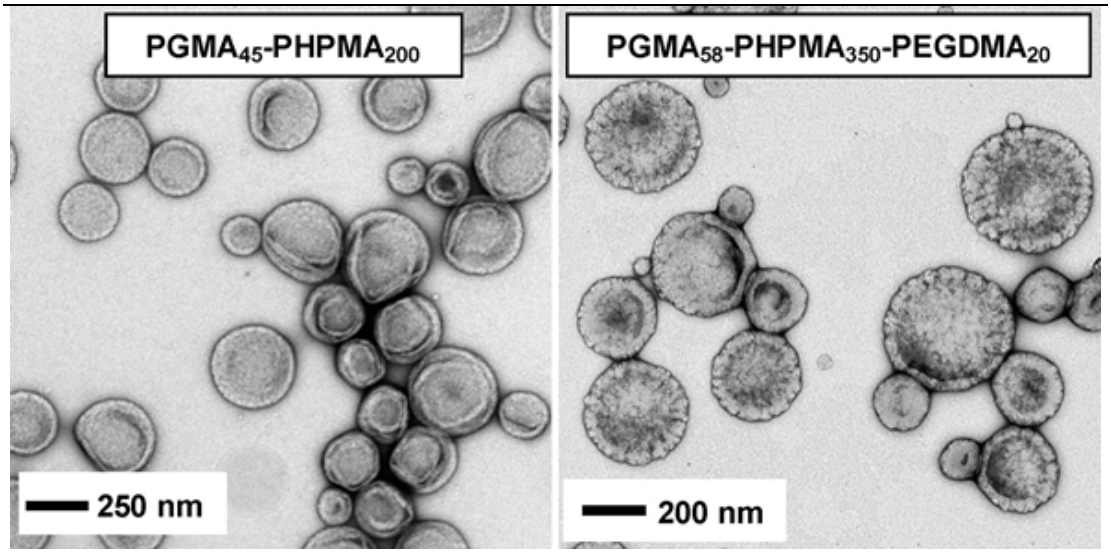

Figure 1.20. TEM images reported for linear $PGMA_{45}$-$PHPMA_{200}$ diblock copolymer vesicles and cross-linked $PGMA_{58}$-$PHPMA_{350}$-$PEGDMA_{20}$ triblock copolymer vesicles.[150]

The cross-linked vesicles adsorbed at the oil-water interface, similar to shell cross-linked micelles.[134-136, 138, 140, 151] In the former case, the emulsion droplet diameter was dependent on the vesicle concentration; smaller oil droplets were obtained when using higher vesicle concentrations, as shown in Figure 1.21. On the other hand, no concentration dependence was observed for molecularly-dissolved linear copolymer chains.

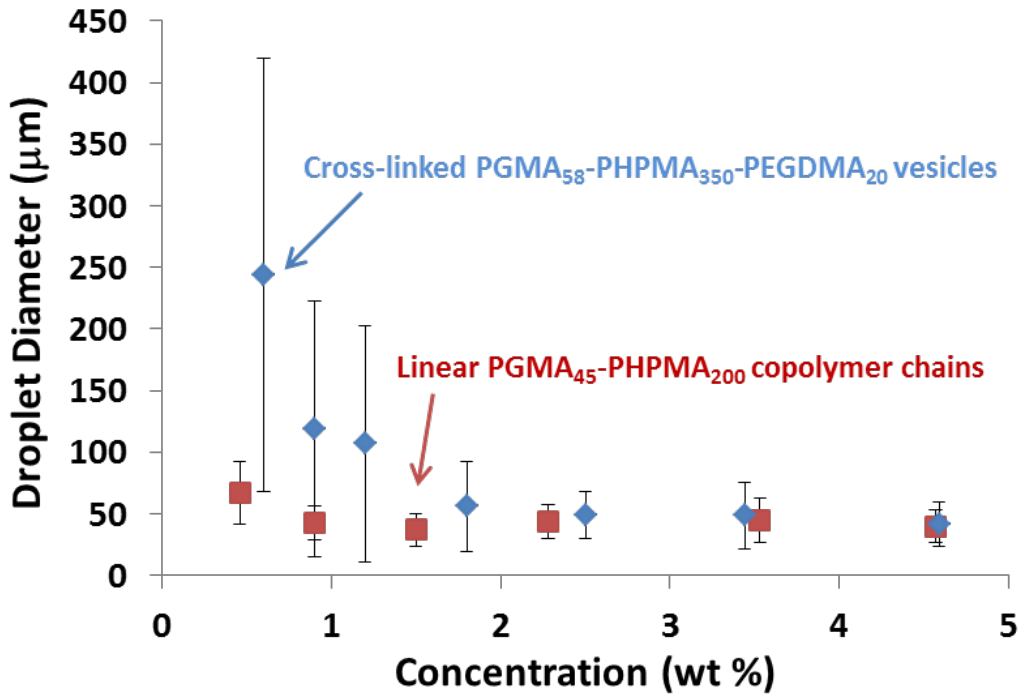

Figure 1.21. Mean droplet diameter (obtained by laser diffraction) vs aqueous vesicle concentration for both linear $PGMA_{45}$-$PHPMA_{200}$ and cross-linked $PGMA_{58}$-$PHPMA_{350}$-$PEGDMA_{20}$ vesicles.[150]

However, turbidimetry experiments showed that the majority of the vesicles did not adsorb at the oil-water interface and instead remained within the continuous phase. The adsorption efficiency increased from 57 to 78 % (see Figure 1.22) as the initial vesicle concentration used to prepare the emulsion was reduced from 2.5 to 0.6 % w/w.[150] The adsorption efficiency became poorer at higher vesicle concentrations since there are more vesicles present than the minimum required to fully coat all the oil droplets. However, even the optimum vesicle concentration led to an adsorption efficiency of less than 70 %.

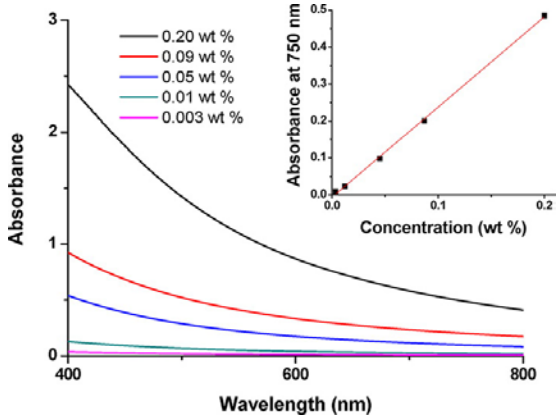

Initial Concentration (wt %)	Adsorbed Concentration (wt %)	Adsorption Efficiency (%)
2.5	1.5	57
1.8	1.1	61
1.2	0.8	67
0.9	0.7	78
0.6	0.4	67

Figure 1.22. Left: Visible absorption spectra recorded for cross-linked vesicle dispersions at various concentrations. A fixed wavelength (750 nm) was used to construct a linear calibration plot (left inset), allowing the concentration of non-adsorbed vesicles remaining in the aqueous phase after emulsification to be determined via turbidimetry. Right: Determination of the adsorption efficiency of cross-linked $PGMA_{58}$-$PHPMA_{350}$-$PEGDMA_{20}$ vesicles as determined by turbidimetric analysis of the lower aqueous phase of the creamed emulsions. [150]

Block Copolymer Spheres and Worms as Pickering Emulsifiers

The use of spherical latex particles to stabilise giant (2 mm diameter) Pickering emulsions has been studied in some detail.[152-154] Thompson et al.[152] investigated the effect of emulsifier particle size and oil type on the droplet coalescence time. Coalescence times increased when the oil phase was changed from *n*-dodecane to sunflower oil, owing to the higher viscosity and lower interfacial tension of the latter oil. Coalescence times were increased when larger (902 nm diameter) PGMA-stabilised polystyrene latex particles were used compared to smaller particles (135 nm diameter), because of the greater distance separating the oil droplets. More recently, Thompson et al.[66] synthesised $PGMA_{100}$-$PHPMA_{200}$ diblock copolymer spheres, $PGMA_{51}$-$PBzMA_{250}$ diblock copolymer spheres[89] and crosslinked $PGMA_{100}$-$PHPMA_{200}$-$PEGDMA_{20}$ triblock copolymer spheres (see Figure 1.23).

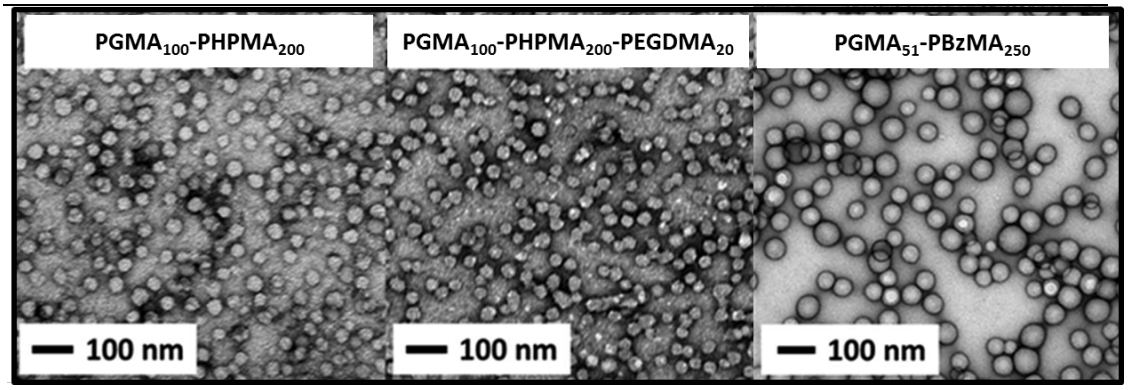

Figure 1.23. TEM images of $PGMA_{100}$-$PHPMA_{200}$ diblock copolymer spheres, $PGMA_{100}$-$PHPMA_{200}$-$PEGDMA_{20}$ triblock copolymer spheres and $PGMA_{51}$-$PBzMA_{250}$ diblock copolymer spheres.[66]

These block copolymer spheres were then compared in terms of their performance as Pickering emulsifiers of millimetre-sized emulsion droplets. The $PGMA_{100}$-$PHPMA_{200}$ spheres do not withstand homogenisation and dissociate *in situ* to form individual diblock copolymer chains, adsorbing at the oil/water interface like surfactants. Both the $PGMA_{100}$-$PHPMA_{200}$-$PEGDMA_{20}$ and $PGMA_{51}$-$PBzMA_{250}$ block copolymer spheres survived homogenisation, because they exhibited concentration-dependent oil droplet diameters. These observations were not unexpected, because it was previously reported that linear diblock copolymer vesicles do not withstand homogenisation, whereas cross-linked triblock copolymer vesicles survive such high-shear conditions.[150] The $PGMA_{51}$-$PBzMA_{250}$ diblock copolymer spheres withstood homogenisation even without cross-linking (see Figure 1.24). The PBzMA block is significantly more hydrophobic than PHPMA, so it is able to confer sufficient stability via greater hydrophobic interactions (physical crosslinking). Conversely, the weakly hydrophobic PHPMA block is much more prone to undergo dissociation so it requires covalent crosslinking to produce stable PHPMA-based nano-objects.

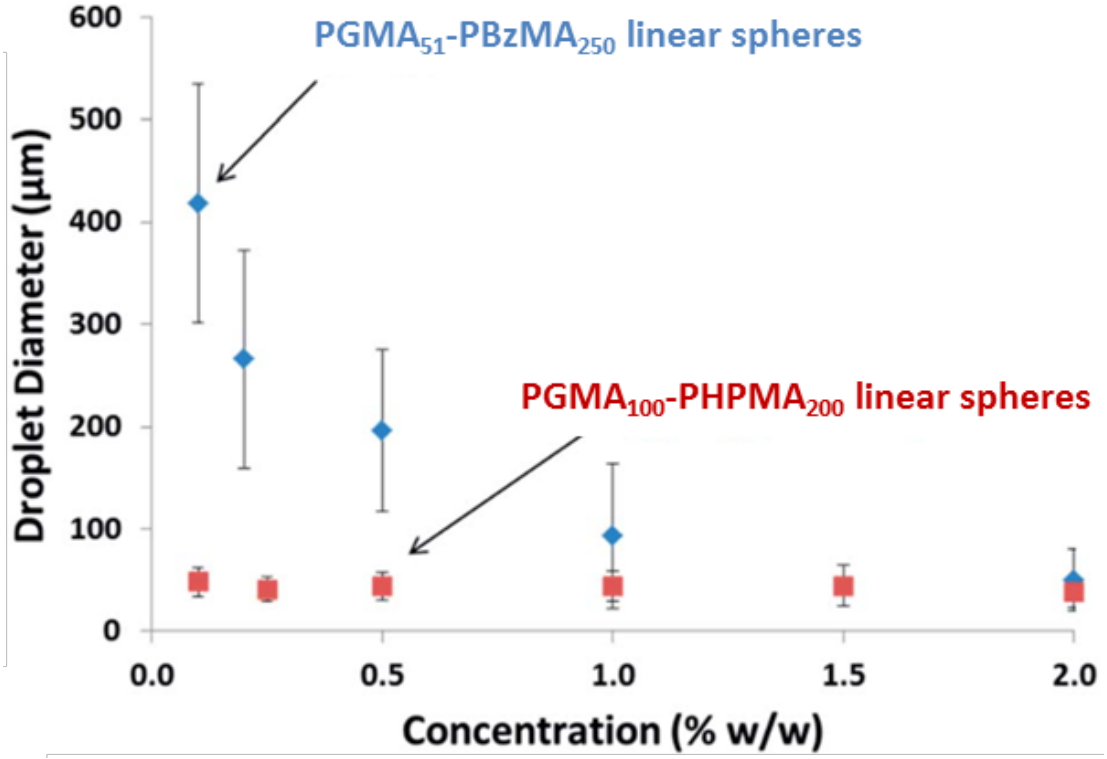

Figure 1.24. Mean laser diffraction droplet diameter versus copolymer concentration for both linear $PGMA_{100}$–$PHPMA_{200}$ spheres and cross-linked $PGMA_{100}$–$PHPMA_{200}$–$PEGDMA_{20}$ spheres. The error bars represent the standard deviation of each mean volume-average droplet diameter, rather than the experimental error.[66]

Similar observations were made when comparing $PGMA_{45}$-$PHPMA_{140}$ diblock copolymer worms, $PGMA_{45}$-$PHPMA_{100}$-$PEGDMA_{10}$ triblock copolymer worms and $PGMA_{37}$-$PHPMA_{60}$-$PBzMA_{30}$ triblock copolymer worms (see Figure 1.26) as Pickering emulsifiers. Again, the linear diblock copolymer disassociated under shear, while the covalently cross-linked triblock copolymer worms and the physically cross-linked triblock copolymer worms withstood homogenisation (see Figure 1.26).

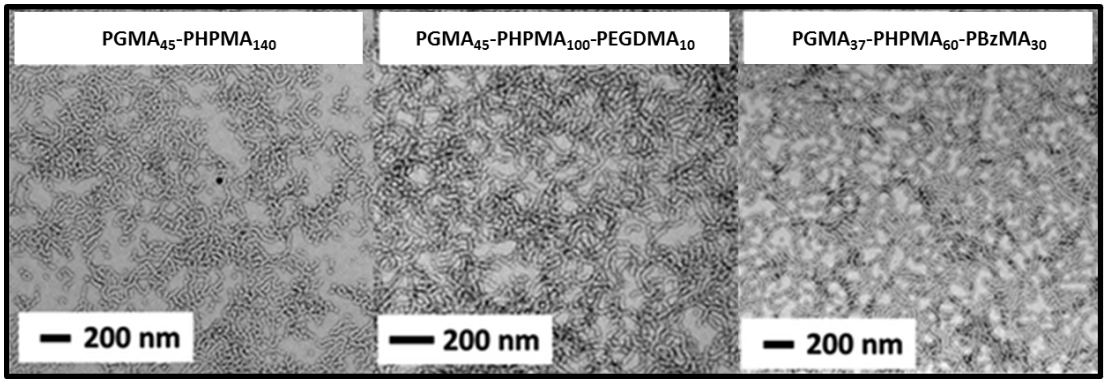

Figure 1.25. TEM images obtained for $PGMA_{45}$-$PHPMA_{140}$ diblock copolymer worms, $PGMA_{45}$-$PHPMA_{100}$-$PEGDMA_{10}$ triblock copolymer worms and $PGMA_{37}$-$PHPMA_{60}$-$PBzMA_{30}$ triblock copolymer worms.[66]

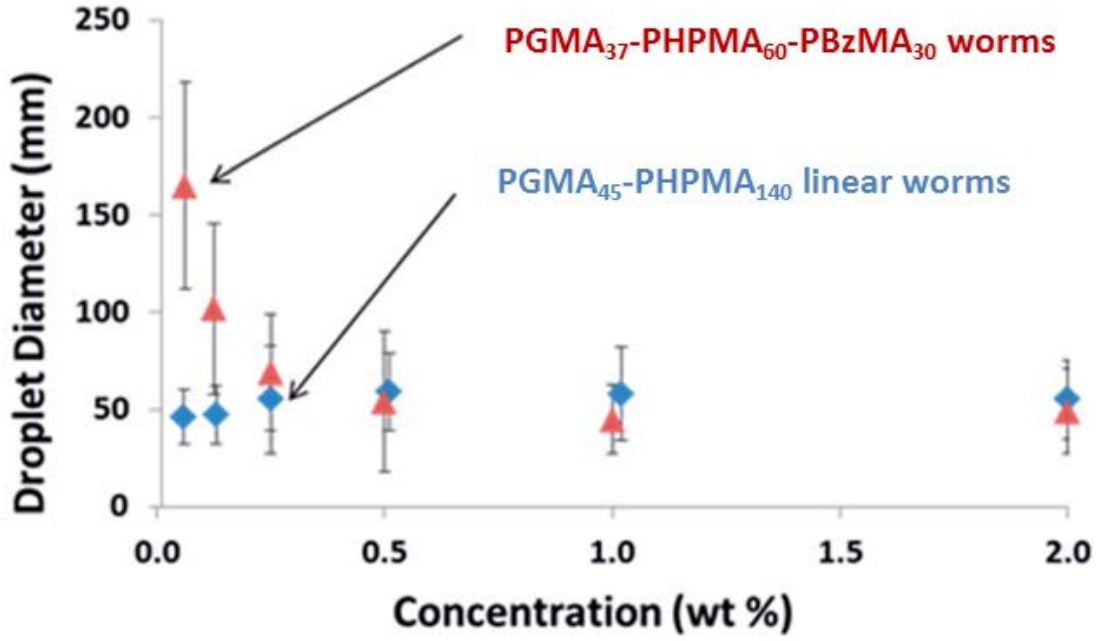

Figure 1.26 Mean laser diffraction droplet diameter versus copolymer concentration for both linear $PGMA_{45}$–$PHPMA_{140}$ worms and $PGMA_{37}$–$PHPMA_{60}$–$PBzMA_{30}$ worms. The error bars represent the standard deviation of each mean volume-average droplet diameter, rather than the experimental error. [66]

Particle Sizing Techniques

Many techniques can be used to measure the size of colloidal particles. There is no single method that is universally used and each technique has various advantages and disadvantages (such as instrument bias resolution, cost, upper or lower size limits etc.). It is important to measure particle size distributions in colloid science because real systems have finite polydispersities. Moreover, a given particle sizing technique will report a specific moment of the size distribution.

Electron Microscopy, Disc Centrifuge Photosedimentometry, Laser Diffraction and Dynamic Light Scattering

Electron microscopy reports the number-average particle diameter, D_n, which is defined as:

$$D_n = \frac{\Sigma N_i D_i}{\Sigma N_i} \qquad (1.14)$$

where N_i is the number of particles with diameter D_i. Ideally, the number-average particle diameter should be readily accessible using simple, statistically robust

characterisation techniques. Unfortunately, this is not often the case. For example, electron microscopy is relatively expensive and particle size distributions are generally approximated by counting hundreds of particles manually (or with the aid of software). Furthermore, some characterisation techniques are more biased towards larger particles, and thus one or more assumptions are generally required to calculate the number-average diameter from raw data. For example, disc centrifuge photosedimentometry (DCP) reports the weight-average diameter, D_w, which can be defined as:

$$D_w = \frac{\Sigma N_i D_i^4}{\Sigma N_i D_i^3} = \frac{\Sigma w_i D_i}{\Sigma w_i} \qquad (1.15)$$

where w_i is the weight (or mass) of a particle of diameter D_i. The weight-average diameter is more biased towards larger particles than the number-average diameter. Similarly, laser diffraction reports the volume-average particle diameter, $D_{4/3}$, which is mathematically equivalent to the weight-average, since volume is directly proportional to mass. DCP is a high resolution particle sizing technique which fractionates particles during analysis, based on the difference between the particle density and that of the continuous phase. Laser diffraction has lower resolution compared to DCP because no fractionation occurs during analysis in the former case.
The intensity-average (or z-average) diameter is even more biased towards larger particles than the weight-average diameter. Dynamic light scattering (DLS) reports the intensity-average diameter, which is more biased towards larger particles because the intensity of scattered light from a particle is proportional to the sixth power of its diameter. Hence larger particles scatter much more light than smaller ones and contribute far more to the detected scattered light intensity. DLS is convenient and widely used, but it is rather sensitive to the presence of dust particles and can often oversize a sample with a broad size distribution (especially one containing a population of smaller particles). For example, DLS cannot easily discriminate between a binary mixture of 1000 nm and 10 nm particles because the contribution to the total light scattered by the smaller particles will be minimal. Furthermore, DLS is

highly sensitive to the onset of particle aggregation, but rather insensitive to particle dissociation.

DLS reports the sphere-equivalent hydrodynamic diameter, D_h, which is calculated from the translational diffusion coefficient, D, using the Stokes-Einstein equation:

$$D_h = \frac{k_B T}{3 \pi \eta D} \qquad (1.16)$$

where k_B is the Boltzmann constant, T is the absolute temperature and η is the solution viscosity.[155] The translational diffusion coefficient of the particles is measured by monitoring the decay of the correlation function over time by following fluctuations in the scattering intensity due to particles undergoing Brownian motion. Smaller particles diffuse faster than larger particles, so possess a larger D value in a given solvent.

Small-Angle X-Ray Scattering (SAXS)

SAXS is a powerful characterisation technique for the analysis of colloidal particles.[156] Measurements are generally conducted on dilute dispersions and provide information on size, shape and nanoparticle interactions in their dispersed state. Furthermore, SAXS is a non-destructive, statistically robust technique since the observed patterns are a result of scattering from many millions of particles.[157]

SAXS works by irradiating a sample with x-rays of a known wavelength. The characteristic length scale is inversely proportional to the scattering vector, q, which is given by Equation 1.17:

$$q = \frac{4 \pi}{\lambda} \sin\theta \qquad (1.17)$$

where 2θ is the scattering angle and λ is the wavelength. Several assumptions are made in the derivation of this equation: (i) x-ray scattering is relatively weak, so that each x-ray is only scattered once, (ii) the x-ray energy is not significantly changed during scattering and (iii) the scattering has no directional properties. The three vectors used to define q are shown in Figure 1.27.

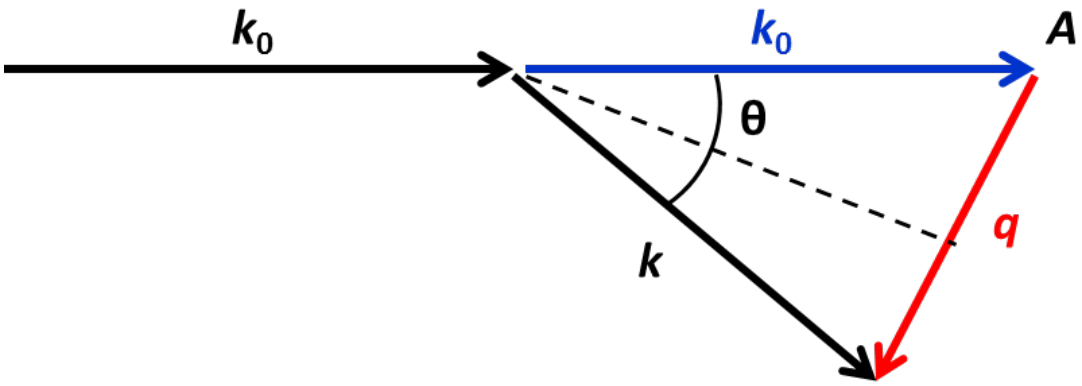

Figure 1.27. Schematic illustration of the scattering vector, *q*, based on the incoming and scattered wave vectors, k_o and *k*, and half the scattering angle, θ.

When x-rays irradiate a sample, any particles present usually scatter the incident radiation as they typically have a different electron density and are similar in size to the x-ray wavelength. SAXS measures the intensity of this angle-dependent distribution of scattered radiation. The scattered intensity, $I(q)$, is measured as a function of the x-ray momentum transfer, q. The normalised scattering intensity for a suspension of uniform particles is given by Equation 1.18 below:

$$I(q) = N V^2 \Delta\xi^2 F(q) S(q) \qquad (1.18)$$

where N in the number density, V is the volume of scattering particles, $\Delta\xi$ is the contrast in scattering length density between the particles and solvent, $F(q)$ is the form factor (which also describes the internal structure of the particles) and $S(q)$ is the structure factor that represents the spatial arrangement of the scattering centres. For dilute dispersions of particles, $S(q)$ is equal to unity because there are no inter-particle interactions.

A SAXS instrument consists of an x-ray source, a collimation system to produce a narrow beam, a beam stop to prevent the incident beam hitting the detector, and a detector to measure the scattered x-rays over a range of angles, see Figure 1.28.

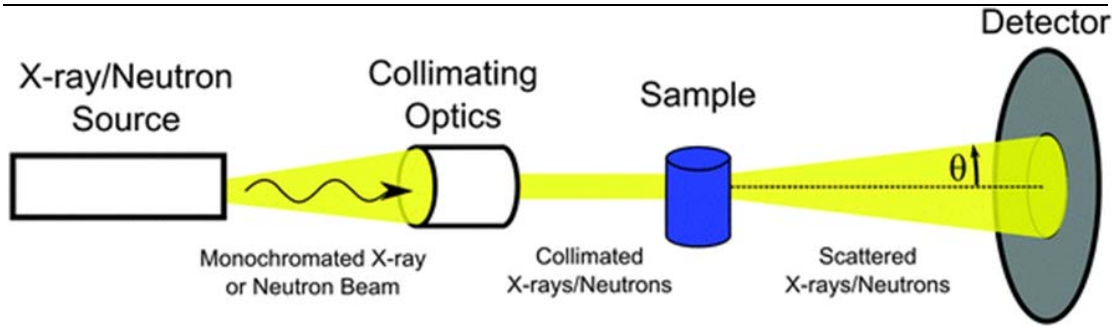

Figure 1.28 Schematic representation of the set up for a small angle x-ray scattering experiment. A monochromatic x-ray beam is collimated then used to irradiate the sample. The scattering of the beam is recorded by the detector.[158]

The detector gives a two-dimensional scattering pattern that is reduced to a 1D profile by taking into account the wavelength, pixel size and sample-to-detector distance. This 1D profile must then be background-corrected to allow analysis of scattering arising solely from the sample, rather than the solvent or sample holder. Interpreting scattering curves involves fitting to an appropriate scattering model, which will often contain many fitting parameters.

In some cases, it is necessary to use more than one model for fitting the SAXS pattern. For example, Balmer et al.[159] found that it was necessary to combine three different models to analyse the morphology of P2VP-silica nanocomposites. The surface morphology of such nanocomposite particles (see Figure 1.29f) is quite similar to that observed for framboidal vesicles (see Figure 1.12b).

In this work, large P2VP-silica nanocomposite particles and small sterically stabilised P2VP latex particles were mixed for 1 h at 20 ^{o}C. SAXS measurements allow the distribution of silica nanoparticles on the latexes to be determined after mixing. If there had been no silica redistribution after mixing these two dispersions, this final scattering pattern would be simply the summation of the nanocomposite and original latex scattering pattern. However, the observed SAXS curve is a superposition of scattering patterns for two partially coated nanocomposite particles of different diameters (see Figure 1.29e). In order to analyse the SAXS curves obtained for the partially coated P2VP-silica nanocomposite particles a three-population model was used. The first population described the large nanocomposite core-shell structure of the particles, the second population described the small nanocomposite core-shell particles, and the third represents the particulate nature of

the silica shell. These SAXS experiments confirm unambiguously that facile silica exchange occurs between nanocomposite and latex particles in aqueous solution.

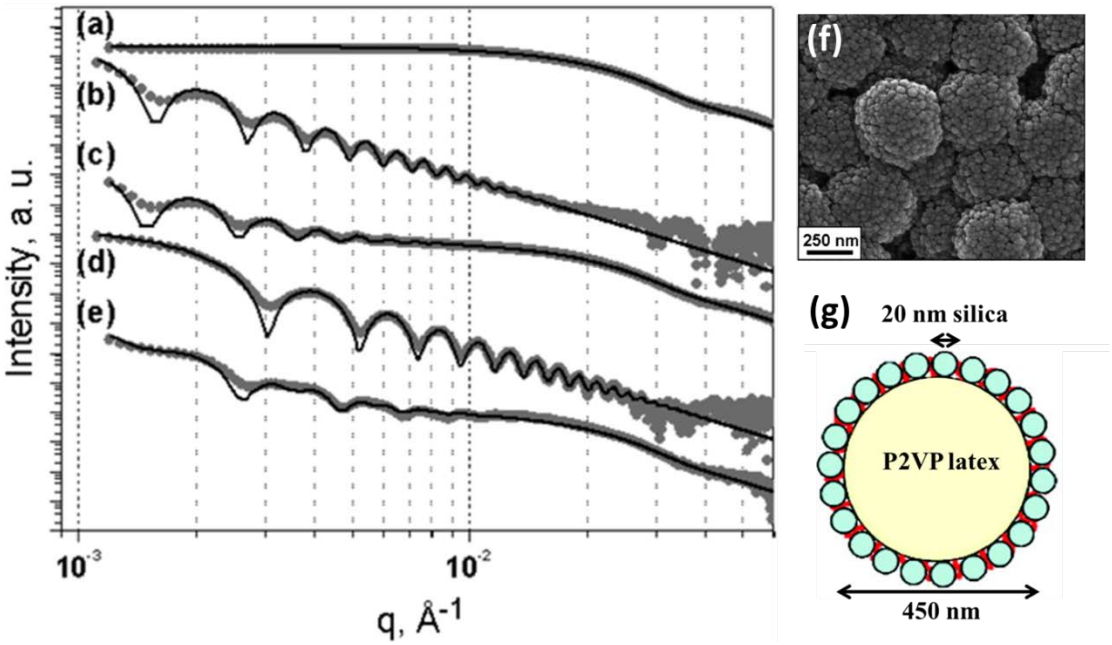

Figure 1.29. SAXS patterns and fits (solid lines) obtained for: (a) 20 nm silica sol; (b) 600 nm sterically stabilised P2VP latex; (c) P2VP-silica nanocomposite particles prepared by coating this 600 nm P2VP latex with 20 nm silica at monolayer coverage; (d) 300 nm sterically stabilised P2VP latex; (e) the final bimodal distribution of partially coated nanocomposite particles obtained after mixing dispersions (c) and (d) and allowing silica exchange to occur for 1 h at 20 °C. Each pattern has been multiplied by an arbitrary coefficient for clarity. (f) TEM image and (g) schematic representation of P2VP-silica nanocomposite particles (prepared by coating 450 nm P2VP latex with 20 nm silica). Figure adapted from Balmer et al.[159]

Thesis Outline

The aim of this thesis is to expand our knowledge of the PGMA-PHPMA diblock copolymer system. There are two chapters which utilise PGMA-PHPMA diblock copolymer vesicles for the *in situ* encapsulation and subsequent release of silica nanoparticles. The other two chapters in this thesis chain-extend this diblock copolymer with BzMA to create new nano-objects.

The aim of the first experimental Chapter in this thesis is to build on the work by Chambon et al.[90] and explore the evolution of the framboidal (raspberry-like) PGMA-PHPMA-PBzMA morphology. This requires the synthesis of a well-defined PGMA macro-CTA with a suitable DP so as to ensure the formation of pure vesicles when subsequently chain-extended with HPMA. These PGMA-PHPMA precursor vesicles are then chain-extended with varying amounts of BzMA in order to observe the gradual evolution of the framboidal morphology. The resulting framboidal

PGMA-PHPMA-PBzMA triblock vesicles are then evaluated as Pickering emulsifiers for the stabilisation of oil-in-water emulsions. The hypothesis that surface roughness promotes Pickering emulsifier efficiency, first postulated by Behrens and San-Miguel,[142] is investigated using this vesicle series, which provides Pickering emulsifiers of gradually increasing surface roughness with no significant change in the particle size distribution. Turbidimetry experiments on the Pickering emulsions are also conducted to assess the Pickering emulsifier adsorption efficiency.

The second experimental Chapter also focuses on PGMA-PHPMA-PBzMA triblock copolymers. However, the target DP of each block differs from the first Chapter. For PGMA-PBzMA diblock copolymers synthesised via RAFT aqueous emulsion polymerisation, Cunningham et al.[89] reported that only kinetically-trapped spheres could be achieved. This Chapter investigates whether higher order morphologies (i.e. worms or vesicles) can be obtained if a PHPMA block is introduced between the PGMA and PBzMA blocks. SAXS studies are used to characterise these nano-objects. Furthermore, the resulting PGMA-PHPMA-PBzMA triblock copolymer worms are evaluated for the preparation of millimetre-sized Pickering emulsions.

The third experimental Chapter explores the *in situ* encapsulation of silica nanoparticles within PGMA-PHPMA diblock copolymer vesicles. Diblock copolymer vesicles are synthesised in the presence of varying amounts of silica nanoparticles, in order to obtain a range of silica-loaded vesicles. Firstly, successful silica encapsulation within the diblock copolymer vesicle lumen is proven by SAXS and TEM studies. Next, the effect of the initial silica concentration is evaluated by calculation of the encapsulation efficiency, number of silica nanoparticles encapsulated per vesicle and loading efficiency using a range of analytical techniques. Thirdly, thermally-triggered release from these silica-loaded vesicles is examined as a function of both time and temperature.

The final experimental Chapter assesses the time scale required for the release of silica nanoparticles from silica-loaded vesicles in more detail. More specifically, the effect of varying the number of silica nanoparticles per vesicle on the thermally-triggered response of the vesicles is explored. Both TEM and SAXS studies are conducted to analyse the copolymer morphologies formed after cooling. Furthermore, by fitting SAXS data to a suitable model, the concentration of released silica can be estimated.

References

1. J. Dechant, *Acta Polymerica*, 1991, **42**, 191-191.
2. P. C. Hiemens and T. P. Lodge, *Polymer Chemistry*, CRC Press:New York, 2nd edn., 2007.
3. K. Matyjaszewski, *Science*, 2011, **333**, 1104-1105.
4. W. A. Braunecker and K. Matyjaszewski, *Progress In Polymer Science*, 2007, **32**, 93-146.
5. D. W. J. Osmond and H. H. Thompson*, Dispersion Polymerisation*, GB893429, 1962.
6. Rohm and Haas*, Polymer dispersions in organic liquid media and methods of preparation*, GB934038, 1963.
7. S. Kawaguchi and K. Ito, *Adv Polym Sci*, 2005, **175**, 299-328.
8. P. A. Lovell and M. S. El-Aasser, *Emulsion Polymerisation and Emulsion Polymers*, John Wiley and Sons, Chichester UK, 1997.
9. R. Arshady, *Colloid And Polymer Science*, 1992, **270**, 717-732.
10. M. P. Stevens, *Polymer Chemistry: an Introduction*, Oxford University Press, Oxford, 3rd edn., 1999.
11. R. J. Hunter, *Introduction to Modern Colloid Science*, Oxford University Press, Oxford, 1993.
12. J. Qiu, B. Charleux and K. Matyjaszewski, *Progress In Polymer Science*, 2001, **26**, 2083-2134.
13. M. Szwarc, M. Levy and R. Milkovich, *Journal of the American Chemical Society*, 1956, **78**, 2656-2657.
14. M. Kamigaito, T. Ando and M. Sawamoto, *Chemical Reviews*, 2001, **101**, 3689-3746.
15. G. Moad, E. Rizzardo and S. H. Thang, *Accounts of Chemical Research*, 2008, **41**, 1133-1142.
16. G. Odian, *Principles of Polymerization*, John Wiley & Sons, Inc., Hoboken, New Jersey, 4th edn., 2004.
17. O. W. Webster, *Science*, 1991, **251**, 887-893.
18. M. Szwarc, *Nature*, 1956, **178**, 1168-1169.
19. G. Holden and R. Milkovich*, Block copolymer with rubberlike properties*, BE627652, 1963.
20. H. M. Walter, H. D. Schwaben, R. Bueschl, K. Bronstert and A. Echte*, Transparent, impact-resistant thermoplastic molding compositions and their preparation and use*, DE 3730886, 1989.
21. K. Knoll and N. Nießner, *Macromolecular Symposia*, 1998, **132**, 231-243.
22. D. Baskaran and A. H. E. Müller, *Progress In Polymer Science*, 2007, **32**, 173-219.
23. R. J. Eckert*, Hydrogenated star-shaped polymer*, US Patent 4116917, 1978.
24. H. Willcock and R. K. O'Reilly, *Polymer Chemistry*, 2010, **1**, 149-157.
25. J. N. Israelachvili, *Intermolecular and Surface Forces*, Academic Press, London, 2nd ed. edn., 1991.
26. F. S. Bates and G. H. Fredrickson, *Annual Review of Physical Chemistry*, 1990, **41**, 525-557.
27. S. Lecommandoux, M. Lazzari and G. Liu, in *Block Copolymers in Nanoscience*, Wiley-VCH Verlag GmbH & Co. KGaA, 2008, DOI: 10.1002/9783527610570.ch1, pp. 1-7.
28. L. Leibler, *Macromolecules*, 1980, **13**, 1602-1617.
29. M. W. Matsen and F. S. Bates, *Macromolecules*, 1996, **29**, 1091-1098.

30. E. L. Thomas, D. M. Anderson, C. S. Henkee and D. Hoffman, *Nature*, 1988, **334**, 598-601.
31. S. Krause, *The Journal of Physical Chemistry*, 1964, **68**, 1948-1955.
32. S. Newman, *Journal of Applied Polymer Science*, 1962, **6**, S15-S16.
33. Y.-Y. Won, H. T. Davis and F. S. Bates, *Science*, 1999, **283**, 960.
34. L. Zhang and A. Eisenberg, *Science*, 1995, **268**, 1728-1731.
35. F. S. Bates, *Science*, 1991, **251**, 898-905.
36. F. S. Bates and G. H. Fredrickson, *Physics Today*, 1999, **52**, 32-39.
37. Y. Mai and A. Eisenberg, *Chemical Society Reviews*, 2012, **41**, 5969-5985.
38. J. M. G. Swann and P. D. Topham, *Polymers*, 2010, **2**, 454-469.
39. A. Blanazs, S. P. Armes and A. J. Ryan, *Macromolecular Rapid Communications*, 2009, **30**, 267-277.
40. G. Battaglia and A. J. Ryan, *Nature Materials*, 2005, **4**, 869-876.
41. F. Meng, G. H. M. Engbers and J. Feijen, *Journal of Controlled Release*, 2005, **101**, 187-198.
42. A. Choucair, P. Lim Soo and A. Eisenberg, *Langmuir*, 2005, **21**, 9308-9313.
43. D. J. Adams, M. F. Butler and A. C. Weaver, *Langmuir*, 2006, **22**, 4534-4540.
44. L. A. Fielding, M. J. Derry, V. Ladmiral, J. Rosselgong, A. M. Rodrigues, L. P. D. Ratcliffe, S. Sugihara and S. P. Armes, *Chemical Science*, 2013, **4**, 2081-2087.
45. L. A. Fielding, J. A. Lane, M. J. Derry, O. O. Mykhaylyk and S. P. Armes, *Journal Of The American Chemical Society*, 2014, **136**, 5790-5798.
46. C. Gonzato, M. Semsarilar, E. R. Jones, F. Li, G. J. P. Krooshof, P. Wyman, O. O. Mykhaylyk, R. Tuinier and S. P. Armes, *Journal Of The American Chemical Society*, 2014, **136**, 11100-11106.
47. J. Tan, H. Sun, M. Yu, B. S. Sumerlin and L. Zhang, *ACS Macro Letters*, 2015, **4**, 1249-1253.
48. S. Sugihara, A. Blanazs, S. P. Armes, A. J. Ryan and A. L. Lewis, *Journal Of The American Chemical Society*, 2011, **133**, 15707-15713.
49. A. Blanazs, J. Madsen, G. Battaglia, A. J. Ryan and S. P. Armes, *Journal Of The American Chemical Society*, 2011, **133**, 16581-16587.
50. A. Blanazs, A. J. Ryan and S. P. Armes, *Macromolecules*, 2012, **45**, 5099-5107.
51. N. J. Warren and S. P. Armes, *Journal Of The American Chemical Society*, 2014, **136**, 10174-10185.
52. N. J. Warren, O. O. Mykhaylyk, A. J. Ryan, M. Williams, T. Doussineau, P. Dugourd, R. Antoine, G. Portale and S. P. Armes, *Journal Of The American Chemical Society*, 2015, **137**, 1929-1937.
53. J. Chiefari, Y. K. Chong, F. Ercole, J. Krstina, J. Jeffery, T. P. T. Le, R. T. A. Mayadunne, G. F. Meijs, C. L. Moad, G. Moad, E. Rizzardo and S. H. Thang, *Macromolecules*, 1998, **31**, 5559-5562.
54. Y. K. Chong, T. P. T. Le, G. Moad, E. Rizzardo and S. H. Thang, *Macromolecules*, 1999, **32**, 2071-2074.
55. G. Moad, E. Rizzardo and S. H. Thang, *Australian Journal of Chemistry*, 2005, **58**, 379-410.
56. A. Goto, K. Sato, Y. Tsujii, T. Fukuda, G. Moad, E. Rizzardo and S. H. Thang, *Macromolecules*, 2001, **34**, 402-408.
57. C. Barner-Kowollik and S. Perrier, *Journal of Polymer Science Part A: Polymer Chemistry*, 2008, **46**, 5715-5723.
58. W. Shen, Q. Qiu, Y. Wang, M. Miao, B. Li, T. Zhang, A. Cao and Z. An, *Macromolecular Rapid Communications*, 2010, **31**, 1444-1448.
59. D. Matioszek, P.-E. Dufils, J. Vinas and M. Destarac, *Macromolecular Rapid Communications*, 2015, **36**, 1354-1361.

60. Y. K. Chong, G. Moad, E. Rizzardo and S. H. Thang, *Macromolecules*, 2007, **40**, 4446-4455.
61. T. D. Michl, K. E. S. Locock, N. E. Stevens, J. D. Hayball, K. Vasilev, A. Postma, Y. Qu, A. Traven, M. Haeussler, L. Meagher and H. J. Griesser, *Polymer Chemistry*, 2014, **5**, 5813-5822.
62. A. Postma, T. P. Davis, G. Moad and M. S. O'Shea, *Macromolecules*, 2005, **38**, 5371-5374.
63. C. P. Jesson, C. M. Pearce, H. Simon, A. Werner, V. J. Cunningham, J. R. Lovett, M. J. Smallridge, N. J. Warren and S. P. Armes, *Macromolecules*, 2017, **50**, 182-191.
64. K. M. Mattson, C. W. Pester, W. R. Gutekunst, A. T. Hsueh, E. H. Discekici, Y. Luo, B. V. K. J. Schmidt, A. J. McGrath, P. G. Clark and C. J. Hawker, *Macromolecules*, 2016, **49**, 8162-8166.
65. Y. T. Li and S. P. Armes, *Angewandte Chemie-International Edition*, 2010, **49**, 4042-4046.
66. K. L. Thompson, C. J. Mable, A. Cockram, N. J. Warren, V. J. Cunningham, E. R. Jones, R. Verber and S. P. Armes, *Soft Matter*, 2014, **10**, 8615-8626.
67. M. Semsarilar, V. Ladmiral, A. Blanazs and S. P. Armes, *Polymer Chemistry*, 2014, **5**, 3466-3475.
68. W. Smulders and M. J. Monteiro, *Macromolecules*, 2004, **37**, 4474-4483.
69. N. J. W. Penfold, J. R. Lovett, N. J. Warren, P. Verstraete, J. Smets and S. P. Armes, *Polymer Chemistry*, 2016, **7**, 79-88.
70. A. M. I. Ali, P. Pareek, L. Sewell, A. Schmid, S. Fujii, S. P. Armes and I. M. Shirley, *Soft Matter*, 2007, **3**, 1003-1013.
71. Y. Li and S. P. Armes, *Angewandte Chemie International Edition*, 2010, **49**, 4042-4046.
72. M. Save, J. V. M. Weaver, S. P. Armes and P. McKenna, *Macromolecules*, 2002, **35**, 1152-1159.
73. L. P. D. Ratcliffe, A. J. Ryan and S. P. Armes, *Macromolecules*, 2013, **46**, 769-777.
74. C. J. Ferguson, R. J. Hughes, B. T. T. Pham, B. S. Hawkett, R. G. Gilbert, A. K. Serelis and C. H. Such, *Macromolecules*, 2002, **35**, 9243-9245.
75. C. J. Ferguson, R. J. Hughes, D. Nguyen, B. T. T. Pham, R. G. Gilbert, A. K. Serelis, C. H. Such and B. S. Hawkett, *Macromolecules*, 2005, **38**, 2191-2204.
76. E. Sprong, J. S. K. Leswin, D. J. Lamb, C. J. Ferguson, B. S. Hawkett, B. T. T. Pham, D. Nguyen, C. H. Such, A. K. Serelis and R. G. Gilbert, *Macromolecular Symposia*, 2005, **231**, 84-93.
77. D. E. Ganeva, E. Sprong, H. de Bruyn, G. G. Warr, C. H. Such and B. S. Hawkett, *Macromolecules*, 2007, **40**, 6181-6189.
78. S. Boisse, J. Rieger, K. Belal, A. Di-Cicco, P. Beaunier, M.-H. Li and B. Charleux, *Chemical Communications*, 2010, **46**, 1950-1952.
79. S. Boissé, J. Rieger, G. Pembouong, P. Beaunier and B. Charleux, *Journal of Polymer Science Part A: Polymer Chemistry*, 2011, **49**, 3346-3354.
80. I. Chaduc, A. Crepet, O. Boyron, B. Charleux, F. D'Agosto and M. Lansalot, *Macromolecules*, 2013, **46**, 6013-6023.
81. M. Manguian, M. Save and B. Charleux, *Macromolecular Rapid Communications*, 2006, **27**, 399-404.
82. J. Rieger, W. Zhang, F. Stoffelbach and B. Charleux, *Macromolecules*, 2010, **43**, 6302-6310.
83. I. Chaduc, W. Zhang, J. Rieger, M. Lansalot, F. D'Agosto and B. Charleux, *Macromolecular Rapid Communications*, 2011, **32**, 1270-1276.

84. X. Zhang, S. Boissé, W. Zhang, P. Beaunier, F. D'Agosto, J. Rieger and B. Charleux, *Macromolecules*, 2011, **44**, 4149-4158.
85. J. Rieger, G. Osterwinter, C. Bui, F. Stoffelbach and B. Charleux, *Macromolecules*, 2009, **42**, 5518-5525.
86. X. Zhang, J. Rieger and B. Charleux, *Polymer Chemistry*, 2012, **3**, 1502-1509.
87. W. Zhang, F. D'Agosto, O. Boyron, J. Rieger and B. Charleux, *Macromolecules*, 2012, **45**, 4075-4084.
88. B. Charleux, G. Delaittre, J. Rieger and F. D'Agosto, *Macromolecules*, 2012, **45**, 6753-6765.
89. V. J. Cunningham, A. M. Alswieleh, K. L. Thompson, M. Williams, G. J. Leggett, S. P. Armes and O. M. Musa, *Macromolecules*, 2014, **47**, 5613-5623.
90. P. Chambon, A. Blanazs, G. Battaglia and S. P. Armes, *Macromolecules*, 2012, **45**, 5081-5090.
91. P. Stano, P. Carrara, Y. Kuruma, T. Pereira de Souza and P. L. Luisi, *Journal of Materials Chemistry*, 2011, **21**, 18887-18902.
92. M. Li, R. L. Harbron, J. V. M. Weaver, B. P. Binks and S. Mann, *Nat Chem*, 2013, **5**, 529-536.
93. A. Pohorille and D. Deamer, *Trends in Biotechnology*, 2002, **20**, 123-128.
94. J. W. Szostak, D. P. Bartel and P. L. Luisi, *Nature*, 2001, **409**, 387-390.
95. T. Nii and F. Ishii, *International Journal of Pharmaceutics*, 2005, **298**, 198-205.
96. L. Schwartz, D. Wolf, A. Markus, S. Wybraniec and Z. Wiesman, *Journal of Agricultural and Food Chemistry*, 2003, **51**, 5972-5976.
97. I. M. Shirley, H. B. Scher, R. M. Perrin, P. J. Wege, M. Rodson, J.-L. Chen and A. W. Rehmke, *Pest Management Science*, 2001, **57**, 129-132.
98. P. H. R. Keen, N. K. H. Slater and A. F. Routh, *Langmuir*, 2014, **30**, 1939-1948.
99. H. N. Yow and A. F. Routh, *Langmuir*, 2009, **25**, 159-166.
100. B. Stadler, A. D. Price, R. Chandrawati, L. Hosta-Rigau, A. N. Zelikin and F. Caruso, *Nanoscale*, 2009, **1**, 68-73.
101. V. P. Torchilin, *Nat Rev Drug Discov*, 2005, **4**, 145-160.
102. M. Antonietti and S. Förster, *Advanced Materials*, 2003, **15**, 1323-1333.
103. B. M. Discher, Y. Y. Won, D. S. Ege, J. C. M. Lee, F. S. Bates, D. E. Discher and D. A. Hammer, *Science*, 1999, **284**, 1143-1146.
104. F. Chécot, S. Lecommandoux, Y. Gnanou and H.-A. Klok, *Angewandte Chemie International Edition*, 2002, **41**, 1339-1343.
105. J. Rodríguez-Hernández and S. Lecommandoux, *Journal Of The American Chemical Society*, 2005, **127**, 2026-2027.
106. D. E. Discher and A. Eisenberg, *Science*, 2002, **297**, 967-973.
107. J. Du, Y. Tang, A. L. Lewis and S. P. Armes, *Journal Of The American Chemical Society*, 2005, **127**, 17982-17983.
108. D. A. Wilson, R. J. M. Nolte and J. C. M. van Hest, *Nature Chemistry*, 2012, **4**, 268-274.
109. A. Napoli, M. Valentini, N. Tirelli, M. Muller and J. A. Hubbell, *Nature Materials*, 2004, **3**, 183-189.
110. P. J. Photos, L. Bacakova, B. Discher, F. S. Bates and D. E. Discher, *Journal of Controlled Release*, 2003, **90**, 323-334.
111. R. P. Brinkhuis, F. Rutjes and J. C. M. van Hest, *Polymer Chemistry*, 2011, **2**, 1449-1462.
112. C. Pegoraro, D. Cecchin, L. S. Gracia, N. Warren, J. Madsen, S. P. Armes, A. Lewis, S. MacNeil and G. Battaglia, *Cancer letters*, 2013, **334**, 328-337.

113. C. Sanson, C. Schatz, J. F. Le Meins, A. Soum, J. Thevenot, E. Garanger and S. Lecommandoux, *Journal of Controlled Release*, 2010, **147**, 428-435.
114. F. Ahmed, R. I. Pakunlu, G. Srinivas, A. Brannan, F. Bates, M. L. Klein, T. Minko and D. E. Discher, *Molecular Pharmaceutics*, 2006, **3**, 340-350.
115. D. A. Christian, S. Cai, D. M. Bowen, Y. Kim, J. D. Pajerowski and D. E. Discher, *European Journal of Pharmaceutics and Biopharmaceutics*, 2009, **71**, 463-474.
116. J. Huang, C. Bonduelle, J. Thévenot, S. Lecommandoux and A. Heise, *Journal Of The American Chemical Society*, 2012, **134**, 119-122.
117. H. Lomas, I. Canton, S. MacNeil, J. Du, S. P. Armes, A. J. Ryan, A. L. Lewis and G. Battaglia, *Advanced Materials*, 2007, **19**, 4238-4243.
118. S. F. M. van Dongen, M. Nallani, J. Cornelissen, R. J. M. Nolte and J. C. M. van Hest, *Chemistry-A European Journal*, 2009, **15**, 1107-1114.
119. I. Canton, M. Massignani, N. Patikarnmonthon, L. Chierico, J. Robertson, S. A. Renshaw, N. J. Warren, J. P. Madsen, S. P. Armes, A. L. Lewis and G. Battaglia, *The FASEB Journal*, 2013, **27**, 98-108.
120. H. Bermudez, A. K. Brannan, D. A. Hammer, F. S. Bates and D. E. Discher, *Macromolecules*, 2002, **35**, 8203-8208.
121. G. Battaglia, A. J. Ryan and S. Tomas, *Langmuir*, 2006, **22**, 4910-4913.
122. S. Qin, Y. Geng, D. E. Discher and S. Yang, *Advanced Materials*, 2006, **18**, 2905-2909.
123. J. Ding and G. Liu, *The Journal of Physical Chemistry B*, 1998, **102**, 6107-6113.
124. F. Ahmed and D. E. Discher, *Journal of Controlled Release*, 2004, **96**, 37-53.
125. U. Borchert, U. Lipprandt, M. Bilang, A. Kimpfler, A. Rank, R. Peschka-Süss, R. Schubert, P. Lindner and S. Förster, *Langmuir*, 2006, **22**, 5843-5847.
126. S. Lecommandoux, O. Sandre, F. Chécot, J. Rodriguez-Hernandez and R. Perzynski, *Journal of Magnetism and Magnetic Materials*, 2006, **300**, 71-74.
127. D. J. Adams, S. Adams, D. Atkins, M. F. Butler and S. Furzeland, *Journal of Controlled Release*, 2008, **128**, 165-170.
128. B. Karagoz, C. Boyer and T. P. Davis, *Macromolecular Rapid Communications*, 2014, **35**, 417-421.
129. S. U. Pickering, *Journal of the Chemical Society*, 1907, **91**, 2001-2021.
130. W. Ramsden, *Proceedings of the Royal Society of London*, 1903, **72**, 156-164.
131. B. P. Binks and S. O. Lumsdon, *Physical Chemistry Chemical Physics*, 1999, **1**, 3007-3016.
132. S. Levine, B. D. Bowen and S. J. Partridge, *Colloids and Surfaces*, 1989, **38**, 325-343.
133. B. P. Binks and S. O. Lumsdon, *Langmuir*, 2001, **17**, 4540-4547.
134. K. L. Thompson, S. P. Armes, J. R. Howse, S. Ebbens, I. Ahmad, J. H. Zaidi, D. W. York and J. A. Burdis, *Macromolecules*, 2010, **43**, 10466-10474.
135. K. L. Thompson, S. P. Armes, D. W. York and J. A. Burdis, *Macromolecules*, 2010, **43**, 2169-2177.
136. A. Walsh, K. L. Thompson, S. P. Armes and D. W. York, *Langmuir*, 2010, **26**, 18039-18048.
137. Y. Cui, M. Threlfall and J. S. van Duijneveldt, *Journal of Colloid and Interface Science*, 2011, **356**, 665-671.
138. B. P. Binks, *Current Opinion in Colloid & Interface Science*, 2002, **7**, 21-41.
139. B. P. Binks and S. O. Lumsdon, *Langmuir*, 2000, **16**, 8622-8631.
140. R. Aveyard, B. P. Binks and J. H. Clint, *Advances in Colloid and Interface Science*, 2003, **100-102**, 503-546.

141. Z. Mao, H. Xu and D. Wang, *Advanced Functional Materials*, 2010, **20**, 1053-1074.
142. A. San-Miguel and S. H. Behrens, *Langmuir*, 2012, **28**, 12038-12043.
143. E. Vignati, R. Piazza and T. P. Lockhart, *Langmuir*, 2003, **19**, 6650-6656.
144. N. D. Denkov, I. B. Ivanov, P. A. Kralchevsky and D. T. Wasan, *Journal of Colloid and Interface Science*, 1992, **150**, 589-593.
145. R. Van Hooghten, L. Imperiali, V. Boeckx, R. Sharma and J. Vermant, *Soft Matter*, 2013, **9**, 10791-10798.
146. R. N. Wenzel, *Industrial & Engineering Chemistry*, 1936, **28**, 988-994.
147. A. B. D. Cassie and S. Baxter, *Transactions of the Faraday Society*, 1944, **40**, 546-551.
148. E. Martines, K. Seunarine, H. Morgan, N. Gadegaard, C. D. W. Wilkinson and M. O. Riehle, *Nano Letters*, 2005, **5**, 2097-2103.
149. D. Öner and T. J. McCarthy, *Langmuir*, 2000, **16**, 7777-7782.
150. K. L. Thompson, P. Chambon, R. Verber and S. P. Armes, *Journal Of The American Chemical Society*, 2012, **134**, 12450-12453.
151. S. Fujii, Y. Cai, J. V. M. Weaver and S. P. Armes, *Journal of the American Chemical Society*, 2005, **127**, 7304-7305.
152. K. L. Thompson, E. C. Giakoumatos, S. Ata, G. B. Webber, S. P. Armes and E. J. Wanless, *Langmuir*, 2012, **28**, 16501-16511.
153. A. J. Morse, S. P. Armes, K. L. Thompson, D. Dupin, L. A. Fielding, P. Mills and R. Swart, *Langmuir*, 2013, **29**, 5466-5475.
154. A. J. Morse, J. Madsen, D. J. Growney, S. P. Armes, P. Mills and R. Swart, *Langmuir*, 2014, **30**, 12509-12519.
155. S. E. Harding, D. B. Sattelle and V. A. Bloomfield, *Laser Light Scattering in Biochemistry*, The Royal Society of Chemistry, Cambridge, 1992.
156. M. Ballauff, *Current Opinion in Colloid & Interface Science*, 2001, **6**, 132-139.
157. L. A. Fielding, PhD Thesis, *Synthesis, Characterisation and Applications of Colloidal Nanocomposite Particles*, University of Sheffield, 2012.
158. A. P. Cocco, G. J. Nelson, W. M. Harris, A. Nakajo, T. D. Myles, A. M. Kiss, J. J. Lombardo and W. K. S. Chiu, *Physical Chemistry Chemical Physics*, 2013, **15**, 16377-16407.
159. J. A. Balmer, O. O. Mykhaylyk, J. P. A. Fairclough, A. J. Ryan, S. P. Armes, M. W. Murray, K. A. Murray and N. S. J. Williams, *Journal Of The American Chemical Society*, 2010, **132**, 2166-2168.

Chapter Two - Framboidal ABC triblock copolymer vesicles: a new class of efficient Pickering Emulsifier

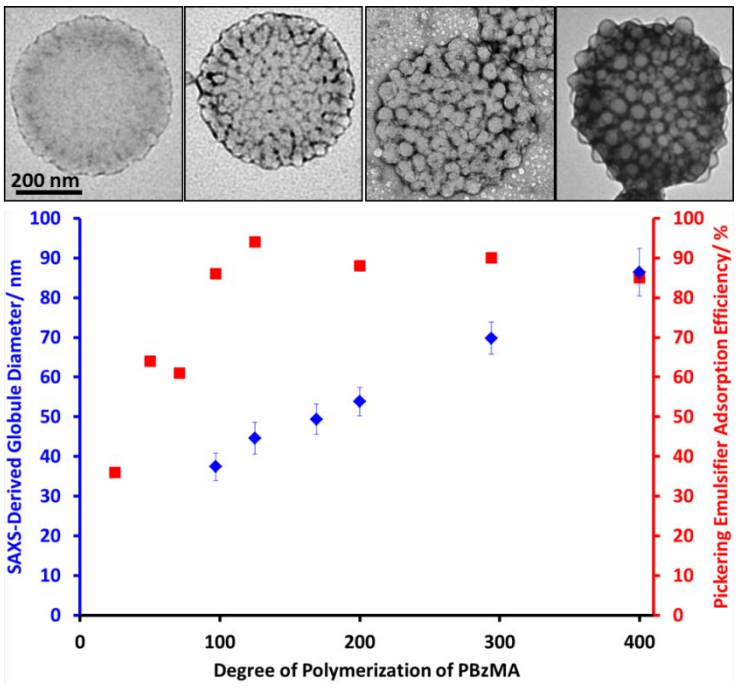

Reproduced in part from [C. J. Mable, N. J. Warren, K. L. Thompson, O. O. Mykhaylyk and S. P. Armes, *Chemical Science*, 2015, **6**, 6179-6188]. Copyright [2015] The Royal Society of Chemistry.

Introduction

Pickering emulsions are water or oil droplets that are stabilised by colloidal particles and have been recognised for more than a century.[1] These systems typically exhibit greater droplet stability compared to surfactant-stabilised emulsions.[2] This is the result of strong, essentially irreversible particle adsorption at the oil-water interface, which minimises the interfacial area between the two immiscible liquids and provides a steric barrier towards droplet coalescence.[2, 3] A wide range of nanoparticles such as silica sols[4,5] polystyrene latexes[6-9] and inorganic clays[10] have been shown to be effective Pickering emulsifiers. More recently, cross-linked block copolymer nanoparticles prepared by reversible addition-fragmentation chain transfer (RAFT) polymerisation[11, 12] have proven to be effective oil-in-water[13] and water-in-oil[14] Pickering emulsifiers. For example, Thompson *et al.*[13] prepared highly stable emulsions using poly(glycerol monomethacrylate)-poly(2-hydroxypropyl methacrylate)-poly(ethylene glycol dimethacrylate) (PGMA-PHPMA-PEGDMA) triblock copolymer vesicles. Turbidimetry studies indicated that these nanoparticles had an adsorption efficiency of as low as 57 %, depending on the vesicle concentration used for homogenisation. This relatively poor adsorption efficiency was in part attributed to the high water content of the vesicles, which leads to a low Hamaker constant compared to solid particles.

In principle, particle wettability can be modulated by increasing surface roughness in order to enhance interfacial adsorption and hence Pickering emulsion stability. This hypothesis has been recently verified by San-Miguel and Behrens, who coated cationic silica microparticles with anionic nanoparticles prepared from a commercial methacrylic acid/methyl methacrylate statistical copolymer (Eudragit S-100; 33 % methacrylic acid). Solvent annealing of the nanoparticle coating was used to control the surface roughness of the microparticles, which were subsequently utilised to prepare oil-in-water Pickering emulsions at pH 5.[15] In a related study, carbon black particles possessing a characteristic fractal morphology were used to stabilise the water/*n*-octane interface.[16]

In the present study, we prepare a series of ABC triblock copolymer vesicles of exquisitely tunable surface roughness via RAFT aqueous dispersion polymerisation.[17] First, a poly(glycerol monomethacrylate) (PGMA) macromolecular chain transfer agent (macro-CTA) is chain-extended using 2-hydroxypropyl

methacrylate (HPMA) in aqueous solution. In situ polymerisation-induced self-assembly (PISA) occurs to form nanoparticles comprising poly(2-hydroxypropyl methacrylate) (PHPMA) cores that are sterically stabilised by the water-soluble PGMA chains.[18-21] Depending on the relative volume fractions of the PGMA and PHPMA blocks, well-defined copolymer spheres, worms or vesicles can be obtained at relatively high solids directly in aqueous solution.[22] The mechanism of formation of the vesicular morphology has been investigated by Blanazs et al.[22, 23] Chambon and co-workers reported that chain extension of such PGMA-PHPMA precursor vesicles using a water-insoluble monomer such as benzyl methacrylate (BzMA) results in the formation of framboidal (raspberry-like) ABC triblock copolymer vesicles via seeded RAFT emulsion polymerisation.[24] Herein, we revisit this formulation in order to gradually increase the target degree of polymerisation (DP) of the PBzMA block over a wide range using the same batch of PGMA-PHPMA diblock copolymer vesicles. This systematic approach enables the evolution of the framboidal morphology to be explored in detail: a series of vesicles with gradually increasing surface roughness are produced, as judged by transmission electron microscopy (TEM) and small-angle x-ray scattering (SAXS). These framboidal vesicles are then employed to prepare oil-in-water Pickering emulsions using either *n*-dodecane or *n*-hexane as the droplet phase. The emulsions are characterised in terms of their droplet size distributions and the particle adsorption efficiency at the oil/water interface is assessed as a function of surface roughness. For the sake of brevity, a shorthand notation is utilised throughout this Chapter to describe the various block copolymers. Thus G, H, B, and E denote glycerol monomethacrylate, 2-hydroxypropyl methacrylate, benzyl methacrylate and ethylene glycol dimethacrylate, respectively. For example, $G_xH_yB_z$ represents a poly(glycerol monomethacrylate)-poly(2-hydroxypropyl methacrylate)-poly(benzyl methacrylate) copolymer, where x, y, and z indicate the mean DP of the three respective blocks.

Experimental Details

Materials

All reagents were used as received unless otherwise stated. Benzyl methacrylate (BzMA), *n*-dodecane and 4, 4'-azobis-4-cyanopentanoic acid (ACVA) were purchased from Sigma-Aldrich (UK). BzMA inhibitor was

removed using an inhibitor removal column (Sigma-Aldrich). Ethanol, dichloromethane, DMSO and DMF were purchased from Fisher Scientific (UK). Glycerol monomethacrylate (GMA) was kindly donated by GEO Specialty Chemicals (Hythe) and used without further purification. 2-Hydroxypropyl methacrylate (HPMA) was purchased from Alfa Aesar (UK) and contained 0.07 mol % dimethacrylate impurity, as judged by high performance liquid chromatography (HPLC). CD_3OD and d_6-DMSO NMR solvents were purchased from Goss Scientific (UK). 4-Cyano-4-(2-phenylethanesulfanylthiocarbonyl)sulfanyl-pentanoic acid (PETTC) was synthesised in-house.[25] Deionised water was obtained using an Elga Elgastat Option 3A water purifier; its pH was approximately 6.2 and its surface tension was 72.0 mN m^{-1} at 20 ^{o}C.

RAFT Synthesis of PGMA Macro-CTA Agent in Ethanol

A round-bottomed flask was charged with GMA (30.0 g; 187 mmol), PETTC (1.01 g; 2.97 mmol), ACVA (167 mg, 0.156 mmol) and ethanol (39.5 g). The sealed reaction vessel was purged with N_2 for 30 min, placed in a pre-heated oil bath at 70 ^{o}C and stirred for 135 min. The resulting PGMA macro-CTA (GMA conversion = 87 %; M_n = 17,600 g mol^{-1}, M_w/M_n = 1.16) was purified by precipitation into excess dichloromethane. A mean DP of 63 was calculated for this macro-CTA using ^{1}H NMR spectroscopy by comparison of the integral from 3.4 ppm to 4.3 ppm due to five protons from the PGMA with that of the peaks around 7 ppm due to the five aromatic protons from the RAFT CTA.

Preparation of Linear PGMA-PHPMA Diblock Copolymer Precursor Vesicles via RAFT Aqueous Dispersion Polymerisation at 15 % w/w Solids

$PGMA_{63}$ macro-CTA (5.00 g, 0.485 mmol), HPMA monomer (24.5 g, 170 mmol) and deionised water (167 g, purged with N_2 for 30 min) were weighed into a 250 mL round-bottomed flask and purged with N_2 for 20 min. ACVA was added (68.9 mg, 0.242 mmol, CTA/ACVA molar ratio = 2.0) and purged with N_2 for a further 10 min prior to immersion in an oil bath set at 70 ^{o}C for 2 h with stirring. Finally, the polymerisation was quenched by cooling to room temperature with subsequent exposure to air.

Preparation of PGMA-PHPMA-PBzMA Triblock Copolymer Vesicles via RAFT Seeded Emulsion Polymerisation at 10-19 % w/w Solids

$PGMA_{63}$-$PHPMA_{350}$ diblock precursor vesicles (15.0 ml of a 10 % w/w copolymer dispersion, 1.50 g copolymer, 0.0247 mmol), ACVA (1.38 mg, 0.00494 mmol, CTA/ACVA molar ratio = 5.0) and BzMA monomer (0. 109 g, 0.617 mmol, target DP = 25) were weighed into a 40 ml sample vial and purged with N_2 for 20 min prior to immersion in an oil bath set at 70 ^{o}C for 4 h. Then the polymerisation was quenched by cooling to room temperature and subsequent exposure to air. A series of similar copolymer syntheses were performed for which the PBzMA target DP ranged from 50 to 400 using BzMA masses varying from 0.218 g to 1.74 g (1.23 mmol to 9.87 mmol), respectively.

Pickering Emulsion Formation

n-Dodecane (2.0 ml) was homogenised with 2.0 ml of a 0.5-3.0 % w/v aqueous vesicle dispersion for 2 min using a IKA Ultra-Turrax T-18 homogeniser with a 10 mm dispersing tool operating at 12,000 rpm. The droplets were imaged by OM and the mean droplet diameter was assessed by laser diffraction. For TEM and SEM studies, *n*-hexane was used instead of *n*-dodecane to ensure complete oil evaporation.

Turbidimetry Experiments

Pickering emulsions were allowed to cream overnight before an appropriate amount of the aqueous phase was extracted and diluted ten-fold, before measuring the absorbance from 400 to 800 nm using visible absorption spectroscopy. Calibration plots were constructed for each vesicle dispersion by recording the absorbance at 750 nm of the vesicle dispersions, varying the copolymer concentration from 0.00625 to 0.1 % w/w.

Dynamic Light Scattering (DLS)

Intensity-average hydrodynamic diameters of the copolymer dispersions were determined using a Malvern Zetasizer NanoZS instrument. Dilute aqueous dispersions (0.10 % w/w) were analysed using disposable cuvettes and all data

were averaged over three consecutive runs to give the hydrodynamic diameter (D_h).

^{1}H NMR Spectroscopy

All NMR spectra were recorded using a 400 MHz Bruker Avance-400 spectrometer and 64 scans were averaged per spectrum. The mean DP of the PBzMA block was calculated as described previously by Chambon et al.[24]

Gel Permeation Chromatography (GPC)

Copolymer molecular weights and polydispersities were determined using a DMF GPC set-up operating at 60 ^{o}C and comprising two Polymer Laboratories PL gel 5 μm Mixed C columns connected in series to a Varian 390 LC multi-detector suite (only the refractive index detector was utilised) and a Varian 290 LC pump injection module. The GPC eluent was HPLC grade DMF containing 10 mM LiBr at a flow rate of 1.0 mL min^{-1}. DMSO was used as a flow-rate marker. Calibration was conducted using a series of ten near-monodisperse poly(methyl methacrylate) standards (M_n = 625 – 618,000 g mol^{-1}). The chromatograms were analysed using Varian Cirrus GPC software (version 3.3) provided by the instrument manufacturer (Polymer Laboratories).

Transmission Electron Microscopy (TEM)

Aggregate solutions were diluted fifty-fold at 20 ^{o}C to generate 0.10 % w/w dispersions. Copper/palladium TEM grids (Agar Scientific) were surface-coated in-house to yield a thin film of amorphous carbon. The grids were then plasma glow-discharged for 30 s to create a hydrophilic surface. Individual samples (0.1 % w/w, 12 μL) were adsorbed onto the freshly glow-discharged grids for 1 min and then blotted with filter paper to remove excess solution. To stain the aggregates, uranyl formate (0.75 % w/v) solution (9 μL) was soaked on the sample-loaded grid for 20 s and then carefully blotted to remove excess stain. The grids were then dried using a vacuum hose. Imaging was performed on a Phillips CM100 instrument at 100 kV, equipped with a Gatan 1 K CCD camera.

Small-Angle X-Ray Scattering (SAXS)

SAXS patterns were recorded at two synchrotron sources (ESRF, station ID02, Grenoble, France and Diamond Light Source, station I22, Didcot, UK). A monochromatic X-ray radiation (wavelength λ = 0.0995 nm and 0.1001 nm, respectively) and 2D SAXS detectors (FReLoN Kodak CCD and Pilatus 2M, respectively) were used for these experiments. The SAXS camera length set-ups covered the q range from 0.009 nm^{-1} to 0.04 nm^{-1} (ESRF) and from 0.02 nm^{-1} to 1.9 nm^{-1} (Diamond), where $q = \frac{4\pi\sin\theta}{\lambda}$ is the modulus of the scattering vector and θ is one-half of the scattering angle. Either a 2.0 mm diameter glass capillary (ESRF) or a liquid cell composed of two mica windows (each of 25 μm thickness) separated by a polytetrafluoroethylene spacer of 1 mm thickness (Diamond) were used as sample holders, respectively. X-ray scattering data were reduced by Nika SAS data reduction macros for Igor Pro (integration, normalisation, background subtraction) and were further analysed using Irena SAS macros for Igor Pro. SAXS measurements were conducted on $G_{63}H_{350}B_z$ (z = 0 – 400, see Table 2.2) dispersions either in water (ESRF and Diamond) or in a 40 % w/w aqueous sucrose solution (Diamond). The copolymer concentration was diluted from 10 % w/w (as-synthesised) to 1.0 % w/w for data collection.

Visible Absorption Spectroscopy

Turbidities of both the initial vesicle dispersions and also the underlying aqueous phase of the corresponding creamed emulsions after homogenisation with *n*-dodecane were assessed by visible absorption spectrophotometry (Perkin-Elmer Lambda 25 instrument) between 400 and 800 nm at a scan speed of 960 nm min^{-1}.

Optical Microscopy (OM)

Optical microscopy images were recorded using a Motic DMBA300 digital biological microscope with a built-in camera and equipped with Motic Images Plus 2.0 ML software.

Laser Diffraction

A Malvern Mastersizer 2000 instrument equipped with a small volume Hydro 2000SM sample dispersion unit (ca. 50 ml), a He-Ne laser operating at 633 nm, and a solid-state blue laser operating at 466 nm was used to size each emulsion. The stirring rate was adjusted to 1,000 rpm in order to avoid creaming of the emulsion during analysis. After each measurement, the cell was rinsed once with ethanol, followed by three rinses with doubly-distilled water; the glass walls of the cell were carefully wiped with lens cleaning tissue to avoid cross- contamination and the laser was aligned centrally to the detector prior to data acquisition. The volume-average diameter was measured and repeated four times for each emulsion.

Results and Discussion

Synthesis and Characterisation

The initial RAFT solution polymerisation of GMA was conducted in ethanol at 70 ^{o}C to generate a near-monodisperse G_{63} macro-CTA (M_w/M_n = 1.16; see Figure 2.1 and Table 2.1). After purification, this water-soluble macro-CTA was utilised for the RAFT aqueous dispersion polymerisation of HPMA at 15 % w/w solids. ^{1}H NMR studies indicated that >99% HPMA conversion was achieved within 2 h at 70 ^{o}C, as expected from previous studies.[23] Gel permeation chromatography (GPC) studies indicated that near-monodisperse diblock copolymers were obtained with minimal macro-CTA contamination and high blocking efficiencies (M_w/M_n = 1.16; see Figure 2.1 and Table 2.1). GPC traces were invariably unimodal but typically exhibited a high molecular weight shoulder. The latter feature is attributable to low levels of dimethacrylate impurity within HPMA (approximately 0.07 mol % as judged by HPLC analysis), which results in light cross-linking of the PHPMA chains.

TEM images (see Figure 2.2, $G_{63}H_{350}$) reveal a pure vesicular morphology, as expected for this asymmetric diblock composition. The vesicle folds that are discernible in the TEM images are the result of buckling and/or partial collapse of these relatively delicate nano-structures under the ultrahigh vacuum conditions. These well-defined $G_{63}H_{350}$ diblock copolymer precursor vesicles were also characterised by DLS (see Table 2.1) and then utilised for the RAFT seeded

emulsion polymerisation of BzMA at 70°C to produce a series of nine $G_{63}H_{350}B_z$ triblock copolymers (where z ranges from 25 to 400).

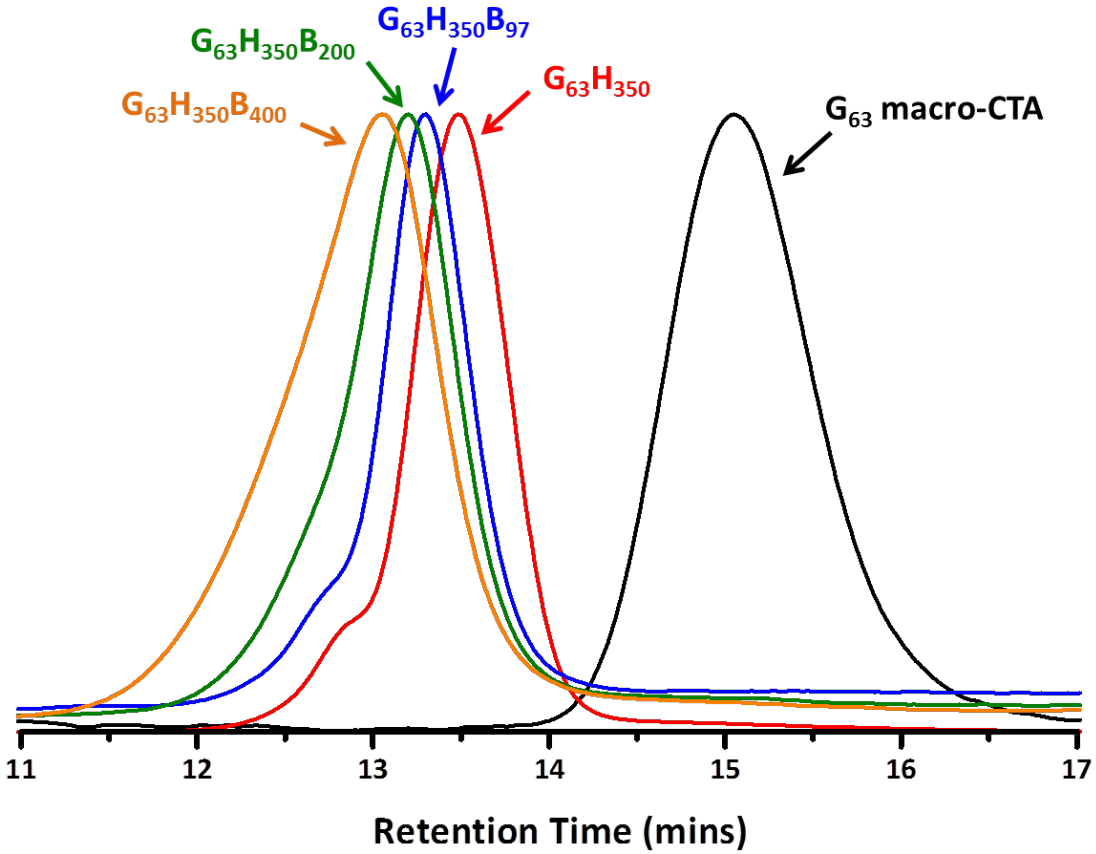

Figure 2.1 DMF GPC curves obtained for the G_{63} macro-CTA, linear $G_{63}H_{350}$ diblock copolymer precursor, and selected $G_{63}H_{350}B_z$ triblock copolymers (where z ranges from 25 to 400). Number-average molecular weights and polydispersities obtained for all nine of these copolymers are shown in Table 2.1.

^{1}H NMR studies for these triblock copolymers (see Figure 2.3) indicate conversions greater than 96 % (see Table 2.1). Signal j at 7.1-7.4 ppm, which is assigned to the five aromatic BzMA protons, increases on targeting higher DPs.

DMF GPC studies confirmed that near-monodisperse triblock copolymers were obtained (M_w/M_n ranges from 1.10 to 1.25) with high blocking efficiencies; see Figure 2.1 and Table 2.1. It is noteworthy that these polydispersities are significantly lower than those reported by Chambon et al., who reported M_w/M_n values as high as 1.50.[24] This is most likely attributable to the higher macro-CTA/initiator molar ratio of 5.0 employed in the present work. In contrast, Chambon et al. used a macro-CTA/initiator molar ratio of just 2.0, which is known to lead to reduced living

character for RAFT polymerisations and may also lead to homopolymer impurities.[26] Moreover, it is worth noting that Chambon et al. only targeted three $G_{58}H_{350}B_z$ copolymers, for which z was 200, 300 or 400.[24]

Table 2.1 Summary of ^{1}H NMR calculated composition and conversion, GPC number-average molecular weight (M_n) and polydispersity (M_w/M_n) and DLS hydrodynamic diameter (D_h) obtained for a G_{63} macro-CTA, linear $G_{63}H_{350}$ diblock copolymer precursor vesicles and framboidal $G_{63}H_{350}B_z$ triblock copolymer vesicles (where z ranges from 25 to 400).

Copolymer Composition	Conversion (%)	M_n (kg mol^{-1})	M_w/M_n	D_h (PDI) (nm)
G_{63}	-	17.6	1.16	-
$G_{63}H_{350}$	>99[a]	82.2	1.16	362 (0.08)
$G_{63}H_{350}B_{25}$	100	87.3	1.16	401 (0.09)
$G_{63}H_{350}B_{50}$	100	100.0	1.10	411 (0.09)
$G_{63}H_{350}B_{71}$	94	102.1	1.10	406 (0.09)
$G_{63}H_{350}B_{97}$	97	104.5	1.11	407 (0.07)
$G_{63}H_{350}B_{125}$	100	112.2	1.12	394 (0.04)
$G_{63}H_{350}B_{169}$	97	114,3	1.13	364 (0.06)
$G_{63}H_{350}B_{200}$	100	117.7	1.15	375 (0.08)
$G_{63}H_{350}B_{294}$	98	130.7	1.18	366 (0.05)
$G_{63}H_{350}B_{400}$	100	140.9	1.25	418 (0.12)

[a] In this case, this corresponds to HPMA conversion.

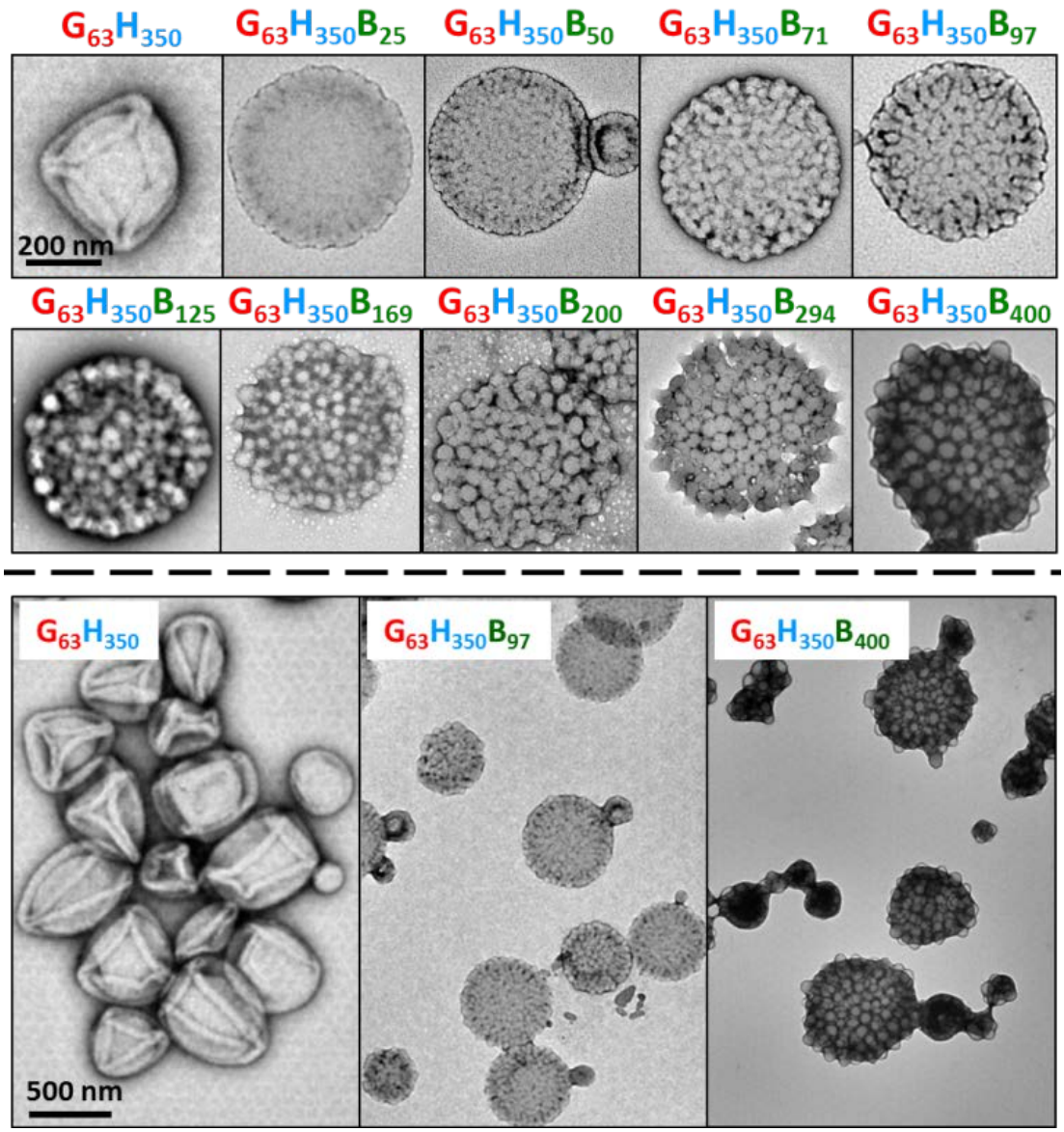

Figure 2.2 Representative TEM images obtained for a series of framboidal $G_{63}H_{350}B_z$ triblock copolymer vesicles (where z = 25-400) and also the precursor $G_{63}H_{350}$ diblock copolymer vesicles. A 200 nm scale bar applies for the first ten images, while a 500 nm scale bar applies for the first ten images, while a 500 nm scale bar applies for the last three images.

In the present study, we explore the evolution of the framboidal morphology in much more detail (nine $G_{63}H_{350}B_z$ copolymers, with z ranging from 25 to 400) while achieving significantly better control over the copolymer molecular weight distribution.

DLS and TEM studies indicate that the vesicle diameter is more or less unchanged as the PBzMA DP is increased (see Table 2.1 and Figure 2.2). TEM analysis of the

$G_{63}H_{350}$ diblock copolymer precursor vesicles indicates a relatively smooth and featureless surface morphology (see Figure 2.2). After chain extension with BzMA, the vesicle surface becomes increasingly rough until individual micelle-like globules of approximately 34 nm can be observed at a block copolymer composition of $G_{63}H_{350}B_{97}$. This suggests that nano-scale phase separation occurs within the vesicle walls during the polymerisation of BzMA, as previously reported by Chambon *et al.*[24] As the target PBzMA DP is increased, the globules grow in size and prominence.

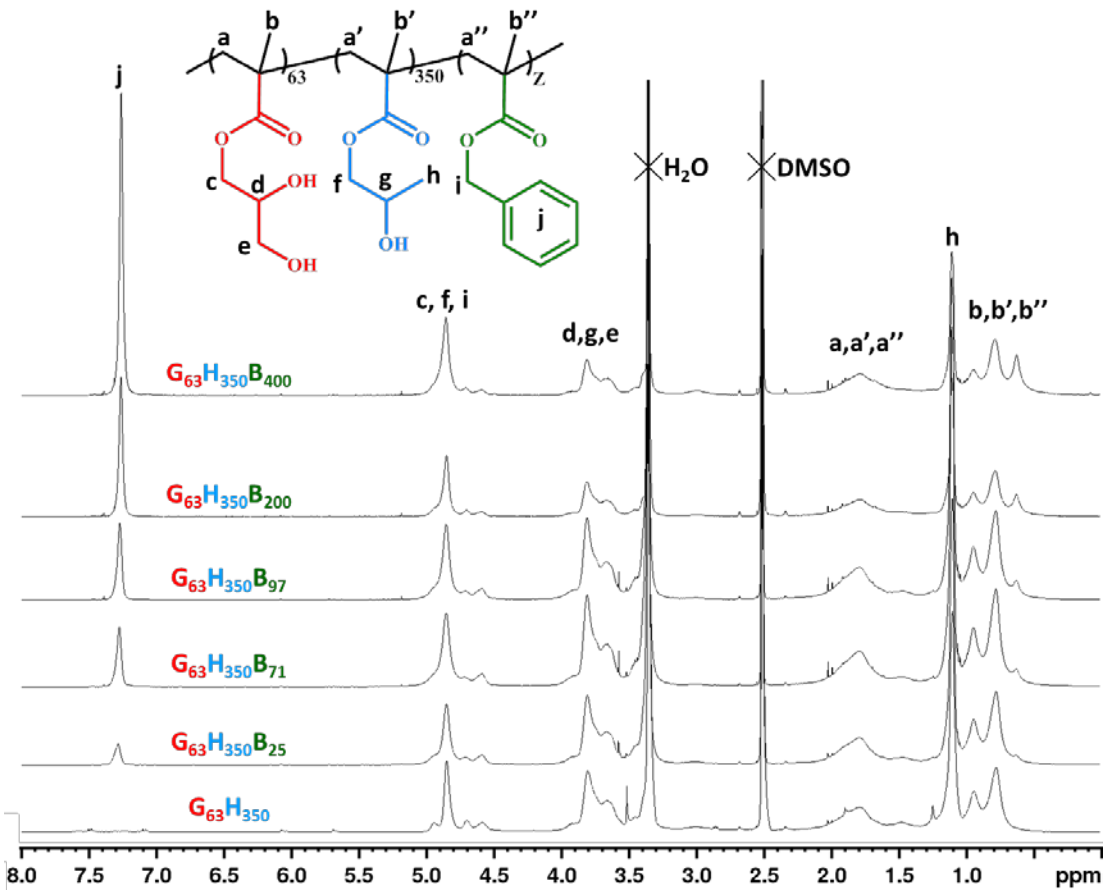

Figure 2.3 Assigned ^{1}H NMR spectra (d_6-DMSO) obtained for the $G_{63}H_{350}$ linear diblock copolymer precursor and five of the corresponding $G_{63}H_{350}B_z$ triblock copolymers (where z ranges from 25 to 400).

SAXS Studies

SAXS is used to further characterise this *framboidal* vesicular morphology. TEM images (Figure 2.2) suggest three distinct particle morphologies: vesicles with smooth membranes (morphology 1), vesicles with pitted membranes (morphology 2) and vesicles with globular membranes (morphology 3) (see Figure 2.4). The latter morphology is comparable to the polymer core-particulate silica shell particles reported by Balmer and co-workers[27-30] In this earlier work, Monte Carlo simulations were utilised to demonstrate[27] that the SAXS patterns obtained for such nanocomposite particles can be described by a two-population model represented by a superposition of two scattering signals originating from a core-shell spherical particle (population 1) and the small spherical silica particles that formed the shell (population 2).

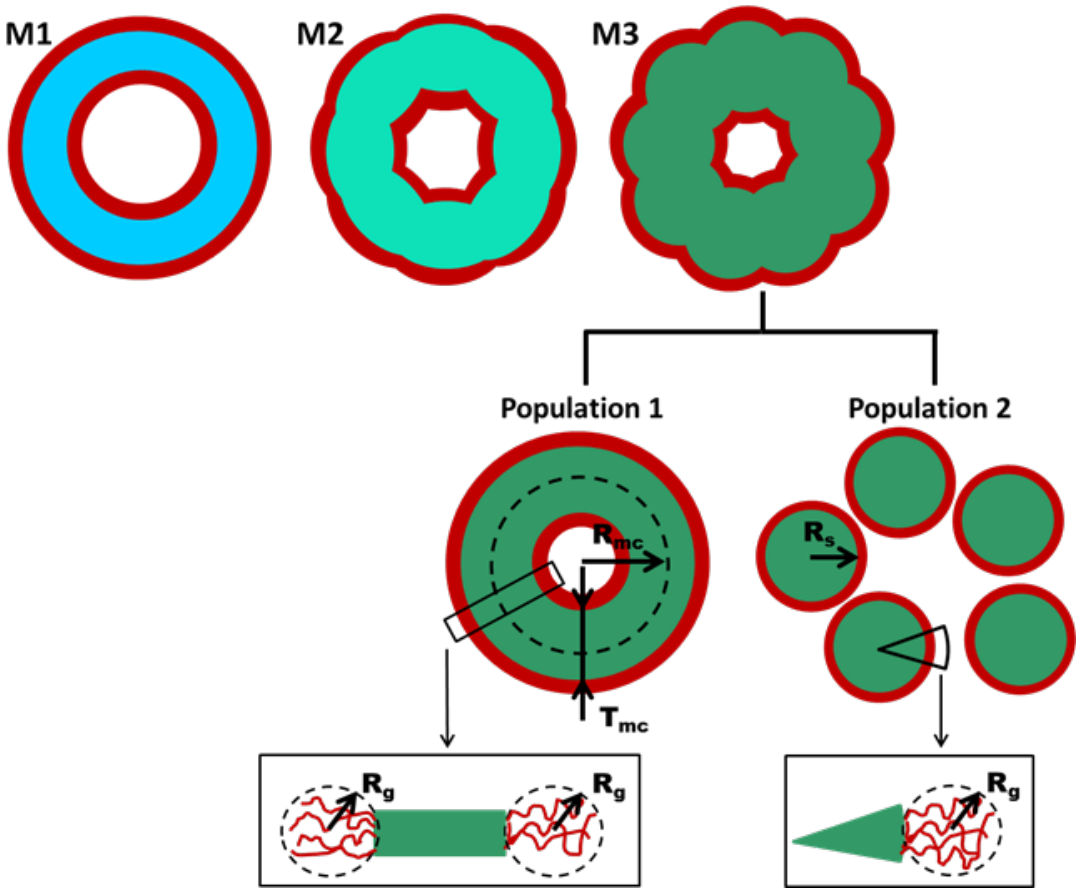

Figure 2.4. Schematic representation of the structural morphology of both a $G_{63}H_{350}$ diblock copolymer precursor vesicle and a series of $G_{63}H_{350}B_z$ triblock copolymer vesicles, where red = PGMA (G), light blue = PHPMA (H), light green = mixed PHPMA and PBzMA (B) membrane where $z \leq 50$, and dark green = mixed PHPMA and PBzMA membrane where $z \geq 97$.

Table 2.2 Structural parameters obtained for a series of $G_{63}H_{350}B_z$ (z = 0 to 400) copolymer dispersions in either pure water or a 40 % w/w aqueous sucrose solution from SAXS analysis using the two-population model (Equation A1.1 in the Appendix, n = 2). Representative parameters of the first population model (population 1) corresponding to vesicles (whose form factor is described by Equation A1.2 in the Appendix): R_{mc} is the radius from the center of the vesicle to the center of the membrane (Figure 2.4) and σ_{Rmc} is the associated standard deviation, T_{mc} is the membrane core thickness and σ_{Tmc} is the associated standard deviation, R_{out} is the total radius of the vesicle ($R_{out} = R_{mc} + \frac{1}{2}T_{mc} + 2R_g$, where the radius of gyration of the corona PGMA block, R_g, is 2.1 nm). Representative parameters of the second population (population 2) corresponding to spherical micelles (whose form factor is described by Equation A1.7 in the Appendix): R_s is the core radius, σ_{Rs} is the standard deviation of the core radius, R_{PY} is the Percus-Yevick correlation radius of densely-packed spherical micelles and F_{PY} is the Percus-Yevick effective volume fraction of the packed micelles. c_2/c_1 is the ratio of the volume fraction of the copolymers forming spherical micelles (population 2) to the volume fraction of the copolymers forming vesicles (population 1). V_{PBzMA} denotes the volume of the hydrophobic PBzMA block. Two sets of fitting parameters are given for $G_{63}H_{350}B_{400}$ in a 40 % w/w aqueous sucrose solution.

Copolymer Composition	V_{PBzMA} /nm^3	ξ_{mc} ×10^{-10} /cm^{-2}	Population 1					c_2/c_1	Population 2			
			R_{mc} (σ_{Rmc}) /nm	T_{mc} (σ_{Tmc})/ nm		R_{out}/ nm			R_s (σ_{Rs})/ nm		R_{PY} /nm	F_{PY} /nm
				Water	Sucrose	Water	Sucrose		Water	Sucrose		
$G_{63}H_{350}$	-	11.11	163(47)	18.9(2.5)	18.9(2.5)*	176	176	-	-	-	-	-
$G_{63}H_{350}B_{25}$	6.378	11.05	155(46)	21.8(3.1)	18.2(2.7)	170	168	-	-	-	-	-
$G_{63}H_{350}B_{50}$	12.76	11.00	156(45)	23.1(3.5)	18.8(4.1)	172	169	-	-	-	-	-
$G_{63}H_{350}B_{97}$	24.75	10.93	155(44)	26.7(3.7)	24.8(3.3)	172	171	0.132	18.7(3.4)	18.7(3.4)*	15.8	0.35
$G_{63}H_{350}B_{125}$	31.89	10.89	155(43)	30.6(4.4)	26.6(4.3)	174	173	0.223	22.3(4.0)	22.3(4.0)*	20.7	0.43
$G_{63}H_{350}B_{169}$	43.11	10.84	156(42)	34.2(5.2)	27.2(3.9)	177	174	0.343	24.7(3.8)	22.7(4.3)	21.8	0.40
$G_{63}H_{350}B_{200}$	51.02	10.81	154(43)	37.8(6.3)	30.7(5.0)	177	173	0.425	26.9(3.6)	25.5(2.1)	22.6	0.36
$G_{63}H_{350}B_{294}$	75.00	10.75	145(46)	45.5(7.6)	35.7(4.6)	172	167	0.575	34.9(4.1)	30.9(3.8)	31.9	0.47
$G_{63}H_{350}B_{400}$	102.0	10.69	142(44)	54.8(8.1)	44.0(10.7)	173	168	0.612	43.2(6.0)	36.7(5.2)	40.2	0.50
	102.0	10.69	142(44)	-	41.3(10.8)	-	167	20.3	-	34.5(6.3)	30.8	0.43

* These data were not considered to be reliable.

Table 2.3 Structural parameters obtained for a series of $G_{63}H_{350}B_z$ (z = 0 to 400) copolymer dispersions in either pure water or a 40 % w/w aqueous sucrose solution from SAXS analysis using the two-population model (Equation A1.1 in the Appendix, n = 2). Representative parameters of the first population model (population 1) corresponding to vesicles (whose form factor is described by Equation A1.2 in the Appendix): x_{sol} is the volume fraction of solvent in the hydrophobic part of the vesicle membrane, R_{mc} is the radius from the center of the vesicle to the center of the membrane (Figure 2.4) and σ_{Rmc} is the associated standard deviation, T_{mc} is the membrane core thickness and σ_{Tmc} is the associated standard deviation, R_{out} is the total radius of the vesicle ($R_{out} = R_{mc} + \frac{1}{2}T_{mc} + 2R_g$, where the radius of gyration of the corona PGMA block, R_g, is 2.1 nm). Representative parameters of the second population (population 2) corresponding to spherical micelles (whose form factor is described by Equation A1.7 in the Appendix): R_s is the core radius, σ_{Rs} is the standard deviation of the core radius, R_{PY} is the Percus-Yevick correlation radius of densely-packed spherical micelles and F_{PY} is the Percus-Yevick effective volume fraction of the packed micelles. c_2/c_1 is the ratio of the volume fraction of the copolymers forming micelles (population 2) to the volume fraction of the copolymers forming vesicles (population 1). V_{PBzMA} denotes the volume of the hydrophobic PBzMA block.

Copolymer Composition	V_{PBzMA} /nm^3	ξ_{mc} ×10^{-10} /cm^{-2}	x_{sol}	Population 1					c_2/c_1	Population 2			
				R_{mc} (σ_{Rmc}) /nm	T_{mc} (σ_{Tmc})/ nm		R_{out}/ nm			R_s (σ_{Rs})/ nm		R_{PY} /nm	F_{PY} /nm
					Water	Sucrose	Water	Sucrose		Water	Sucrose		
$G_{63}H_{350}$	-	11.11	0.5	163(47)	18.9(2.5)	18.9(2.5)*	176	176	-	-	-	-	-
$G_{63}H_{350}B_{25}$	6.378	11.05	0.46	155(46)	21.9(3.1)	18.3(2.8)	170	168	-	-	-	-	-
$G_{63}H_{350}B_{50}$	12.76	11.00	0.42	156(45)	23.2(3.5)	18.7(4.1)	172	169	-	-	-	-	-
$G_{63}H_{350}B_{97}$	24.75	10.93	0.37	155(44)	26.3(3.6)	24.8(3.1)	172	171	0.158	14.3(5.1)	14.3(5.1)*	10.4	0.31
$G_{63}H_{350}B_{125}$	31.89	10.89	0.34	155(43)	30.4(4.9)	26.3(3.5)	174	173	0.321	23.3(3.6)	20.8(4.0)*	20.9	0.49
$G_{63}H_{350}B_{169}$	43.11	10.84	0.31	156(42)	33.9(5.6)	27.0(4.4)	177	174	0.388	25.2(3.6)	22.7(4.3)	21.8	0.42
$G_{63}H_{350}B_{200}$	51.02	10.81	0.29	154(43)	37.2(7.0)	30.7(5.3)	177	173	0.452	27.3(3.3)	25.7(2.5)	22.4	0.39
$G_{63}H_{350}B_{294}$	75.00	10.75	0.24	145(46)	45.0(8.0)	36.1(4.4)	172	167	0.611	34.5(3.7)	31.5(3.9)	30.1	0.46
$G_{63}H_{350}B_{400}$	102.0	10.69	0.20	142(44)	54.3(8.9)	43.4(15.7)	173	169	0.693	42.5(6.0)	36.6(2.8)	38.1	0.46
					-	46.0 (10.7)	-	169	1.818	-	36.2 (6.1)	31.8	0.46

* These data were not considered to be reliable.

A similar approach to SAXS analysis has been undertaken in the present study. Accordingly, population 1 represents the vesicles and population 2 describes the globules within the vesicle membrane (see Figure 2.4, morphology 3 and Equation A1.1 to Equation A1.10 in the Appendix). Population 1 of the proposed two-population model corresponds to the initial morphology 1 (smooth vesicles) and is thus appropriate for SAXS analysis of the $G_{63}H_{350}$ diblock copolymer precursor. Morphology 1 is well described by the vesicle model (population 1 in Equation A1.1 in the Appendix),which produced a reasonably good fit to the SAXS pattern over six orders of magnitude of X-ray scattering intensity (Figure 2.5, Table 2.2, $G_{63}H_{350}$).

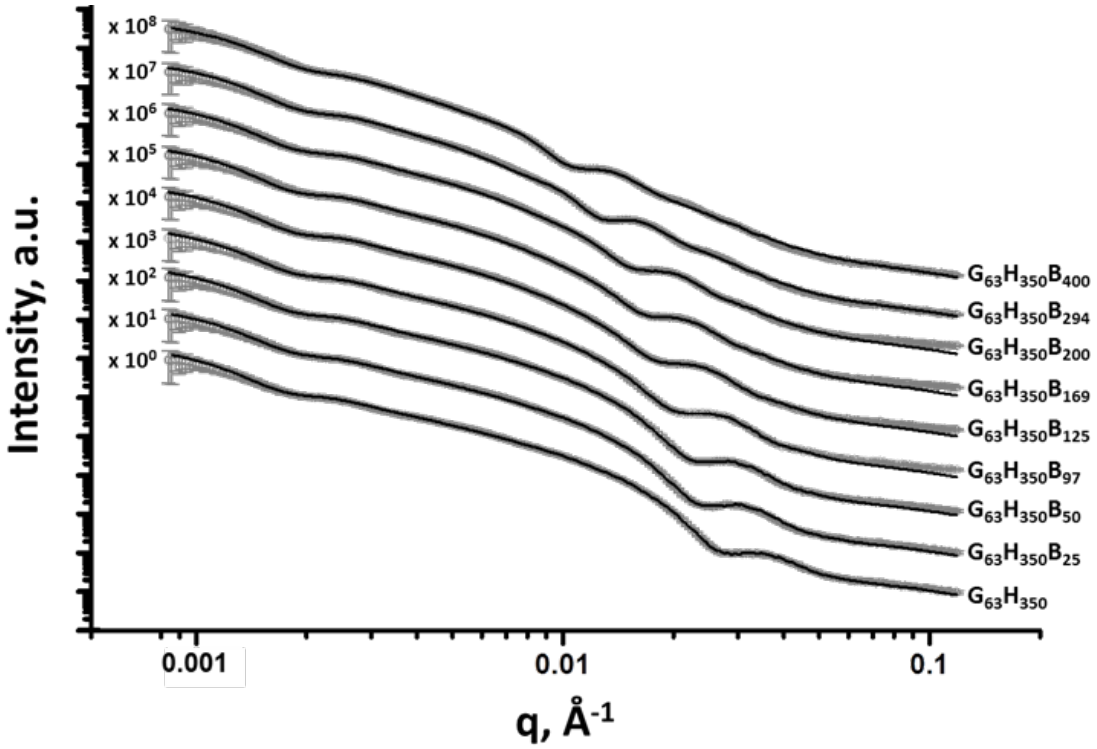

Figure 2.5. SAXS patterns obtained for 1.0 % w/w aqueous dispersions of $G_{63}H_{350}$ diblock copolymer precursor vesicles (z = 0) and a series of framboidal $G_{63}H_{350}B_z$ triblock copolymer vesicles, where z = 25, 50, 97, 125, 169, 200, 294 or 400. Solid lines represent fitting curves: For z = 0, 25 or 50, a single population model was sufficient, whereas two populations were required for higher z values. For clarity, the SAXS patterns are shifted upward by an arbitrary factor indicated in the figure.

The calculated vesicle radius, R_{out}, of 176 nm (Table 2.2) is consistent with both TEM observations (Figure 2.2) and DLS data (Table 2.1). The mean vesicle diameter is estimated to be 350 nm by TEM analysis, while DLS studies indicate a mean

hydrodynamic vesicle diameter (D_h) of 362 nm with a relatively low polydispersity index (PDI) of 0.08. The radius of gyration (R_g) of the G_{63} corona block was determined to be 2.1 nm from model fitting of the $G_{63}H_{350}$ SAXS pattern. This experimental value is comparable to a theoretical estimate: the projected contour length of a single GMA monomer is 0.255 nm (two carbon bonds in all-trans conformation), the total contour length of a G_{63} block, L_{PGMA} = 63 x 0.255 nm = 16.07 nm and the Kuhn length of 1.53 nm, based on the literature value for poly(methyl methacrylate)[31], result in an estimated R_g of $(16.07 \times 1.53/6)^{1/2}$, or 2.02 nm. The water volume fraction, x_{sol}, in the membrane core is approximately 0.50 according to the SAXS data fit. The vesicle model (population 1) also produced a good fit to the experimental SAXS patterns corresponding to the triblock copolymer vesicles containing a relatively short PBzMA block corresponding to morphology 2 (Figure 2.5 and Table 2.2, samples $G_{63}H_{350}B_{25}$ and $G_{63}H_{350}B_{50}$). This result is consistent with TEM observations (Figure 2.2), which suggests that such copolymer compositions produce only surface-pitted vesicles that do not significantly affect their membrane structure. However, in order to produce satisfactory fits to SAXS patterns obtained for genuine framboidal vesicles prepared by targeting longer PBzMA blocks (e.g. $G_{63}H_{350}B_z$, z = 97-400) incorporation of population 2 (spherical micelles, which correspond to the micelle-like globules) into the model, Equation A1.1 in the Appendix, was essential (Figure 2.6, SAXS data corresponding to a continuous phase comprising pure water). A superposition of scattering signals from two populations (vesicles and spherical micelles) used in the model produces good fits to the SAXS data over a wide range of PBzMA block DPs (Figure 2.5 and Table 2.2).

It is assumed that both the R_g of the PGMA block and the water content within the hydrophobic vesicles membrane do not change during the growth of the PBzMA block. Thus, the R_g and x_{sol} values obtained for the $G_{63}H_{350}$ diblock precursor vesicles were used as fixed parameters for SAXS fitting of the final triblock copolymers. The same batch of PGMA macro-CTA was used for all copolymer syntheses described in this work, so the assumption of a fixed R_g for this block is perfectly reasonable. At first sight, it is questionable whether x_{sol} should remain constant when growing a progressively longer PBzMA block. This is because PBzMA is significantly more hydrophobic than PHPMA, hence a gradual reduction

in x_{sol} with increasing PBzMA content might be expected. However, the developing framboidal character of the vesicle membrane necessarily leads to the incorporation of additional water molecules (see Figure 2.7). The following discussion shows that this feature is sufficient to maintain a constant x_{sol}, regardless of the PBzMA content of the copolymer.

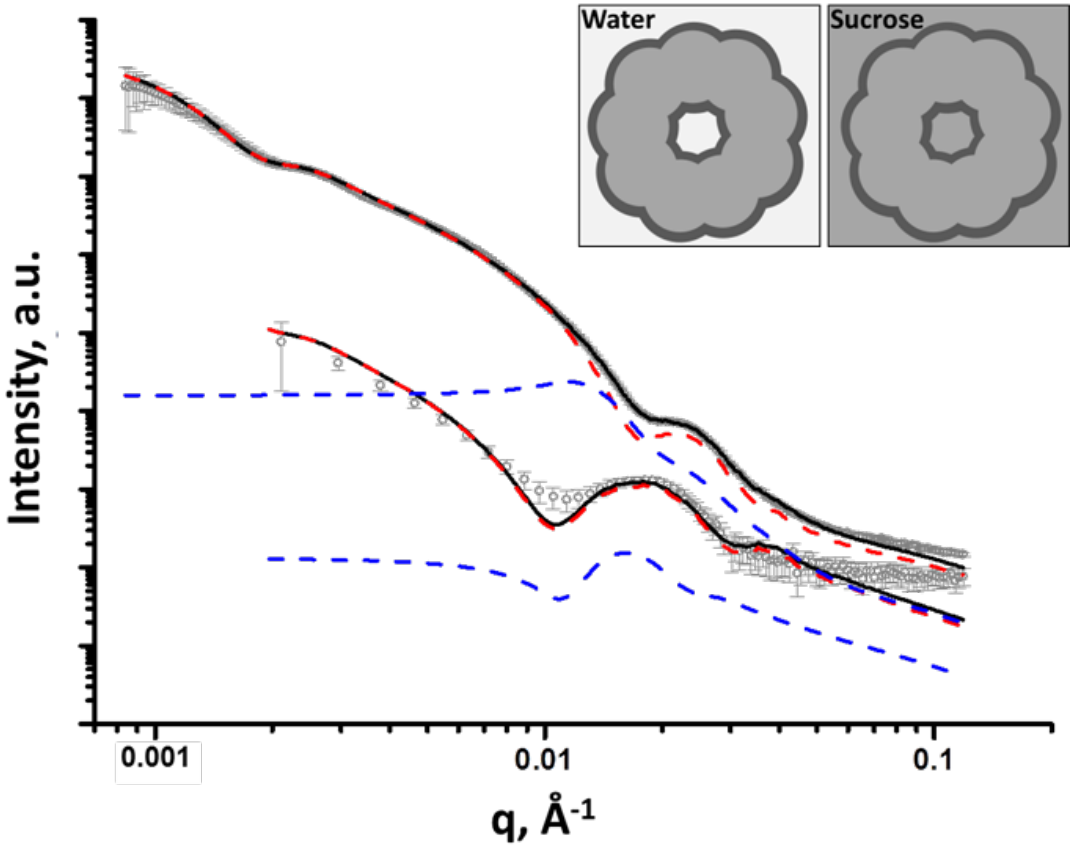

Figure 2.6. SAXS patterns obtained for both 1.0 % w/w aqueous sucrose and aqueous dispersions of framboidal $G_{63}H_{350}B_{125}$ triblock copolymer vesicles. Fitting curves are represented by solid black lines. A two-population model was required for fitting [morphology 3 (M3) in Figure 2.4]: population 1 is represented by red dashed lines and population 2 is represented by blue dashed lines. Inset: schematic representations of the X-ray contrast achieved in both pure water and aqueous sucrose solutions.

An x_{sol} of 0.50 is obtained for the membrane-forming PHPMA block of the precursor $G_{63}H_{350}$ diblock copolymer vesicles. This value is consistent with recent work by Warren et al., who reported x_{sol} values ranging from 0.38 to 0.66 for $G_{55}H_y$ vesicles when varying y from 200 to 1000, respectively.[32] Assuming additivity, if the PBzMA component has a water content of zero then x_{sol} might be expected to decrease from

0.50 for $G_{63}H_{350}$ diblock copolymer vesicles to 0.20 for $G_{63}H_{350}B_{400}$ triblock copolymer vesicles (see Table 2. 3). Using these x_{sol} values as fitting parameters produces comparable results to those obtained when x_{sol} is kept constant at 0.50 (see Table 2.2 and Table 2.3). This suggests that the SAXS parameters are relatively insensitive to x_{sol}. However, marginally better fits to the model, especially at high q, are obtained when x_{sol} is taken to be 0.50, regardless of the copolymer composition. This is most likely because, for population 1 of the SAXS model, it is assumed that water is distributed evenly within the hydrophobic component of the vesicle membrane (see Figure 2.5).

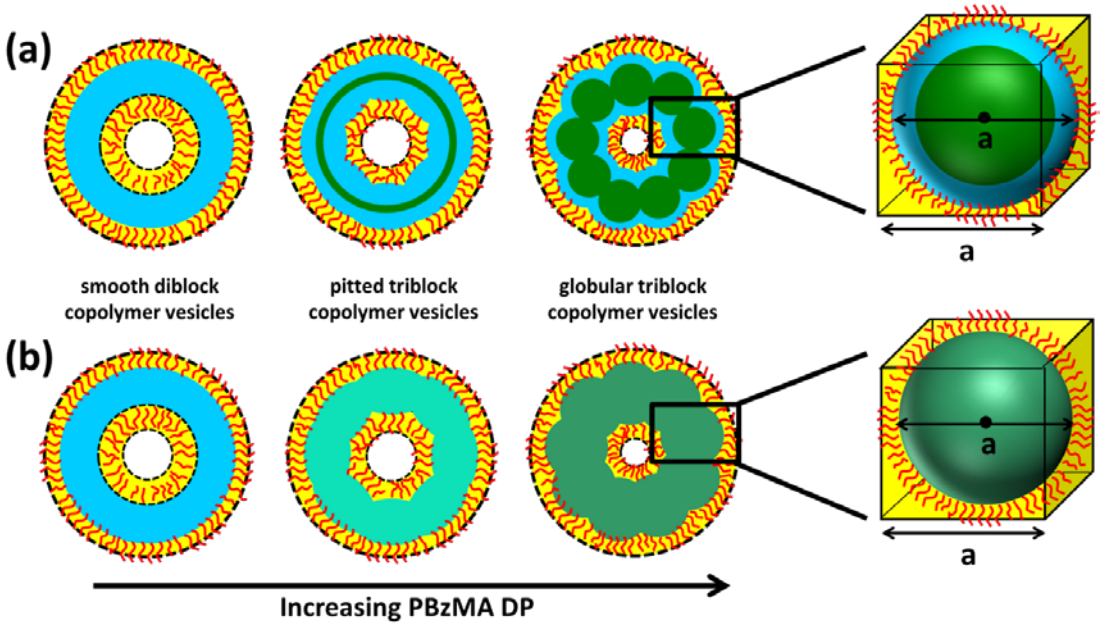

Figure 2.7 Schematic illustration of the effect of varying the PBzMA DP (z) on the value of x_{sol} for $G_{63}H_{350}B_z$ vesicles. (a) The originally predicted phase-separated three-layer cross-section model, where red = PGMA, blue = PHPMA and green = PBzMA. (b) The continuous core model which assumes the hydrophobic PHPMA and PBzMA blocks are uniformly distributed within the membrane, where red = PGMA, light blue = PHPMA, light green = mixed PHPMA plus PBzMA membrane where $z \leq 50$, and dark green = mixed PHPMA plus PBzMA membrane where $z \geq 97$. In each case, the yellow areas indicate the presence of water between adjacent globules. The inset cubes indicate the approximate volume occupied by each globule within the vesicle membrane.

It is true that the overall volume fraction of water associated with the hydrophobic block(s) is reduced as the diblock copolymer precursor is chain-extended with BzMA. However, the local increase in curvature caused by the growth of the pseudo-spherical globules actually leads to a higher volume fraction of water becoming associated with the membrane as a whole (see yellow regions in Figure 2.7). This

water volume fraction (or x_{sol}) can be estimated geometrically by calculating the free volume associated with a sphere of radius 0.5*a* placed within a cube of length *a*:

$$\frac{V_{sphere}}{V_{cube}} = \frac{1/6\,\pi a^3}{a^3} = \frac{\pi}{6} \approx 0.50$$

SAXS analysis shows that the thickness of the hydrophobic component of the vesicle membrane (T_{mc}) increases on targeting higher DPs for the PBzMA block (Table 2.2 and Figure 2.8).

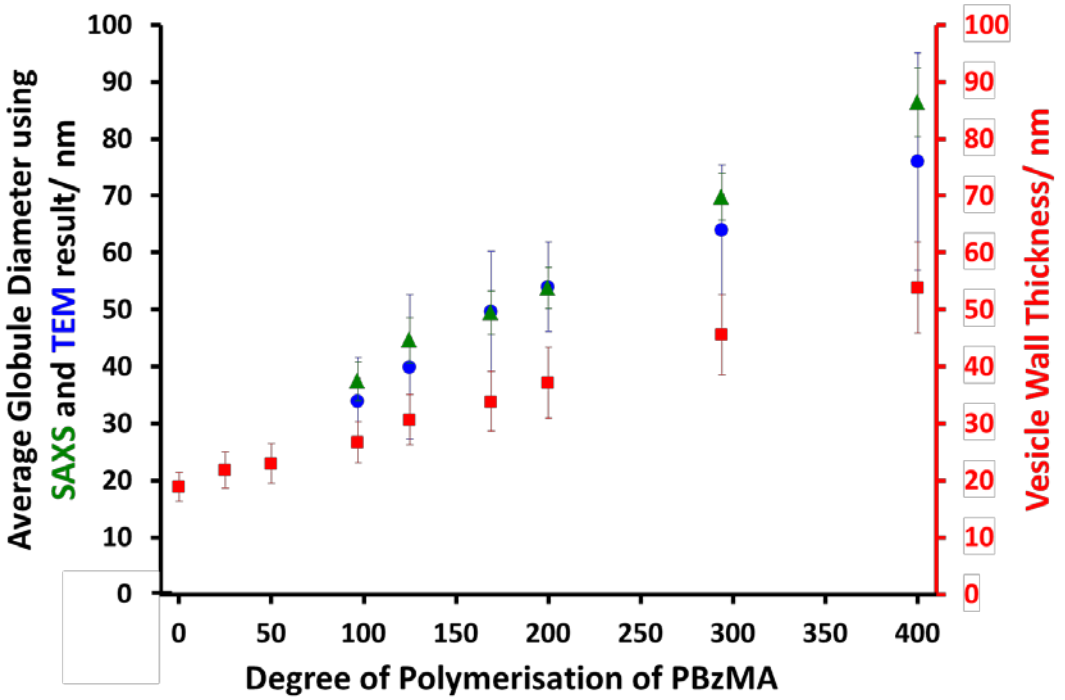

Figure 2.8 Variation in mean micelle/globule diameter and vesicle wall thickness (T_{mc}) with degree of polymerisation (z) for $G_{63}H_{350}B_z$ triblock copolymer vesicles obtained from SAXS (▲, ■) and TEM (●) data. [N.B. No mean globule diameters can be determined for z = 0, 25 and 50 because these vesicles do not exhibit framboidal character.]

However, the overall vesicle dimensions remain virtually constant over all copolymer compositions (R_{out} ~ 174 nm, Table 2.2), which is consistent with our TEM observations (Figure 2.2) and DLS studies (Table 2.1). Taken together, these data suggest that the vesicle growth mechanism leads to a gradual reduction in the volume of the vesicle lumen, as reported recently by Warren and co-workers for non-framboidal $G_{55}H_y$ vesicles, where y ranges from 200 to 2000.[33] The nanoscale phase

separation that occurs within the vesicle membrane described by the spherical micelle model (population 2) can also be identified from SAXS analysis. Both the spherical micelle radius (R_s) and the relative concentration of the second population (c_2/c_1) increase at a higher PBzMA block volume fraction, V_{PBzMA} (Table 2.2). Moreover, the R_s values are consistent with those estimated from TEM images (Figure 2.8). TEM studies suggest that the mean micelle/globule diameter ($2R_s$) for the framboidal $G_{63}H_{350}B_z$ vesicles increases from 34 nm to 76 nm as z is increased from 97 to 400. Similarly, SAXS analyses indicate that $2R_s$ increases from 36 nm to 85 nm for the same set of samples. However, it is worth emphasising that only a few hundred globules were analysed by TEM, whereas the SAXS data are averaged over many millions of globules, which ensures far more robust statistics. Some difference between micelle/globule diameters measured by TEM and SAXS is likely because SAXS interrogates partially hydrated globules in aqueous solution. In contrast, TEM is performed on dehydrated globules under ultrahigh vacuum conditions, which accounts for the marginally smaller dimensions in this case.

The proposed structural model (Figure 2.4) does not account for the nanoscale phase separation between the PHPMA and PBzMA blocks which might be expected to occur during PBzMA growth (see Figure 2.2). However, the difference between the scattering length densities of the copolymer components (ξ_{PGMA}, ξ_{PHPMA} and ξ_{PBzMA}) and water (ξ_{H2O}) significantly exceeds the difference between the scattering length densities of the copolymer components alone (see Appendix 1 for full details of the structural models used in the SAXS analysis). Thus SAXS is simply not particularly sensitive to the phase separation between the PHPMA and PBzMA blocks that is responsible for the evolution in morphology from smooth vesicles to framboidal vesicles during the PISA synthesis. Thus, in order to scrutinise the anticipated phase separation between the PHPMA and PBzMA blocks, a contrast variation technique was employed in this study. Accordingly, the vesicle dispersions were prepared using a 40 % w/w aqueous sucrose solution instead of water.

This solution is a good solvent for the PGMA stabiliser block and has a scattering length density of $\xi_{H2O+sucrose}$ = 10.88 x 10^{10} cm^{-2}, which lies between ξ_{PHPMA} and ξ_{PBzMA} (see Appendix 1). This contrast variation approach significantly reduces the scattering length density difference between the copolymer components and the continuous phase and consequently increases the sensitivity of SAXS towards the

structural changes occurring within the vesicle membrane. It is emphasised that the PGMA stabiliser block has the highest scattering length density and hence produces a significant contribution to the scattering signal. Thus in principle contrast-matching the corona block (ξ_{PGMA} = 11.94 x 10^{10} cm^{-2}) to the solvent would be informative, but unfortunately this was not possible because of the limited solubility of sucrose in water. The contrast-matched copolymer dispersions were prepared in two steps: (1) preparation of a 44 % w/w aqueous sucrose stock solution followed by (2) dilution of the copolymer dispersion prepared in pure water from 10 % w/w to 1 % w/w solids using this aqueous sucrose solution. The fitting parameters obtained for the purely aqueous dispersions were also used for SAXS analysis of the aqueous sucrose dispersions, while the solvent scattering length density used in the model was changed from that of water to that for 40 % w/w aqueous sucrose solution. Assuming that the vesicle morphology and the copolymer concentration remain unchanged in the aqueous sucrose dispersion, only six parameters are required for the SAXS fitting: the membrane thickness corresponding to the parameters used for population 1, the spherical micelle radius corresponding to population 2, their corresponding standard deviations and relative concentrations of both populations. For each sample, the concentration ratio, c_2/c_1, was kept constant during the fitting at the same value obtained for the dispersions in pure water (Table 2.2). This relatively constrained model produced satisfactory data fits for the SAXS patterns of the aqueous sucrose dispersions (see Figure 2.6, Figure 2.9 and Table 2.2). A significant inconsistency is only observed for the triblock copolymer prepared with the longest PBzMA block (Figure 2.9, see $G_{63}H_{350}B_{400}$). In this case, including additional fitting parameters in the model associated with the spherical micelle packing (R_{PY} and F_{PY}) and removing the c_2/c_1 ratio constraint produced a better data fit (Figure 2.9, solid red line). This latter fit indicated a significantly higher relative concentration for the second population (see the last entry in Table 2.2). This suggests that these nano-objects are best described as strongly interacting (i.e. aggregated) spherical micelles, with little or no vesicular character.

In general, SAXS analysis of this series of vesicles dispersed in aqueous sucrose solution demonstrates that both the vesicle membrane thickness and the mean micelle radius are slightly reduced relative to the corresponding values determined for the same vesicles dispersed in pure water. The observed 15 vol % reduction in

membrane volume (see Table 2.2) is the result of a lower degree of solvent plasticisation. Presumably, this is simply because aqueous sucrose is a poorer solvent for the two blocks located in the membrane than water alone. Unfortunately, the relatively weak scattering from the aqueous sucrose dispersions means that SAXS pattern fits involving the other model parameters, including x_{sol}, are considered unreliable. Nevertheless, the original SAXS model used for analysis of vesicle dispersions in pure water (Figure 2.4) were consistent with the SAXS patterns recorded for dispersions in aqueous sucrose solution.

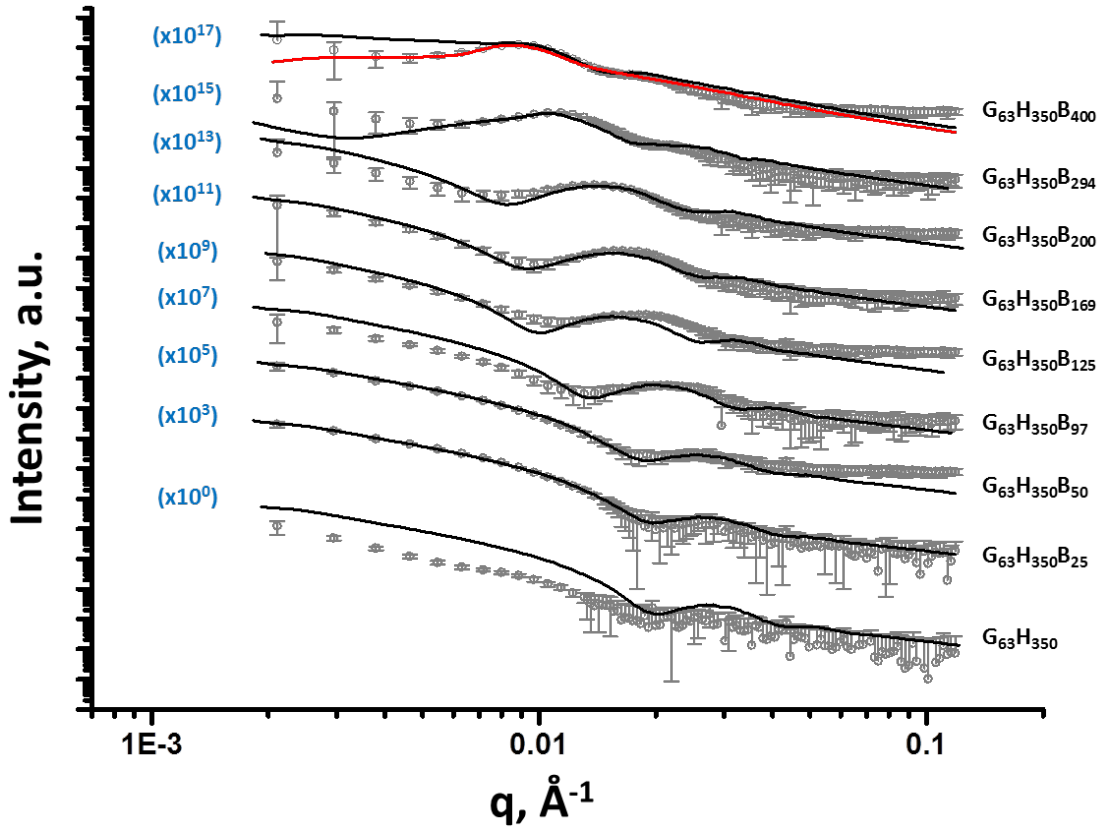

Figure 2.9 SAXS patterns and data fits obtained for a 1.0 % w/w dispersion of $G_{63}H_{350}$ diblock copolymer precursor vesicles in 40 % w/w aqueous sucrose and eight framboidal $G_{63}H_{350}B_z$ triblock copolymer vesicles, where z ranges from 25 to 400. Solid black lines represent data fits assuming that the hydrophobic PHPMA and PBzMA blocks are uniformly distributed within the membrane (Figure 2.4): the first three vesicle samples were analysed assuming a single vesicle population (Equation A1.1 in the Appendix, n = 1), but for vesicles with a PBzMA DP of 97 or above a two-population model was required for satisfactory data fits (Equation A1.1 in the Appendix, n = 2). The solid red line represents the data fit obtained for $G_{63}H_{350}B_{400}$ triblock copolymer vesicles when a different set of fitting parameters were used based on an aggregated sphere model for which c_2/c_1 was allowed to vary (see Table A1.1). The SAXS patterns are shifted upward by an arbitrary factor, which is displayed in blue.

In order to probe the nanoscale phase separation between the PHPMA and PBzMA blocks within the vesicle membrane, a more sophisticated two-population model composed of vesicles with a three-layer hydrophobic membrane and spherical core-shell-corona micelles was developed (see Figure 2.10, Equation A1.1 and Equation A1.11 to Equation A1.17 in the Appendix).

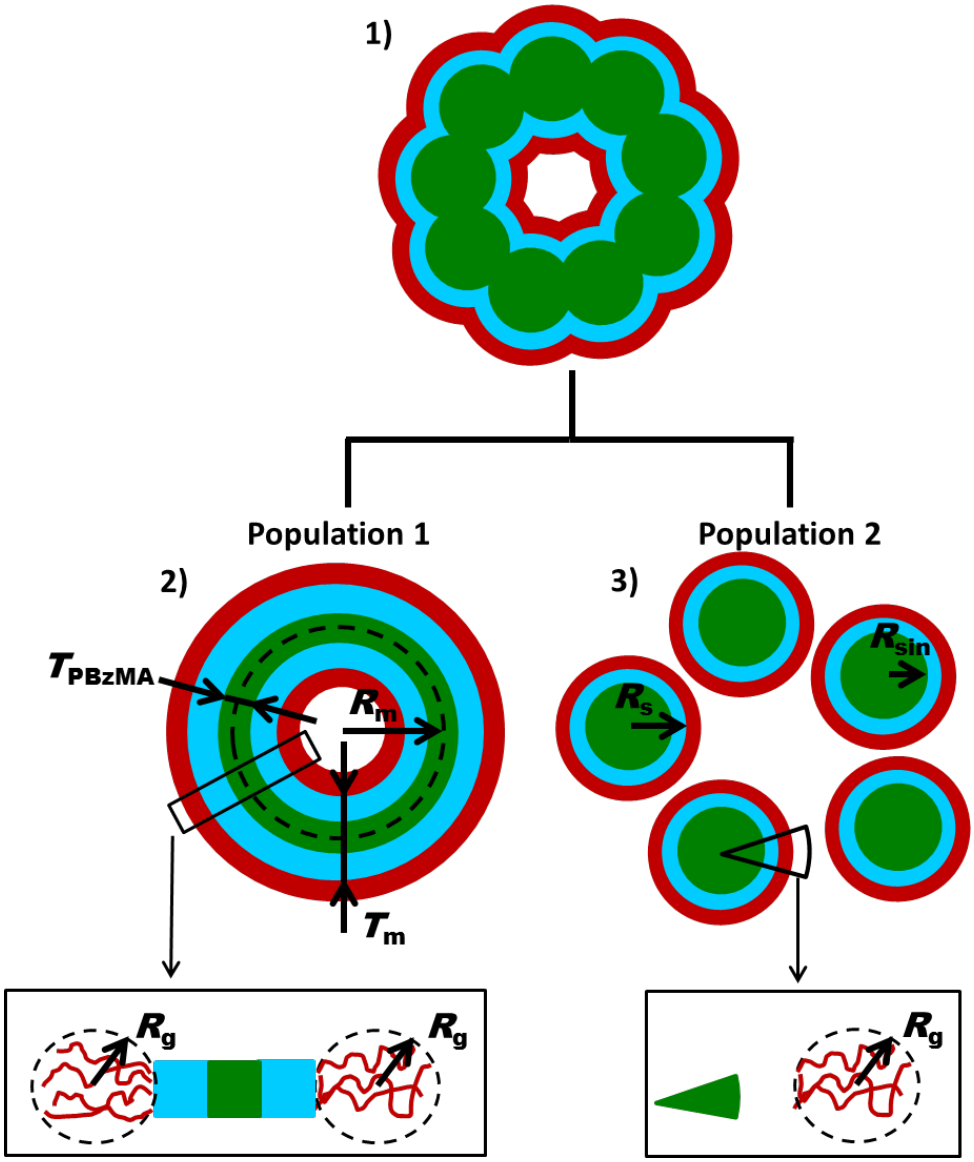

Figure 2.10 Schematic representation illustrating the three-layer, phase-separated membrane model (red = PGMA, blue = PHPMA and green = PBzMA) used to fit SAXS data, where (1) is a cartoon showing a three-layer vesicle model for which the following two-population model is required; (2) represents population 1, which is a vesicle model comprising a three-layer membrane, and (3) represents population 2, which is a spherical micelle model (core-shell-corona).

In this model, it is assumed that the PBzMA block occupies the central layer of the membrane. In principle, vesicles with the mean scattering length density of the hydrophobic component of the membrane that is closest to that of the aqueous sucrose solution (Table 2.2, see $G_{63}H_{350}B_{125}$ and $G_{63}H_{350}B_{169}$) should be most sensitive to nanoscale phase separation. If there is a homogeneous distribution of PHPMA and PBzMA blocks within the membrane (continuous core model, see Figure 2.4), then the hydrophobic component of the membrane should barely contribute to the X-ray scattering as the difference between ξ_{mc} and $\xi_{H2O+sucrose}$ is almost zero. Alternatively, if there is nanoscale phase separation between the PHPMA and PBzMA blocks (three-layer model, see Figure 2.10) the hydrophobic component of the membrane should produce a strong contribution to the scattering signal because of the significant difference between ξ_{PHPMA} and $\xi_{H2O+sucrose}$ and between $\xi_{H2O+sucrose}$ and ξ_{PBzMA}. Given that phase separation between the PHPMA and PBzMA blocks should cause a redistribution of solvent concentration within the vesicle membrane, two scenarios for the sophisticated two-population model (Equations A1.1, A1.11 and A1.14 in the Appendix) were considered. As for the SAXS analyses summarised in Table 2.2, in one scenario it is assumed that the solvent fraction in the PBzMA layer and two PHPMA layers of the membrane are equal (i.e., $x_{PBzMAsol} = x_{PHPMAsol} = 0.50$). In an alternative scenario associated with Table 2.3, it is assumed that $x_{PBzMAsol} = 0$ and $x_{PHPMAsol} = 0.50$. Comparison of SAXS patterns calculated for the continuous core (single-layer) model and these two more sophisticated three-layer models indicates that the continuous core model is actually more consistent with the experimental data (Figure 2.11).

To summarise the vesicle morphology studies, as the $G_{63}H_{350}$ diblock precursor is chain-extended with progressively longer PBzMA blocks, the overall vesicle diameter remains essentially constant (as indicated by DLS, TEM and SAXS) but the vesicle membrane thickness (as calculated by SAXS) increases. As a result, the vesicle lumen volume is gradually reduced on increasing the DP of the PBzMA. Finally, SAXS can be used to quantify the evolution in surface roughness indicated for these framboidal vesicles on the basis of TEM studies (see Figure 2.2). For $G_{63}H_{350}B_z$ triblock copolymer vesicles, both SAXS and TEM studies indicate that well-defined globules are only formed when $z > 97$ and the mean globule diameter increases monotonically from 36 nm ($z = 97$) to 85 nm ($z = 400$). However, a

contrast variation approach used for SAXS analysis provides no evidence for the anticipated nanoscale phase separation between the hydrophobic PHPMA and PBzMA blocks within the membrane. This suggests that the PHPMA and PBzMA blocks may only be weakly segregated within the vesicle membrane, rather than strongly segregated (see Figure 2.11).

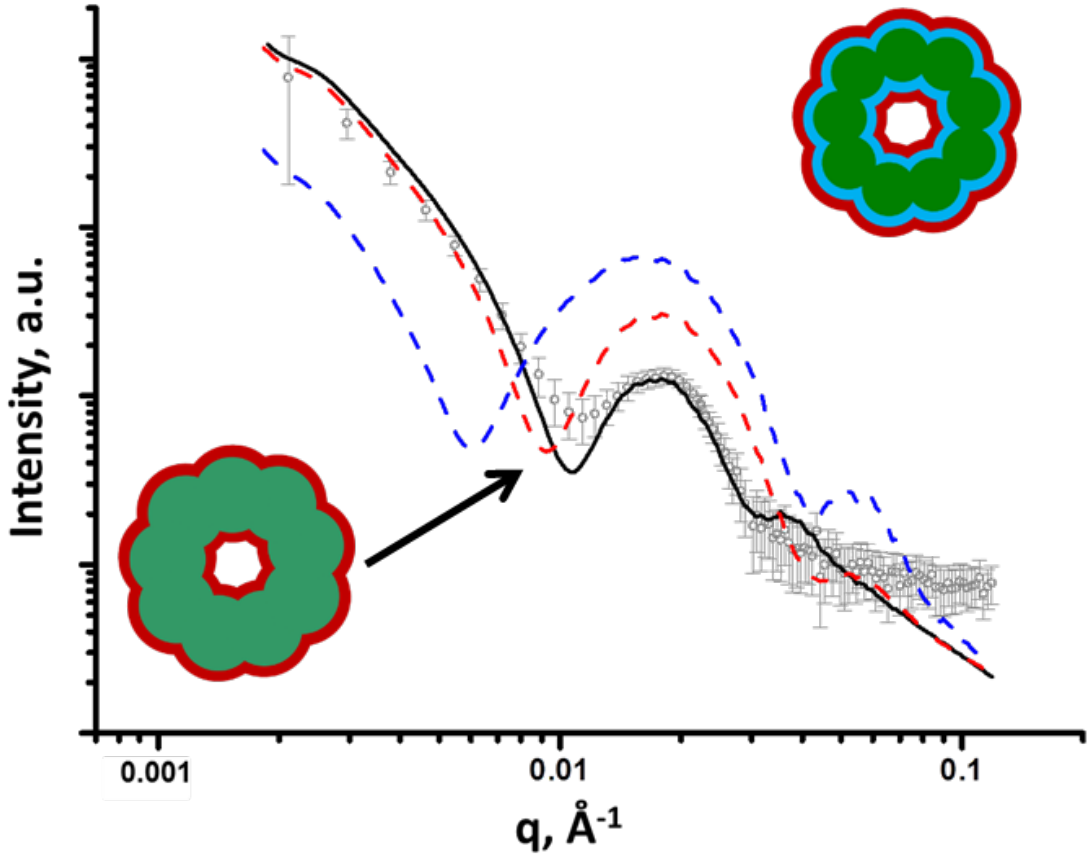

Figure 2.11. SAXS patterns obtained for a 1.0 % w/w aqueous sucrose dispersion of framboidal $G_{63}H_{350}B_{125}$ triblock copolymer vesicles. The solid black line represents the fit when a continuous core model is used, the dashed red and blue lines represent the fits when a fully phase-separated three-layer model with x_{sol} parameters of 0.5 (red) and 0.34 (blue) were used for fitting. Inset: schematic representations of the continuous core model (left) and the phase-separated three-layer model (right).

Pickering Emulsion Studies

Framboidal $G_{63}H_{350}B_{200}$ triblock copolymer vesicles (an intermediate PBzMA block length) and linear $G_{63}H_{350}$ diblock copolymer vesicles were each evaluated as Pickering emulsifiers for the stabilisation of *n*-dodecane emulsion droplets in water. Aqueous vesicle dispersions (0.5 to 3.0 % w/w) were homogenised with an equal volume of *n*-dodecane at 12,000 rpm for two minutes at 20 ^{o}C to produce Pickering emulsions. The concentration dependence of the mean droplet diameter of the resulting emulsions was determined by laser diffraction and optical microscopy (see Figure 2.12).

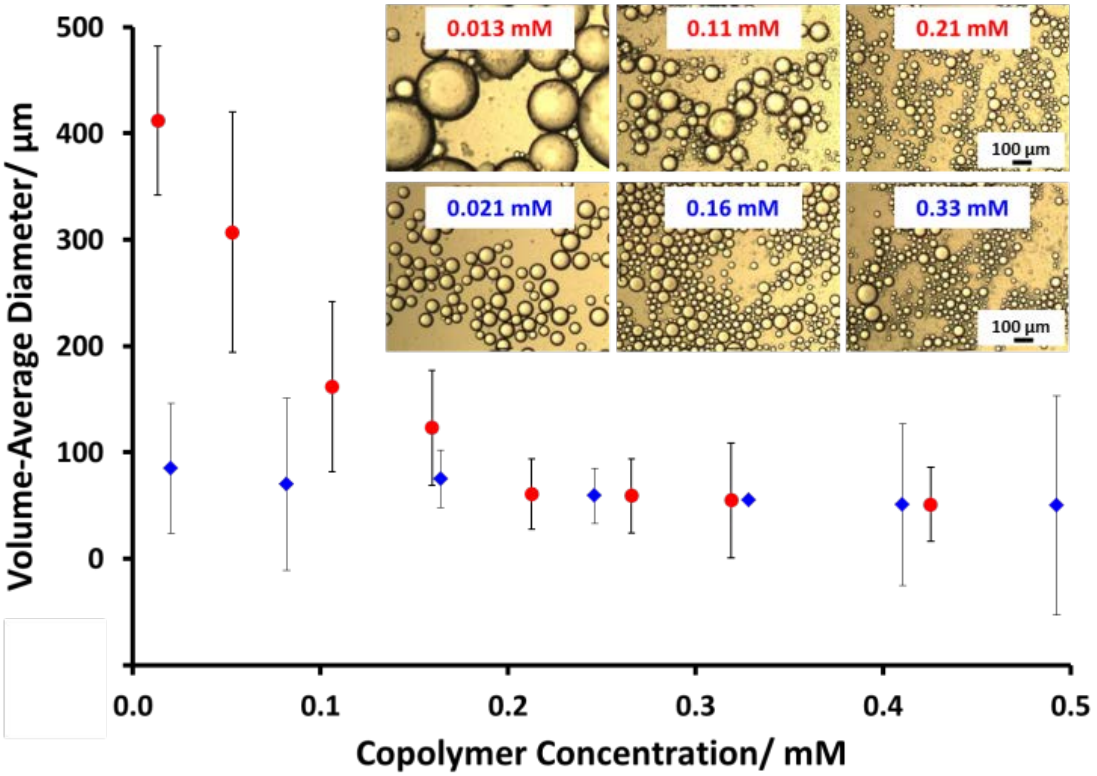

Figure 2.12 Volume-average diameter (determined for *n*-dodecane droplets by laser diffraction) vs. copolymer concentration for (♦) linear $G_{63}H_{350}$ diblock copolymer vesicles and (●) framboidal $G_{63}H_{350}B_{200}$ triblock copolymer vesicles. Inset shows representative optical microscopy images for selected emulsions prepared at the stated copolymer concentration. The scale bars are valid for all six images.

Increasing the concentration of linear $G_{63}H_{350}$ vesicles led to a constant mean droplet diameter of ~ 70 µm. This suggests that the linear $G_{63}H_{350}$ vesicles do not withstand the high shear conditions required for emulsion preparation, and instead dissociate to produce individual copolymer chains, as previously reported by Thompson *et al.*[13, 34] In contrast, the mean emulsion droplet

diameter prepared using the $G_{63}H_{350}B_{200}$ triblock copolymer vesicles increases from 55 μm up to 412 μm over the same concentration range.

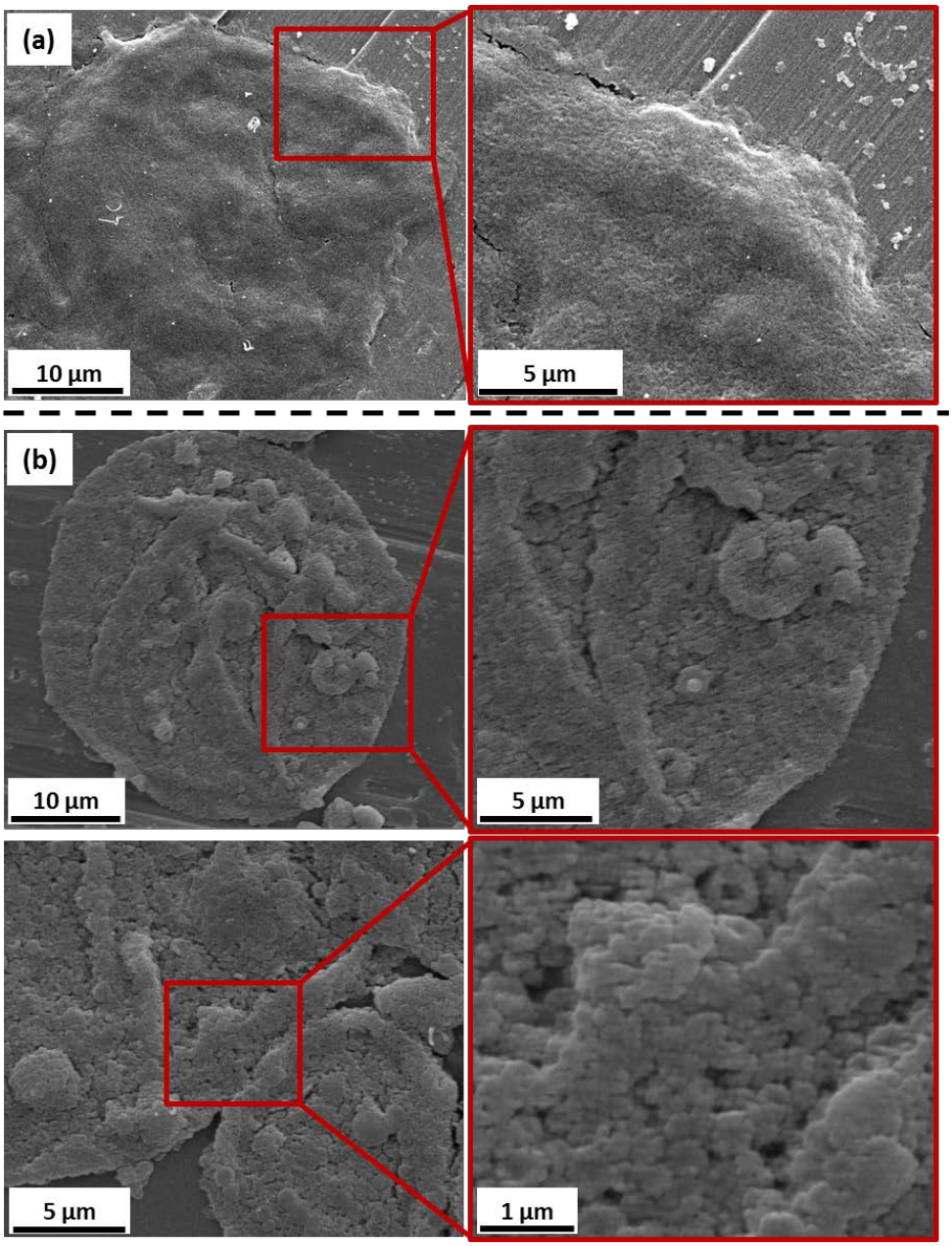

Figure 2.13 SEM images obtained for *n*-hexane-in-water Pickering emulsions stabilised by 2 % w/w dispersions of (a) smooth $G_{63}H_{350}$ diblock copolymer vesicles and (b) framboidal $G_{63}H_{350}B_{400}$ triblock copolymer vesicles. The images show that the former $G_{63}H_{350}$ vesicles dissociate during high shear homogenisation, leading to the formation of an emulsion stabilised by individual diblock copolymer chains, rather than a genuine Pickering emulsion. In contrast, the latter framboidal vesicles proved to be stable when subjected to the same emulsification conditions and hence a genuine Pickering emulsion is produced.

Similar concentration-dependent droplet diameters were observed for other $G_{63}H_{350}B_z$ copolymer vesicles. These observations suggest that the $G_{63}H_{350}B_z$ triblock copolymer vesicles survive high shear homogenisation and

consequently adsorb as intact triblock copolymer vesicles to produce genuine Pickering emulsions. Remarkably, only a relatively short PBzMA block is required to stabilise the vesicles during homogenisation; presumably, the highly hydrophobic nature of this third block is sufficient to prevent vesicle dissociation. SEM (Figure 2.13b) and TEM studies (Figure 2.14a) were carried out using *n*-hexane as the oil phase to ensure complete oil evaporation. These studies confirm that intact framboidal vesicles indeed act as Pickering emulsifiers. Hence the observed concentration dependence for the droplet diameter is readily explained: higher vesicle concentrations are required for stabilisation of smaller oil droplets because of the concomitant increase in total surface area.

The Pickering emulsifier adsorption efficiency, A_{eff}, was determined by turbidimetry experiments, as described by Thompson et al.[13] First, scattering curves were recorded and calibration plots were constructed for each triblock copolymer vesicle evaluated (see Appendix 2 and 3).The scattering intensity increased monotonically as the PBzMA DP is increased in the $G_{63}H_{350}B_z$ triblock copolymer series, because of the significantly higher refractive index of this aromatic block. The Pickering emulsions proved to be highly stable towards coalescence, but creaming of the lower density droplet phase occurred on standing for 24 h at 20 ^{o}C. The turbidity of this lower aqueous phase was analysed by visible absorption spectroscopy to determine the amount of vesicles remaining in the aqueous solution and hence the adsorbed amount by difference (see Appendix 2 and Appendix 3). To confirm the validity of this turbidimetric assay, the vesicles were also sized by DLS before and after homogenisation in order to ensure that no size fractionation occurred during vesicle adsorption at the *n*-dodecane/water interface.

At a copolymer concentration of 0.20 mM, the A_{eff} increased from 36 % up to 94 % on increasing the PBzMA DP from 25 to 125 (see Figure 2.14b). For PBzMA DPs greater than 125, the A_{eff} is progressively reduced, resulting in an A_{eff} of 85 % at a mean DP of 400 (see Figure 2.14b). These observations are similar to those reported by San-Miguel and Behrens,[15] who observed that both the nanoparticle wettability and emulsion stability attained maximum values at the same root-mean-squared (rms) surface roughness. However, the latter parameter was calculated indirectly from AFM measurements performed on a planar surface that had been subjected to

the same coating conditions as the spherical microparticles. Nevertheless, it was suggested that wetting of microparticles with up to 6 nm rms roughness occurred within the Wenzel regime,[35] whereas the roughest microparticles (rms roughness = 7.5 nm) corresponded to the Cassie-Baxter regime.[36] The former regime led to optimal Pickering emulsifier performance.

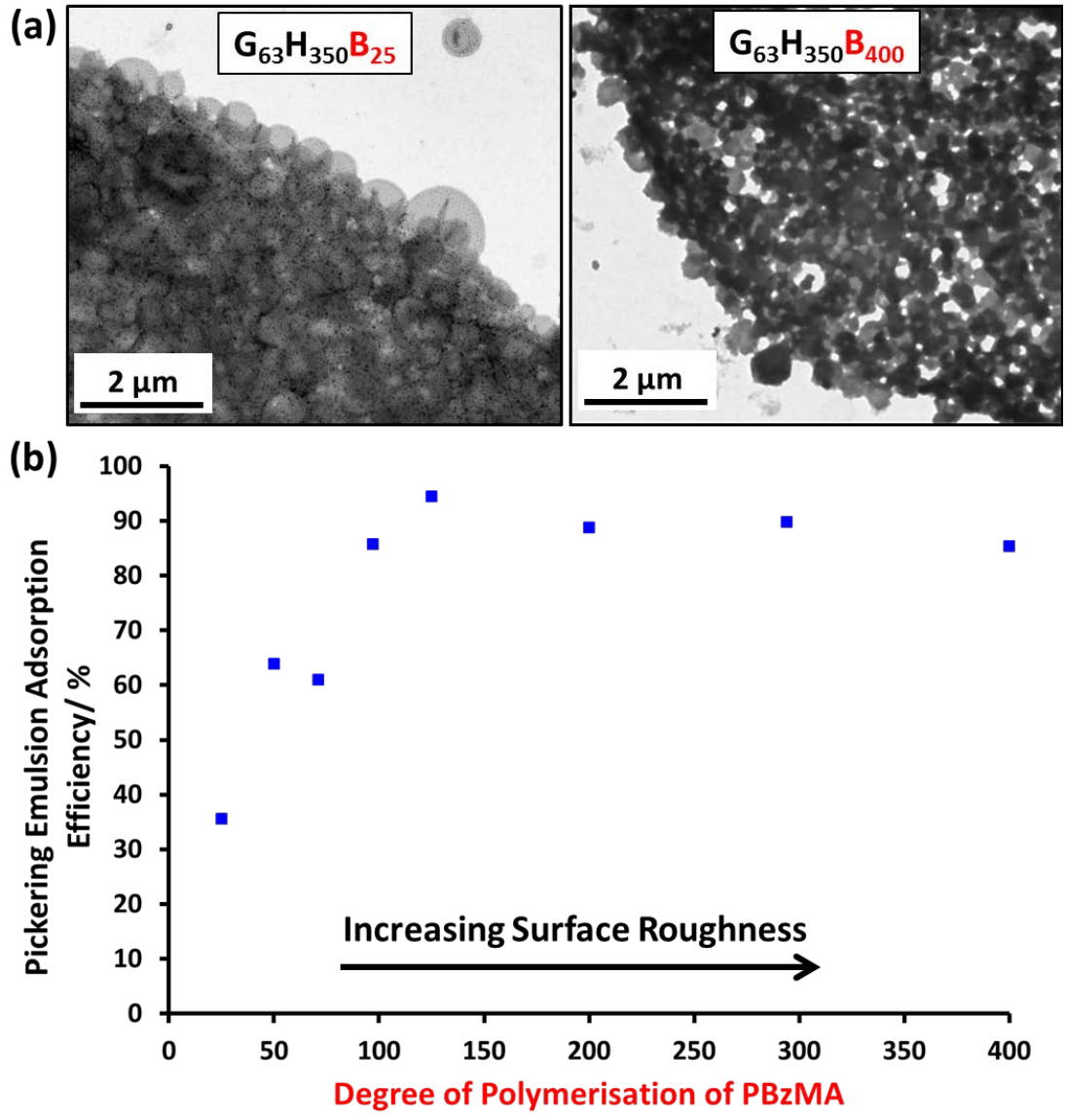

Figure 2.14 (a) TEM images obtained for Pickering emulsions of *n*-hexane stabilised by aqueous vesicle dispersions of $G_{63}H_{350}B_{25}$ and $G_{63}H_{350}B_{400}$ triblock copolymer vesicles. (b) Plot of A_{eff} vs. PBzMA DP in a series of $G_{63}H_{350}B_z$ triblock copolymer vesicles (0.20 mM) with increasing surface roughness.

In the present study, the model framboidal vesicles exhibit substantially enhanced A_{eff} values compared to non-framboidal $G_{58}H_{350}E_{20}$ cross-linked vesicles, for which a A_{eff} of 67 % has been reported for a similar copolymer concentration.[13] Presumably, the much higher surface roughness of the former nanoparticles (mean globule diameter ~ 45 nm) is responsible for this observation. This is significantly different to the critical length scale reported by San-Miguel and Behrens.[15] However, it seems likely that other parameters, e.g. charge vs. steric stabilisation or differences in copolymer composition, also influence the particle contact angle (and hence surface wettability).

Conclusions

$G_{63}H_{350}$ diblock copolymer precursor vesicles were chain-extended with BzMA via seeded RAFT emulsion polymerisation at 70 ^{o}C to prepare a series of framboidal $G_{63}H_{350}B_z$ triblock copolymer vesicles (where z ranged from 25 to 400). TEM images reveal that the vesicle surface becomes increasingly pitted and rough until individual PBzMA globules can be observed protruding from the membrane. As higher PBzMA DPs are targeted, these globules gradually increase in size and become more prominent. SAXS provides a more in-depth analysis of surface roughness compared to TEM and DLS. Both SAXS and TEM studies confirm that topologically smooth vesicles are obtained prior to chain extension with BzMA, after which the vesicles acquire framboidal character (and hence surface roughness) depending on the DP of the PBzMA. A two-population SAXS model has been developed in order to characterise the globules protruding from the vesicle membrane. The mean globule diameter increases monotonically from 36 nm to 85 nm when the diblock copolymer precursor is chain-extended with 97-400 units of BzMA. Unlike the $G_{63}H_{350}$ diblock copolymer precursor vesicles, the framboidal triblock copolymer vesicles withstand high shear homogenisation conditions and can therefore act as Pickering emulsifiers for the stabilisation of *n*-dodecane droplets. Turbidimetry data support the literature hypothesis that greater surface roughness does indeed promote higher Pickering emulsifier efficiencies. More specifically, framboidal vesicles with mean globule dimensions of 45 nm exhibit a A_{eff} of up to 94%. PISA represents a highly

convenient and versatile synthetic route to colloidal particles of exquisitely tunable surface roughness. Such nanoparticles may also be of interest for other fundamental scientific studies, such as the effect of surface topology on cell uptake kinetics.[37]

References

1. S. U. Pickering, *Journal of the Chemical Society*, 1907, **91**, 2001-2021.
2. B. P. Binks, *Current Opinion in Colloid & Interface Science*, 2002, **7**, 21-41.
3. Z. Mao, H. Xu and D. Wang, *Advanced Functional Materials*, 2010, **20**, 1053-1074.
4. B. P. Binks and S. O. Lumsdon, *Physical Chemistry Chemical Physics*, 1999, **1**, 3007-3016.
5. S. Levine, B. D. Bowen and S. J. Partridge, *Colloids and Surfaces*, 1989, **38**, 325-343.
6. B. P. Binks and S. O. Lumsdon, *Langmuir*, 2001, **17**, 4540-4547.
7. K. L. Thompson, S. P. Armes, J. R. Howse, S. Ebbens, I. Ahmad, J. H. Zaidi, D. W. York and J. A. Burdis, *Macromolecules*, 2010, **43**, 10466-10474.
8. K. L. Thompson, S. P. Armes, D. W. York and J. A. Burdis, *Macromolecules*, 2010, **43**, 2169-2177.
9. A. Walsh, K. L. Thompson, S. P. Armes and D. W. York, *Langmuir*, 2010, **26**, 18039-18048.
10. Y. Cui, M. Threlfall and J. S. van Duijneveldt, *Journal of Colloid and Interface Science*, 2011, **356**, 665-671.
11. J. Chiefari, Y. K. Chong, F. Ercole, J. Krstina, J. Jeffery, T. P. T. Le, R. T. A. Mayadunne, G. F. Meijs, C. L. Moad, G. Moad, E. Rizzardo and S. H. Thang, *Macromolecules*, 1998, **31**, 5559-5562.
12. W. Zhang, F. D'Agosto, P.-Y. Dugas, J. Rieger and B. Charleux, *Polymer*, 2013, **54**, 2011-2019.
13. K. L. Thompson, P. Chambon, R. Verber and S. P. Armes, *Journal Of The American Chemical Society*, 2012, **134**, 12450-12453.
14. Z. Wang, M. C. M. van Oers, F. P. J. T. Rutjes and J. C. M. van Hest, *Angewandte Chemie International Edition*, 2012, **51**, 10746-10750.
15. A. San-Miguel and S. H. Behrens, *Langmuir*, 2012, **28**, 12038-12043.
16. R. Van Hooghten, L. Imperiali, V. Boeckx, R. Sharma and J. Vermant, *Soft Matter*, 2013, **9**, 10791-10798.
17. Y. Li and S. P. Armes, *Angewandte Chemie International Edition*, 2010, **49**, 4042-4046.
18. B. Charleux, G. Delaittre, J. Rieger and F. D'Agosto, *Macromolecules*, 2012, **45**, 6753-6765.
19. Z. An, Q. Shi, W. Tang, C.-K. Tsung, C. J. Hawker and G. D. Stucky, *Journal Of The American Chemical Society*, 2007, **129**, 14493-14499.
20. G. Delaittre, M. Save and B. Charleux, *Macromolecular Rapid Communications*, 2007, **28**, 1528-1533.
21. J. Rieger, C. Grazon, B. Charleux, D. Alaimo and C. Jérôme, *Journal of Polymer Science Part A: Polymer Chemistry*, 2009, **47**, 2373-2390.
22. A. Blanazs, A. J. Ryan and S. P. Armes, *Macromolecules*, 2012, **45**, 5099-5107.
23. A. Blanazs, J. Madsen, G. Battaglia, A. J. Ryan and S. P. Armes, *Journal Of The American Chemical Society*, 2011, **133**, 16581-16587.

24. P. Chambon, A. Blanazs, G. Battaglia and S. P. Armes, *Macromolecules*, 2012, **45**, 5081-5090.
25. E. R. Jones, M. Semsarilar, A. Blanazs and S. P. Armes, *Macromolecules*, 2012, **45**, 5091-5098.
26. L. Houillot, C. Bui, M. Save, B. Charleux, C. Farcet, C. Moire, J.-A. Raust and I. Rodriguez, *Macromolecules*, 2007, **40**, 6500-6509.
27. J. A. Balmer, O. O. Mykhaylyk, A. Schmid, S. P. Armes, J. P. A. Fairclough and A. J. Ryan, *Langmuir*, 2011, **27**, 8075-8089.
28. J. A. Balmer, O. O. Mykhaylyk, J. P. A. Fairclough, A. J. Ryan, S. P. Armes, M. W. Murray, K. A. Murray and N. S. J. Williams, *Journal Of The American Chemical Society*, 2010, **132**, 2166-2168.
29. L. A. Fielding, O. O. Mykhaylyk, S. P. Armes, P. W. Fowler, V. Mittal and S. Fitzpatrick, *Langmuir*, 2012, **28**, 2536-2544.
30. L. A. Fielding, O. O. Mykhaylyk, A. Schmid, D. Pontoni, S. P. Armes and P. W. Fowler, *Chemistry of Materials*, 2014, **26**, 1270-1277.
31. L. J. Fetters, D. J. Lohse and R. H. Colby, in *Physical Properties of Polymers Handbook*, ed. J. Mark, Springer New York, 2007, DOI: 10.1007/978-0-387-69002-5_25, ch. 25, pp. 447-454.
32. N. J. Warren, O. O. Mykhaylyk, A. J. Ryan, M. Williams, T. Doussineau, P. Dugourd, R. Antoine, G. Portale and S. P. Armes, *Journal Of The American Chemical Society*, 2015, **137**, 1929-1937.
33. N. J. Warren, O. O. Mykhaylyk, A. J. Ryan, M. Williams, T. Doussineau, P. Dugourd, R. Antoine, G. Portale and S. P. Armes, *Journal Of The American Chemical Society*, 2014, DOI: 10.1021/ja511423m.
34. K. L. Thompson, C. J. Mable, A. Cockram, N. J. Warren, V. J. Cunningham, E. R. Jones, R. Verber and S. P. Armes, *Soft Matter*, 2014, **10**, 8615-8626.
35. R. N. Wenzel, *Industrial & Engineering Chemistry*, 1936, **28**, 988-994.
36. A. B. D. Cassie and S. Baxter, *Transactions of the Faraday Society*, 1944, **40**, 546-551.
37. I. Canton and G. Battaglia, *Chemical Society Reviews*, 2012, **41**, 2718-2739.

Chapter Three - ABC Triblock Copolymer Worms: Synthesis, Characterisation and Evaluation as Pickering Emulsifiers for Millimetre-Sized Droplets

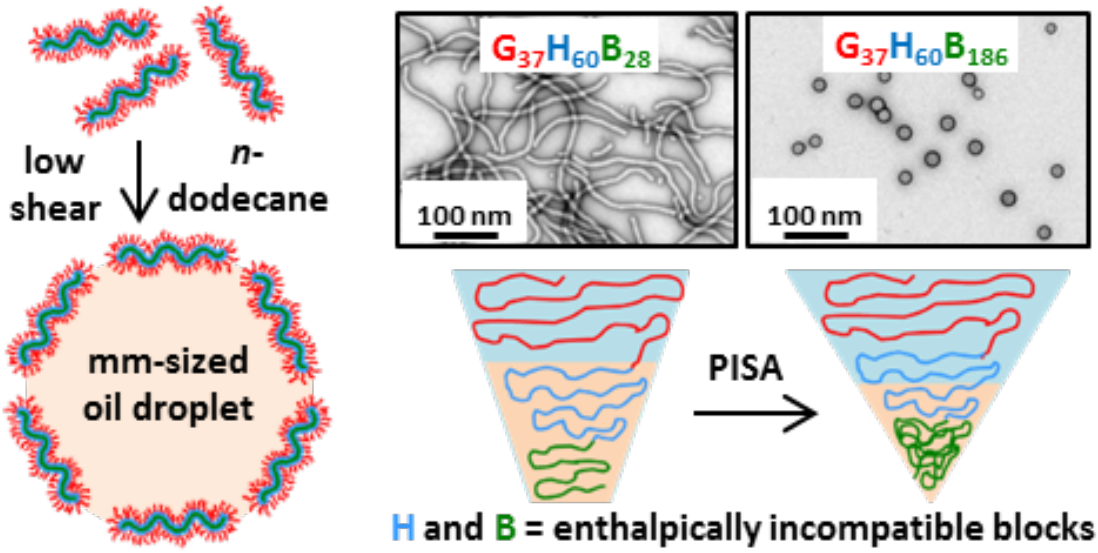

Reproduced in part from [C. J. Mable, K. L. Thompson, M. J. Derry, O. O. Mykhaylyk, B. P. Binks and S. P. Armes, *Macromolecules*, 2016, **49** (20), 7897–7907]. Copyright [2016] American Chemical Society.

Introduction

Particle-stabilised emulsions, otherwise known as Pickering emulsions, have been recognised for more than a century.[1] Many classes of particles including silica,[2-6] polymer latexes[6-10] and clays[11-14] can be used to stabilise such emulsions, with surface wettability usually dictating the emulsion type. Thus relatively hydrophilic particles tend to favour the formation of oil-in-water (o/w) emulsions, whereas relatively hydrophobic particles usually produce water-in-oil (w/o) emulsions.[15-17] Over the last decade or so, increasing attention has been paid to the use of highly anisotropic particles. For example, Noble *et al*. reported the use of polymeric microrods to prepare water-in-oil emulsions, and ultimately colloidosomes.[18] More recently, Kalashnikova *et al*. evaluated various types of cellulose-based Pickering emulsifiers of ribbon-like shape.[19-21] Similarly, Wege *et al*.[22] utilised hydrophobic anisotropic cellulose microparticles to stabilise water-in-oil emulsions. Vermant and co-workers[23] employed a multiple back-scattering technique to demonstrate that more stable Pickering emulsions are obtained when employing ellipsoidal polystyrene latexes (mean aspect ratio ~ 9) compared to conventional spherical latex particles. Similar results were also reported for ellipsoidal hematite particles (mean aspect ratio ~ 6).[23]

Over the past decade, the Armes research group and others have utilised polymerisation-induced self-assembly (PISA) to prepare a wide range of diblock copolymer nano-objects of tunable size, shape and surface chemistry in the form of concentrated colloidal dispersions.[24-28] Of particular relevance to the present work, PISA provides an extremely attractive route to highly anisotropic block copolymer worms,[29] enabling their synthesis on a multi-gram scale in either polar solvents (e.g. water[24, 30] or ethanol[25, 31]) or non-polar solvents (e.g. *n*-alkanes[32, 33]). Reproducible PISA syntheses of such worms usually require the construction of phase diagrams,[34, 35] although ad hoc syntheses can sometimes also be effective.[36] Recently, we compared the performance of hydrophilic linear and cross-linked poly(glycerol monomethacrylate)-poly(2-hydroxypropyl methacrylate) [PGMA-PHPMA] diblock copolymer worms prepared via PISA in aqueous solution as Pickering emulsifiers for the production of o/w emulsions.[36] The linear worms did not

survive the high-energy homogenisation conditions required to generate the oil droplets: instead, worm dissociation occurs to generate individual copolymer chains, which then act as a polymeric surfactant to stabilise the emulsion. However, the corresponding cross-linked worms (which were obtained *via* addition of a small amount of ethylene glycol dimethacrylate) survived homogenisation, leading to the formation of genuine Pickering emulsions. In related work, hydrophobic linear poly(lauryl methacrylate)-poly(benzyl methacrylate) [PLMA-PBzMA] worms prepared via PISA in *n*-dodecane survived homogenisation to produce w/o Pickering emulsions.[16] In this case the worms exhibited thermo-responsive behaviour: heating to 150 ^{o}C led to a worm-to-sphere transition that was essentially irreversible if it is conducted in sufficiently dilute solution (1.0 % w/w). Thus this system provided a unique opportunity to compare the effect of particle morphology on Pickering emulsifier performance for chemically identical spheres and worms.[16] It was found that the worms were more effective stabilisers, because they produced finer, more stable oil droplets than the spheres when directly compared under the same conditions. This is understandable, because worms are 1-2 orders of magnitude more strongly adsorbed at the oil-water interface than spheres, yet have a comparable surface area per unit mass, A_s (the A_s for highly anisotropic worms is estimated to be only approximately 33% less than the A_s for the corresponding spheres). [16, 36] Given these intrinsic advantages, and the relative ease with which block copolymer worms can now be accessed *via* PISA syntheses, further exploration of the use of such anisotropic particles as Pickering emulsifiers is clearly warranted.

In this work, we revisit our recent empirical (and serendipitous) discovery that linear PGMA-PHPMA-PBzMA triblock copolymers can form sufficiently robust worms to act as Pickering emulsifiers for o/w emulsions.[36] More specifically, we examine the scope and limitations of the PISA synthesis of such worms, explain why the copolymer morphology does not evolve further to produce vesicles, characterise the worm dimensions using transmission electron microscopy (TEM) and small-angle X-ray scattering (SAXS), and assess the performance of such worms as hydrophilic Pickering emulsifiers for the production of millimetre-sized oil droplets.

Experimental Details

Materials

All reagents were used as received unless otherwise stated. Benzyl methacrylate (BzMA), *n*-dodecane, 2-cyano-2-propyl benzodithioate (CPDB) and 4, 4'-azobis-4-cyanopentanoic acid (ACVA) were purchased from Sigma-Aldrich (UK). BzMA inhibitor was removed by passing this monomer through an inhibitor removal column. Ethanol, dichloromethane, DMSO and DMF were purchased from Fisher Scientific (UK). Glycerol monomethacrylate (GMA) was kindly donated by GEO Specialty Chemicals (Hythe) and used without further purification. 2-Hydroxypropyl methacrylate (HPMA) was purchased from Alfa Aesar (UK) and contained 0.07 mol % dimethacrylate impurity, as judged by high performance liquid chromatography (HPLC). Deuterated methanol (d_4-CD_3OD), dimethyl sulfoxide (d_6-DMSO) and dimethyformamide (d_7-DMF) NMR solvents were purchased from Goss Scientific (UK). Deionised water was obtained using an Elga Elgastat Option 3A water purifier; its pH was approximately 6.2 and its surface tension was 72.0 mN m^{-1} at 20 ^{o}C.

RAFT Synthesis of PGMA Macro-CTA Agent in Ethanol

The G_{37} macro-CTA was synthesised by Dr Vincent Ladmiral and the G_{92} macro-CTA was synthesised by Rheanna Perry, following previously reported protocols.[35]

Preparation of $G_{37}H_{60}$ Diblock Copolymer Precursor via RAFT Aqueous Solution Polymerisation at 15 % w/w Solids

G_{37} macro-CTA (5.00 g, 0.813 mmol), HPMA monomer (7.04 g, 48.8 mmol), deionised water (68.6 g) and ACVA (76.0 mg, 0.271 mmol, CTA/ACVA molar ratio = 3.0) were weighed into a 100 mL round-bottomed flask and purged with N_2 for 30 min prior to immersion in an oil bath set at 70 ^{o}C for 2 h. Finally, the polymerisation was quenched by cooling to room temperature with subsequent exposure to air.

Preparation of $G_{37}H_{60}B_z$ Triblock Copolymers (Where z Ranges from 10-550) *via* RAFT Seeded Emulsion Polymerisation at 11-46 % w/w Solids

Protocol for $G_{37}H_{60}B_{30}$ triblock copolymer worms: $G_{37}H_{60}$ diblock copolymer precursor (8.00 g of a 10 % w/w copolymer solution, 1.00 g copolymer, 0.0541 mmol), ACVA (3.03 mg, 0.0108 mmol, CTA/ACVA molar ratio = 5.0) and BzMA monomer (0. 286 g, 1.62 mmol, target degree of polymerisation (DP) = 30) were weighed into a 25 ml sample vial and purged with N_2 for 20 min prior to immersion in an oil bath set at 70 ^oC for 4 h with stirring. The polymerisation was quenched by cooling to room temperature and subsequent exposure to air. This polymerisation was conducted at 13 % w/w solids. A series of similar copolymer syntheses were performed for which the PBzMA target DP ranged from 10 to 550 using BzMA masses varying from 0.0953 g to 5.23 g (0.541 mmol to 29.7 mmol), respectively, with the copolymer solids concentration increasing from 11 to 46 % w/w.

Preparation of Linear $G_{37}H_{90}$ Diblock Copolymer Worms *via* RAFT Aqueous Dispersion Polymerisation at 13 % w/w Solids

G_{37} macro-CTA (1.00 g, 0.163 mmol), HPMA monomer (2.11 g, 14.6 mmol), deionised water (20.9 g) and ACVA (15.1 mg, 0.0542 mmol, CTA/ACVA molar ratio = 3.0) were weighed into a 50 mL round-bottomed flask and purged with N_2 for 30 min prior to immersion in an oil bath set at 70 ^oC for 2 h with stirring. Finally, the polymerisation was quenched by cooling to room temperature with subsequent exposure to air.

Preparation of Linear $G_{92}B_{30}$ Diblock Copolymer Spheres *via* RAFT Aqueous Emulsion Polymerisation at 13 % w/w Solids

G_{92} macro-CTA (0.5 g, 0.0334 mmol), BzMA monomer (0.177 g, 1.00 mmol), deionised water (4.55 g) and ACVA (3.12 mg, 0.011 mmol, CTA/ACVA molar ratio = 3.0) were weighed into a 25 mL vial and purged with N_2 for 30 min prior to immersion in an oil bath set at 70 ^oC for 4 h with stirring. Finally, the polymerisation was quenched by cooling to room temperature with subsequent exposure to air.

Pickering Emulsion Formation

Either *n*-dodecane or *n*-hexane (20 vol. %) was shaken by hand with 2.0 ml of a 0.00188 - 1.0 % w/w aqueous worm dispersion for 2 min at 20 ^{o}C. The droplets were imaged by OM and the mean droplet diameter was determined by laser diffraction.

^{1}H NMR Spectroscopy

All NMR spectra were recorded using a 400 MHz Bruker Avance-400 spectrometer and 64 scans were averaged per spectrum.

Gel Permeation Chromatography (GPC)

Copolymer molecular weights and polydispersities were determined using a DMF GPC set-up operating at 60 ^{o}C and comprising two Polymer Laboratories PL gel 5 μm Mixed C columns connected in series to a Varian 390 LC multi-detector suite (only the refractive index detector was utilised) and a Varian 290 LC pump injection module. The GPC eluent was HPLC grade DMF containing 10 mM LiBr at a flow rate of 1.0 mL min^{-1}. DMSO was used as a flow-rate marker. Calibration was conducted using a series of ten near-monodisperse poly(methyl methacrylate) standards (M_n = 625 – 618,000 g mol^{-1}). The chromatograms were analysed using Varian Cirrus GPC software (version 3.3) provided by the instrument manufacturer (Polymer Laboratories).

Dynamic Light Scattering (DLS)

Intensity-average hydrodynamic diameters of the copolymer dispersions were determined using a Malvern Zetasizer NanoZS instrument. Dilute aqueous dispersions (0.10 % w/w) were analysed using disposable cuvettes and all data were averaged over three consecutive runs to give the hydrodynamic diameter (D_h).

Transmission Electron Microscopy (TEM)

As-synthesised copolymer dispersions were diluted at 20 ^{o}C to generate 0.10 % w/w dispersions. Copper/palladium TEM grids (Agar Scientific) were surface-coated in-house to yield a thin film of amorphous carbon. The grids were then plasma glow-discharged for 30 s to create a hydrophilic surface. Individual samples of aqueous copolymer dispersions (0.1 % w/w, 12 μL)

were adsorbed onto the freshly glow-discharged grids for 20 s and then blotted with filter paper to remove excess solution. To stain the copolymer dispersions, uranyl formate (0.75 % w/v) solution (9 μL) was soaked on the sample-loaded grid for 20 s and then carefully blotted to remove excess stain. The grids were then dried using a vacuum hose. Imaging was performed on a Phillips CM100 instrument at 100 kV, equipped with a Gatan 1 K CCD camera. A similar protocol was followed for the emulsion droplet grid preparation. The emulsion was shaken and a sample (12 μL) was adsorbed onto the freshly glow discharged grid. The grids were not blotted with filter paper to remove excess dispersion – instead the hexane oil droplet evaporated after several min at ambient temperature. The staining protocol was the same as that for the aqueous copolymer dispersions.

Small-Angle X-Ray Scattering (SAXS)

SAXS patterns were recorded at Diamond Light Source (station I22, Didcot, UK). A monochromatic X-ray radiation (of wavelength λ = 0.1239 nm) and 2D SAXS detector (Pilatus 2M) were used for the experiment. The SAXS camera length set-ups covered the q range from 0.02 nm^{-1} to 1.9 nm^{-1}, where $q = 4\pi\sin\theta/\lambda$ is the modulus of the scattering vector and θ is half of the scattering angle. A glass capillary cell of 1 mm thickness was used as the sample holder. X-ray scattering data were reduced by Dawn software, and were further analysed using Irena SAS macros for Igor Pro.[37] SAXS measurements were conducted on various aqueous dispersions, for which the copolymer concentration was diluted to 1.0 % w/w for data collection. A scattering pattern of the homopolymer solution was collected using a laboratory SAXS instrument (a modified Bruker AXS Nanostar equipped with a microfocus Genix 3D Cu Kα radiation X-ray source and a collimator comprised of two sets of motorised scatterless slits by Xenocs, a camera length of 1.46 m and a 2D HiSTAR multiwire gas detector), glass capillaries of 2 mm diameter were used as a sample holder.

Optical Microscopy (OM)

Optical microscopy images were recorded using a Motic DMBA300 digital biological microscope with a built-in camera and equipped with Motic Images Plus 2.0 ML software.

Laser Diffraction

A Malvern Mastersizer 2000 instrument equipped with a small volume Hydro 2000SM sample dispersion unit (*ca*. 50 ml), a HeNe laser operating at 633 nm, and a solid-state blue laser operating at 466 nm was used to size each emulsion. The stirring rate was adjusted to 1,000 rpm in order to avoid creaming of the emulsion during analysis. After each measurement, the cell was rinsed once with ethanol, followed by three rinses with doubly-distilled water; the glass walls of the cell were carefully wiped with lens cleaning tissue to avoid cross-contamination and the laser was aligned centrally to the detector prior to data acquisition. The volume-average diameter was measured and repeated four times for each emulsion.

Results and Discussion

Synthesis and Characterisation of Block Copolymers

For the sake of brevity, a shorthand notation is utilised throughout this Chapter to describe the various block copolymers. Thus G, H and B are used to represent glycerol monomethacrylate (GMA), 2-hydroxypropyl methacrylate (HPMA) and benzyl methacrylate (BzMA), respectively. Thus $G_xH_yB_z$ denotes poly(glycerol monomethacrylate)-poly(2-hydroxypropyl methacrylate)-poly(benzyl methacrylate), where x, y, and z indicate the mean DP of the three respective blocks.

The initial RAFT solution polymerisation of GMA was conducted in ethanol at 70 ^{o}C to generate a near-monodisperse G_{37} macromolecular chain transfer agent (macro-CTA) (M_w/M_n = 1.19; see Figure 3.1 and Table 3.1). After purification, this water-soluble macro-CTA was utilised for the *in situ* RAFT aqueous solution polymerisation of HPMA at 15 % w/w solids, yielding a 100 g batch of $G_{37}H_{60}$ diblock copolymer precursor (see Figure 3.2a).

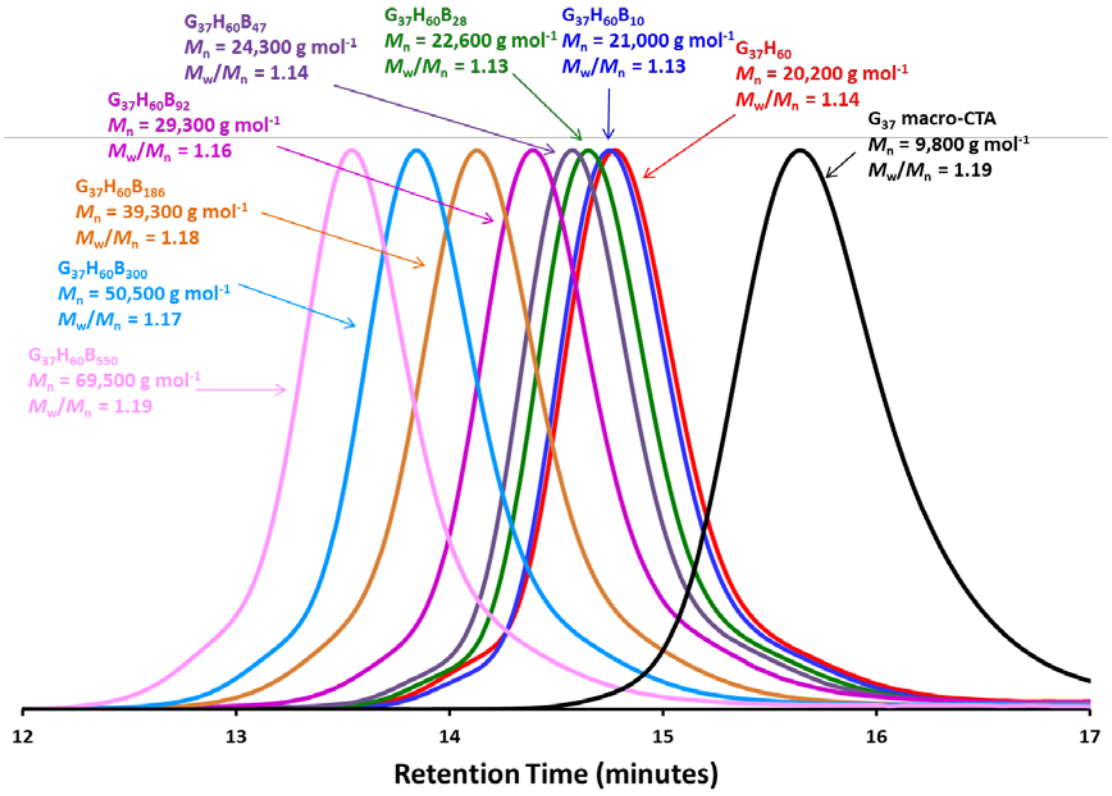

Figure 3.1. DMF GPC curves vs. poly(methyl methacrylate) (PMMA) standards obtained for a G_{37} macro-CTA, a $G_{37}H_{60}$ diblock copolymer precursor and a series of $G_{37}H_{60}B_z$ triblock copolymers (where z ranges from 10 to 550).

^{1}H NMR studies indicated that more than 99 % HPMA conversion was achieved within 2 h at 70 ^{o}C (see Figure 3.3), as expected from previous studies.[34] Gel permeation chromatography (GPC) studies indicated that a near-monodisperse diblock copolymer was obtained with high blocking efficiencies and minimal macro-CTA contamination (M_w/M_n = 1.14; see Figure 3.1 and Table 3.1). The GPC trace was unimodal but a high molecular weight shoulder was discernible, which has been attributed to low levels of dimethacrylate impurity in the HPMA monomer (approximately 0.07 mol % as judged by HPLC analysis), which results in light branching of the PHPMA chains. Dynamic light scattering (DLS) studies of this $G_{37}H_{60}$ diblock copolymer reveal a relatively low count rate of 50 kcps and ^{1}H NMR studies confirm that the PHPMA block is fully soluble in water (see Figure 3.4), suggesting that self-assembly does not occur for this relatively short PHPMA block.

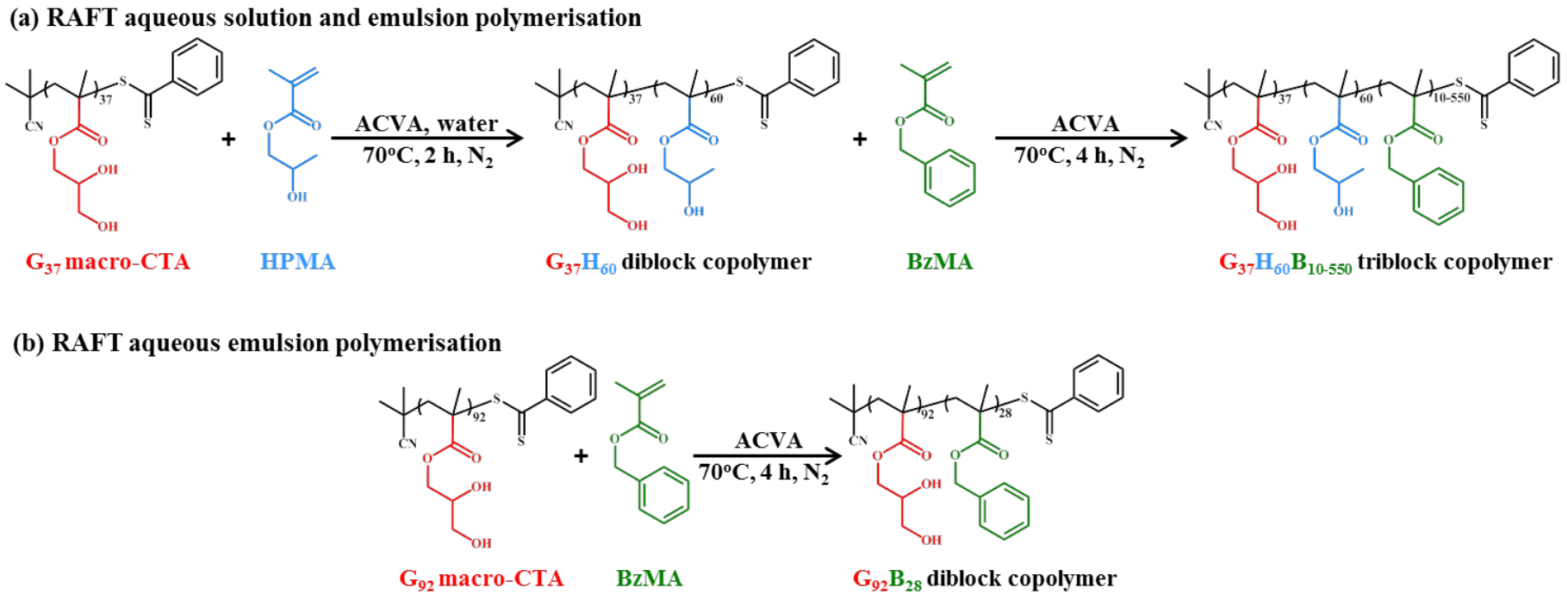

Figure 3.2. Synthesis of (a) $G_{37}H_{60}B_{10\text{-}550}$ triblock copolymer via RAFT aqueous solution polymerisation of HPMA followed by RAFT seeded emulsion polymerisation of BzMA and (b) $G_{92}B_{28}$ diblock copolymer prepared via RAFT aqueous emulsion polymerisation of BzMA.

Table 3.1. Summary of ^{1}H NMR-derived monomer conversion, apparent DLS hydrodynamic diameter (D_h) and polydispersity, number-average molecular weight (M_n) and polydispersity (M_w/M_n) determined for a G_{37} macro-CTA, a $G_{37}H_{60}$ diblock copolymer precursor, a series of seven $G_{37}H_{60}B_z$ triblock copolymers (where z ranges from 10 to 550), a $G_{37}H_{90}$ diblock copolymer control, a G_{92} macro-CTA precursor and a $G_{92}B_{28}$ diblock copolymer control.

Copolymer Composition	BzMA conversion/ %	D_h (PDI)[c] / nm	M_n[b] / g mol^{-1}	M_w/M_n[b]
G_{37} macro-CTA			9 800	1.19
$G_{37}H_{60}$	>99[a]	119 (0.31)	20 200	1.14
$G_{37}H_{60}B_{10}$	98	41 (0.13)	21 000	1.13
$G_{37}H_{60}B_{28}$	94	147 (0.23)	22 600	1.13
$G_{37}H_{60}B_{47}$	95	79 (0.16)	24 300	1.14
$G_{37}H_{60}B_{92}$	92	45 (0.03)	29 300	1.16
$G_{37}H_{60}B_{186}$	93	63 (0.04)	39 300	1.18
$G_{37}H_{60}B_{300}$	>99	86 (0.14)	50 500	1.17
$G_{37}H_{60}B_{550}$	>99	120 (0.06)	69 500	1.19
$G_{37}H_{90}$	>99[a]	46 (0.13)	25 500	1.11
G_{92} macro-CTA			23 900	1.12
$G_{92}B_{28}$	94	28 (0.36)	26 300	1.14

[a] Data correspond to HPMA conversion, rather than BzMA conversion.
[b] DMF GPC data recorded using a refractive index detector and calibrated using a series of poly(methyl methacrylate) standards.
[c] D_h is a sphere-equivalent diameter in the case of worms.

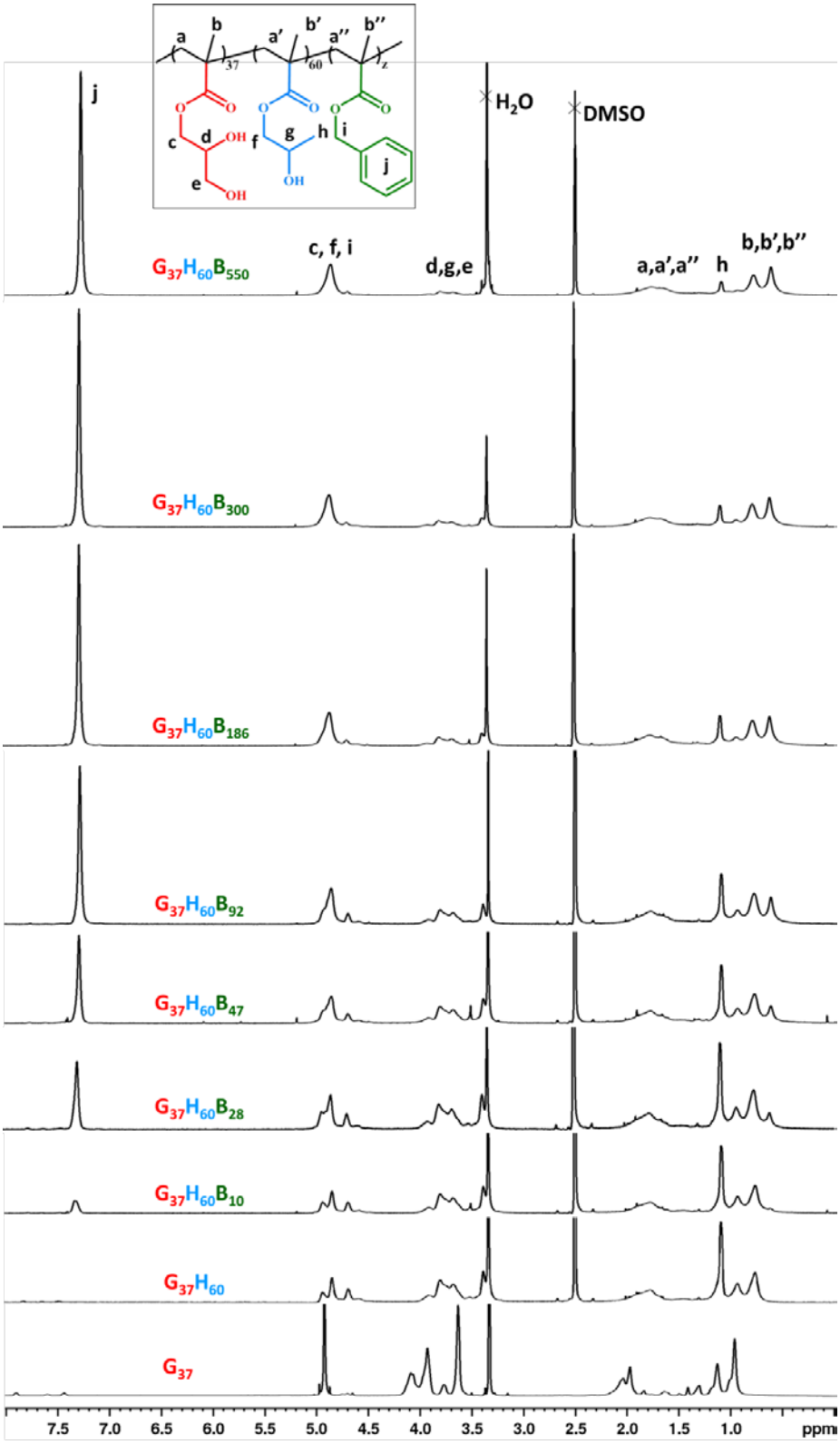

Figure 3.3. Assigned ^{1}H NMR spectra obtained for a G_{37} macro-CTA (d_4-CD_3OD), $G_{37}H_{60}$ diblock copolymer precursor (d_6-DMSO) and a series of $G_{37}H_{60}B_z$ triblock copolymers, where z ranges from 10 to 550 (d_6-DMSO).

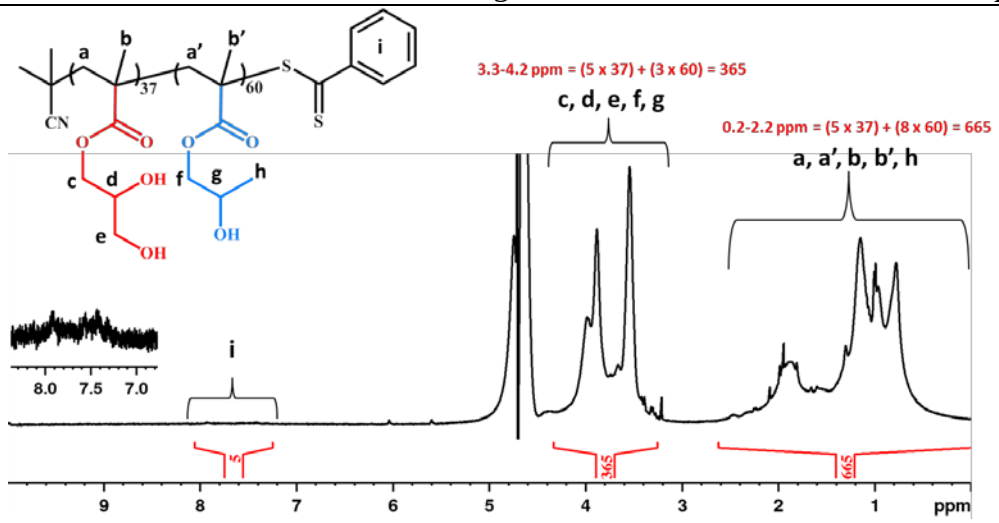

Figure 3.4. Assigned ^{1}H NMR spectra (D_2O) obtained for a $G_{37}H_{60}$ diblock copolymer. The integrals suggest that both the PGMA and PHPMA blocks are solvated, hence the PHPMA DP of 60 is insufficient to induce micellisation.

Furthermore, no nanoparticles can be observed by TEM (see Figure 3.5, $G_{37}H_{60}$), which again indicates that the PHPMA block is not sufficiently long to induce micellar nucleation. This is consistent with observations made by Blanazs and co-workers, who found that a minimum PHPMA DP of around 90 was required to induce nucleation when using a $PGMA_{47}$ macro-CTA.[34] However, it should be noted that this minimum critical DP is expected to be rather sensitive to the precise PISA formulation.[38]

This $G_{37}H_{60}$ diblock copolymer precursor was then utilised as a macro-CTA for the RAFT seeded emulsion polymerisation of BzMA at 70 ^oC to produce a series of seven $G_{37}H_{60}B_z$ triblock copolymers, where z ranged from 10 to 550 (see Figure 3.2a). ^{1}H NMR studies confirmed that BzMA conversions greater than 92 % were obtained in each case (see Figure 3.3 and Table 3.1). Dimethyl formamide (DMF) GPC studies indicated that near-monodisperse triblock copolymers were obtained (M_w/M_n < 1.20, see Table 3.1) with high blocking efficiencies (see Figure 3.1). TEM images shown in Figure 3.5 and DLS studies (see Table 3.1) indicated that spheres with a hydrodynamic diameter (D_h) of 41 nm were formed when z = 10, thus chain extension with just 10 units of BzMA is sufficient to induce micellar nucleation. When targeting a PBzMA DP of 30 (and achieving a DP of 28), TEM studies indicated the formation of highly anisotropic worms (Figure 3.5), similar to those reported recently.[36]

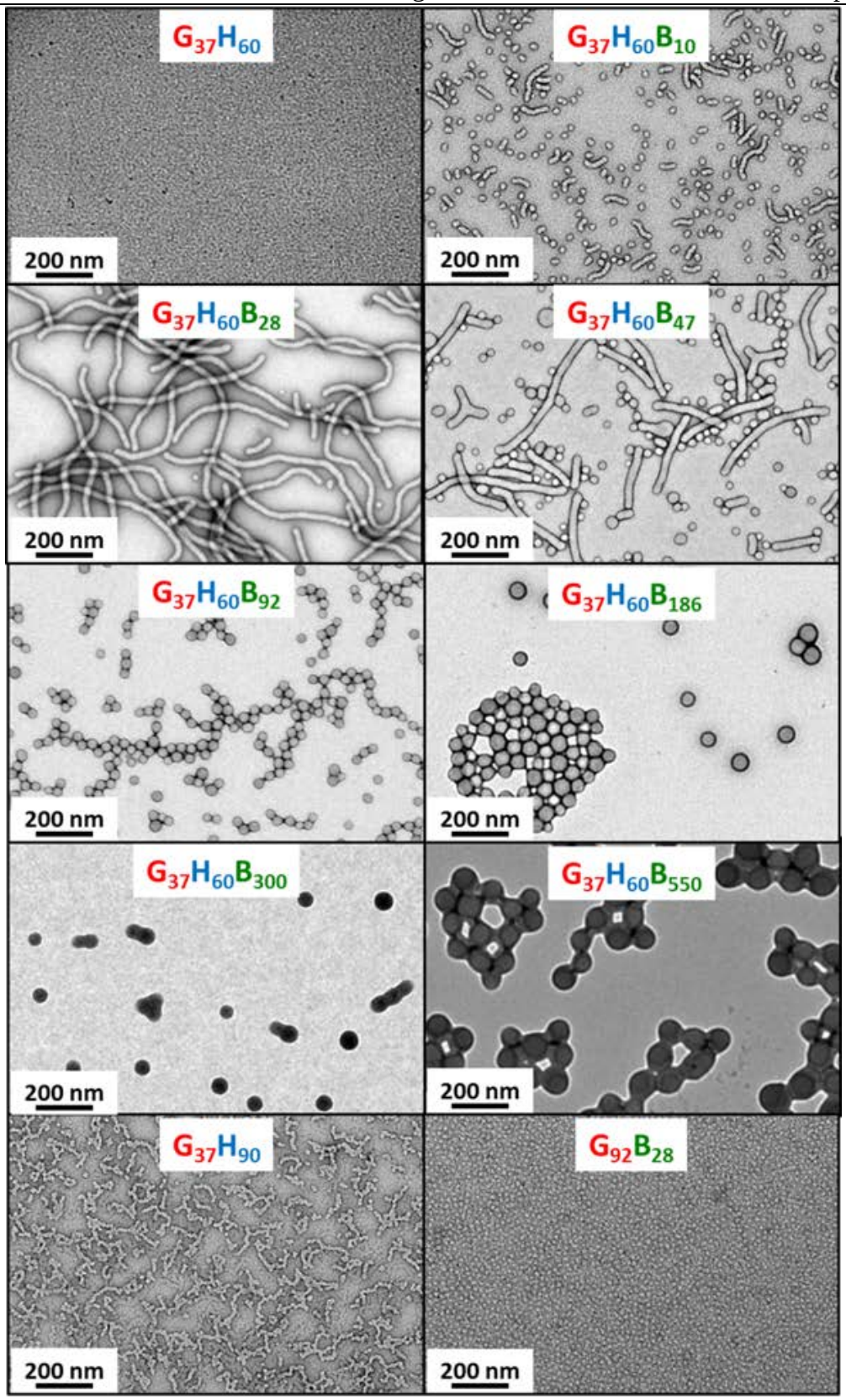

Figure 3.5. TEM images obtained for dried dilute aqueous dispersions of the $G_{37}H_{60}$ diblock copolymer precursor, a series of seven $G_{37}H_{60}B_z$ triblock copolymers (where z ranges from 10 to 550), the $G_{37}H_{90}$ diblock copolymer worms and the $G_{92}B_{28}$ diblock copolymer spheres.

These $G_{37}H_{60}B_{28}$ worms were further characterised by SAXS. The worm model[39-41] provided an excellent fit to the SAXS pattern over six orders of magnitude of X-ray scattering intensity (see Figure 3.6a). The mean worm contour length (L_w) was determined to be 653 nm, which is consistent with TEM observations. Assuming a circular worm cross-section, the mean worm width (W_w), was calculated to be 25.6 ± 1.7 nm, which is also consistent with that estimated from TEM images (for which W_w = 24.2 ± 3.2 nm), where $W_w = 2R_{sw} + 4R_g$, with R_{sw} representing the radius of the worm core cross-section and R_g representing the radius of gyration of the corona chains. The R_g of the G_{37} corona block of these worms was determined to be 1.7 nm from the data fit to the SAXS pattern. This experimental value is comparable to a theoretical estimate: the projected contour length of a single GMA monomer is 0.255 nm (two carbon bonds in an all-*trans* conformation), the total contour length of a G_{37} block, L_{PGMA} = 37 x 0.255 nm = 9.44 nm and the literature value of the Kuhn length for poly(methyl methacrylate) is 1.53 nm,[42] resulting in an R_g of $(9.44 \times 1.53/6)^{1/2}$, or 1.55 nm. A worm model fit to the SAXS data pattern of $G_{37}H_{60}B_{28}$ (Figure 3.6a) has shown that the solvent volume fraction in the core (x_{sol}) is 0.03, which suggests that the hydrophobic worm cores are essentially non-solvated. This is significantly different to x_{sol} values reported recently by Warren *et al.*[28] for $G_{55}H_y$ diblock copolymer *vesicles*, which ranged from 0.38 to 0.66 as y was increased from 200 to 1000. It is evident that extension with approximately 28 units of BzMA not only changes the nanoparticle morphology from spheres to worms, but also drastically changes the extent of hydration of the nanoparticle cores.

Based on the PISA literature,[38, 43-46] it was anticipated that vesicular morphologies should be obtained for these $G_{37}H_{60}B_z$ triblock copolymers as the target DP of the PBzMA block was gradually increased. However, only branched worms and spheres were obtained when z = 47 (see TEM images in Figure 3.5). Furthermore, both TEM and DLS studies indicated that only spheres were obtained when $z \geq 92$ (see Figure 3.5 and Table 3.1, respectively). The spheres progressively increase in mean diameter from 45 nm to 120 nm as z was systematically varied from 92 to 550, but vesicular morphologies were never obtained.

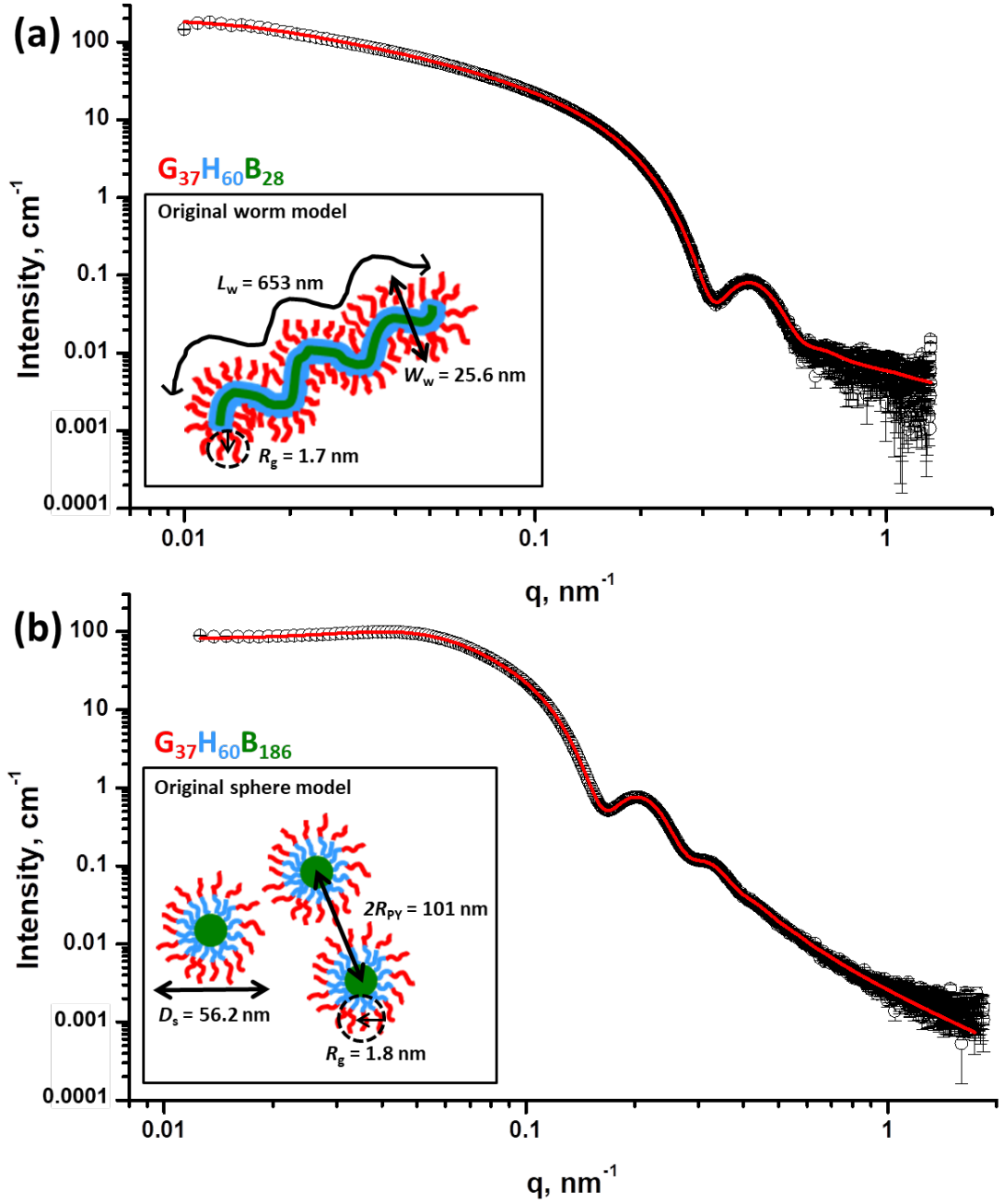

Figure 3.6. SAXS data (open black circles) and fits (red lines) for dilute aqueous dispersions of (a) $G_{37}H_{60}B_{28}$ triblock copolymer worms and (b) $G_{37}H_{60}B_{186}$ triblock copolymer spheres. Insets: schematic cartoons of the corresponding morphologies, where L_w = the mean worm contour length, W_w = the mean worm width, R_g = the radius of gyration, D_s = the diameter of the sphere and R_{PY} = the Percus-Yevick correlation radius of densely-packed spheres. Note: the structural morphologies are not drawn to scale.

Hypothetically, the spherical morphology observed by TEM might actually correspond to small vesicles. However, the SAXS pattern recorded for the $G_{37}H_{60}B_{186}$ triblock copolymer has a gradient that tends to zero at low q (see Figure 3.6b) indicating typical spherical particles,[47] rather than hollow spheres (or vesicles).

Analysis of the $G_{37}H_{60}B_{186}$ SAXS pattern using a spherical micelle model[39-41, 48] gave an excellent data fit over six orders of magnitude of x-ray scattering intensity (Figure 3.6b). The SAXS-derived mean sphere diameter (D_s) was calculated to be 56.2 ± 5.4 nm, which is similar to that reported by DLS (63 nm, see Table 3.1). The structure factor peak observed in the SAXS pattern at $q \sim 0.05$ nm^{-1} (Figure 3.6b) suggests that the spheres are weakly aggregated. The Percus-Yevick correlation radius of packed spheres (R_{PY}) was obtained to be 50.5 nm. The TEM images obtained for dispersions when $z \geq 92$ also show that the spheres may be partially fused/weakly aggregated. However, the number-average diameter estimated from TEM images recorded for $G_{37}H_{60}B_{92\text{-}550}$ triblock copolymer spheres corresponds quite closely to the hydrodynamic diameter obtained from DLS studies (see entries 6-9 in Table 3.1).

Although these results are somewhat counter-intuitive when compared to most of the recent PISA literature,[37, 42-45] it is perhaps not too surprising that only spheres are obtained when targeting higher DPs for the PBzMA block. For example, Cunningham *et al.*[27] prepared a series of $G_{51}B_y$ diblock copolymer spheres *via* RAFT aqueous emulsion polymerisation of BzMA, with y ranging from 50 to 1000. Only spherical nanoparticles were obtained in all cases, regardless of the total solids content. In the present study, a weakly hydrophobic PHPMA block lies between the hydrophilic PGMA and highly hydrophobic PBzMA blocks, which allows triblock copolymer worms to be prepared for compositions containing just 31 mol % PBzMA. However, targeting higher PBzMA contents only leads to the formation of triblock copolymer spheres. The most likely explanation for these unexpected observations is that the PBzMA block is enthalpically highly incompatible with the PHPMA block, whereas the PHPMA block is only rather weakly incompatible with the PGMA block. Thus, when the $G_{37}H_{60}$ diblock copolymer is chain-extended with BzMA, at least some fraction of the partially hydrated PHPMA block[24] is gradually driven out of the increasingly hydrophobic core to become co-located with the PGMA stabiliser chains in the hydrophilic corona (see the schematic cartoon shown in Figure 3.7). If this is the case, it would lead to an effectively longer stabiliser block, with a theoretical maximum DP of 97 (*i.e.* the sum of G_{37} and H_{60}).

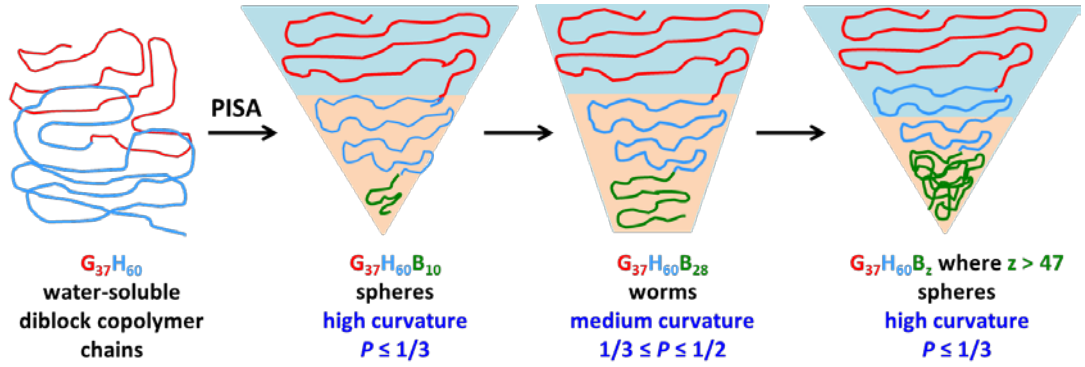

Figure 3.7. Schematic cartoon to illustrate the conformational behaviour of $G_{37}H_{60}B_z$ triblock copolymer chains as z is systematically increased. Hydrophilic regions are represented by blue and hydrophobic regions are represented by orange. The packing parameter, *P*, is given by $P = v/a_o l_c$ where *v* is the volume of the hydrophobic chains, a_o is the optimal area of the head group, and l_c is the length of the hydrophobic tail.[43, 49] Initially, the $G_{37}H_{60}$ diblock copolymer precursor chains are molecularly dissolved in the aqueous phase. For z ~ 10, the relatively short PBzMA block induces nucleation, producing spherical micelles with mixed cores comprising the $PHPMA_{60}$ and the $PBzMA_{10}$ blocks. For z ~ 30, the growing PBzMA block leads to an increase in *P*, which drives a sphere-to-worm transition during PISA. When z ~ 47, the PHPMA block becomes at least partly co-located within the stabiliser corona layer, rather than the core. This is because the weakly hydrophobic PHPMA block is actually less enthalpically incompatible with the hydrophilic PGMA block than with the highly hydrophobic PBzMA block. This inevitably causes a *reduction* in *P*, which leads to a worm-to-sphere transition.

SAXS analysis allows this hypothesis to be examined.[50] A SAXS pattern was collected for a 10 % w/w aqueous solution of the G_{37} macro-CTA (i.e., for molecularly dissolved chains below their overlap concentration). A satisfactory data fit was obtained for this pattern using a Gaussian coil model,[51] which indicated a R_g of 1.7 nm (see Figure 3.8a). This is very close to the R_g value for the stabiliser chains obtained from fitting the $G_{37}H_{60}B_{28}$ SAXS pattern using the worm model (see Table 3.2). This suggests that all of the weakly hydrophobic $PHPMA_{60}$ blocks are located within the core of the worms, while the hydrophilic $PGMA_{37}$ blocks occupy the worm corona. To test this hypothesis, the worm model was slightly modified (see Equations A4.15 To A4.22 in the Appendix for the modified SAXS model) by incorporating an additional fitting parameter (η) corresponding to the volume fraction of the PHPMA block within the core domain. This η parameter enables the volume of the core and corona to be determined, rather than fixing these values based on the known block compositions. By definition, if the whole PHPMA block is located within the core, η should be equal to unity. In contrast, η should be zero if the PHPMA block is solely located in the corona. A good data fit was obtained for the $G_{37}H_{60}B_{28}$ SAXS pattern using the modified worm model (see Figure 3.8b). The

fitting parameters were similar to those obtained when using the unmodified, original worm model (see Table 3.2). The R_g for the G_{37} corona block of this triblock copolymer was determined to be 1.7 nm, which is identical to that obtained for the G_{37} macro-CTA alone (see Figure 3.8a). Moreover, η tends towards unity, indicating that all of the PHPMA block is located in the worm core (see Figure 3.7).

A spherical micelle model[39-41, 48] was similarly modified by incorporating η as an additional fitting parameter (see Equations A4.3 To A4.14 in the Appendix for the modified SAXS model and Table 3.2). Analysis of the $G_{37}H_{60}B_{186}$ spheres using this more sophisticated model gave a reasonably good data fit to the SAXS pattern over six orders of magnitude of X-ray scattering intensity (Figure 3.8c). Again, the fitting parameters were similar to those obtained when using the original unmodified sphere model (see Table 3.2). However, the R_g of the G_{37} corona block for this $G_{37}H_{60}B_{186}$ triblock copolymer was determined to be 3.3 nm from this analysis, which is significantly larger than that obtained for the $G_{37}H_{60}B_{28}$ worms. Notwithstanding the imperfect data fit at high q, this indicates that the stabiliser corona is somewhat thicker in the former case, even though the same $G_{37}H_{60}$ diblock precursor was used for the PISA synthesis of the $G_{37}H_{60}B_{28}$ and $G_{37}H_{60}B_{186}$ triblocks. Moreover, η was found to be 0.62, which suggests that a significant fraction of the PHPMA block is now located in the corona, rather than in the core (see Figure 3.7). This provides direct experimental evidence for a higher effective DP for the corona block when targeting a longer PBzMA core-forming block. For the $G_{37}H_{60}B_{186}$ triblock copolymer spheres, SAXS analysis indicates that around 23 HPMA repeat units [$(1 - 0.62) \times 60 \approx 23$] in each PHPMA block are located within the corona, while the remaining 37 repeat units occupy the core along with the PBzMA chains. This increase in the effective stabiliser block DP leads to a reduction in the packing parameter, P, which in turn causes the observed worm-to-sphere transition (see Figure 3.7). The driving force for relocating approximately one-third of the PHPMA block within the corona is the greater incompatibility within the PHPMA and PBzMA blocks as the DP of the PBzMA block is increased. In this context, in Chapter two of this thesis we show that systematically varying the PBzMA block DP (or z) from 25 to 400 leads to an evolution in framboidal morphology for a series of $G_{63}H_{350}B_z$

triblock copolymer vesicles.[52] Thus it is not really surprising that enthalpic demixing between the PHPMA and PBzMA blocks leads to a dramatic change in morphology in the work carried out in this Chapter. In summary, SAXS provides useful insight into the unusual (and at first sight counter-intuitive) evolution in copolymer morphology for this particular PISA formulation, which can be rationalised by considering subtle changes in the relative enthalpic incompatibilities between the three blocks during the growth of the PBzMA core-forming block.

In order to examine whether the intermediate PHPMA block is really essential for worm formation, a $G_{92}B_{28}$ diblock copolymer was synthesised via RAFT aqueous emulsion polymerisation of BzMA using a G_{92} macro-CTA (see Figure 3.2b). The G_{92} block was designed to have a comparable DP to that of the combined DP of the G_{37} and H_{60} blocks, while a PBzMA DP of 30 was targeted because this produced worms for the ABC triblock formulation. ^{1}H NMR studies indicated that 94% BzMA conversion was achieved after 4 h at 70 ^{o}C (see Figure 3.9a). GPC studies indicated that a low-polydispersity diblock copolymer was obtained with a high blocking efficiency and minimal macro-CTA contamination (M_w/M_n = 1.14; see Figure 3.9b and Table 3.1). DLS studies indicate a mean D_h of 28 nm (see Table 3.1). TEM images confirmed the formation of very small spheres of around 11.3 ± 2.5 nm diameter (based on analysing 100 nanoparticles) with no evidence for the presence of any worms (see Figure 3.5).

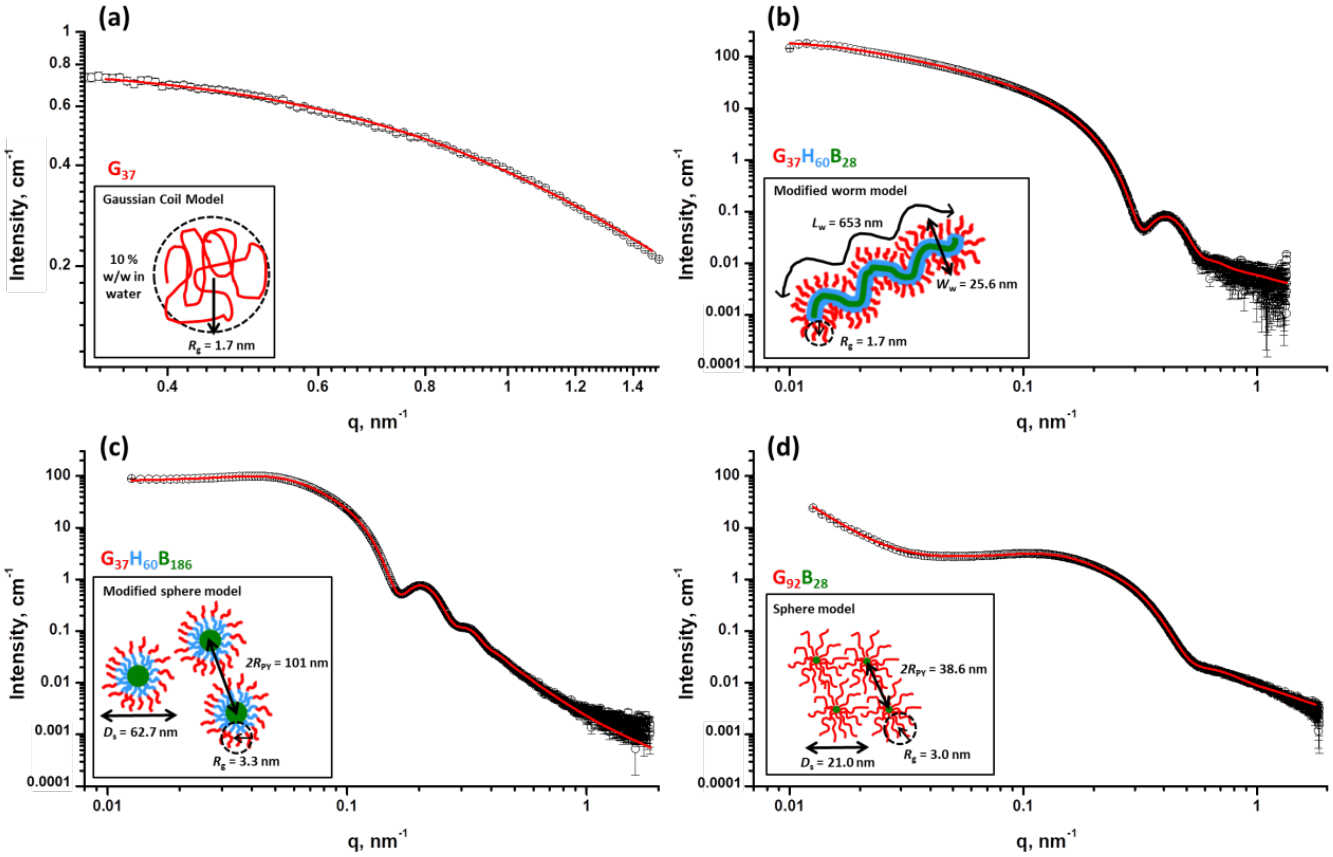

Figure 3.8. SAXS data (open black circles) and fits (red lines) for (a) a G_{37} macro-CTA and dilute aqueous dispersions of (b) $G_{37}H_{60}B_{28}$ triblock copolymer worms, (c) $G_{37}H_{60}B_{186}$ triblock copolymer spheres and (d) $G_{92}B_{28}$ diblock copolymer spheres. Insets: schematic cartoons of the corresponding morphologies, where L_w = the contour length of the worm, W_w = width of the worm, R_g = radius of gyration, D_s = diameter of the sphere and R_{PY} = Percus-Yevick correlation radius of densely-packed spheres (see Table 3.2).

Table 3.2. Structural parameters obtained from SAXS analysis of a series of five block copolymers in water using appropriate sphere and worm models. Representative parameters are denoted as follows: V_{PGMA}, V_{PHPMA} and V_{PBzMA} are the volumes of the PGMA, PHPMA and PBzMA blocks, respectively, R_g represents the radius of gyration of the G_{37} (or G_{92}) corona chains, x_{sol} denotes the volume fraction of solvent in the core, and η represents the volume fraction of the PHPMA block located within the core domain. For the worm models: L_w is the mean worm contour length, L_k is the mean worm Kuhn length and R_{sw} represents the radius of the worm core cross-section. For the sphere models: R_s is the sphere core radius and σ_{Rs} is the standard deviation of the sphere core radius. A related homopolymer precursor (G_{37}) was also analysed using a Gaussian coil model.

Copolymer Composition	Model used for fitting	V_{PGMA} / Å^3	V_{PHPMA}/ Å^3	V_{PBzMA}/ Å^3	Volume fraction	R_s / nm	σ_{Rs} / nm	L_w / nm	L_k / nm	R_g / nm	x_{sol}	η
G_{37}	Gaussian coil[51]	7512			0.16300					1.69 ± 0.08		
$G_{37}H_{60}B_{28}$	worm[40, 53]	7512	11871	14515	0.00973	9.36*	0.84	653	163	1.74	0.031	
$G_{37}H_{60}B_{28}$	modified worm				0.00946	9.37*	0.84	653	163	1.73	0.010	1.00
$G_{37}H_{60}B_{186}$	sphere[39, 40]	7512	11871	57443	0.00883	24.49	2.69			1.80	0.000	
$G_{37}H_{60}B_{186}$	modified sphere				0.01080	24.67	2.70			3.33	0.001	0.62
$G_{92}B_{28}$	star-like sphere[48, 54]	18678		8647	0.00746	4.549	0.70			3.02		

*These radii correspond to R_{sw} (the radius of the worm core cross-section).

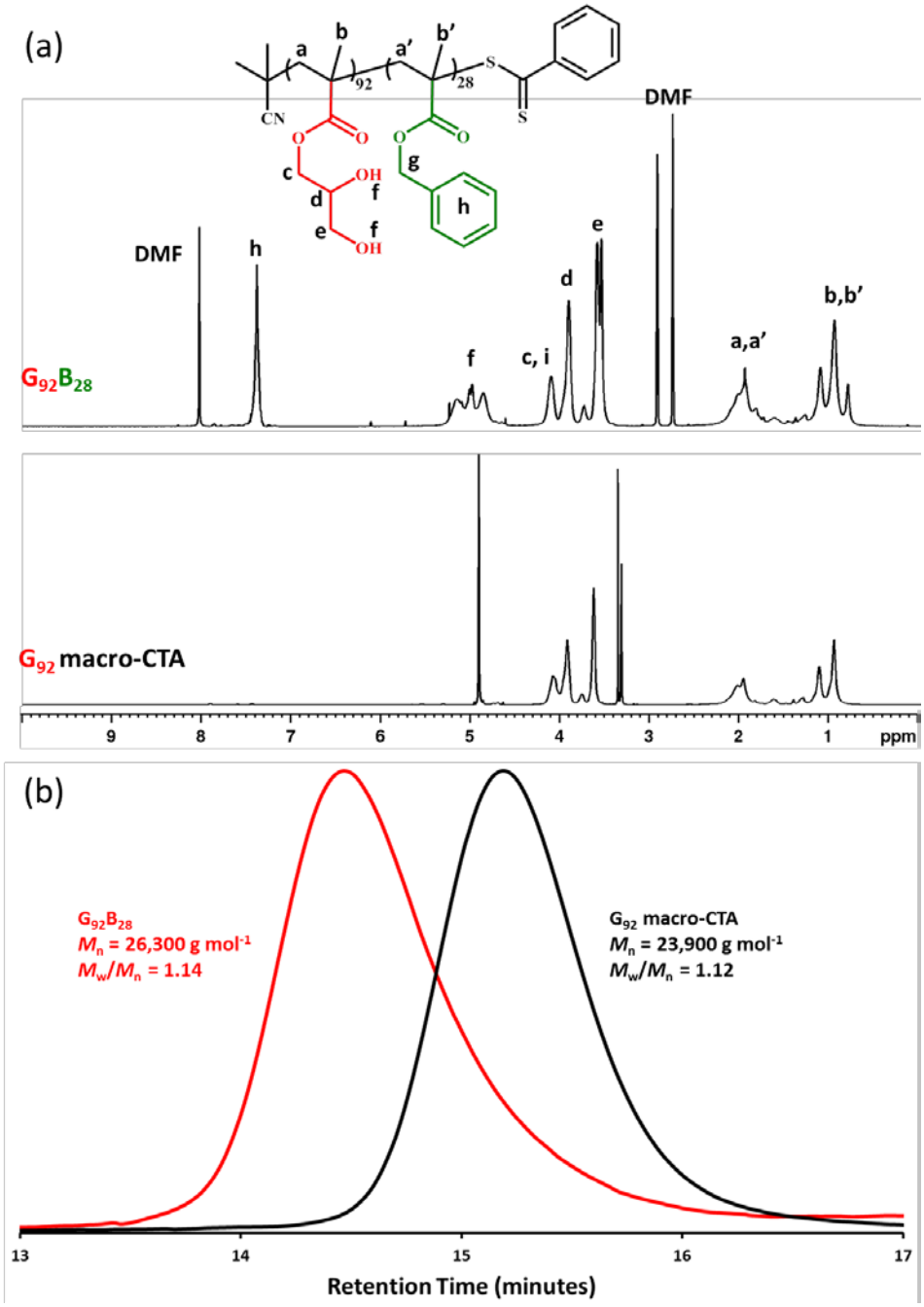

Figure 3.9. (a) Assigned ^{1}H NMR spectra obtained for a G_{92} macro-CTA (d_4-CD_3OD) and a $G_{92}B_{28}$ diblock copolymer (d_7-DMF). (b) DMF GPC curves *vs.* poly(methyl methacrylate) (PMMA) standards obtained for a G_{92} macro-CTA and a $G_{92}B_{28}$ diblock copolymer.

SAXS analysis confirmed that spheres are indeed formed with the gradient of the SAXS pattern tending to zero in the low *q* region, which is characteristic of spheres.[47] Analysis of this SAXS pattern using a star-like micelle model[48, 54] provided a satisfactory data fit over five orders of magnitude of X-ray

scattering intensity (see Figure 3.8d). The mean sphere diameter, D_s, was calculated to be 21.0 ± 1.4 nm, which is comparable to that suggested by DLS, while the R_g of the G_{92} corona block for this $G_{92}B_{28}$ diblock copolymer was determined to be 3.0 nm. This experimental value is larger than the theoretical estimate (where R_g was calculated to be 2.45 nm) due to the star-like nature of the spheres. The spherical core diameter was determined to be 9.0 ± 1.4 nm, which is comparable to that estimated from TEM images. The correlation radius for densely-packed spheres, R_{PY}, was determined to be 19.3 nm. This is simply a consequence of the star-like nature of the former copolymer,[48, 55] which has a much higher effective volume fraction and hence a significantly lower critical overlap concentration. There is a significant upturn in the X-ray scattered intensity at low q (below 0.017 nm^{-1}; see Figure 3.8d). This could indicate the formation of aggregates (or mass fractals) most likely due to the extensive overlap between stabiliser chains of the micelles. The formation of spherical star-like micelles by this $G_{92}B_{28}$ diblock copolymer suggests that an intermediate PHPMA block is an essential prerequisite for obtaining a worm morphology. A reasonable explanation for this unexpected observation is outlined in Figure 3.7.

Millimetre-Sized Pickering Emulsion Droplets

Recently, Thompson *et al*. reported that $G_{45}H_{200}$ diblock copolymer vesicles were unstable with respect to dissociation when used as a Pickering emulsifier. However, chemical crosslinking of such vesicles using ethylene glycol dimethacrylate as a third block dramatically improved their stability towards high-shear homogenisation: TEM studies of dried emulsion droplets confirmed that such covalently-stabilised vesicles were adsorbed intact at the oil-water interface.[56] More recently, Thompson *et al*. reported that $G_{45}H_{140}$ diblock copolymer worms similarly could not withstand high-shear homogenisation, whereas $G_{37}H_{60}B_{30}$ triblock copolymer worms proved to be highly efficient Pickering emulsifiers.[36] Moreover, DLS studies showed that the former worms were thermo-responsive, as expected based on previous work by Verber *et al*.[30] In contrast, the $G_{37}H_{60}B_{30}$ triblock copolymer worms were *not* thermo-

responsive; this indicates that introducing the more hydrophobic PBzMA block stabilises the worm morphology.

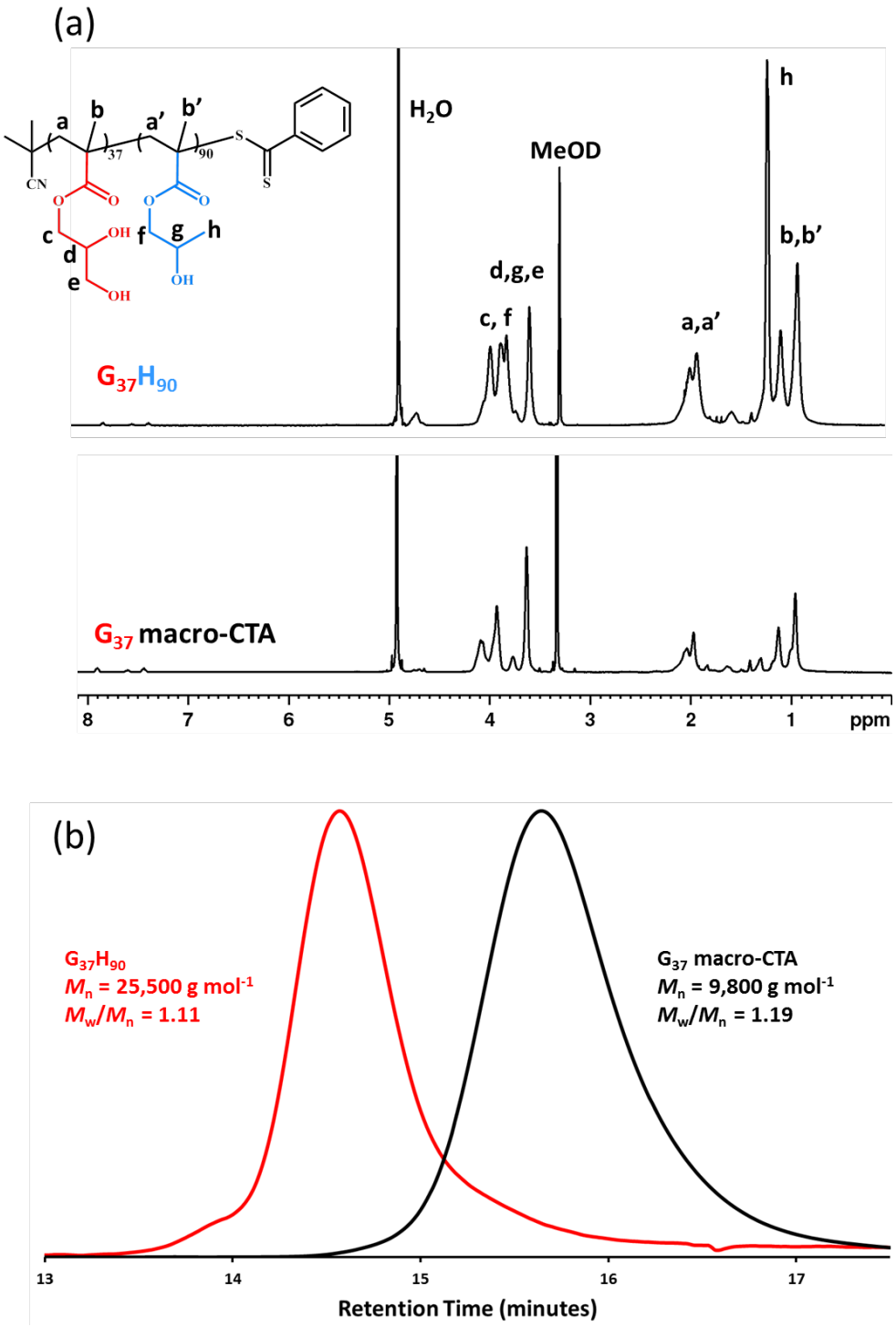

Figure 3.10. (a) Assigned ^{1}H NMR spectra (d_4-CD_3OD) obtained for a G_{37} macro-CTA and a $G_{37}H_{90}$ diblock copolymer. (b) DMF GPC curves [*vs.* poly(methyl methacrylate) (PMMA) standards] obtained for a G_{37} macro-CTA and a $G_{37}H_{90}$ diblock copolymer.

In the present study, we have used RAFT aqueous dispersion polymerisation (see Figure 3.2a) to prepare $G_{37}H_{90}$ diblock copolymer worms, which were designed to be analogous to the $G_{37}H_{60}B_{28}$ triblock copolymer worms. ^{1}H NMR studies confirmed that more than 99 % HPMA conversion was achieved after 2 h at 70 ^{o}C (see Figure 3.10a). GPC studies indicated that a near-monodisperse diblock copolymer was obtained with a high blocking efficiency and minimal macro-CTA contamination (M_w/M_n = 1.11; see Figure 3.10b and Table 3.1). DLS studies (see Table 3.1) and TEM images (see Figure 3.5) were consistent with the targeted pure worm morphology.

Incorporating the highly hydrophobic PBzMA block enables the $G_{37}H_{60}B_{28}$ worms to act as an effective Pickering emulsifier. Previously, we reported that $G_{37}H_{60}B_{28}$ worms can survive the high-shear homogenisation conditions required for emulsification, whereas $G_{45}H_{140}$ worms undergo dissociation to form individual copolymer chains under these conditions.[36] In the present study, we examined homogenisation under much lower shear conditions, *i.e*. hand-shaking.

More specifically, both $G_{37}H_{60}B_{28}$ and $G_{37}H_{90}$ worms were evaluated as putative Pickering emulsifiers for the stabilisation of *n*-dodecane emulsion droplets in water. Aqueous worm dispersions (1.88 x 10^{-3} to 1.00 % w/w) were hand-shaken with 20 vol % *n*-dodecane for two min at 20 ^{o}C to produce emulsions. In order to examine whether the worms were adsorbed intact at the oil-water interface, optical microscopy (OM) and laser diffraction were used to determine the mean oil droplet diameters (see Figure 3.11). According to OM studies, the oil droplets became larger as the $G_{37}H_{60}B_{28}$ worm concentration was lowered, as shown in Figure 3.11a. These observations were corroborated by laser diffraction studies: the mean oil droplet diameter increased from 115 to 483 μm as the worm dispersion concentration was reduced from 1.00 to 0.0075 % w/w (see Figure 3.11c). This concentration-dependent behaviour is consistent with the formation of genuine Pickering emulsions (see Figure 3.12).[5, 57-59] This was expected because Thompson *et al*. recently reported that such triblock copolymer worms can withstand high-shear homogenisation, so they should also survive low-shear homogenisation.[36]

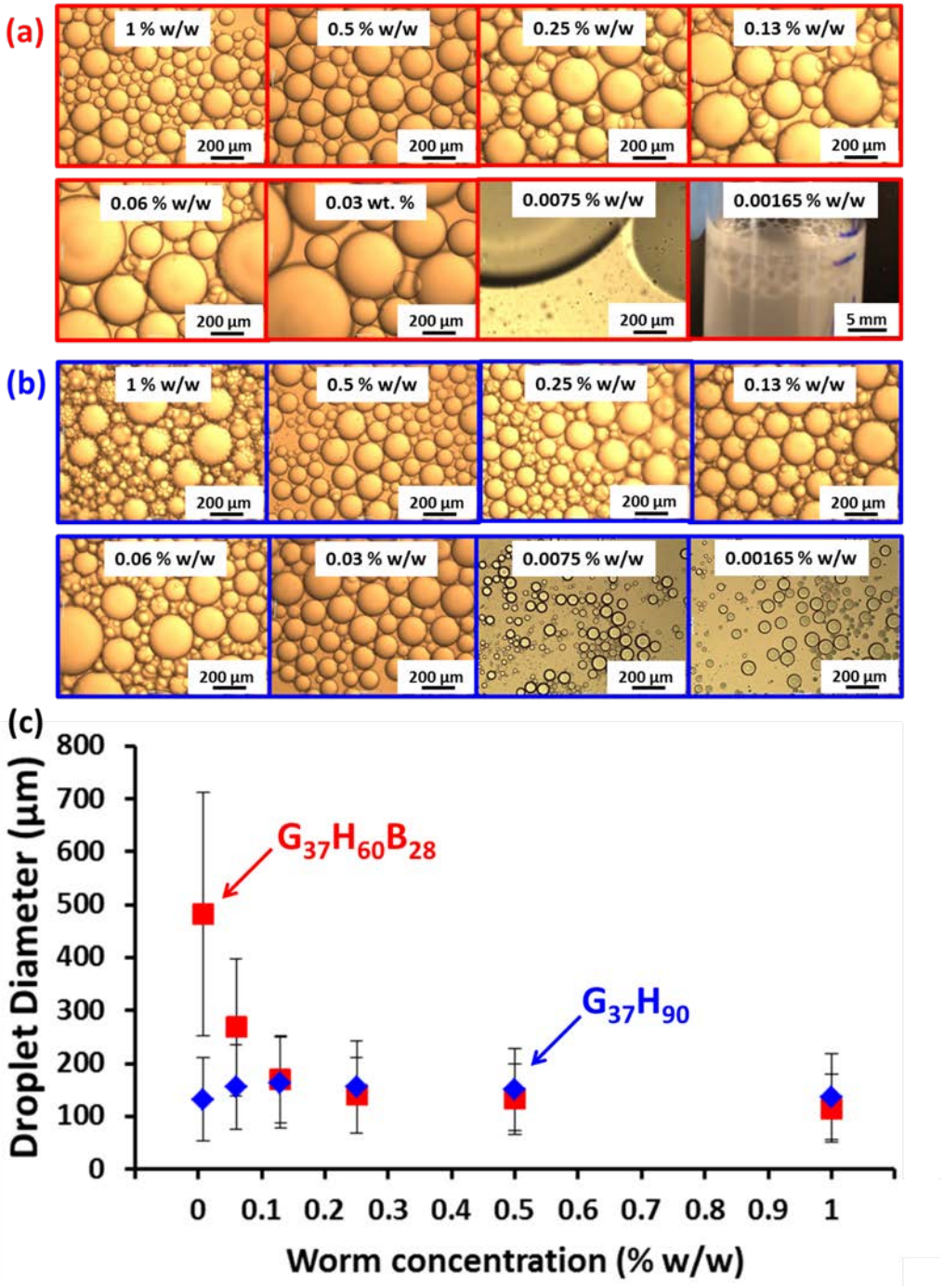

Figure 3.11. Optical microscopy images obtained for *n*-dodecane-in-water emulsion droplets prepared using either (a) $G_{37}H_{60}B_{28}$ or (b) $G_{37}H_{90}$ worms under low-shear conditions (*i.e.* hand-shaking). (c) Plots of mean droplet diameter (obtained by laser diffraction) *vs.* worm concentration for emulsions prepared by hand-shaking dilute aqueous dispersions of $G_{37}H_{60}B_{28}$ worms (red, ■) and $G_{37}H_{90}$ worms (blue, ♦) with 20 volume % *n*-dodecane.

It is worth emphasising that the mean oil droplet diameters are much larger when using hand-shaking for emulsification (approximately 115 µm at 1.00 % w/w) compared to those obtained using high-shear homogenisation (approximately 45 µm at 1.00 % w/w).[36] When the worm dispersion

concentration was lowered to 1.88 x 10^{-3} % w/w, the oil droplets proved to be too unstable to be assessed by laser diffraction. However, the droplet diameter was estimated (from digital photographs recorded immediately after emulsification) to be 1.11 ± 0.42 mm (based on measuring 120 droplets). Droplet coalescence occurs within a few hours, but reconstitution of the original emulsions can be achieved *via* further hand-shaking. This differs from the highly stable millimetre-sized emulsions prepared using partially hydrophobised silica particles reported by Arditty *et al.*[60] The instability observed in the present work suggests that worm desorption occurs; similar observations have been recently reported by Rizelli and co-workers for worm-stabilised Pickering non-aqueous emulsions.[61] In contrast, it is emphasised that the finer o/w emulsions prepared at higher worm concentrations (≥ 0.03 % w/w) remain stable indefinitely.

In contrast, both OM and laser diffraction studies indicated that the mean oil droplet diameter remained relatively constant on lowering the concentration of the $G_{37}H_{90}$ worms, (Figure 3.11b and Figure 3.11c). This indicates that these worms are so delicate that they cannot survive even low-shear hand-shaking. Instead, dissociation to form individual $G_{37}H_{90}$ copolymer chains occurs, which then adsorb at the oil-water interface to stabilise the oil droplets (see Figure 3.12). Again, mean oil droplet diameters were significantly larger (~ 136 μm) than those reported previously when using high-shear homogenisation (~ 45 μm).

For emulsions stabilised using either $G_{37}H_{90}$ or $G_{37}H_{60}B_{28}$ worms, creaming of the low-density oil droplet phase occurred on standing for 24 h at 20 ^{o}C. The lower aqueous phase, which contained excess non-adsorbed copolymer, was carefully removed and analysed by DLS to examine whether the worms remained intact after hand-shaking. DLS studies of the $G_{37}H_{90}$ aqueous phase indicated a hydrodynamic diameter of 41 nm (polydispersity = 0.18) and a much lower count rate (2,500 kcps) than that observed for the original worms (37,000 kcps). This 93 % reduction in count rate is fully consistent with substantial worm dissociation during hand-shaking. In contrast, DLS studies of the aqueous phase removed from the $G_{37}H_{60}B_{28}$–stabilised emulsion indicated an apparent hydrodynamic diameter of 153 nm, a polydispersity of 0.23 and

count rate of 21,000 kcps, which are comparable to the DLS data obtained before emulsification. These observations confirm that these $G_{37}H_{60}B_{28}$ worms remain intact after emulsification *via* hand-shaking.

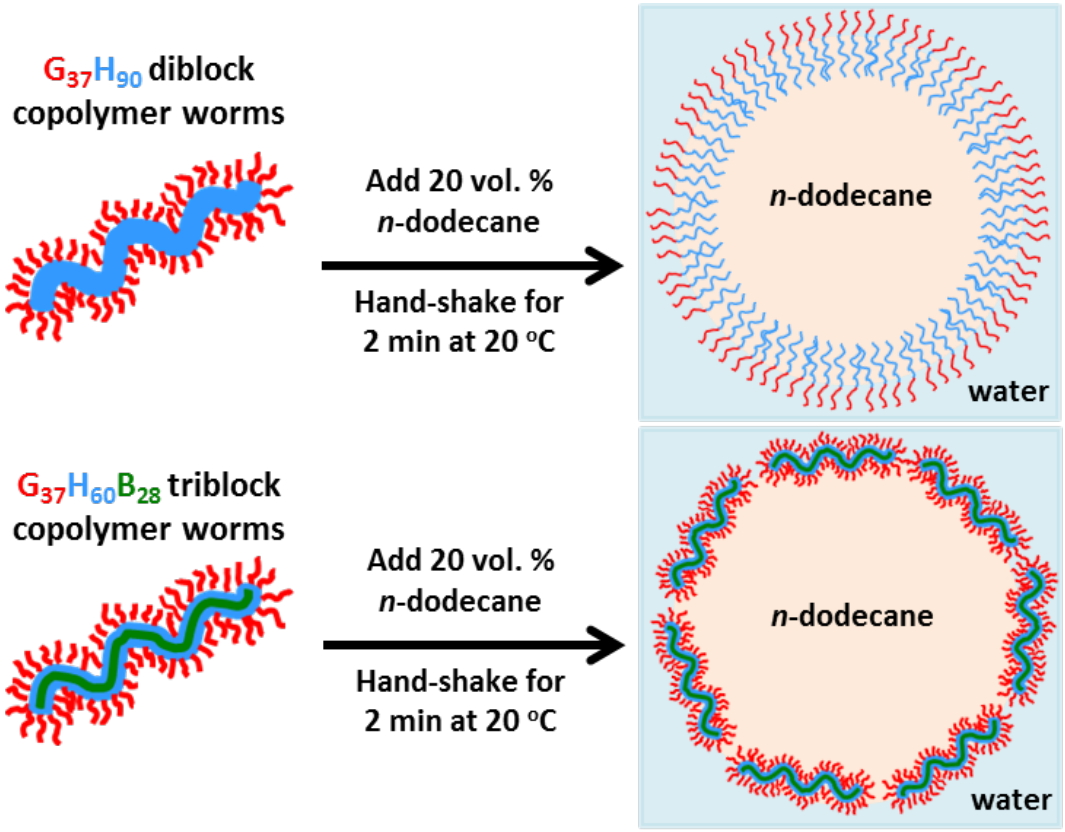

Figure 3.12. Schematic illustration of the attempted formation of Pickering emulsions using either $G_{37}H_{90}$ or $G_{37}H_{60}B_{28}$ worms under low-shear conditions (*i.e.* hand-shaking).

Finally, closely-related emulsions were prepared using *n*-hexane instead of *n*-dodecane to enable more convenient removal of the oil phase via evaporation at ambient temperature. Figure 3.13 shows TEM images obtained from emulsions prepared using the $G_{37}H_{60}B_{28}$ and $G_{37}H_{90}$ worms. In the latter case, the surface of the dried emulsion droplet is smooth and featureless, with no evidence for any adsorbed nanoparticles (see Figure 3.13a). Similar TEM observations were reported for both $G_{45}H_{150}$ diblock copolymer worms and $G_{45}H_{200}$ diblock copolymer vesicles in previous studies of shear-induced dissociation of diblock copolymer nano-objects.[36, 56]

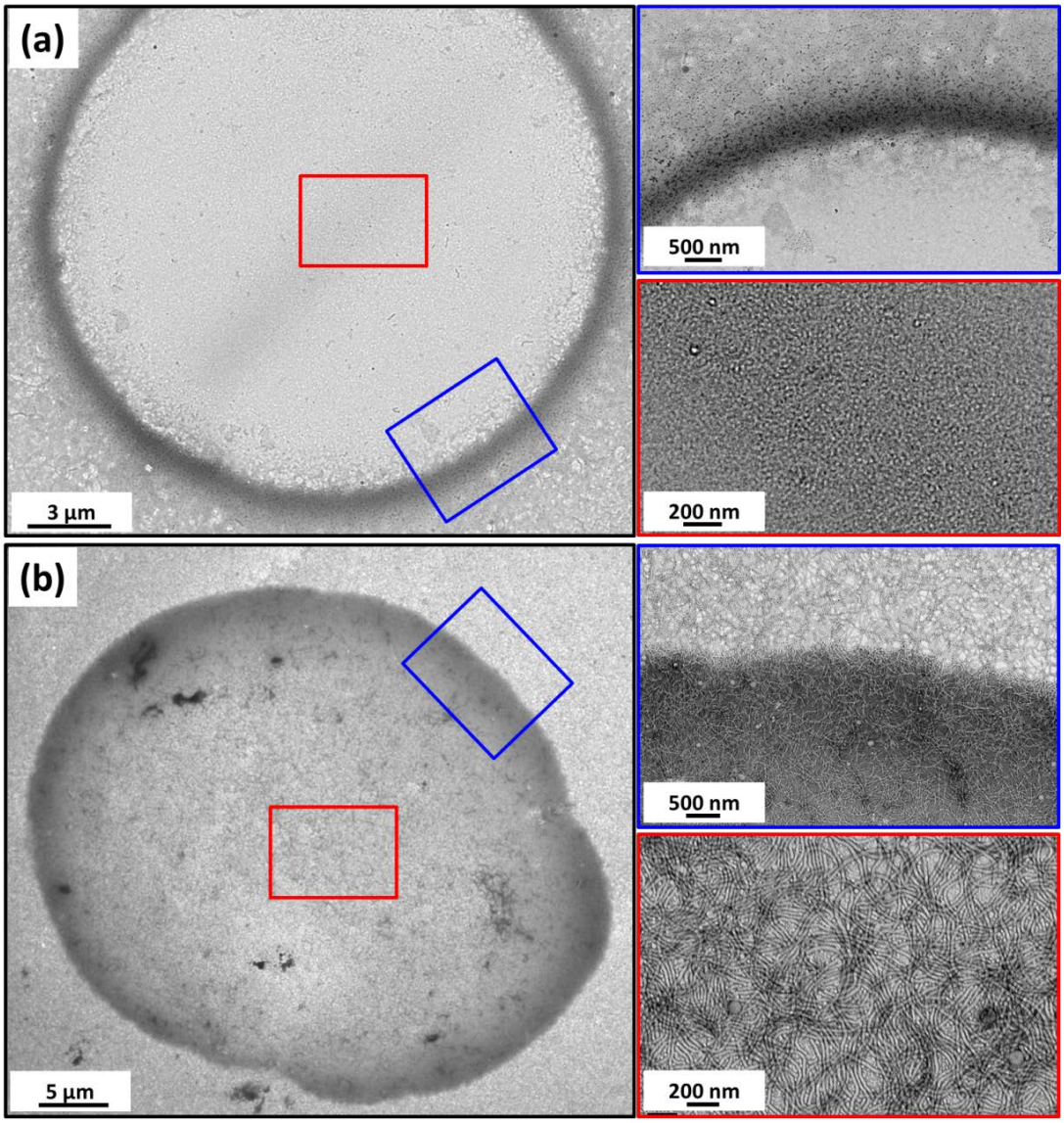

Figure 3.13. TEM images obtained for *n*-hexane-in-water emulsion droplets dried at 20 °C using (a) 0.25 % w/w $G_{37}H_{90}$ diblock copolymer worms and (b) 0.25 % w/w $G_{37}H_{60}B_{28}$ triblock copolymer worms. The edge (blue) and top-surface (red) of the dried emulsion droplets are shown at higher magnification on the right-hand side. No worms are visible when using the $G_{37}H_{90}$ diblock copolymer since this undergoes dissociation even during low-shear homogenisation (hand-shaking). In contrast, worms are clearly discernible when using the $G_{37}H_{60}B_{28}$ triblock copolymer, indicating that a genuine Pickering emulsion had been obtained.

In contrast, the dried emulsions prepared using the $G_{37}H_{60}B_{28}$ worms clearly comprise intact worms adsorbed at the oil-water interface (see Figure 3.13b). Thus, all the experimental evidence suggests that, regardless of their morphology, G_xH_y nanoparticles are not sufficiently robust to survive emulsification under any conditions, even low-shear hand-shaking. However, incorporating highly hydrophobic PBzMA as a third block, produces much

more robust worms that can withstand high-shear homogenisation and allow the formation of millimetre-sized emulsion droplets.

Conclusions

A series of PGMA-PHPMA-PBzMA triblock copolymer nano-objects have been prepared in concentrated aqueous solution *via* polymerisation-induced self-assembly (PISA). For certain triblock compositions, highly anisotropic worm-like nanoparticles can be obtained with a mean contour length of 653 nm as determined by SAXS studies. Surprisingly, chain extension of the hydrophobic core-forming block of these worm-like nanoparticles does *not* lead to vesicle formation, with spherical micelles being formed instead. SAXS and ^{1}H NMR studies shed some light on these unexpected observations, which are best explained by considering changes in the relative enthalpic incompatibilities between the PGMA, PHPMA and PBzMA blocks during the *in situ* growth of the latter block. In particular, SAXS data fits suggest that the effective R_g of the corona block actually *increases* as the PGMA-PHPMA diblock copolymer is chain-extended with BzMA, even though the *same* diblock precursor was used for all copolymer syntheses. Thus, at least some fraction of the partially hydrated PHPMA blocks must be gradually driven out of the increasingly hydrophobic core to become co-located with the hydrophilic PGMA stabiliser chains in the corona. SAXS analysis suggests that approximately one-third of the HPMA units are displaced from the particle cores via this mechanism. This counter-intuitive finding highlights the subtle switch from weak to strong segregation between incompatible blocks and its hitherto unappreciated effect on the evolution in copolymer morphology during PISA.

Finally, the PGMA-PHPMA-PBzMA triblock copolymer worms were evaluated as Pickering emulsifiers for *n*-dodecane oil droplets in water. Unlike the PGMA-PHPMA diblock copolymer worms reported previously,[36] these triblock worms do not exhibit thermo-responsive behaviour. However, they are much more robust when subjected to high-shear, which makes them much more effective Pickering emulsifiers. Low-shear emulsification (hand-shaking) enables the formation of metastable millimetre-sized oil droplets.

References

1. S. U. Pickering, *Journal of the Chemical Society*, 1907, **91**, 2001-2021.
2. S. Levine, B. D. Bowen and S. J. Partridge, *Colloids and Surfaces*, 1989, **38**, 325-343.
3. B. P. Binks and S. O. Lumsdon, *Physical Chemistry Chemical Physics*, 1999, **1**, 3007-3016.
4. B. P. Binks and S. O. Lumsdon, *Physical Chemistry Chemical Physics*, 2000, **2**, 2959-2967.
5. B. P. Binks and C. P. Whitby, *Langmuir*, 2004, **20**, 1130-1137.
6. F. Gautier, M. Destribats, R. Perrier-Cornet, J.-F. Dechezelles, J. Giermanska, V. Heroguez, S. Ravaine, F. Leal-Calderon and V. Schmitt, *Physical Chemistry Chemical Physics*, 2007, **9**, 6455-6462.
7. B. P. Binks and S. O. Lumsdon, *Langmuir*, 2001, **17**, 4540-4547.
8. K. L. Thompson, S. P. Armes, D. W. York and J. A. Burdis, *Macromolecules*, 2010, **43**, 2169-2177.
9. K. L. Thompson, S. P. Armes, J. R. Howse, S. Ebbens, I. Ahmad, J. H. Zaidi, D. W. York and J. A. Burdis, *Macromolecules*, 2010, **43**, 10466-10474.
10. A. Walsh, K. L. Thompson, S. P. Armes and D. W. York, *Langmuir*, 2010, **26**, 18039-18048.
11. S. Cauvin, P. J. Colver and S. A. F. Bon, *Macromolecules*, 2005, **38**, 7887-7889.
12. S. A. F. Bon and P. J. Colver, *Langmuir*, 2007, **23**, 8316-8322.
13. Y. Cui, M. Threlfall and J. S. van Duijneveldt, *Journal of Colloid and Interface Science*, 2011, **356**, 665-671.
14. Y. Cui and J. S. van Duijneveldt, *Langmuir*, 2012, **28**, 1753-1757.
15. Y. Yang, Y. Ning, C. Wang and Z. Tong, *Polymer Chemistry*, 2013, **4**, 5407-5415.
16. K. L. Thompson, L. A. Fielding, O. O. Mykhaylyk, J. A. Lane, M. J. Derry and S. P. Armes, *Chemical Science*, 2015, **6**, 4207-4214.
17. K. L. Thompson, C. J. Mable, J. A. Lane, M. J. Derry, L. A. Fielding and S. P. Armes, *Langmuir*, 2015, **31**, 4137-4144.
18. P. F. Noble, O. J. Cayre, R. G. Alargova, O. D. Velev and V. N. Paunov, *Journal Of The American Chemical Society*, 2004, **126**, 8092-8093.
19. I. Kalashnikova, H. Bizot, B. Cathala and I. Capron, *Langmuir*, 2011, **27**, 7471-7479.
20. I. Kalashnikova, H. Bizot, B. Cathala and I. Capron, *Biomacromolecules*, 2012, **13**, 267-275.
21. I. Kalashnikova, H. Bizot, P. Bertoncini, B. Cathala and I. Capron, *Soft Matter*, 2013, **9**, 952-959.
22. H. A. Wege, S. Kim, V. N. Paunov, Q. Zhong and O. D. Velev, *Langmuir*, 2008, **24**, 9245-9253.
23. B. Madivala, S. Vandebril, J. Fransaer and J. Vermant, *Soft Matter*, 2009, **5**, 1717-1727.
24. A. Blanazs, R. Verber, O. O. Mykhaylyk, A. J. Ryan, J. Z. Heath, C. W. I. Douglas and S. P. Armes, *Journal Of The American Chemical Society*, 2012, **134**, 9741–9748.
25. M. Semsarilar, E. R. Jones, A. Blanazs and S. P. Armes, *Advanced Materials (Weinheim, Germany)*, 2012, **24**, 3378-3382.
26. L. A. Fielding, M. J. Derry, V. Ladmiral, J. Rosselgong, A. M. Rodrigues, L. P. D. Ratcliffe, S. Sugihara and S. P. Armes, *Chemical Science*, 2013, **4**, 2081-2087.
27. V. J. Cunningham, A. M. Alswieleh, K. L. Thompson, M. Williams, G. J. Leggett, S. P. Armes and O. M. Musa, *Macromolecules*, 2014, **47**, 5613-5623.

28. N. J. Warren, O. O. Mykhaylyk, A. J. Ryan, M. Williams, T. Doussineau, P. Dugourd, R. Antoine, G. Portale and S. P. Armes, *Journal Of The American Chemical Society*, 2015, **137**, 1929-1937.
29. Y.-Y. Won, H. T. Davis and F. S. Bates, *Science*, 1999, **283**, 960-963.
30. R. Verber, A. Blanazs and S. P. Armes, *Soft Matter*, 2012, **8**, 9915-9922.
31. E. R. Jones, M. Semsarilar, A. Blanazs and S. P. Armes, *Macromolecules*, 2012, **45**, 5091-5098.
32. L. A. Fielding, J. A. Lane, M. J. Derry, O. O. Mykhaylyk and S. P. Armes, *Journal Of The American Chemical Society*, 2014, **136**, 5790-5798.
33. M. J. Derry, L. A. Fielding and S. P. Armes, *Polymer Chemistry*, 2015, **6**, 3054-3062.
34. A. Blanazs, J. Madsen, G. Battaglia, A. J. Ryan and S. P. Armes, *Journal Of The American Chemical Society*, 2011, **133**, 16581-16587.
35. A. Blanazs, A. J. Ryan and S. P. Armes, *Macromolecules*, 2012, **45**, 5099-5107.
36. K. L. Thompson, C. J. Mable, A. Cockram, N. J. Warren, V. J. Cunningham, E. R. Jones, R. Verber and S. P. Armes, *Soft Matter*, 2014, **10**, 8615-8626.
37. J. Ilavsky and P. R. Jemian, *Journal of Applied Crystallography*, 2009, **42**, 347-353.
38. N. J. Warren and S. P. Armes, *Journal Of The American Chemical Society*, 2014, **136**, 10174-10185.
39. J. S. Pedersen, *Journal of Applied Crystallography*, 2000, **33**, 637-640.
40. J. S. Pedersen and P. Schurtenberger, *Macromolecules*, 1996, **29**, 7602-7612.
41. V. J. Cunningham, L. P. D. Ratcliffe, A. Blanazs, N. J. Warren, A. J. Smith, O. O. Mykhaylyk and S. P. Armes, *Polymer Chemistry*, 2014, **5**, 6307-6317.
42. L. J. Fetters, D. J. Lohse and R. H. Colby, in *Physical Properties of Polymers Handbook*, ed. J. Mark, Springer New York, 2007, DOI: 10.1007/978-0-387-69002-5_25, ch. 25, pp. 447-454.
43. A. Blanazs, S. P. Armes and A. J. Ryan, *Macromolecular Rapid Communications*, 2009, **30**, 267-277.
44. B. Charleux, G. Delaittre, J. Rieger and F. D'Agosto, *Macromolecules*, 2012, **45**, 6753-6765.
45. X. Zhang, S. Boissé, W. Zhang, P. Beaunier, F. D'Agosto, J. Rieger and B. Charleux, *Macromolecules*, 2011, **44**, 4149-4158.
46. W. Zhang, F. D'Agosto, O. Boyron, J. Rieger and B. Charleux, *Macromolecules*, 2012, **45**, 4075-4084.
47. O. Glatter and O.Kratky, *Small-angle X-ray Scattering*, Academic Press, London, 1982.
48. J. S. Pedersen and M. C. Gerstenberg, *Macromolecules*, 1996, **29**, 1363-1365.
49. J. N. Israelachvili, D. J. Mitchell and B. W. Ninham, *Journal of the Chemical Society, Faraday Transactions 2: Molecular and Chemical Physics*, 1976, **72**, 1525-1568.
50. Proton and carbon NMR spectroscopy studies were performed in deuterium oxide in order to attempt to monitor any changes in the degree of solvation of the core-forming PHPMA block as a function of target DP. In situ proton NMR experiments in deuterium oxide were also conducted whereby the PGMA-PHPMA diblock copolymer precursor was chain-extended with BzMA. Unfortunately, in all cases, the PGMA and PHPMA signals were poorly resolved and prevented meaningful analysis. Peak overlap is even more problematic since both the GMA and HPMA residues are present in two isomeric forms. Therefore, NMR spectroscopy is of no use in this particular case.

51. B. Hammouda, *Probing Nanoscale Structures - The SANS Toolbox*, National Institute of Standards and Technology, 2008.
52. C. J. Mable, N. J. Warren, K. L. Thompson, O. O. Mykhaylyk and S. P. Armes, *Chemical Science*, 2015, **6**, 6179-6188.
53. J. Pedersen, *Journal of Applied Crystallography*, 2000, **33**, 637-640.
54. D. J. Growney, O. O. Mykhaylyk, T. Derouineau, L. A. Fielding, A. J. Smith, N. Aragrag, G. D. Lamb and S. P. Armes, *Macromolecules*, 2015, **48**, 3691-3704.
55. A. S. Lee, A. P. Gast, V. Bütün and S. P. Armes, *Macromolecules*, 1999, **32**, 4302-4310.
56. K. L. Thompson, P. Chambon, R. Verber and S. P. Armes, *Journal Of The American Chemical Society*, 2012, **134**, 12450-12453.
57. B. P. Binks and S. O. Lumsdon, *Langmuir*, 2000, **16**, 8622-8631.
58. B. P. Binks, *Current Opinion in Colloid & Interface Science*, 2002, **7**, 21-41.
59. R. Aveyard, B. P. Binks and J. H. Clint, *Advances in Colloid and Interface Science*, 2003, **100-102**, 503-546.
60. S. Arditty, C. P. Whitby, B. P. Binks, V. Schmitt and F. Leal-Calderon, *The European Physical Journal E*, 2003, **11**, 273-281.
61. S. L. Rizzelli, E. R. Jones, K. L. Thompson and S. P. Armes, *Colloid And Polymer Science*, 2015, **294**, 1-12.

Chapter Four - Loading of Silica Nanoparticles in Block Copolymer Vesicles During PISA: Encapsulation Efficiency and Thermally Triggered Release

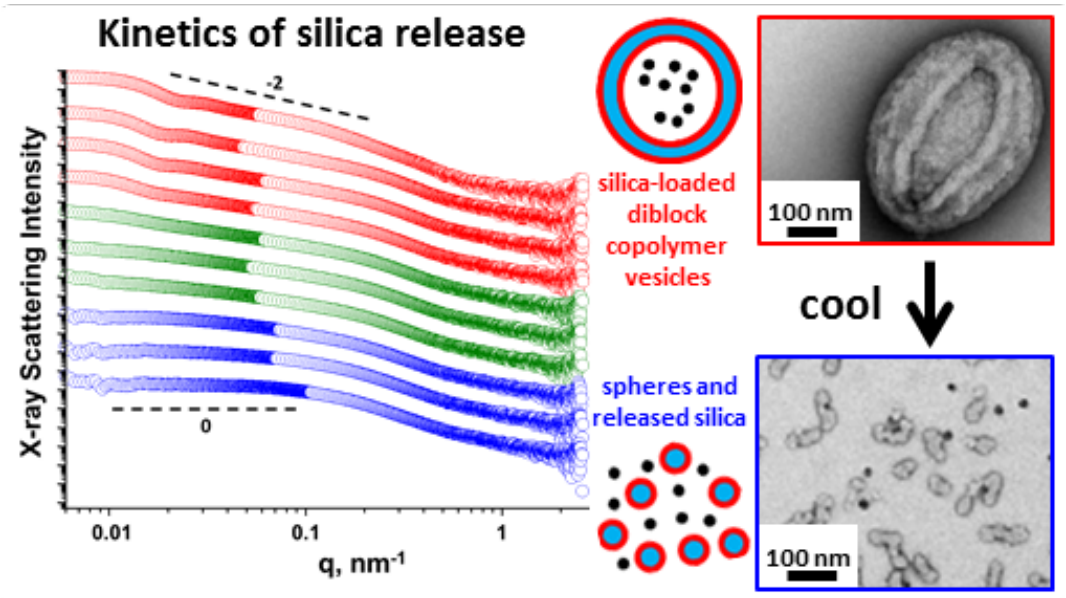

Introduction

Microcompartmentalisation is widely acknowledged to be a fundamental prerequisite for life on Earth.[1-4] Many intracellular processes require spatial separation of components via impermeable lipid membranes, with membrane proteins allowing the selective diffusion of various chemical species in and out of cells.[5] Similarly, microencapsulation is important for many industrial formulations, ranging from orally-administered drugs[6] to agrochemicals[7, 8] and laundry products.[9, 10] This enables the controlled release of active components and can also prevent the premature deactivation of mutually incompatible components, such as enzyme denaturation by bleach chemicals in liquid laundry products. In particular, liposomes[11] and block copolymer vesicles[12-19] (or 'polymersomes') are some of the most widely used carriers in the development of drug delivery applications.[20-22] Typically, such hollow nanoparticles are loaded with water-soluble drugs,[23-25] oligonucleotides,[25-27] enzymes[28] or antibodies.[29] In this context, there are also a few reports describing the incorporation of magnetic nanoparticles within block copolymer vesicle membranes, which may enable active targeting of tumors.[30]

Over the last five years or so, polymerisation-induced self-assembly (PISA) has become established as a powerful tool for the rational design and efficient synthesis of a wide range of diblock copolymer nano-objects in either aqueous or non-aqueous media.[31-33] Of particular relevance to the present study, RAFT aqueous dispersion polymerisation can be utilised to prepare block copolymer vesicles at copolymer concentrations of up to 25 % w/v solids.[34-38] Periodic sampling during such syntheses has confirmed a progressive evolution in copolymer morphology, with transmission electron microscopy (TEM) studies revealing that the transformation of highly anisotropic worms into well-defined vesicles proceeds via a so-called 'jellyfish' intermediate.[35] These observations suggest an intriguing question: can the efficient encapsulation of nanoparticles within the vesicles be achieved *during* such PISA syntheses? This question is directly addressed herein, with an aqueous silica sol being selected as a model cargo. These nanoparticles were chosen for the following five reasons: (i) they are commercially available in the form of concentrated dispersions; (ii) they possess sufficient electron contrast to allow their visualisation by TEM; (iii) they are relatively strong X-ray scatterers; (iv) their density is sufficiently high to aid sedimentation-based particle size analysis; (v) their

encapsulation efficiency can be readily determined using thermogravimetry. Moreover, Rose and co-workers[39] have recently reported that silica nanoparticles enable the convenient repair of cleaved synthetic hydrogels or biological tissue (e.g. organs such as the liver). Hence such silica nanoparticles are likely to be a biomedically relevant *active* species, in addition to serving as a model cargo.

In the present study, a series of silica-loaded AB diblock copolymer vesicles were readily prepared via RAFT aqueous dispersion polymerisation[36, 37, 40] by chain-extending a water-soluble poly(glycerol monomethacrylate) (PGMA) macromolecular chain transfer agent (macro-CTA) using 2-hydroxypropyl methacrylate (HPMA) in the presence of varying concentrations of aqueous silica nanoparticles.

Provided that an appropriate diblock copolymer composition is targeted, the resulting amphiphilic PGMA-PHPMA diblock copolymer chains undergo *in situ* self-assembly via a complex multi-step mechanism that ultimately leads to the formation of large polydisperse vesicles.[35] An open-ended 'jellyfish' structure is generated just prior to vesicle formation,[35] hence silica nanoparticles can diffuse within the 'jellyfish' before membrane formation is complete, leading to their *in situ* encapsulation. It is perhaps worth emphasising that vesicle formation via this pathway circumvents the problem of encapsulation discussed by Adams et al. for vesicles prepared via post-polymerisation processing of preformed diblock copolymers.[41]

Experimental Details

Materials

All reagents were used as received unless otherwise stated. 4, 4'-Azobis-4-cyanopentanoic acid (ACVA) and 2-cyano-2-propyl benzodithioate (CPDB) were purchased from Sigma-Aldrich (UK). Ethanol and dichloromethane were purchased from Fisher Scientific (UK). Glycerol monomethacrylate (GMA) was kindly donated by GEO Specialty Chemicals (Hythe, UK) and used without further purification. 2-Hydroxypropyl methacrylate (HPMA) was purchased from Alfa Aesar (UK) and contained 0.07 mol % dimethacrylate impurity, as judged by high performance liquid chromatography (HPLC). CD_3OD (^1H NMR solvent) was purchased from Goss Scientific (UK). Bindzil

CC401 colloidal silica (supplied as a 40 % w/w aqueous dispersion; manufacturer's nominal particle diameter = 12 nm) was kindly donated by AkzoNobel Pulp and Performance Chemicals AB (Sweden). Deionised water was obtained using an Elga Elgastat Option 3A water purifier; its pH was approximately 6.2 and its surface tension was 72.0 mN m^{-1} at 20 ^{o}C.

RAFT Synthesis of G_{58} Macro-CTA Agent in Ethanol

A round-bottomed flask was charged with GMA (30.0 g; 187 mmol), CPDB (0.823 g; 2.97 mmol), ACVA (167 mg, 0.156 mmol) and ethanol (39.2 g). The sealed reaction vessel was purged with N_2 for 30 min and placed in a pre-heated oil bath at 70 ^{o}C for 150 min with stirring. The resulting PGMA macro-CTA (GMA conversion = 80 %; M_n = 15,400 g mol^{-1}, M_w/M_n = 1.13) was purified by precipitation into excess dichloromethane. A mean DP of 58 was calculated for this macro-CTA using ^{1}H NMR spectroscopy by comparing the integral from 3.4 ppm to 4.3 ppm assigned to the five protons on the PGMA units with that of the aromatic signals at around 7 ppm assigned to the five protons on the RAFT CTA end-group.

Preparation of $G_{58}H_{250}$ Diblock Copolymer Precursor Vesicles via RAFT Aqueous Dispersion Polymerisation at 10 % w/w Solids in the Presence of 0 to 35 % w/w Silica

The protocol used for a silica concentration of 20 % w/w solids is shown here: G_{58} macro-CTA (0.200 g, 0.021 mmol), HPMA monomer (0.758 g, 5.26 mmol), CC401 silica sol (4.80 g, 40 % w/w in water) and deionised water (3.84 g) were weighed into a sample vial and purged with N_2 for 20 min. ACVA was added (1.18 mg, 0.0042 mmol, CTA/ACVA molar ratio = 5.0) and purged with N_2 for a further 10 min prior to immersion in an oil bath set at 70 ^{o}C for 2 h with stirring. Finally, the polymerisation was quenched by cooling to room temperature with subsequent exposure to air. Table 4.1 summarises the amounts of CC401 silica sol and deionised water used in various formulations.

Table 4.1. Silica sol and deionised water required to prepare a target silica concentration for in situ PISA encapsulation experiments.

Silica concentration during PISA (% w/w)	CC401 silica sol (g)	Deionised water (g)
0	0	8.63
5	1.20	7.43
10	2.40	6.23
15	3.60	5.04
20	4.80	3.84
25	6.00	2.64
30	7.19	1.44
35	8.39	0.24

^{1}H NMR Spectroscopy

All NMR spectra were recorded using a 400 MHz Bruker Avance-400 spectrometer and 64 scans were averaged per spectrum.

Gel Permeation Chromatography (GPC)

Copolymer molecular weights and polydispersities were determined using a DMF GPC set-up operating at 60 ^{o}C and comprising two Polymer Laboratories PL gel 5 μm Mixed C columns connected in series to a Varian 390 LC multi-detector suite (only the refractive index detector was utilised) and a Varian 290 LC pump injection module. The GPC eluent was HPLC-grade DMF containing 10 mM LiBr at a flow rate of 1.0 mL min^{-1}. DMSO was used as a flow-rate marker. Calibration was conducted using a series of ten near-monodisperse poly(methyl methacrylate) standards (M_n = 625 – 618,000 g mol^{-1}). The chromatograms were analysed using Varian Cirrus GPC software (version 3.3) provided by the instrument manufacturer (Polymer Laboratories).

Dynamic Light Scattering (DLS)

Intensity-average hydrodynamic diameters of the copolymer dispersions were determined at a scattering angle of 173^o using a Malvern Zetasizer NanoZS

instrument. Dilute aqueous dispersions (0.10 % w/w) were analysed at 25 ^{o}C using disposable cuvettes and all data were averaged over three consecutive runs to give the hydrodynamic diameter (D_h).

Transmission Electron Microscopy (TEM)

Copolymer dispersions were diluted fifty-fold at 20 ^{o}C to generate 0.10 % w/w dispersions. Copper/palladium TEM grids (Agar Scientific) were surface-coated in-house to yield a thin film of amorphous carbon. The grids were then plasma glow-discharged for 30 s to create a hydrophilic surface. Individual samples (0.1 % w/w, 12 μL) were adsorbed onto the freshly glow-discharged grids for 60 seconds and then blotted with filter paper to remove excess solution. To stain the aggregates, uranyl formate (0.75 % w/v) solution (9 μL) was soaked on the sample-loaded grid for 20 seconds and then carefully blotted to remove excess stain. The grids were then dried using a vacuum hose. Imaging was performed on a Phillips CM100 instrument at 100 kV, equipped with a Gatan 1 K CCD camera.

Cryogenic Transmission Electron Microscopy (cryo-TEM)

Sample vitrification was conducted using an automated vitrification robot (FEI VitrobotTM Mark III) for the liquid ethane quench. Cryo-TEM 200 mesh copper grids with a 'lacey' carbon film (EM Resolutions, UK) were used with plasma treatment. For visualisation, the dispersions were diluted to the following concentrations: 1 % w/w for the polymer vesicles and silica-containing vesicles, and 0.1 % w/w for silica nanoparticles. For vitrification, typically 3 μl of the dispersion was applied to a cryo-TEM grid inside the vitrobot chamber at 20 °C and 99% humidity. Samples were examined using a FEI Tecnai Spirit TEM instrument equipped with a Gatan 1k MS600CW CCD camera operating at 120 kV under low-dose conditions. Vitrified grids were mounted onto a cryo-transfer holder pre-cooled to -175 °C using liquid nitrogen and then transferred into the microscope. Micrographs were recorded at magnifications ranging from 9,000 to 68,000 times, with defocus values of between -100 μm and -5 μm, depending upon the magnification.

Small-Angle X-Ray Scattering (SAXS)

SAXS patterns were recorded at a synchrotron source (ESRF, station ID02, Grenoble, France). A monochromatic X-ray radiation (wavelength λ = 0.0995 nm) and 2D SAXS CCD detector (Rayonix MX-170HS) were used for these experiments. The SAXS camera lengths (two camera lengths were used) covered the q range from 0.004 nm^{-1} to 2.0 nm^{-1}, where $\boldsymbol{q} = \frac{\mathbf{4\pi \sin\theta}}{\boldsymbol{\lambda}}$ is the modulus of the scattering vector and θ is half of the scattering angle. For static measurements, a vitrified quartz capillary flow-through cell (diameter 1.68 mm) was used as a sample holder. For time-resolved measurements, a glass capillary was inserted into a heating stage which was connected to a linkam. X-ray scattering data were reduced (integration and normalisation) using standard routines from the beamline. SAXSutilities and Irena SAS macros for Igor Pro were utilised for further analysis (background subtraction). The scattering intensity of water was used for absolute scale calibration of the X-ray scattering pattern. SAXS measurements were conducted on silica sols with variable concentrations as well as on $G_{58}H_{250}$ diblock copolymer vesicles prepared in the presence of increasing amounts of 0 to 35 % w/w aqueous dispersions silica nanoparticles. The concentration of copolymer vesicles was diluted from 10 % w/w (as-synthesised) to 1.0 % w/w and underwent six centrifugation-redispersion cycles for data collection.

Disc Centrifuge Photosedimentometry (DCP)

A CPS model DC24000 instrument was used to obtain weight-average particle size distributions. The disk centrifuge was run at 24,000 rpm, and the spin fluid contained a density gradient constructed from 8.0 to 2.0 % w/w aqueous sucrose solutions; a small volume of *n*-dodecane (0.50 mL) was used to extend the lifetime of the gradient. The disc centrifuge was calibrated with a poly(vinyl chloride) latex with a weight-average particle diameter of 263 nm and a known density of 1.385 g cm^{-3}.

Thermogravimetric Analysis (TGA)

Analyses were conducted on freeze-dried samples that were heated in air to 800 °C at a heating rate of 20 °C min^{-1} using a TA Instruments Q500. The

observed mass loss was attributed to complete pyrolysis of the copolymer component (300-600 ^{o}C), with the remaining incombustible residues being attributed to pure silica. The surface glycerol groups on the surface of the silica nanoparticles resulted in some weight loss due to pyrolysis of this organic component.

Helium Pycnometry

The solid-state density of the dried Bindzil CC401 silica sol was determined using a Micromeritics AccuPyc 1330 helium pycnometer at 20 °C.

Results and Discussion

Synthesis and Characterisation of Silica-Loaded Vesicles

RAFT solution polymerisation of GMA was conducted in ethanol at 70 ^{o}C to generate a near-monodisperse G_{58} macro-CTA (M_w/M_n = 1.13). After purification, this water-soluble macro-CTA was utilised for the RAFT aqueous dispersion polymerisation of HPMA at 10 % w/w solids (see Figure 4.1a) to obtain $PGMA_{58}$-$PHPMA_{250}$ diblock copolymers, denoted herein as $G_{58}H_{250}$ for the sake of brevity.

Gel permeation chromatography (GPC) studies indicated that near-monodisperse diblock copolymers were obtained with minimal macro-CTA contamination and high blocking efficiencies (M_w/M_n = 1.12; see Figure 4.2). RAFT aqueous dispersion polymerisation of HPMA was also conducted in the presence of 5 to 35 % w/w silica nanoparticles. ^{1}H NMR studies (see Figure 4.3) indicated that > 99% HPMA conversion was achieved within 2 h at 70 ^{o}C, regardless of the presence of silica nanoparticles. TEM images (see Figure 4.4) reveal a pure vesicular morphology for the control experiments performed in the absence of any silica nanoparticles, as expected when targeting such an asymmetric $G_{58}H_{250}$ diblock copolymer composition.[35, 36]

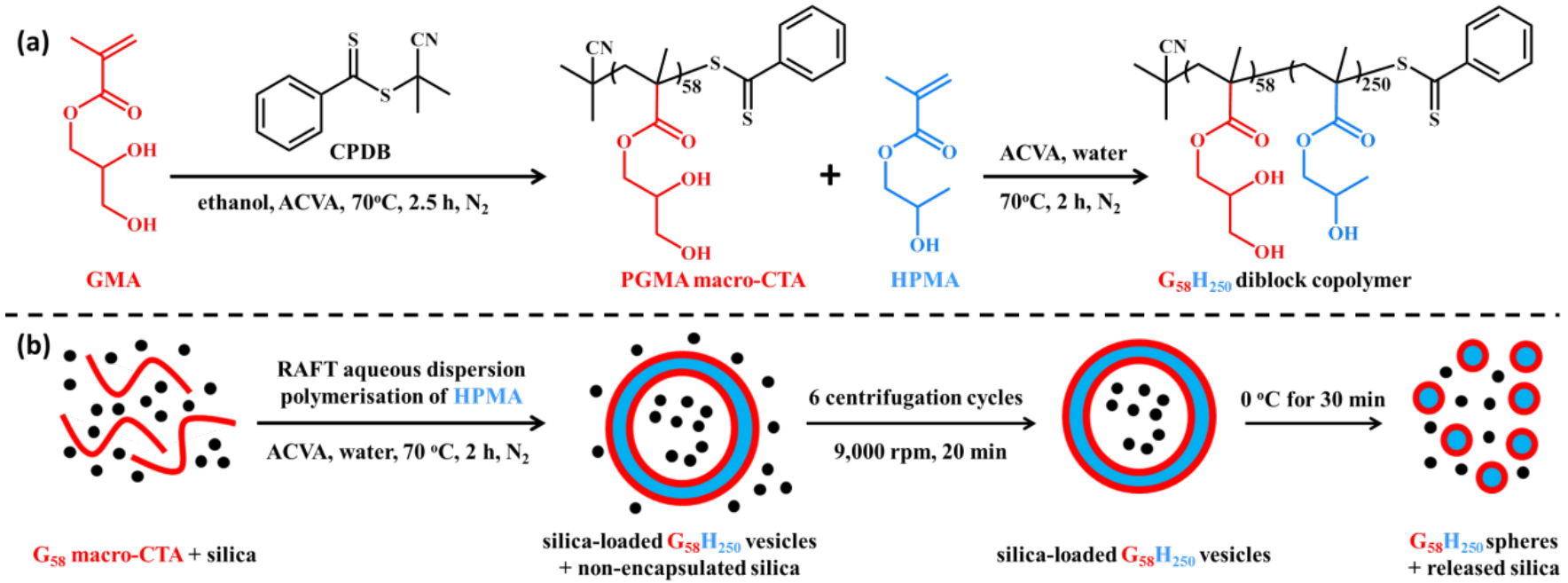

Figure 4.1. (a) Synthesis of a G_{58} macro-CTA via RAFT solution polymerisation and subsequent synthesis of $G_{58}H_{250}$ diblock copolymer via RAFT aqueous dispersion polymerisation (targeting this copolymer composition is known to lead to vesicle formation[35, 36]). (b) Schematic cartoon illustrating in situ encapsulation of silica nanoparticles during the synthesis of $G_{58}H_{250}$ diblock copolymer vesicles via RAFT aqueous dispersion polymerisation and subsequent release of such silica nanoparticles on cooling to 0 °C, which induces vesicle dissociation.

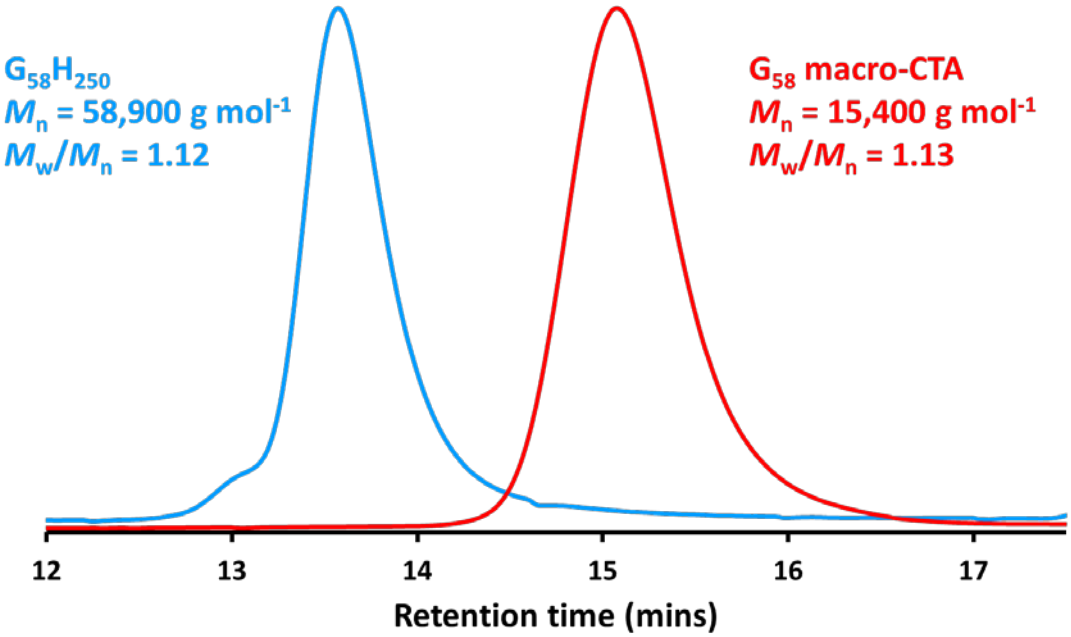

Figure 4.2. DMF GPC curves obtained for the G_{58} macro-CTA and $G_{58}H_{250}$ diblock copolymer (versus poly(methyl methacrylate) (PMMA) calibration standards).

Dynamic light scattering (DLS) studies indicated a mean vesicle diameter of 350 nm with a polydispersity index (PDI) of 0.08 (see Table 4.2). The folds that are discernible in the TEM images are the result of vesicle buckling and/or partial collapse of these relatively delicate nano-structures under ultrahigh vacuum. For experiments conducted in the presence of silica nanoparticles, TEM images reveal that a pure vesicular morphology is still obtained, with lots of excess, non-encapsulated silica nanoparticles also present. In order to remove the non-encapsulated silica, the vesicles were centrifuged at 9,000 rpm for 20 min and redispersed in deionised water (see cartoon in Figure 4.1b). After six centrifugation-redispersion cycles, TEM images suggest that the vast majority of the non-encapsulated silica is removed and that the remaining silica nanoparticles reside within the vesicles, forming *silica-loaded vesicles* (see Figure 4.4).

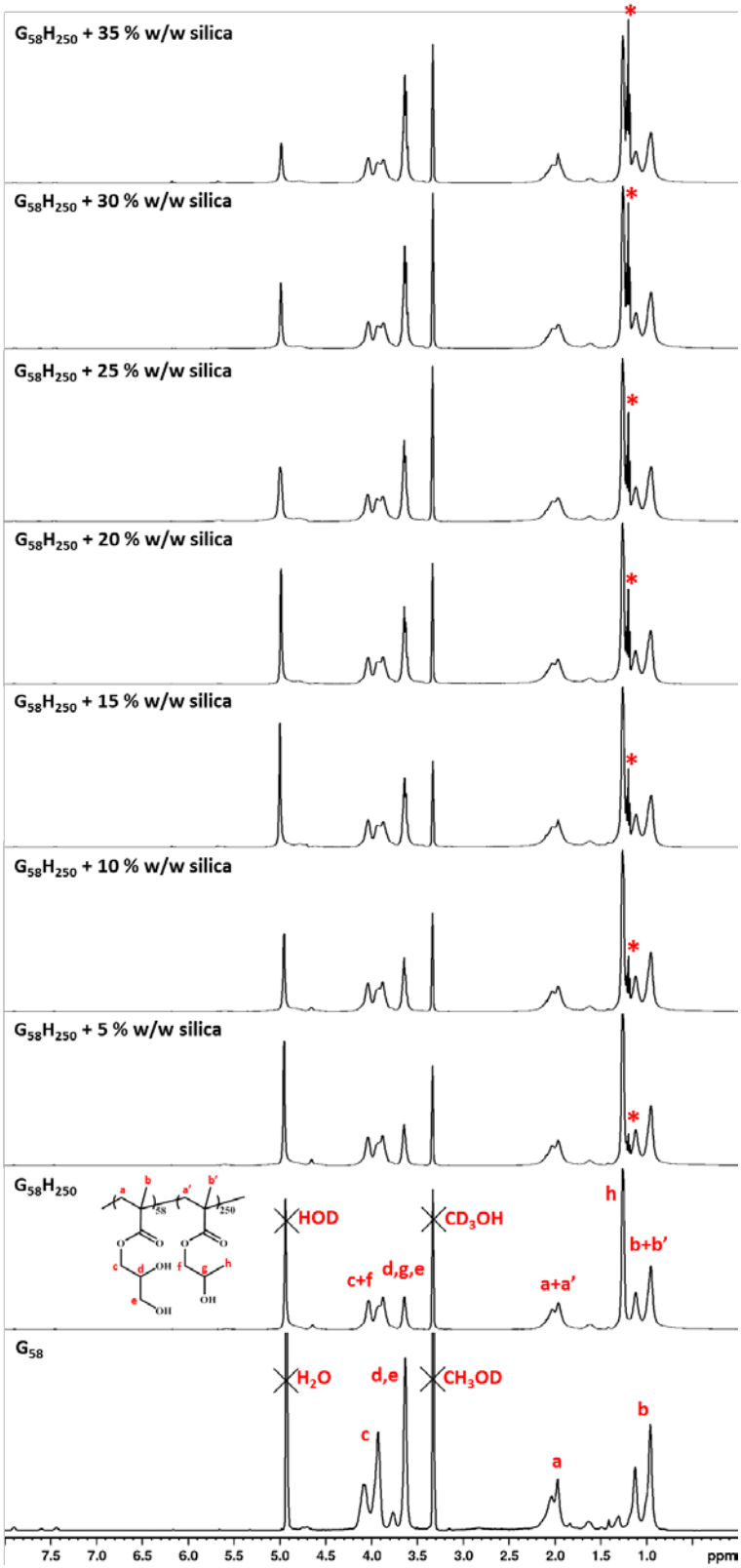

Figure 4.3. Assigned ^{1}H NMR spectra (CD_3OD) obtained for the G_{58} macro-CTA and the $G_{58}H_{250}$ diblock copolymer vesicles prepared in the presence of increasing amounts of silica nanoparticles (5 to 35 % w/w silica). The asterisks indicate the signal resulting from ethanol, which has a concentration of 2.5 % w/w in the as-supplied Bindzil CC401 silica sol. This signal becomes more intense as the $[silica]_0$ increases, as expected.

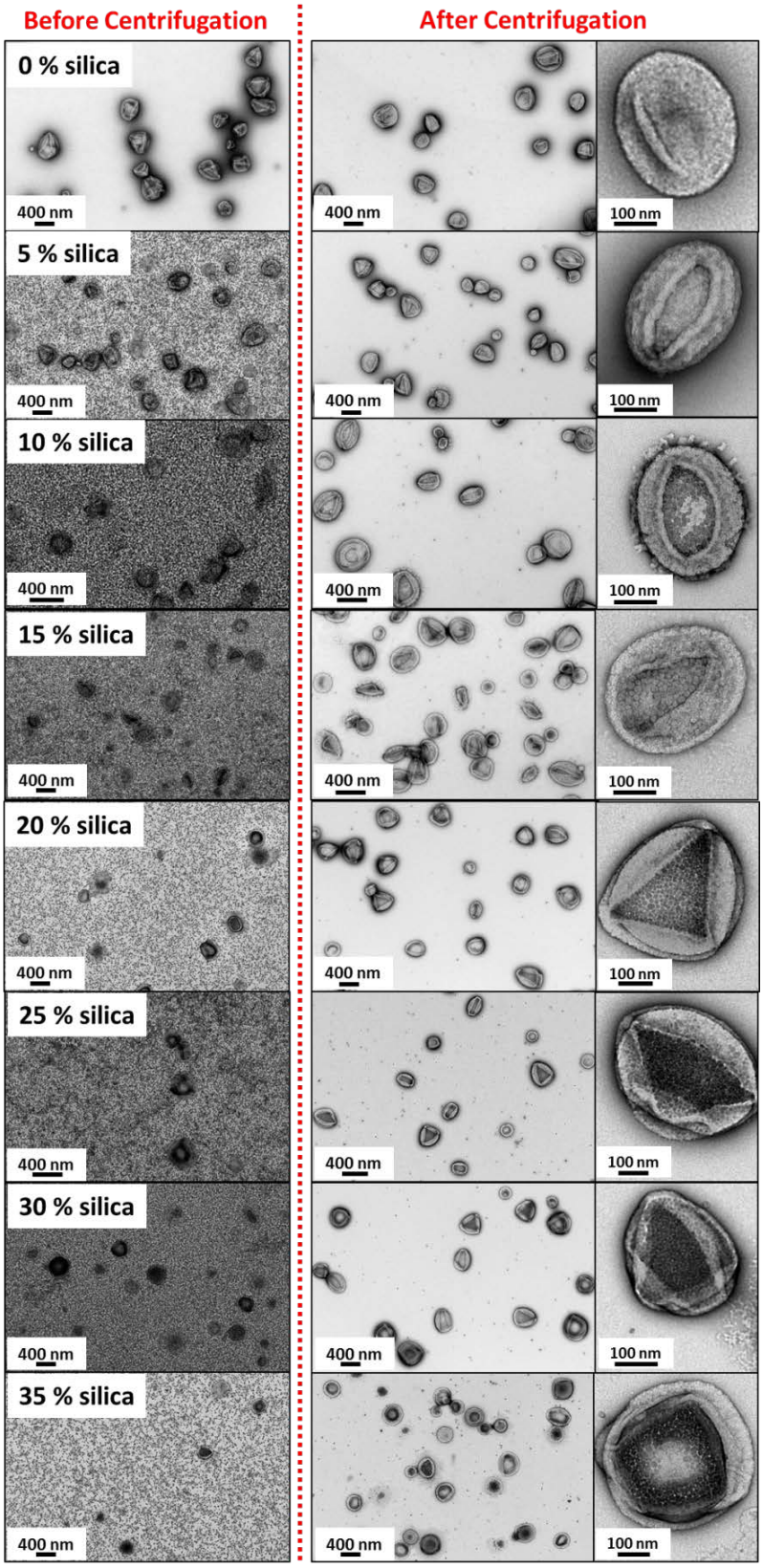

Figure 4.4. TEM images of $G_{58}H_{250}$ diblock copolymer vesicles synthesised in the presence of increasing amounts of silica nanoparticles (0 to 20 % w/w silica). Left: as-synthesised dried dispersions containing excess silica, right: after six centrifugation-redispersion cycles to remove excess silica.

However, hypothetically these TEM observations could be the result of drying artefacts. In contrast, cryo-TEM allows the direct observation of hydrated vesicles that have not been dried, stained or fixed; thus this technique is much more representative of their native environment. Cryo-TEM images (see Figure 4.5) confirm that the silica nanoparticles are indeed located inside the vesicle lumen. Both DLS and TEM studies indicate that the vesicle diameter is essentially unchanged, regardless of the initial silica concentration, $[silica]_0$.

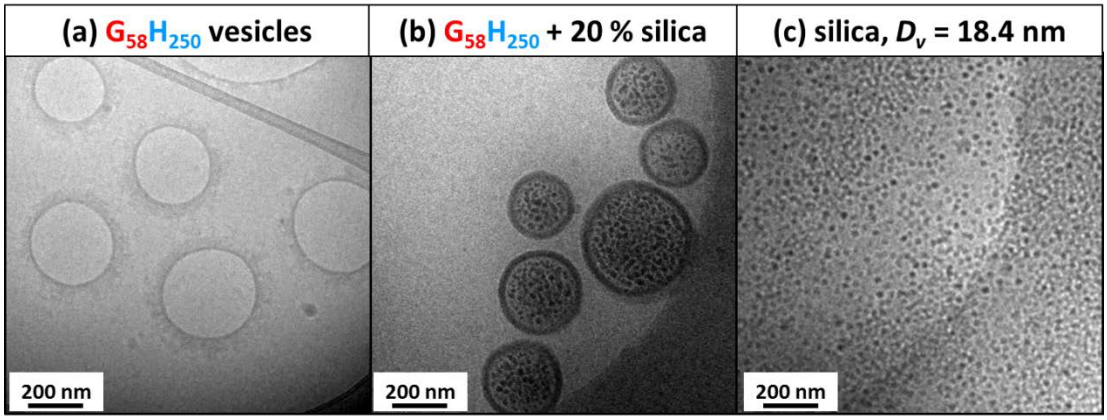

Figure 4.5. Cryo-TEM images obtained for (a) $G_{58}H_{250}$ diblock copolymer vesicles, (b) $G_{58}H_{250}$ diblock copolymer vesicles prepared in the presence of 20 % w/w silica nanoparticles (after centrifugation to remove excess silica nanoparticles) and (c) the silica nanoparticles alone, where the SAXS-derived vesicle diameter (D_v) is 18.4 nm.

Simple geometric considerations suggest that the maximum number of silica nanoparticles encapsulated per vesicle during these PISA syntheses should be given by the total vesicle lumen volume multiplied by the number of silica nanoparticles per unit volume in the aqueous solution, which depends on $[silica]_0$. In order to quantify the amount of silica encapsulated within the vesicle lumen, the following three characterisation techniques were utilised.

Table 4.2. Summary of DLS hydrodynamic diameters (D_h), initial and final silica contents determined by thermogravimetric analysis (TGA) before and after centrifugation and TGA-derived silica loading efficiency (LE_{TGA}), effective density (ρ_{eff}), number of silica nanoparticles per vesicle (N_{sv}), and encapsulation efficiency (EE_{DCP}) determined using disk centrifuge photosedimentometry (DCP), SAXS-derived vesicle diameter (where $D_v = 2R_v$ and σ_{Dv} is its standard deviation) and the concentration of encapsulated silica obtained for a series of $G_{58}H_{250}$ diblock copolymers prepared in the presence of 0 to 35 % w/w silica.

$[silica]_0$ /% w/w	DLS D_h (PDI) /nm	Initial TGA silica content /%	Final TGA silica content /%	LE_{TGA} /%	DCP ρ_{eff} /g cm^{-3}	DCP N_{sv}	EE_{DCP} /%	SAXS $D_v \pm \sigma_{Dv}$ /nm	SAXS-derived concentration of encapsulated silica /% w/w
0	350 (0.08)	0.25	0.25	0.0	1.071	0	0	291 ± 7	0
5	364 (0.17)	37.7	3.78	7.85	1.076	9	13.2	296 ± 6	0.20
10	390 (0.18)	51.5	8.72	9.55	1.084	24	16.9	295 ± 5	0.41
15	317 (0.20)	63.5	13.6	10.5	1.093	40	18.9	323 ± 5	1.12
20	402 (0.17)	73.1	17.0	10.2	1.106	66	24.6	335 ± 6	1.87
25	382 (0.15)	78.2	19.2	9.51	1.119	91	25.6	301 ± 5	1.75
30	410 (0.16)	83.8	21.0	8.85	1.130	112	26.2	332 ± 5	2.03
35	346 (0.09)	86.5	22.1	8.12	1.141	133	26.6	301 ± 5	1.79

Disc Centrifuge Photosedimentometry (DCP)

DCP reports the weight-average particle diameter, which lies between the number-average and intensity-average diameters reported by TEM and DLS, respectively.[42] Assuming a spherical particle morphology, a DCP weight-average diameter can be readily calculated, provided that the particle density is accurately known. Since the PHPMA membrane is highly plasticised by water[38] the vesicle density was *estimated* to be 1.10 g cm^{-3}. When arbitrarily fixing the vesicle density at this value, the mean vesicle diameter increases monotonically and the vesicle size distribution becomes significantly broader when the [silica]$_0$ is increased from 0 to 35 % w/w (see Figure 4.6a). Given that the silica density is 2.06 g cm^{-3} (as judged by helium pycnometry), this suggests that the number of silica nanoparticles encapsulated per vesicle increases at higher [silica]$_0$, as expected. Hence the effective vesicle density increases, resulting in much faster sedimentation of the vesicles relative to the non-encapsulated silica nanoparticles. This means that DCP analyses can be conducted on the as-synthesised dispersions, since the excess silica nanoparticles cannot be detected on the same (short) time scale as the vesicles. However, the vesicle size distribution has finite width and larger vesicles contain many more silica nanoparticles than smaller vesicles. This leads to a density distribution being superimposed on the vesicle size distribution, which results in its artificial broadening. In principle, this problem can be corrected by calculating the particle density for a given diameter, as reported by Fielding et al.[42] However, this refinement was not necessary in the present work.

SAXS analysis of the $G_{58}H_{250}$ diblock copolymer vesicles prepared in the presence of silica nanoparticles indicated volume-average vesicle diameters of 295-335 nm, which are comparable to the mean diameter of 291 ± 7 nm obtained for empty vesicles (see Table 4.2). This suggests that the presence of the silica nanoparticles does not significantly affect the PISA synthesis. Taking the SAXS diameter of the empty vesicles to be the true DCP diameter for both empty and silica-loaded vesicles, the effective vesicle density (ρ_{eff}) must vary from 1.071 to 1.141 g cm^{-3} on increasing the [silica]$_0$ from 0 to 35 % w/w (see Figure 4.6b). This difference in ρ_{eff} allows calculation of (i) the mean number of silica nanoparticles encapsulated per vesicle (N_{sv}), (ii) the volume of the vesicle lumen occupied by silica nanoparticles

(V_{sl}) and (iii) the encapsulation efficiency (EE_{DCP}, see Equations A5.1 to A5.8 in the Appendix for calculations).

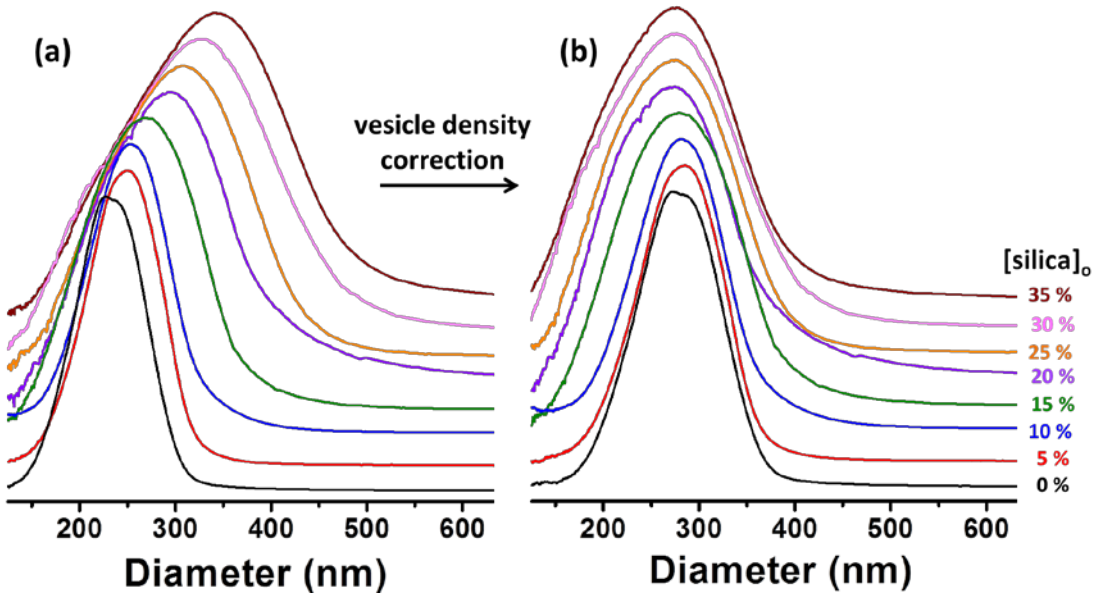

Figure 4.6. DCP data recorded for $G_{58}H_{250}$ diblock copolymer vesicles prepared in the presence of increasing amounts of silica nanoparticles (0 to 35 % w/w silica). (a) Uncorrected weight-average vesicle size distributions for which an arbitrary vesicle density of 1.10 g cm^{-3} was utilised. (b) Corrected weight-average vesicle size distributions whereby the weight-average diameter was held constant at 291 nm (as calculated from SAXS analysis of vesicles prepared in the absence of any silica nanoparticles) by adjusting the vesicle density from 1.071 to 1.141 g cm^{-3}, see Table 4.2. These densities were then used to calculate the silica content of the vesicles. N.B. The apparent broadening of these DCP size distributions is an artefact caused by the superposition of a density distribution on the size distribution (because larger vesicles will contain more silica nanoparticles).

This analysis suggests that N_{sv} increases from 0 to 126 (see Figure 4.7a and Table 4.2), V_{sl} increases from 0 to 4.76 % and EE_{DCP} increases from 0 to 27 % on increasing $[silica]_0$ from 0 to 35 % w/w (see Figure 4.7b and Table 4.2). The N_{sv} increases monotonically with $[silica]_0$. However, N_{sv} is lower than the theoretical N_{sv} calculated from geometric considerations. Naively, it was expected that the N_{sv} would be simply comparable to the number of silica nanoparticles that occupy a certain volume for a given $[silica]_0$. However, the silica concentration inside the vesicle lumen is lower than that outside the vesicles. This suggests a mass transport problem: diffusion of the silica nanoparticles within the 'jellyfish' during PISA appears to be relatively slow on the time scale of vesicle formation. Thus only approximately 27 % of the theoretical maximum amount of silica is actually encapsulated within the vesicle lumen (see Figure 4.7b).

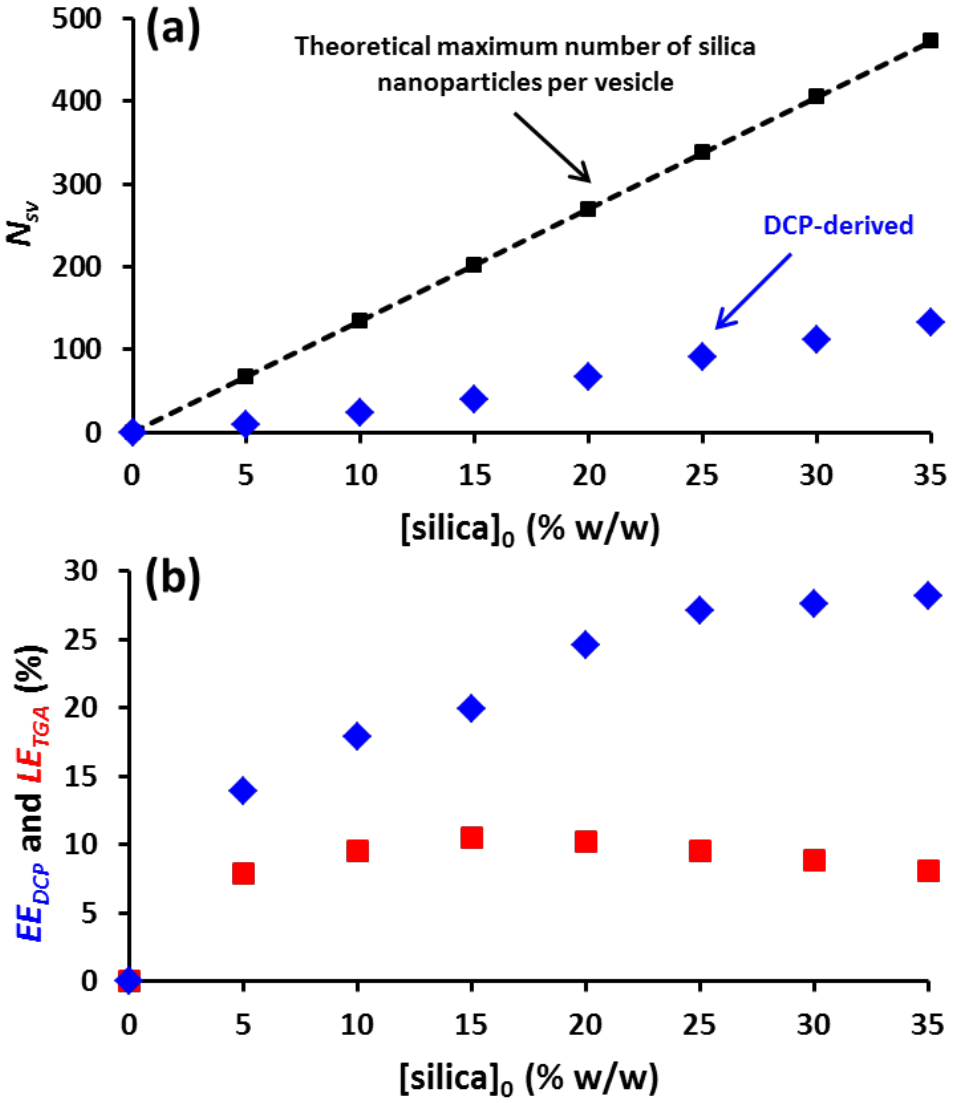

Figure 4.7. Effect of varying the initial silica concentration, [silica]$_0$, during the in situ loading of silica nanoparticles into $G_{58}H_{250}$ diblock copolymer vesicles prepared via RAFT aqueous dispersion polymerisation at 70 °C. (a) Comparison of the theoretical maximum number of silica nanoparticles encapsulated per vesicle with that calculated experimentally from DCP data. (b) Comparison of DCP-derived silica encapsulation efficiency (EE_{DCP}) and the TGA-derived loading efficiency (LE_{TGA}).

Thermogravimetric Analysis (TGA)

Pyrolysis of the methacrylic copolymer used in this study leaves no incombustible residues on heating up to 800 °C in air. In contrast, the silica nanoparticles are thermally stable under these conditions. Thus TGA can be used to determine the encapsulated silica content of dried vesicles after removal of the excess non-encapsulated silica via six centrifugation-redispersion cycles (see TEM images in Figure 4.4).

The silica nanoparticles used in this work lose ~ 10.1 % mass on heating to 350 ^{o}C in air during TGA analysis. This is attributed to a combination of surface moisture and also pyrolysis of surface glycerol groups (at ~350 ^{o}C), which are present for this particular commercial grade. This mass loss must be taken into account when calculating the silica content of the silica-loaded vesicles (see Equation A6.1 in the Appendix and data shown in Table 4.2). As expected, TGA curves recorded prior to centrifugation (see Figure 4.8a) indicate higher silica contents than those observed after centrifugation (see Figure 4.8b).

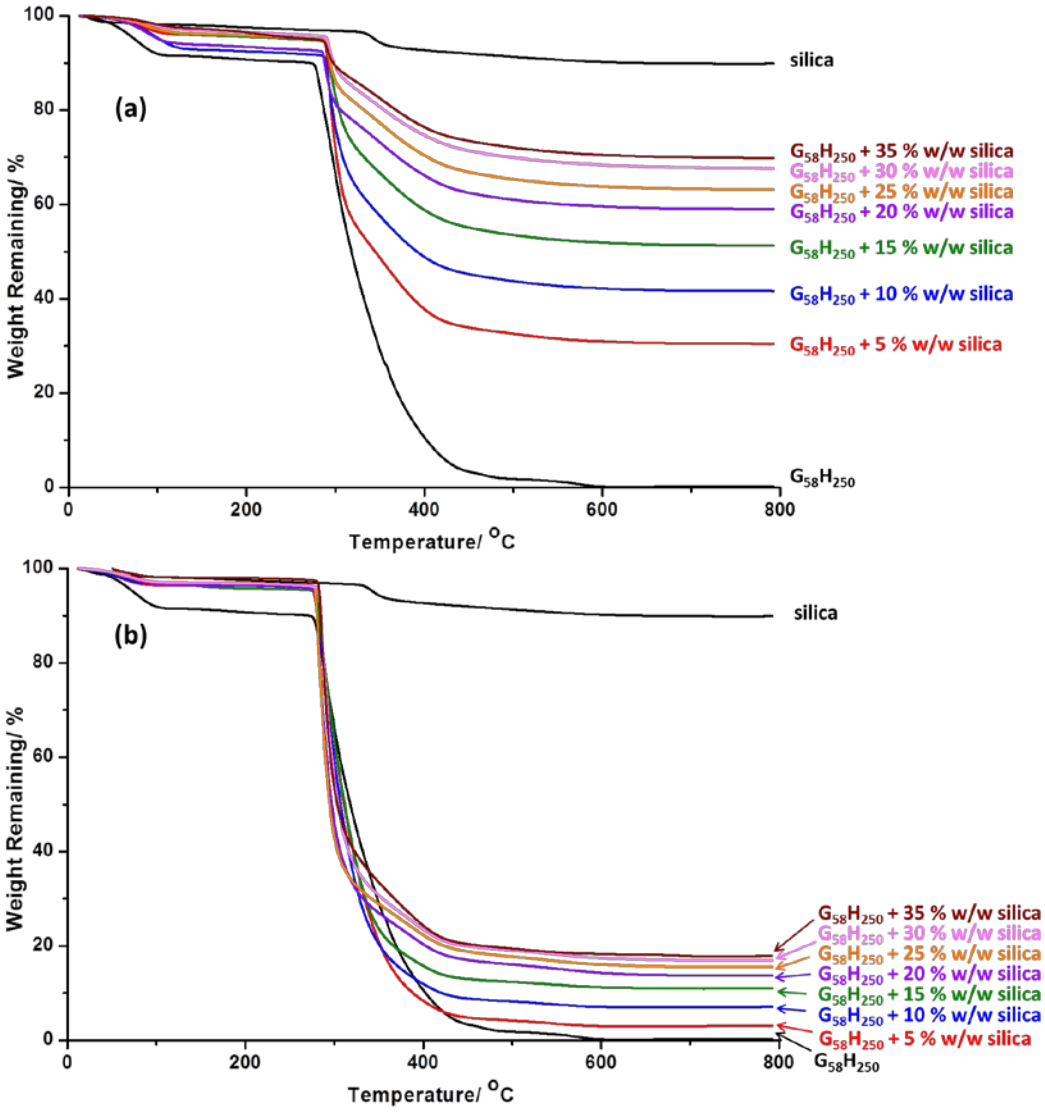

Figure 4.8. TGA data recorded for $G_{58}H_{250}$ diblock copolymer vesicles prepared in the presence of increasing amounts of silica nanoparticles (0 to 35 % w/w silica) where (a) is post-polymerisation prior to centrifugation, and (b) is post-polymerisation after centrifugation (i.e. after removal of the excess silica nanoparticles). A weight loss curve is also shown for the dried silica nanoparticles alone as a reference.

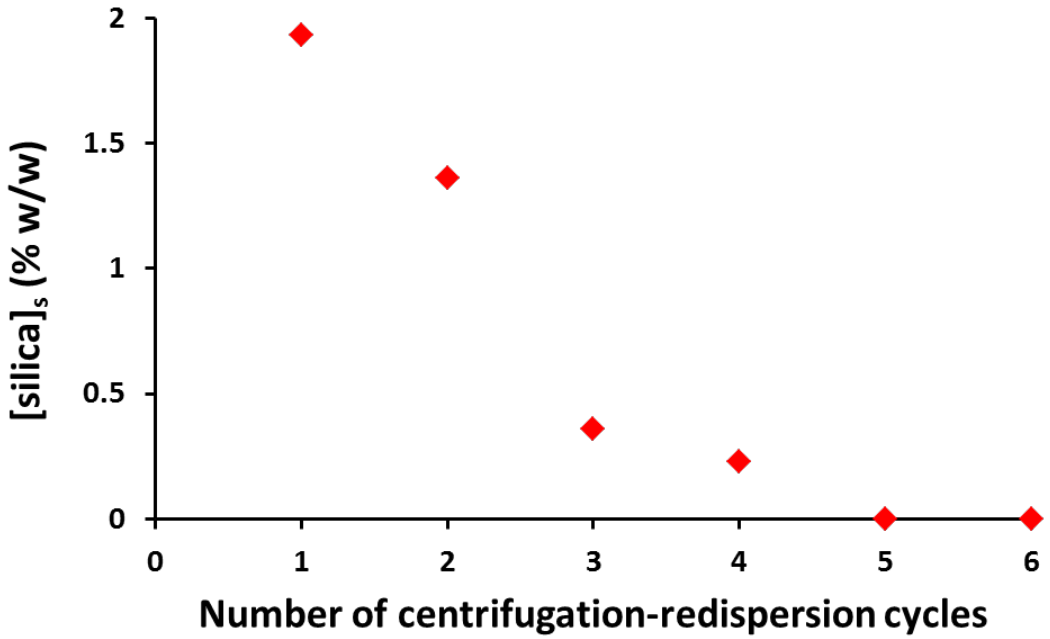

Figure 4.9. Concentration of silica nanoparticles in the supernatant, $[silica]_s$, after each centrifugation-redispersion cycle, as determined by gravimetric analysis, for $G_{58}H_{250}$ diblock copolymer vesicles synthesised in the presence of 35 % w/w silica.

In calculating the TGA-derived loading efficiency (LE_{TGA}, see Equation A6.1 and 6.2 in the Appendix), it is assumed that (i) all the copolymer present has formed vesicles, (ii) there are no empty vesicles and (iii) all of the excess/non-encapsulated silica was removed via centrifugation (which is likely to be the case in view of the gravimetric analysis results shown in Figure 4.9).

The LE_{TGA} remains relatively constant at around 8 % regardless of the $[silica]_0$ (see Figure 4.7b). It is perhaps worth emphasising the difference between LE_{TGA} and EE_{DCP}. The former parameter is calculated from experimental TGA data and represents the proportion of silica that is encapsulated within the vesicles relative to $[silica]_0$. In contrast, EE_{DCP} is calculated by combining the DCP and SAXS data. SAXS is used to determine an accurate weight-average vesicle diameter, vesicle membrane thickness and vesicle lumen volume. The numerator term is the mean number of silica nanoparticles per vesicle (determined by using the SAXS data to calculate the precise vesicle density required to correct the raw DCP data), while the denominator is calculated by multiplying the $[silica]_0$ by the total vesicle lumen volume divided by the total volume of the solution. This calculation assumes that there are no interactions between the copolymer and the silica. For a given vesicle

diameter and $[silica]_0$, the denominator term can be used to calculate the theoretical maximum number of silica nanoparticles per vesicle.

Small Angle X-Ray Scattering (SAXS)

In order to analyse the synchrotron SAXS data obtained for these silica-loaded vesicles, it was necessary to develop an appropriate analytical model. Three types of particles are present in these samples: empty copolymer vesicles (morphology 1), spherical silica nanoparticles (morphology 2) and silica-loaded copolymer vesicles (morphology 3). In general, the silica component scatters X-rays much more strongly than the copolymer, but it is perhaps worth emphasising that the silica nanoparticles (morphology 2) dominate the scattering intensity at high *q*, whereas the much larger vesicles (morphology 1) dominate the scattering at low *q*. Drawing on previously reported structural characterisation of core-shell nanocomposite particles comprising polymer cores and particulate silica shells,[43] the scattering patterns associated with morphology 3 can be satisfactorily described using a two-population model. In this case population 1 corresponds to silica-loaded vesicles and population 2 describes the particulate nature of the corresponding lumen. Thus, this two-population model includes a modified version of morphology 1 and morphology 2 and can be applied to all three morphologies. In general, the scattering intensity of a system composed of *n* different (non-interacting) populations of polydisperse objects can be expressed as:

$$I(q) = \sum_{l=1}^{n} S_l(q) N_l \int_0^\infty \dots \int_0^\infty F_l(q, r_{l1}, \dots, r_{lk}) \Psi_l(r_{l1}, \dots, r_{lk}) dr_{l1} \dots dr_{lk} \quad (4.1)$$

where $F_l(q, r_{l1}, \dots, r_{lk})$ is the form factor, $\Psi_l(r_{l1}, \dots, r_{lk})$ is the distribution function, N_l is the number density per unit volume and $S_l(q)$ is the structure factor of the l^{th} population in the system. r_{l1},...,r_{lk} is a set of *k* parameters describing the structural morphology of the l^{th} population. The two-population model can be derived from Equation 4.1 by taking $n = 2$ and assigning the silica-loaded copolymer vesicles to population 1 ($l = 1$) and the spherical silica nanoparticles within the vesicle lumen to population 2 ($l = 2$). The form factor for population 1 (vesicles) can be described as:[44]

$$F_1(q) = [A_{\mathrm{m}l}(q)]^2 + N_{\mathrm{agg}}\beta_{\mathrm{c}}^2 F_{\mathrm{c}}(qR_{\mathrm{g}}) + N_{\mathrm{agg}}(N_{\mathrm{agg}} - 1)\beta_{\mathrm{c}}^2[A_{\mathrm{c}}(q)]^2 + 2N_{\mathrm{agg}}\beta_{\mathrm{c}}A_{\mathrm{m}l}(q)A_{\mathrm{c}}(q) \quad (4.2)$$

However, this expression requires modification to represent *silica-loaded* vesicles: the amplitude of the membrane self-term in Equation 4.2 must be replaced by an amplitude representing both the membrane and the silica-loaded lumen expressed as the form factor amplitude for a core-shell spherical particle:[45]

$$A_{\mathrm{m}l}(q) = (1 - x_{\mathrm{sol}})(\xi_{\mathrm{m}} - \xi_{\mathrm{sol}})V_{\mathrm{out}}\phi(qR_{\mathrm{out}}) + [\xi_l - \xi_{\mathrm{sol}} - (1 - x_{\mathrm{sol}})(\xi_{\mathrm{m}} - \xi_{\mathrm{sol}})]V_{\mathrm{in}}\phi(qR_{\mathrm{in}}) \quad (4.3)$$

where $R_{\mathrm{in}} = R_{\mathrm{m}} - \frac{1}{2}T_{\mathrm{m}}$ is the radius of the lumen, $R_{\mathrm{out}} = R_{\mathrm{m}} + \frac{1}{2}T_{\mathrm{m}}$ is the outer radius of the membrane, $V_{\mathrm{in}} = \frac{4}{3}\pi {R_{\mathrm{in}}}^3$ is the volume of the vesicle lumen and $V_{\mathrm{out}} = \frac{4}{3}\pi {R_{\mathrm{out}}}^3$ is the volume of the vesicle. R_{m} is the radius from the center of the vesicle to the middle of the membrane, T_{m} is the membrane thickness (Figure 4.10) and $\phi(x) = \frac{3[\sin(x) - x\cos(x)]}{(x)^3}$ is the form factor amplitude for a homogeneous sphere. The vesicle aggregation number (i.e. the mean number of copolymer chains per vesicle) is given by $N_{\mathrm{agg}} = (1 - x_{\mathrm{sol}})(V_{\mathrm{out}} - V_{\mathrm{in}})/V_{\mathrm{m}}$ where x_{sol} is the solvent fraction in the membrane and V_{m} is the volume of the membrane-forming hydrophobic PHPMA block ($V_{\mathrm{m}} = V_{\mathrm{PHPMA250}}$). The X-ray scattering length contrast for the corona block is $\beta_{\mathrm{c}} = V_{\mathrm{c}}(\xi_{\mathrm{c}} - \xi_{\mathrm{sol}})$, where V_{c} is the corona block volume (V_{PGMA58}). The block volumes are calculated from $V = \frac{M_{\mathrm{w}}}{\rho N_{\mathrm{A}}}$ using the weight-average molecular weight, M_{w}, of the block components and the mass densities of the three blocks comprising the copolymer (ρ_{PHPMA} = 1.21 ± 0.01 g cm^{-3} and ρ_{PGMA} = 1.31 ± 0.01 g cm^{-3}, these values were determined for the corresponding homopolymers using a helium pycnometer). ξ_{sol}, ξ_{m}, ξ_{c}, and ξ_l are the X-ray scattering length densities of the surrounding solvent ($\xi_{\mathrm{H_2O}}$ = 9.42 x 10^{10} cm^{-2}), the membrane-forming hydrophobic block (ξ_{PHPMA} = 11.11 x 10^{10} cm^{-2}), the vesicle corona block (ξ_{PGMA} = 11.94 x 10^{10} cm^{-2}) and the vesicle lumen [$\xi_l = (1 - V_{\mathrm{SiO_2}}/V_{\mathrm{in}})\xi_{\mathrm{H_2O}} + (V_{\mathrm{SiO_2}}/V_{\mathrm{in}})\xi_{\mathrm{SiO_2}}$, where $\xi_{\mathrm{SiO_2}}$ = 17.5 × 10^{10} cm^{-2}, and $V_{\mathrm{SiO_2}}$ is the volume occupied by silica nanoparticles within the lumen]. It should be mentioned

that the X-ray scattering length contrast for the membrane block is $\beta_{\mathrm{m}} = V_{\mathrm{m}}(\xi_{\mathrm{m}} - \xi_{\mathrm{sol}})$. Thus, the $(\beta_{\mathrm{c}}/\beta_{\mathrm{m}})^2$ ratio is approximately 0.08, which suggests that the profile of the electron density distribution within the corona should be included in the model. However, recent modeling of experimental data on a similar system has demonstrated that incorporation of a profile function in the model has a negligible effect on the derived structural parameters.[38] The self-correlation term for the corona block in Equation 4.2 is given by the Debye function, $F_{\mathrm{c}}(qR_{\mathrm{g}}) = \frac{2[\exp(-q^2R_{\mathrm{g}}^2)-1+q^2R_{\mathrm{g}}^2]}{q^4R_{\mathrm{g}}^4}$, where R_{g} is the radius of gyration of the corona block (Figure 4.10). Assuming that there is no penetration of the corona blocks within the membrane, the amplitude of the corona self-term is expressed as:

$$A_{\mathrm{c}}(q) = \Psi(qR_{\mathrm{g}})\frac{1}{2}\left[\frac{sin[q(R_{\mathrm{out}}+R_{\mathrm{g}})]}{q(R_{\mathrm{out}}+R_{\mathrm{g}})} + \frac{sin[q(R_{\mathrm{in}}-R_{\mathrm{g}}]}{q(R_{\mathrm{in}}-R_{\mathrm{g}})}\right] \quad (4.4)$$

where $\Psi(qR_{\mathrm{g}}) = \frac{1-\exp(-qR_{\mathrm{g}})}{(qR_{\mathrm{g}})^2}$ is the form factor amplitude of the corona chain. The polydispersities for two parameters (R_{m} and T_{m}), expressed as a Gaussian distribution, are considered for the first (silica-loaded vesicle) population:

$$\Psi_1(r_{11}, r_{12}) = \frac{1}{\sqrt{2\pi\sigma_{R\mathrm{m}}^2}} e^{-\frac{(r_{11}-R_{\mathrm{m}})^2}{2\sigma_{R\mathrm{m}}^2}} \frac{1}{\sqrt{2\pi\sigma_{T\mathrm{m}}^2}} e^{-\frac{(r_{12}-T_{\mathrm{m}})^2}{2\sigma_{T\mathrm{m}}^2}} \quad (4.5)$$

where σ_{Rm} and σ_{Tm} are the standard deviations for R_{m} and T_{m}, respectively. The number density per unit volume of population 1 (l = 1 in Equation 4.1) is expressed as:

$$N_1 = \frac{c_1}{\int_0^\infty \int_0^\infty V_1(r_{11},r_{12})\Psi_1(r_{11},r_{12})dr_{11}dr_{12}} \quad (4.6)$$

where c_1 is the total volume fraction of copolymer molecules forming vesicles in the sample and $V_1(r_{11}, r_{12})$ is the total volume of copolymers in a vesicle [$V_1(r_{11}, r_{12}) = (V_{\mathrm{m}} + V_{\mathrm{c}})N_{\mathrm{agg}}(r_{11}, r_{12})$]. It is assumed that the vesicle dispersion is sufficiently dilute to enable the structure factor for population 1 to be set to unity [$S_1(q) = 1$].

Population 1 describes scattering from a vesicle with a homogeneous lumen. However, the lumen actually has a particulate structure arising from the encapsulated silica nanoparticles. This generates an additional scattering signal that can be described by population 2, for which l = 2 in Equation 4.1. The form factor for this population is simply that for a homogeneous sphere:

$$F_2(q) = \left(\xi_{\mathrm{SiO_2}} - \xi_{\mathrm{sol}}\right)^2 \phi^2(qR_{\mathrm{SiO_2}}) \quad (4.7)$$

where $R_{\mathrm{SiO_2}}$ is the mean radius of the silica nanoparticles. All other parameters and functions in the model for population 2 are analogous to those for population 1 (Equation 4.2). The polydispersity of one parameter ($R_{\mathrm{SiO_2}}$), expressed as a Gaussian distribution, is considered for population 2:

$$\Psi_2(r_{2l}) = \frac{1}{\sqrt{2\pi\sigma^2_{R_{\mathrm{SiO_2}}}}} e^{-\frac{\left(r_{21} - R_{\mathrm{SiO_2}}\right)^2}{2\sigma^2_{R_{\mathrm{SiO_2}}}}} \quad (4.8)$$

where $\sigma_{\mathrm{R_{SiO_2}}}$ is the standard deviation for $R_{\mathrm{SiO_2}}$. The number density per unit volume of population 2 is expressed as:

$$N_2 = \frac{c_2}{\int_0^\infty V_2(r_{21})\Psi_2(r_{21})dr_{21}} \quad (4.9)$$

where c_2 is the total volume fraction of silica particles in the sample and $V_2(r_{21}) = \frac{4}{3}\pi r_{21}^3$ is the volume of a single spherical silica nanoparticle. Since inter-particle interactions are expected for silica particles occupying the vesicle lumen, a hard-sphere interaction structure factor based on the Percus-Yevick approximation[46] was introduced into the model for population 2:

$$S_2(q) = S_{\mathrm{PY}}(q, R_{\mathrm{PY}}, f_{\mathrm{PY}}) \quad (4.10)$$

where R_{PY} is the interaction radius and f_{PY} is an effective hard-sphere volume fraction. The model was incorporated in Irena SAS macros for Igor Pro software[47] and numerical integration of Equations 4.1, 4.6 and 4.9 was used for data fitting.

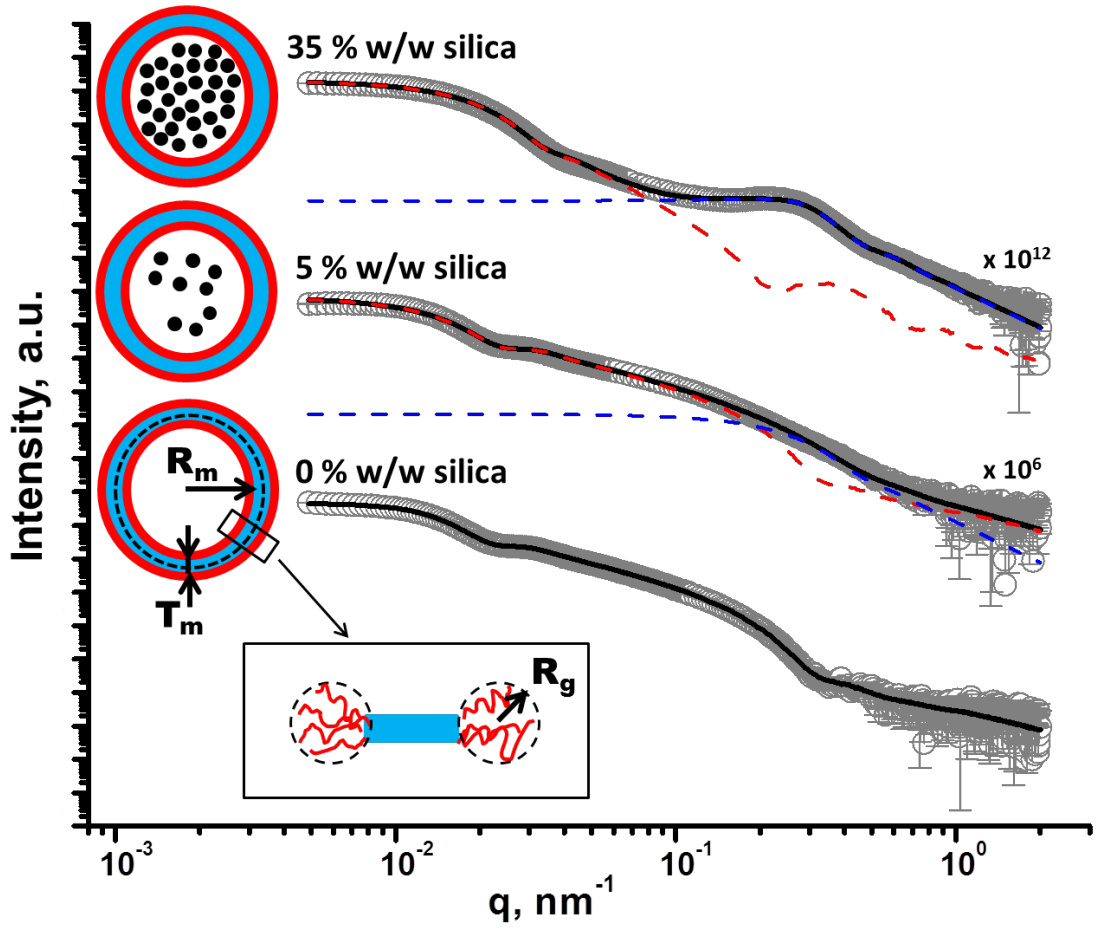

Figure 4.10. SAXS patterns obtained for 1.0 % w/w aqueous dispersions of $G_{58}H_{250}$ diblock copolymer vesicles prepared via PISA in the presence of varying amounts of silica nanoparticles (0, 5 and 35 % w/w silica). Grey circles represent data and solid lines represent fitting curves: when no silica was present during the vesicle synthesis, a single population vesicle model was sufficient to fit the corresponding SAXS pattern, whereas two populations were required when silica nanoparticles were present during the PISA synthesis. Red and blue dashed lines represent populations 1 and 2, respectively. For clarity, the upper two SAXS patterns are shifted vertically by arbitrary scaling factors, as shown on the plot. Inset: schematic representation of empty and silica-loaded $G_{58}H_{250}$ diblock copolymer vesicles, where small black circles represent silica nanoparticles, red = PGMA block (G), light blue = PHPMA block (H), R_m is the radius from the center of the vesicle to the middle of the membrane, T_m is the membrane thickness and R_g is the radius of gyration of the corona.

Table 4.3. Structural parameters obtained by SAXS analysis of $G_{58}H_{250}$ diblock copolymer vesicles prepared in the presence of varying silica concentrations (0 to 35 % w/w) after centrifugation to remove non-encapsulated silica nanoparticles. Fitting of the SAXS data required using a two-population model: population 1 corresponds to vesicles with a silica-loaded lumen and population 2 corresponds to spherical silica nanoparticles. Representative parameters for population 1: R_m is the radius from the center of the vesicle to the center of the membrane and σ_{Rm} is the associated standard deviation, T_m is the membrane thickness and σ_{Tm} is the associated standard deviation, R_v is the total radius of the vesicle ($R_v = R_m + \frac{1}{2}T_m + 2R_g$), where the radius of gyration of the corona PGMA block, R_g, is 2.3 nm - see the main text for further details). Representative parameters for population 2: R_{SiO2} is the silica nanoparticle radius, σ_{RSiO2} is the associated standard deviation, R_{PY} is the Percus-Yevick correlation radius of densely-packed spherical micelles and f_{PY} is the Percus-Yevick effective volume fraction of the packed micelles. c_2/c_1 is the ratio of the volume fraction of the spherical silica nanoparticles (population 2) to the volume fraction of the copolymer vesicles (population 1).

$[silica]_0$/ % w/w	Population 1			c_2/c_1	Population 2		
	R_m (σ_{Rm}) /nm	T_m (σ_{Tm})/ nm	R_v/ nm		R_{SiO_2} (σ_{RSiO_2})/ nm	R_{PY} /nm	f_{PY} /nm
0	125.0 (3.4)	15.9 (2.5)	145.5	-	-	-	-
5	127.8 (3.0)	15.4 (2.2)	147.8	0.015	9.2 (2.1)	-	-
10	129.8 (2.5)	13.2 (2.5)	147.6	0.037	9.2 (2.1)	-	-
15	138.4 (2.6)	18.5 (3.4)	161.5	0.219	9.2 (2.1)	162.49	0.0900
20	145.8(2.8)	17.2 (1.8)	167.6	0.375	9.2 (2.1)	129.39	0.1336
25	134.6 (2.4)	15.8 (2.2)	150.4	0.635	9.2 (2.1)	112.99	0.1553
30	145.4 (2.7)	15.9 (2.2)	165.9	0.928	9.2 (2.1)	110.96	0.1860
35	132.1 (2.3)	13.7 (2.2)	150.4	1.229	9.2 (2.1)	99.551	0.2200
0.1[a]	-	-	-	-	9.2 (2.1)	-	-
1[a]	-	-	-	-	9.1 (2.1)	291.71	0.0915
5_a	-	-	-	-	9.1 (2.1)	194.22	0.1645
30[b]	132.8 (3.1)	15.9 (2.5)	153.3	0.542	9.2 (2.1)	-	-

[a] Data correspond to silica sols.

[b] Data correspond to a control experiment, whereby a known amount of silica sol was added to $G_{58}H_{250}$ diblock copolymer vesicles after their PISA synthesis. Thus none of the silica nanoparticles are encapsulated in this case.

Accordingly, use of population 1 alone was sufficient for satisfactory data fits to SAXS patterns obtained for empty $G_{58}H_{250}$ diblock copolymer vesicles synthesised in the absence of any silica nanoparticles. Use of the vesicle model (l = 1 in Equation 4.1 and $\xi_l = \xi_{\text{sol}}$ in Equation 4.3) produced a reasonably good fit over seven orders of magnitude of X-ray scattering intensity (see Figure 4.10). The overall vesicle radius, $R_{\text{v}} = R_{\text{out}} + 2R_{\text{g}}$, was calculated to be 145.5 nm (Table 4.3), which is consistent with both TEM observations (Figure 4.4) and DLS data (Table 4.2).

The R_{g} of the G_{58} corona block was determined to be 2.3 nm from fitting of the $G_{58}H_{250}$ SAXS pattern.[38] This experimental value is comparable to a theoretical estimate: the projected contour length of a single GMA monomer is 0.255 nm (two carbon bonds in all-trans conformation), the total contour length of a G_{58} block, L_{PGMA} = 58 x 0.255 nm = 14.79 nm and the Kuhn length of 1.53 nm, based on the literature value for poly(methyl methacrylate)[48], result in an estimated R_{g} of (14.79 x 1.53/6)$^{1/2}$, or 1.94 nm. The SAXS data fit suggested that the hydrophobic PHPMA component of the vesicle membrane was solvated, x_{sol} = 0.16. In order to produce satisfactory fits to SAXS patterns obtained for $G_{58}H_{250}$ diblock copolymer vesicles prepared in the presence of silica nanoparticles, incorporation of population 2 (l = 2 in Equation 4.1) into the model was essential. It was also assumed for the fitting that all silica nanoparticles represented by population 2 are located within the vesicles. Thus, the volume fraction of silica nanoparticles, c_2, and the scattering length density of the lumen, ξ_l, must be related in order to produce a self-consistent model. In this respect, the scattering length density of the lumen can be expressed as $\xi_l = (1 - c_2/c_l)\xi_{\text{H}_2\text{O}} + (c_2/c_l)\xi_{\text{SiO}_2}$, where $c_l = \frac{c_1 V_{\text{in}}}{(V_{\text{out}} - V_{\text{in}})(1 - x_{\text{sol}})}$, is the total volume fraction of vesicle lumen.

Structural parameters for the silica nanoparticles alone were obtained from SAXS patterns recorded for 0.1, 1 and 5 % w/w aqueous silica sols (see Figure 4.11). In this case, only population 2 of the model was required for satisfactory data fits. The silica nanoparticle radius (R_{SiO_2}) was estimated to be 9.2 ± 2.1 nm in all cases. Fittings for the 1 and 5 % w/w silica SAXS patterns required a hard-sphere interaction structure factor (see Equation 4.10), because a pronounced peak at q ~ 0.25 nm^{-1} is observed at

higher silica concentrations. In contrast, no structure factor was observed for the 0.1 % w/w silica sol, as expected.

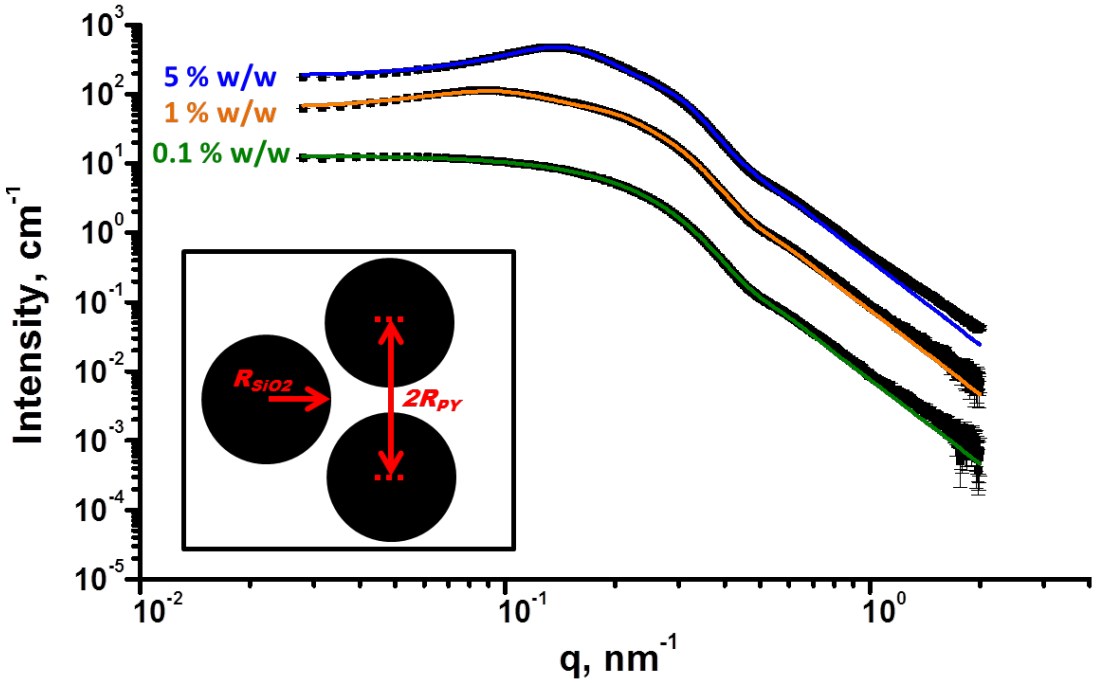

Figure 4.11. SAXS patterns obtained for 5.0, 1.0 and 0.1 % w/w aqueous silica dispersions. Solid lines represent fitting curves; for all data a simple spheroid model was appropriate. For the 5.0 and 1.0 % w/w silica sols, it was necessary to use a hard-sphere interaction, whereas no structure factor was observed for the 0.1 % w/w silica sol. Inset: schematic representation of the parameters obtained when fitting the spheroid model to these aqueous silica dispersions, where R_{SiO2} is the radius of the silica nanoparticle and R_{PY} is the correlation distance between silica nanoparticles.

A superposition of X-ray scattering signals from the two populations used in the model produced good fits to the SAXS data obtained for vesicles synthesised in the presence of silica nanoparticles, after removal of excess non-encapsulated silica (Figure 4.10 and Table 4.3). It is assumed that both the R_g of the PGMA block and the water content within the vesicle membrane are independent of [silica]$_0$. This is reasonable, because the same batch of PGMA macro-CTA was utilised and the same PHPMA block degree of polymerisation (DP) was targeted in all cases. Thus the R_g and x_{sol} values obtained for $G_{58}H_{250}$ diblock copolymer vesicles synthesised in the *absence* of any silica were also used for SAXS fitting of the vesicles synthesised in the *presence* of silica nanoparticles. Moreover, SAXS analysis shows that both the T_m and R_v remain virtually constant regardless of [silica]$_0$ (T_m ~ 15.9 nm and R_v ~ 145.5 nm, Table 4.3), which is consistent with our TEM observations (Figure 4.4) and DLS data (Table 4.2). This confirms that the dimensions of the empty vesicles

produced using this PISA formulation in the absence of any silica are comparable to those obtained in the presence of the silica nanoparticles (see Table 4.2). It is emphasised that the broad peak at $q \sim 0.25$ nm^{-1}, which is associated with interacting silica nanoparticles, confirms successful silica encapsulation within the vesicles. Moreover, increasing the $[\text{silica}]_0$ leads to both a higher effective volume fraction and a reduction in the correlation distance between silica nanoparticles (f_{PY} and R_{PY}, respectively, see Table 4.3), which suggests a greater packing density for the silica nanoparticles within the vesicle lumen. This was corroborated by control experiments in which silica nanoparticles were added to empty vesicles to afford dispersions of the same overall silica concentration. SAXS patterns recorded for such dispersions did not possess any peak at $q \sim 0.25$ nm^{-1} corresponding to silica nanoparticles, indicating that no structure factor is required in this case (see Figure 4.12). These SAXS observations confirm beyond any reasonable doubt that the silica nanoparticles are undoubtedly encapsulated within the vesicles during these PISA syntheses.

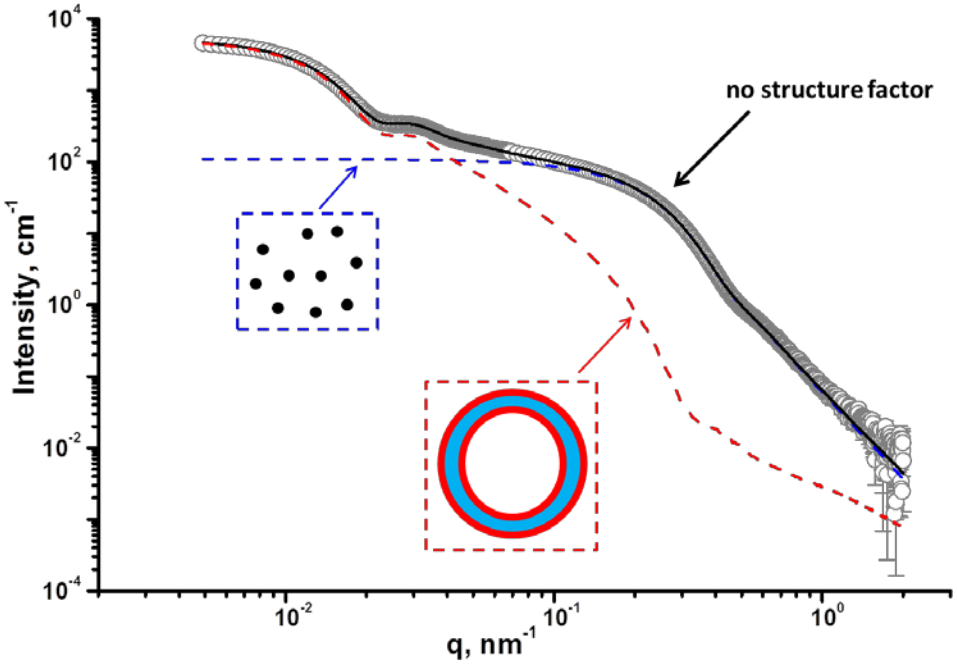

Figure 4.12. SAXS pattern obtained for a 7.5 % w/w aqueous silica dispersion added to 10 % w/w $G_{58}H_{250}$ diblock copolymer vesicles after their PISA synthesis. These ratios were used to mimic the encapsulated silica/vesicle mass ratio for $[\text{silica}]_0$ = 30 % w/w, based on 25 % silica encapsulation estimated from TGA. The solid black line represents the data fit, for which a two-population model was required. Population 1 (red dashed line) represents the vesicles and population 2 (blue dashed line) represents the spherical silica nanoparticles. Inset: schematic representations obtained for the empty vesicles and the silica sol in the sample.

The concentration of encapsulated silica nanoparticles (see Table 4.2), can be estimated using the volume fraction of silica nanoparticles (c_2) obtained from the fitted SAXS patterns. In general, the SAXS data are in fairly good agreement with the corresponding TGA data (see Figure 4.13). However, SAXS tends to underestimate the concentration of encapsulated silica at higher $[silica]_0$. In principle, this might be because TGA cannot distinguish between the silica nanoparticles located within the vesicles and any excess, non-encapsulated silica that might remain in the aqueous continuous phase. In contrast, the two-population SAXS model used in this work is mainly sensitive to silica nanoparticles located within the vesicle lumen. However, TEM studies coupled with gravimetric analysis of successive supernatants suggest that there is relatively little, if any, non-encapsulated silica present after six centrifugation-redispersion cycles (see Figure 4.4 and Figure 4.9, respectively). This discrepancy arises because DCP reports artificially broadened, highly asymmetric size distributions at higher $[silica]_0$, as discussed earlier. This is essentially a polydispersity effect: heavier vesicles containing relatively high silica loadings appear larger in the DCP size distribution, whereas lighter vesicles containing fewer encapsulated silica nanoparticles appear *smaller*, giving rise to an artificially skewed distribution.

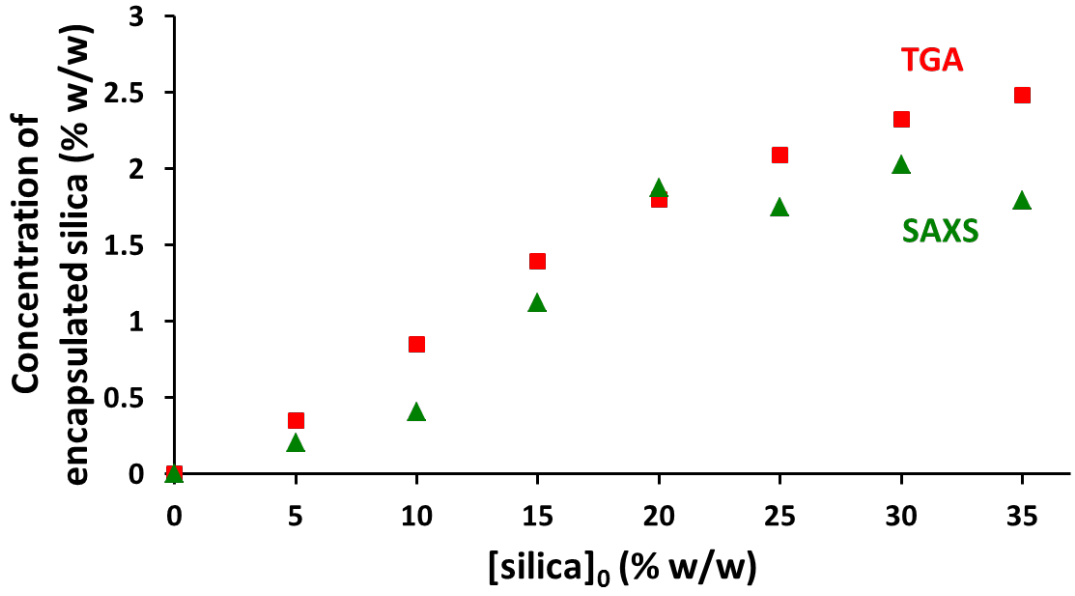

Figure 4.13. Effect of varying the initial silica concentration, $[silica]_0$, on the concentration of encapsulated silica, as calculated using SAXS (▲, measured at 1.0 % w/w copolymer) and TGA (■) for $G_{58}H_{250}$ diblock copolymer vesicles prepared at 10 % w/w in the presence of 0 to 35 % w/w silica nanoparticles (after six centrifugation-redispersion cycles).

This polydispersity effect also leads to uncertainty in the calculated copolymer volume fraction (c_1). The copolymer concentration was actually kept constant at 1.0 % w/w for all SAXS measurements. However, the SAXS model incorrectly suggests that the copolymer concentration is reduced ten-fold as the $[silica]_0$ is increased from 0 to 35 % w/w. Such a significant discrepancy must be associated with the broad distribution of N_{sv} indicated by DCP measurements. The latter technique shows that at low $[silica]_0$ there is a relatively symmetric (approximately Gaussian) distribution of silica nanoparticles per vesicle. However, vesicle dispersions prepared at higher $[silica]_0$ exhibit significantly broader, highly asymmetric distributions skewed to higher mass (Figure 4.6). This effect is enhanced because ξ_{SiO_2} is rather higher than that of the copolymer (17.5×10^{10} cm^{-2} vs. 11.11×10^{10} cm^{-2}, respectively), so heavily-loaded vesicles scatter much more strongly than lightly-loaded (or empty) vesicles. This bias becomes important at higher $[silica]_0$, resulting in a lower *apparent* copolymer concentration. In contrast, for $[silica]_0$ = 5 % w/w, the particle size distribution is relatively narrow and symmetric (approximately Gaussian), meaning that the SAXS data are more reliable in this regime. For PISA syntheses conducted at this relatively low $[silica]_0$, the mean number of silica nanoparticles per vesicle is calculated to be 9 and 14 for DCP and SAXS, respectively.

In principle, the problem in the SAXS analysis observed at high $[silica]_0$ could be rectified by incorporating an additional function in order to account for the polydispersity of N_{sv}. However, the current SAXS model already incorporates three polydispersity functions (Equation 4.5 and 4.8): an extra function describing the asymmetric distribution of N_{sv} would significantly complicate the data analysis and is beyond the scope of this work.

Thermally-Triggered Release of Silica Nanoparticles

In principle, the controlled release of silica nanoparticles from vesicles could offer a self-repair mechanism for either synthetic hydrogels or living tissues.[39] For the $G_{58}H_{250}$ diblock copolymer vesicles described herein, a relatively short mean DP was targeted for the thermo-responsive PHPMA block because the controlled release of the encapsulated silica nanoparticles was to be examined.

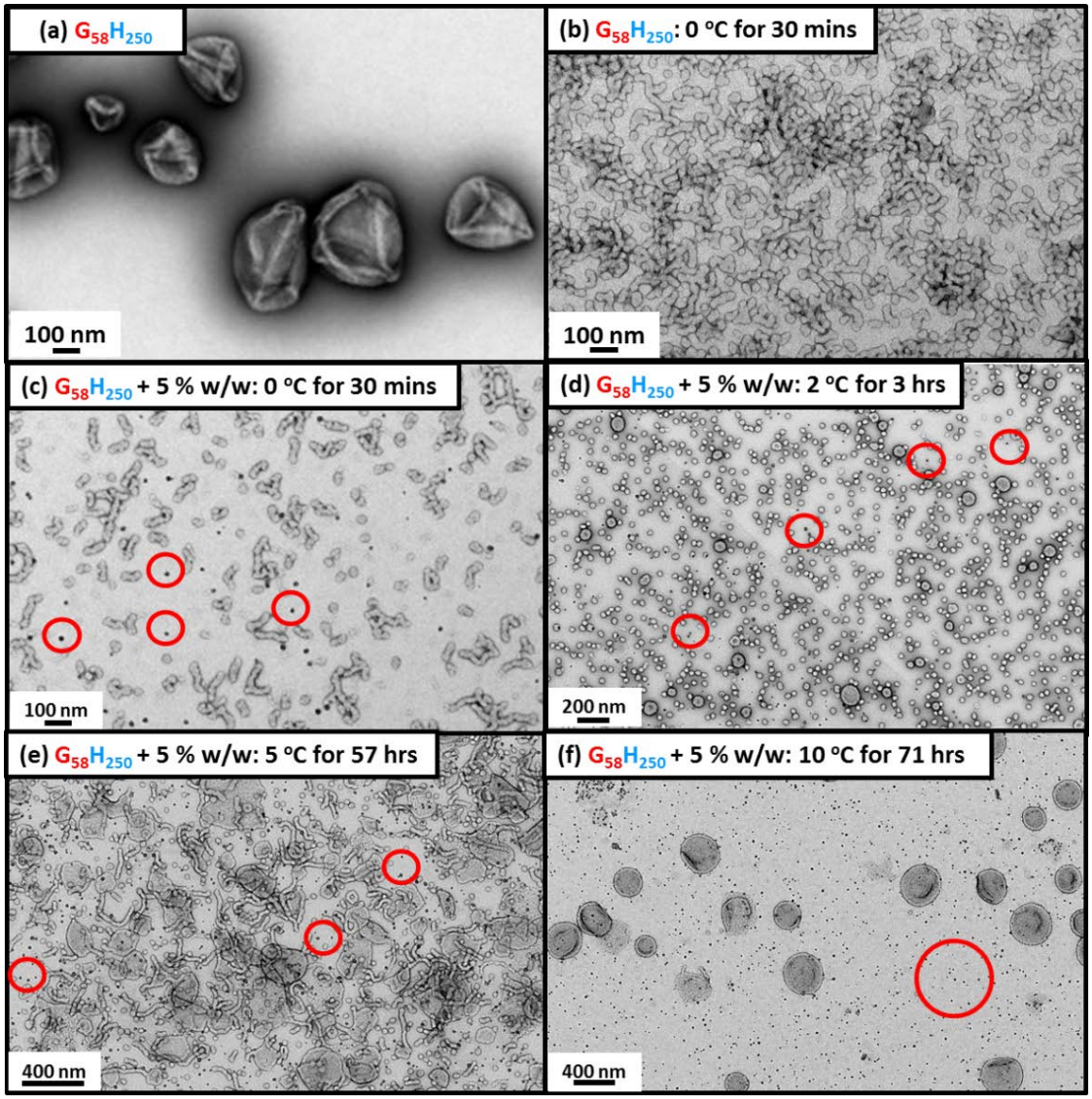

Figure 4.14. TEM images obtained for (a) empty $G_{58}H_{250}$ diblock copolymer vesicles and (b) after cooling to 0 °C for 30 min, the vesicles dissociate to form a mixture of spheres and short worm-like micelles. TEM images obtained for $G_{58}H_{250}$ diblock copolymer vesicles synthesised in the presence of 5 % w/w silica nanoparticles (see Figure 4.4) after cooling to (c) 0 °C for 30 min, (d) 2 °C for 3 h, (e) 5 °C for 57 h and (f) 10 °C for 71 h. Cooling results in the release of the encapsulated silica nanoparticles, which are more electron-dense than the copolymer nanoparticles (red circles depict free silica nanoparticles). Cooling to 0 or 2 °C causes vesicles to dissociate to spherical micelles and short worm-like micelles, to 5 °C results in jellyfish, worms and lamellae and cooling to only 10 °C results in minimal vesicle disintegration.

In control experiments performed in the absence of any silica nanoparticles, TEM studies confirmed that the $G_{58}H_{250}$ diblock copolymer vesicles underwent a morphology change to produce a mixture of diblock copolymer spheres and short worm-like micelles on cooling to 0 °C for 30 min (see Figure 4.14).

For silica-loaded $G_{58}H_{250}$ diblock copolymer vesicles prepared in the presence of 5 % w/w silica nanoparticles, a similar change in morphology was observed on cooling (see Figure 4.14c). Such vesicle dissociation leads to release of the encapsulated silica nanoparticles, which results in loss of the silica structure factor in the corresponding SAXS pattern. Thus this thermally-triggered transition confirms that the silica nanoparticles are indeed encapsulated within the vesicle lumen.

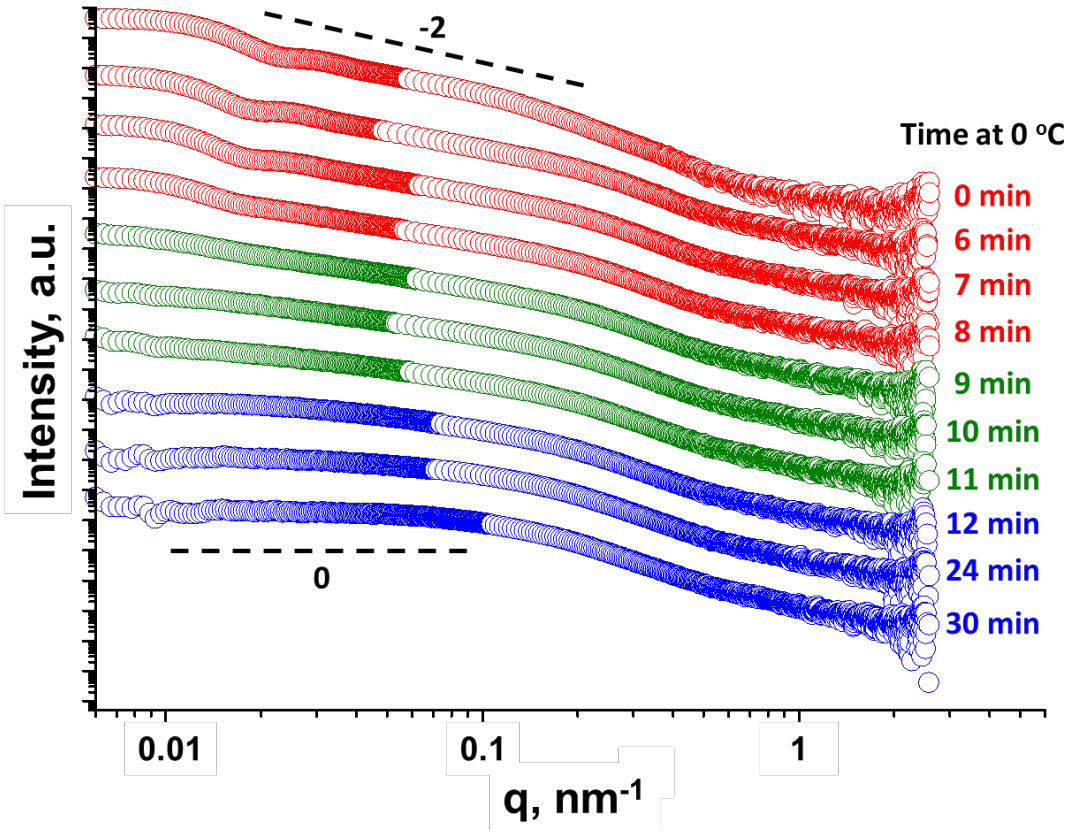

Figure 4.15. SAXS patterns obtained for 1.0 % w/w aqueous dispersions of $G_{58}H_{250}$ diblock copolymer vesicles (originally prepared via PISA at 10 % w/w copolymer in the presence of 5 % w/w silica). The excess/non-encapsulated silica nanoparticles were removed via six centrifugation-redispersion cycles. Then the purified silica-loaded $G_{58}H_{250}$ vesicles were cooled to 0 °C for 30 min while scattering patterns were collected every 15 s. Selected SAXS patterns recorded after various times at 0 °C are shown (for clarity, these patterns are shifted vertically by an arbitrary scaling factor). Silica-loaded vesicles are present up to 8 min (○), but undergo disassociation to form worm-like micelles after 9 min (○), followed by the further transformation to produce mainly spheres after 12 min (○).

SAXS was utilised to explore the kinetics of silica nanoparticle release at 0 °C (see Figure 4.15). Time-resolved SAXS studies indicated that intact silica-loaded vesicles are still present after six minutes at 0 °C. Close inspection of these SAXS patterns confirms that the local minimum at q ~ 0.02 nm^{-1}, which is associated with the

vesicle form factor, disappears after 9 min at 0 ^{o}C. Moreover, the gradient of the scattering pattern at low *q* is reduced from -2 to -1 after 9 min, indicating the formation of worm-like micelles. This gradient tends to zero after 12 min at 0 ^{o}C, suggesting further vesicle disassociation to form a mixture of spheres and short worm-like micelles. Furthermore, the final pattern after 30 min at 0 ^{o}C is identical to that obtained after 12 min, confirming that the morphological transition is essentially complete after 12 min. Further time-resolved SAXS studies were conducted for silica-loaded vesicles prepared in the presence of 10-35 % w/w silica nanoparticles, which is discussed in Chapter Five of this thesis.

Leibler's recent pioneering study[39] suggests that silica nanoparticles can be utilised as remarkably effective adhesives for the repair of both synthetic hydrogels and biological tissue. More specifically, two cut pieces of either polydimethylacrylamide gel or calf's liver can be glued together simply by spreading an aqueous solution of 30 nm commercial silica nanoparticles on the two freshly cleaved interfaces and applying light pressure for 30 s. In the context of the present study, we hypothesise that silica nanoparticles encapsulated within vesicles are not available for the repair of either synthetic hydrogels or biological tissue. However, after their thermally-triggered release from the vesicles, the silica nanoparticles should be able to act as an effective adhesive. However, for a useful self-healing system it may be preferable to achieve silica nanoparticle release at higher temperatures than 0 ^{o}C. Temperature-dependent DLS studies (see Figure 4.16a) indicate the onset of vesicle dissociation at around 10 ^{o}C, as judged by the reduction in count rate and mean particle diameter (D_h). Time-resolved DLS studies show that the rate of dissociation is significantly faster at lower temperature. For example, D_h decreases from approximately 350 nm to 76 nm after 2 h at 2 ^{o}C, with a concomitant reduction in count rate from 22,000 to 1,000 kcps (see Figure 4.16b). TEM images verify release of the encapsulated silica nanoparticles, plus the co-existence of copolymer spheres (see Figure 4.14d). However, after ageing at 5 ^{o}C for 57 h, D_h *increases* to 523 nm before *decreasing* to 284 nm, which suggests vesicle swelling prior to their dissociation (see Figure 4.16c). However, the final D_h value is not consistent with sphere formation. This is confirmed by TEM, which reveals the formation of a complex mixture of lamellae and worm-like micelles under these conditions (see Figure 4.14e). Nevertheless, the encapsulated silica nanoparticles are still released (see red circles in Figure 4.14e).

Moreover, ageing for 71 h at 10 ^{o}C, both D_h and the count rate remain constant at around 350 nm and 20,000 kcps, respectively, which at first sight suggests that the silica-loaded vesicles are not thermo-responsive under these conditions (see Figure 4.16d). Indeed, TEM images reveal that some vesicles are still intact, yet at least some originally-encapsulated silica nanoparticles were released, indicating that a minor fraction of vesicles undergo disassociation (see Figure 4.14f). In summary, both the extent and rate of release of encapsulated silica nanoparticles can be fine-tuned by varying the release temperature and ageing time. In principle, it would be desirable to conduct time-resolved SAXS studies of the silica-loaded vesicles at 2, 5 or 10 ^{o}C, but the much longer experimental timescales required (days) preclude such experiments.

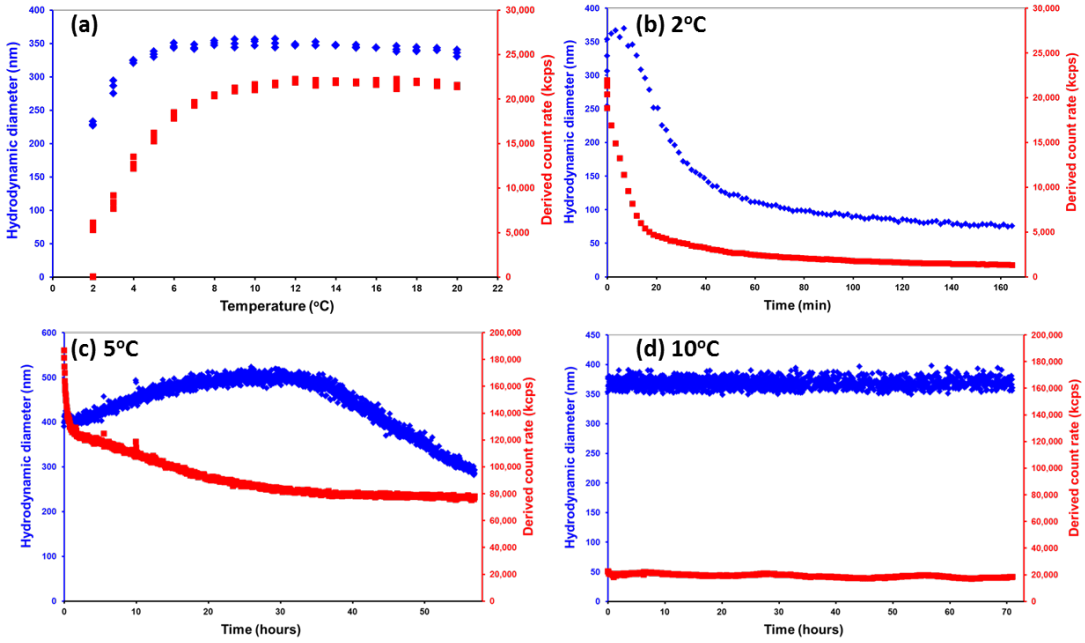

Figure 4.16. Plots of hydrodynamic diameter (♦) and derived count rate (■) against (a) temperature and time at constant temperature of (b) 2 ^{o}C, (c) 5 ^{o}C and (d) 10 ^{o}C for $G_{58}H_{250}$ diblock copolymer vesicles synthesised in the presence of 5 % w/w silica after excess silica has been removed via six centrifugation-redispersion cycles.

During the course of this work, Zhang et al.[49] reported successful encapsulation of silica nanoparticles within PEG-PHPMA vesicles prepared at 20 ^{o}C using a photo-initiated PISA formulation. However, compared to the present study, only limited characterisation of the extent of encapsulation was undertaken.

Conclusions

In summary, we report the *in situ* encapsulation of silica nanoparticles within PGMA-PHPMA diblock copolymer vesicles prepared via PISA in concentrated aqueous solution. Excess silica is readily removed via centrifugation-redispersion cycles and the presence of the silica nanoparticles within the purified vesicles is confirmed by cryo-TEM studies. Thermogravimetric analysis enables the loading efficiency to be directly determined and these results are fully consistent with quantitative data derived from both disc centrifuge photosedimentometry and small-angle X-ray scattering studies. The former technique indicates that silica encapsulation leads to a density distribution being superimposed on the vesicle size distribution, which results in its artificial broadening. The latter technique required development of a new analytical model to calculate the silica volume fraction within the vesicles. SAXS studies also reveal a silica structure factor, which provides compelling evidence for successful nanoparticle encapsulation within the vesicles. As far as we are aware, this is the most detailed study yet of a model vesicle encapsulation system. Having established optimal conditions for *in situ* vesicle loading, this approach should enable the efficient encapsulation of various globular proteins, including enzymes and antibodies. Ideally, such formulations would require PISA syntheses to be conducted at no more than 37 ^{o}C in order to minimise protein denaturation. In this context, it is noteworthy that there are many literature reports of RAFT polymerisations being successfully conducted at ambient temperature (20-25 ^{o}C).[50, 51] Moreover, we demonstrate that the encapsulated silica nanoparticles can be released in a controlled manner via thermally-triggered vesicle dissociation. Time-resolved SAXS studies indicated that the vesicle-to-sphere morphological transition is complete after 12 min at 0 ^{o}C. DLS studies and TEM images further show that this morphological transition requires much longer time scales (hours/days) when cooling to 2, 5 or 10 ^{o}C. Our findings suggest the possibility of a 'self-healing' formulation for synthetic hydrogels, and perhaps also biological tissues.

References

1. P. Stano, P. Carrara, Y. Kuruma, T. Pereira de Souza and P. L. Luisi, *Journal of Materials Chemistry*, 2011, **21**, 18887-18902.
2. M. Li, R. L. Harbron, J. V. M. Weaver, B. P. Binks and S. Mann, *Nat Chem*, 2013, **5**, 529-536.

3. A. Pohorille and D. Deamer, *Trends in Biotechnology*, 2002, **20**, 123-128.
4. J. W. Szostak, D. P. Bartel and P. L. Luisi, *Nature*, 2001, **409**, 387-390.
5. B. Stadler, A. D. Price, R. Chandrawati, L. Hosta-Rigau, A. N. Zelikin and F. Caruso, *Nanoscale*, 2009, **1**, 68-73.
6. T. Nii and F. Ishii, *International Journal of Pharmaceutics*, 2005, **298**, 198-205.
7. L. Schwartz, D. Wolf, A. Markus, S. Wybraniec and Z. Wiesman, *Journal of Agricultural and Food Chemistry*, 2003, **51**, 5972-5976.
8. I. M. Shirley, H. B. Scher, R. M. Perrin, P. J. Wege, M. Rodson, J.-L. Chen and A. W. Rehmke, *Pest Management Science*, 2001, **57**, 129-132.
9. P. H. R. Keen, N. K. H. Slater and A. F. Routh, *Langmuir*, 2014, **30**, 1939-1948.
10. H. N. Yow and A. F. Routh, *Langmuir*, 2009, **25**, 159-166.
11. V. P. Torchilin, *Nat Rev Drug Discov*, 2005, **4**, 145-160.
12. M. Antonietti and S. Förster, *Advanced Materials*, 2003, **15**, 1323-1333.
13. B. M. Discher, Y. Y. Won, D. S. Ege, J. C. M. Lee, F. S. Bates, D. E. Discher and D. A. Hammer, *Science*, 1999, **284**, 1143-1146.
14. F. Chécot, S. Lecommandoux, Y. Gnanou and H.-A. Klok, *Angewandte Chemie International Edition*, 2002, **41**, 1339-1343.
15. J. Rodríguez-Hernández and S. Lecommandoux, *Journal Of The American Chemical Society*, 2005, **127**, 2026-2027.
16. D. E. Discher and A. Eisenberg, *Science*, 2002, **297**, 967-973.
17. J. Du, Y. Tang, A. L. Lewis and S. P. Armes, *Journal Of The American Chemical Society*, 2005, **127**, 17982-17983.
18. D. A. Wilson, R. J. M. Nolte and J. C. M. van Hest, *Nature Chemistry*, 2012, **4**, 268-274.
19. A. Napoli, M. Valentini, N. Tirelli, M. Muller and J. A. Hubbell, *Nature Materials*, 2004, **3**, 183-189.
20. P. J. Photos, L. Bacakova, B. Discher, F. S. Bates and D. E. Discher, *Journal of Controlled Release*, 2003, **90**, 323-334.
21. R. P. Brinkhuis, F. Rutjes and J. C. M. van Hest, *Polymer Chemistry*, 2011, **2**, 1449-1462.
22. C. Pegoraro, D. Cecchin, L. S. Gracia, N. Warren, J. Madsen, S. P. Armes, A. Lewis, S. MacNeil and G. Battaglia, *Cancer letters*, 2013, **334**, 328-337.
23. C. Sanson, C. Schatz, J. F. Le Meins, A. Soum, J. Thevenot, E. Garanger and S. Lecommandoux, *Journal of Controlled Release*, 2010, **147**, 428-435.
24. F. Ahmed, R. I. Pakunlu, G. Srinivas, A. Brannan, F. Bates, M. L. Klein, T. Minko and D. E. Discher, *Molecular Pharmaceutics*, 2006, **3**, 340-350.
25. D. A. Christian, S. Cai, D. M. Bowen, Y. Kim, J. D. Pajerowski and D. E. Discher, *European Journal of Pharmaceutics and Biopharmaceutics*, 2009, **71**, 463-474.
26. J. Huang, C. Bonduelle, J. Thévenot, S. Lecommandoux and A. Heise, *Journal Of The American Chemical Society*, 2012, **134**, 119-122.
27. H. Lomas, I. Canton, S. MacNeil, J. Du, S. P. Armes, A. J. Ryan, A. L. Lewis and G. Battaglia, *Advanced Materials*, 2007, **19**, 4238-4243.
28. S. F. M. van Dongen, M. Nallani, J. Cornelissen, R. J. M. Nolte and J. C. M. van Hest, *Chemistry-A European Journal*, 2009, **15**, 1107-1114.
29. I. Canton, M. Massignani, N. Patikarnmonthon, L. Chierico, J. Robertson, S. A. Renshaw, N. J. Warren, J. P. Madsen, S. P. Armes, A. L. Lewis and G. Battaglia, *The FASEB Journal*, 2013, **27**, 98-108.
30. S. Lecommandoux, O. Sandre, F. Chécot, J. Rodriguez-Hernandez and R. Perzynski, *Journal of Magnetism and Magnetic Materials*, 2006, **300**, 71-74.

31. L. A. Fielding, M. J. Derry, V. Ladmiral, J. Rosselgong, A. M. Rodrigues, L. P. D. Ratcliffe, S. Sugihara and S. P. Armes, *Chemical Science*, 2013, **4**, 2081-2087.
32. L. A. Fielding, J. A. Lane, M. J. Derry, O. O. Mykhaylyk and S. P. Armes, *Journal Of The American Chemical Society*, 2014, **136**, 5790-5798.
33. C. Gonzato, M. Semsarilar, E. R. Jones, F. Li, G. J. P. Krooshof, P. Wyman, O. O. Mykhaylyk, R. Tuinier and S. P. Armes, *Journal Of The American Chemical Society*, 2014, **136**, 11100-11106.
34. S. Sugihara, A. Blanazs, S. P. Armes, A. J. Ryan and A. L. Lewis, *Journal Of The American Chemical Society*, 2011, **133**, 15707-15713.
35. A. Blanazs, J. Madsen, G. Battaglia, A. J. Ryan and S. P. Armes, *Journal Of The American Chemical Society*, 2011, **133**, 16581-16587.
36. A. Blanazs, A. J. Ryan and S. P. Armes, *Macromolecules*, 2012, **45**, 5099-5107.
37. N. J. Warren and S. P. Armes, *Journal Of The American Chemical Society*, 2014, **136**, 10174-10185.
38. N. J. Warren, O. O. Mykhaylyk, A. J. Ryan, M. Williams, T. Doussineau, P. Dugourd, R. Antoine, G. Portale and S. P. Armes, *Journal Of The American Chemical Society*, 2015, **137**, 1929-1937.
39. S. Rose, A. Prevoteau, P. Elziere, D. Hourdet, A. Marcellan and L. Leibler, *Nature*, 2014, **505**, 382-385.
40. Y. Li and S. P. Armes, *Angewandte Chemie International Edition*, 2010, **49**, 4042-4046.
41. D. J. Adams, S. Adams, D. Atkins, M. F. Butler and S. Furzeland, *Journal of Controlled Release*, 2008, **128**, 165-170.
42. L. A. Fielding, O. O. Mykhaylyk, S. P. Armes, P. W. Fowler, V. Mittal and S. Fitzpatrick, *Langmuir*, 2012, **28**, 2536-2544.
43. J. A. Balmer, O. O. Mykhaylyk, A. Schmid, S. P. Armes, J. P. A. Fairclough and A. J. Ryan, *Langmuir*, 2011, **27**, 8075-8089.
44. J. Bang, S. M. Jain, Z. B. Li, T. P. Lodge, J. S. Pedersen, E. Kesselman and Y. Talmon, *Macromolecules*, 2006, **39**, 1199-1208.
45. J. S. Pedersen, *Advances in Colloid and Interface Science*, 1997, **70**, 171-210.
46. D. J. Kinning and E. L. Thomas, *Macromolecules*, 1984, **17**, 1712-1718.
47. J. Ilavsky and P. R. Jemian, *Journal of Applied Crystallography*, 2009, **42**, 347-353.
48. L. J. Fetters, D. J. Lohse and R. H. Colby, in *Physical Properties of Polymers Handbook*, ed. J. Mark, Springer New York, 2007, DOI: 10.1007/978-0-387-69002-5_25, ch. 25, pp. 447-454.
49. J. Tan, H. Sun, M. Yu, B. S. Sumerlin and L. Zhang, *ACS Macro Letters*, 2015, DOI: 10.1021/acsmacrolett.5b00748, 1249-1253.
50. L. Martin, G. Gody and S. Perrier, *Polymer Chemistry*, 2015, **6**, 4875-4886.
51. A. J. Convertine, B. S. Lokitz, A. B. Lowe, C. W. Scales, L. J. Myrick and C. L. McCormick, *Macromolecular Rapid Communications*, 2005, **26**, 791-795.

Chapter Five - Time-Resolved SAXS Studies of the Kinetics of Thermally-Triggered Release of Encapsulated Silica Nanoparticles from Block Copolymer Vesicles

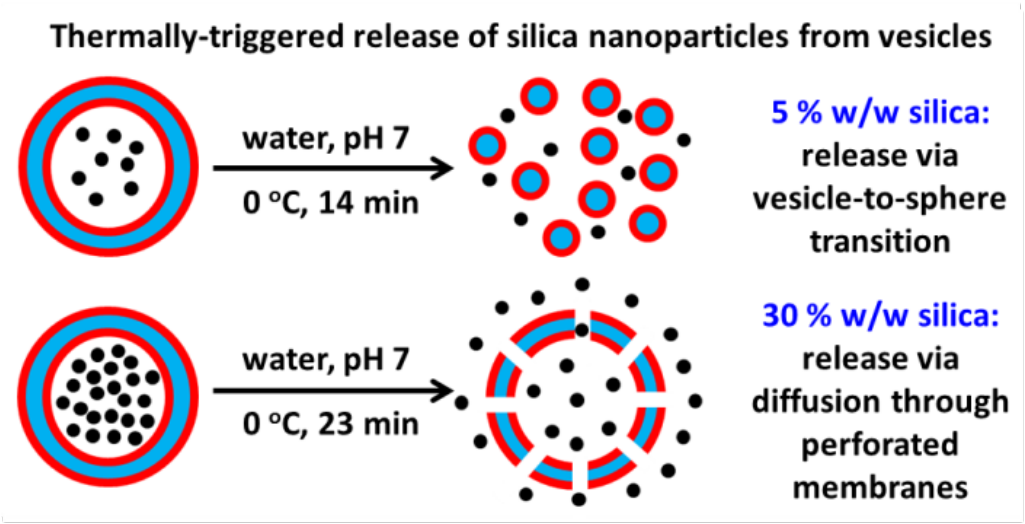

Reproduced in part from [C. J. Mable, M. J. Derry, K. L. Thompson, L. A. Fielding, O. O. Mykhaylyk and S. P. Armes, *Macromolecules*, 2017, **50**, 4465-4473]. Copyright [2017] The Royal Society of Chemistry.

Introduction

Chapter Four reported the successful *in situ* encapsulation of silica nanoparticles within poly(glycerol monomethacrylate)-poly(2-hydroxypropyl methacrylate) (PGMA-PHPMA) diblock copolymer vesicles prepared *via* PISA.[1] These vesicles were synthesised at 10 % w/w solids in the presence of 0 to 35 % w/w silica nanoparticles followed by extensive purification *via* six centrifugation-redispersion cycles. Small-angle x-ray scattering (SAXS), disk centrifuge photosedimentometry and cryo-TEM studies confirmed successful silica encapsulation within the vesicle lumen.

Given their biocompatibility and commercial availability, silica nanoparticles constitute a useful model cargo. Moreover, their high electron contrast aids transmission electron microscopy (TEM) studies, they scatter X-rays strongly which facilitates SAXS analysis and their excellent thermally stability enables convenient quantification *via* thermogravimetric analysis. Furthermore, silica nanoparticles are potentially an 'active' payload. Recently, Rose et al.[2] reported that strong adhesion between a freshly-cleaved hydrogel can be rapidly achieved at ambient temperature simply by spreading an aqueous droplet containing silica nanoparticles on one of the two surfaces of the cleaved gel prior to contact. This approach can also be used for biological tissues such as calf's liver, which suggests potential biomedical applications. However, silica nanoparticles encapsulated within block copolymer vesicles must be first released to become available for such tissue repair. It is well-known that certain vesicles can undergo morphological transitions when exposed to an external stimulus such as temperature,[3-5] light,[6] salt[7, 8] or pH.[5, 9-12] In this Chapter, time-resolved SAXS studies are used to monitor the rate of release of silica nanoparticles encapsulated within PGMA-PHPMA diblock copolymer vesicles by utilising a thermally-triggered morphological transition. A remarkable range of physical behaviour is observed depending on the initial concentration of silica nanoparticles within such vesicles.

Experimental Details

Materials

All reagents were used as received unless otherwise stated. 4, 4'-Azobis-4-cyanopentanoic acid (ACVA) and 2-cyano-2-propyl dithiobenzoate (CPDB) were purchased from Sigma-Aldrich (UK). Ethanol and dichloromethane were purchased from Fisher Scientific (UK). Glycerol monomethacrylate (GMA; 99.8 % purity; 0.06 mol% dimethacrylate impurity) was kindly donated by GEO Specialty Chemicals (Hythe, UK) and used without further purification. 2-Hydroxypropyl methacrylate (HPMA) was purchased from Alfa Aesar (UK) and contained 0.07 mol % dimethacrylate impurity, as judged by HPLC analysis. CD_3OD was purchased from Goss Scientific (UK). Bindzil colloidal silica (CC401; supplied as a 40 % w/w aqueous dispersion; manufacturer's nominal particle diameter = 12 nm) was kindly donated by AkzoNobel Pulp and Performance Chemicals AB (Bohus, Sweden). 2,2'-Azobis[2-(2-imidazolin-2-yl)propane]dihydrochloride (VA-044) was purchased from Wako Specialty Chemicals (Japan). Deionised water (pH 6.2; surface tension = 72.0 mN m^{-1} at 20 ^{o}C) was obtained using an Elga Elgastat Option 3A water purifier.

Synthesis of Silica-Loaded $G_{58}H_{250}$ Diblock Copolymer Vesicles

Such syntheses were described in detail in Chapter Four.[1] The protocol used for a 20 % w/w aqueous silica dispersion is representative and is described here. G_{58} macro-CTA (0.200 g, 0.021 mmol), HPMA monomer (0.758 g, 5.26 mmol), CC401 silica sol (4.80 g, 40 % w/w aqueous dispersion) and deionised water (3.84 g) were weighed into a sample vial and purged with N_2 for 20 min. ACVA was added (1.18 mg, 0.0042 mmol, CTA/ACVA molar ratio = 5.0) and purged with N_2 for a further 10 min prior to immersion in an oil bath set at 70 ^{o}C for 2 h. Finally, the HPMA polymerisation was quenched by cooling to room temperature with subsequent exposure to air. The protocol used for the 0, 5, 10, and 30 % w/w aqueous silica dispersion formulations are the same, except the relative amounts of silica sol and deionised water are varied (Table 5.1). To remove excess, non-encapsulated silica nanoparticles, the vesicles were diluted from

10 % w/w to 1.0 % w/w prior to performing six centrifugation-redispersion cycles (9,000 rpm for 20 min for each cycle).

Table 5.1. Summary of the specific amounts of silica sol (40 % w/w) and deionised water used in order to obtain a specific aqueous silica concentration.

Silica concentration (% w/w)	CC401 silica sol (g)	Deionised water (g)
0	0	8.63
5	1.20	7.43
10	2.40	6.23
20	4.80	3.84
30	7.19	1.44

Dynamic Light Scattering (DLS)

Intensity-average hydrodynamic diameters were recorded for aqueous copolymer dispersions and determined using a Malvern Zetasizer NanoZS instrument. Dilute aqueous dispersions (0.10 % w/w) were analysed at 25^{o}C using disposable cuvettes and all data were averaged over three consecutive runs to give the hydrodynamic diameter (D_h).

Transmission Electron Microscopy (TEM)

As-synthesised copolymer dispersions were diluted at 25 ^{o}C to generate 0.10 % w/w dispersions. Copper/palladium TEM grids (Agar Scientific, UK) were surface-coated in-house to produce a thin film of amorphous carbon. The grids were then plasma glow-discharged for 30 s to create a hydrophilic surface. Individual samples of aqueous copolymer dispersions (0.1 % w/w, 12 μL) were adsorbed onto the freshly glow-discharged grids for 20 s and then blotted with filter paper to remove excess solution. To stain the copolymer dispersions, uranyl formate solution (0.75 % w/v; 9 μL) solution was placed on the sample-loaded grid for 20 s and then carefully blotted to remove excess stain. The grids were then dried using a vacuum hose. Imaging was performed at 100 kV using a Phillips CM100 instrument equipped with a Gatan 1 K CCD camera.

Small-Angle X-ray Scattering (SAXS)

SAXS patterns were recorded at a synchrotron (ESRF, station ID02, Grenoble, France). A monochromatic X-ray beam (λ = 0.0995 nm) and a 2D SAXS detector (Rayonix MX-170HS) were used for these experiments. A q range of 0.004 nm^{-1} to 2.0 nm^{-1} was used for measurements, where $q = \frac{4\pi\sin\theta}{\lambda}$ corresponds to the modulus of the scattering vector and θ is half of the scattering angle. For these time-resolved measurements, a glass capillary of 2 mm thickness was inserted into a heating stage (HFSX350-CAP, Linkam Scientific Instruments, Tadworth, UK). X-ray scattering data were reduced (integration, normalisation and background subtraction) using standard routines available at the ID02 beamline. The scattering intensity of water was used for absolute scale calibration of the X-ray scattering patterns. Irena SAS macros[13] for Igor Pro were utilised for modelling and further SAXS analysis. Copolymer vesicle dispersions were diluted from 10 % w/w (as-synthesised) to 1.0 % w/w and then subjected to six centrifugation-redispersion cycles prior to data collection. For time-resolved studies, dilute aqueous dispersions were cooled to 0 ^{o}C for 30 min with SAXS patterns being collected every 15 s.

Results and Discussion

Results

For the sake of brevity, a shorthand notation is utilised throughout this Chapter to describe the copolymer. Thus $G_{58}H_{250}$ represents a PGMA-PHPMA diblock copolymer, where 58 and 250 indicate the mean degrees of polymerisation (DP) of the two respective blocks.

The thermoresponsive behaviour of 1.0 % w/w copolymer dispersions of both empty and silica-loaded $G_{58}H_{250}$ vesicles (originally prepared *via* PISA at 10% w/w copolymer in the presence of either 5, 10, 20 or 30 % w/w silica nanoparticles, followed by purification *via* multiple centrifugation-redispersion cycles to remove excess free silica) was examined in Chapter Four by cooling to approximately 0 °C using an ice bath. The initial vesicle dispersions were turbid at room temperature, as expected. After cooling for 30 min, the samples prepared in the presence of either 0

% or 5.0 % w/w silica were no longer turbid, whereas those prepared using 10, 20 and 30 % w/w silica remained turbid.

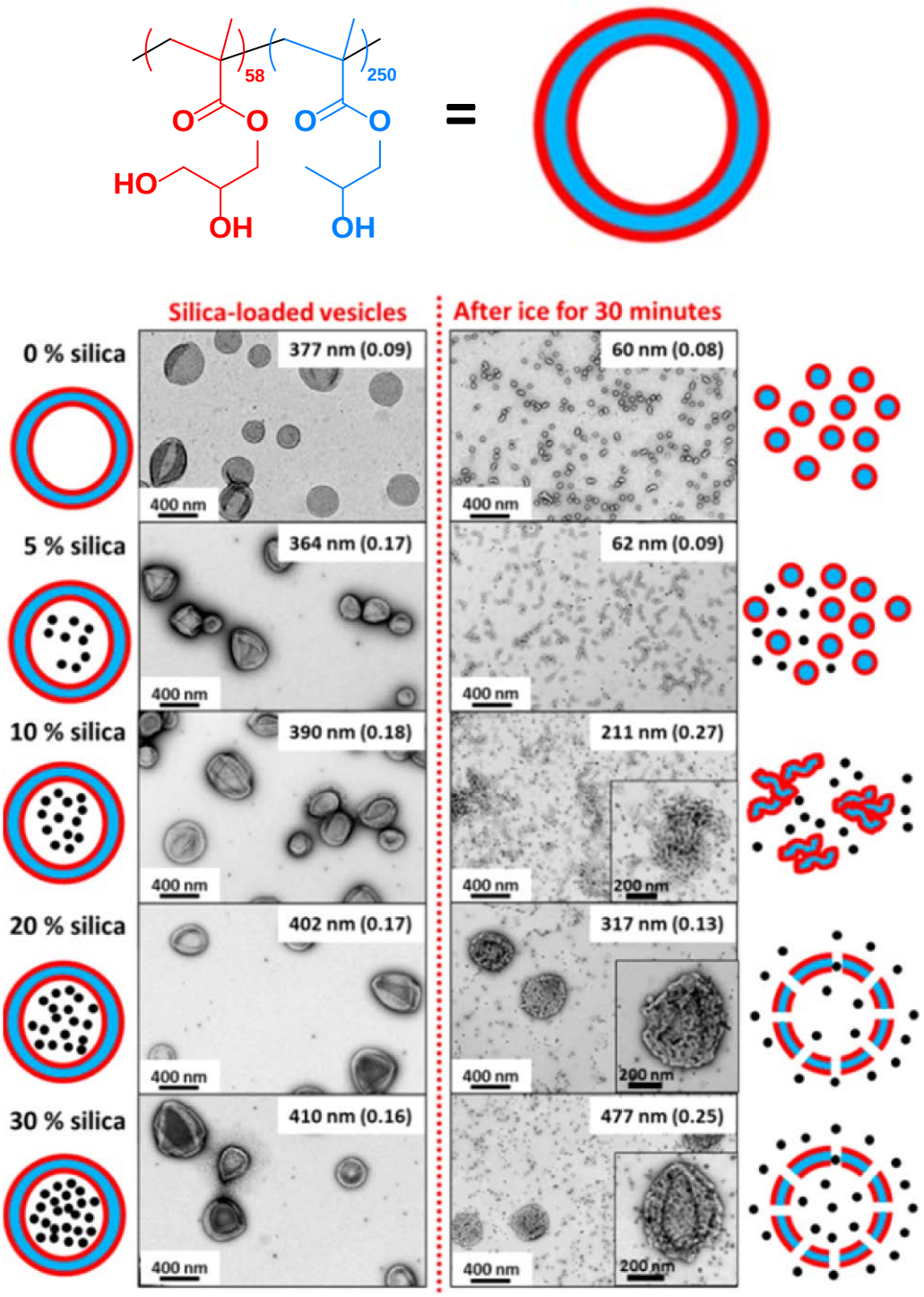

Figure 5.1. Chemical structure of the $G_{58}H_{250}$ diblock copolymer, TEM images and schematic cartoons of silica-loaded $G_{58}H_{250}$ diblock copolymer vesicles synthesised in the presence of varying amounts of silica nanoparticles (0−30 % w/w silica) after six centrifugation-redispersion cycles to remove excess silica, before (left) and after (right) being held in ice for 30 min. Dynamic light scattering hydrodynamic diameters and associated polydispersities are stated in the inset of each TEM image.

TEM images and dynamic light scattering (DLS) studies indicated that the empty and silica-loaded $G_{58}H_{250}$ vesicles each had a mean hydrodynamic diameter (D_h) of approximately 350 nm at 25 °C (see Figure 5.1). However, when the empty vesicles were cooled in ice for 30 min, spheres were obtained with a D_h of 60 nm (see Figure 5.1). This morphological transition was expected, because a mean DP of 250 was targeted for the structure-directing PHPMA block so as to produce vesicles that lie close to the worm-vesicle phase boundary.[5] Cooling leads to greater surface plasticisation of the PHPMA membranes, which results in a thermally-triggered morphological transition to produce either worms or spheres.

Similar observations were made for the silica-loaded $G_{58}H_{250}$ diblock copolymer vesicles synthesised in the presence of 5.0 % w/w silica nanoparticles. After cooling to 0 °C for 30 min, a mixture of pseudo-spherical copolymer nanoparticles and free silica nanoparticles can be observed by TEM (see Figure 5.1). Moreover, the D_h is reduced from 364 nm at 25 °C to 62 nm after 30 min at 0 °C. These results confirm that the silica-loaded vesicles dissociate to form spheres under these conditions, thus releasing the encapsulated silica nanoparticles.

For the silica-loaded $G_{58}H_{250}$ vesicles synthesised in the presence of 10 % w/w silica, worm-like aggregates and free silica nanoparticles are observed by TEM after 30 min at 0 °C (see Figure 5.1). Furthermore, for silica-loaded $G_{58}H_{250}$ vesicles synthesised in the presence of 20 or 30 % w/w silica, TEM analysis suggests that at least some of the vesicles remain intact, despite apparent release of the encapsulated silica nanoparticles (see Figure 5.1). In both cases, DLS studies indicate little change in D_h. However, close inspection reveals that the remaining vesicles after cooling to 0 °C for 30 min appear to have perforated membranes (see cartoon in Figure 5.1**)**. Prior to this study, we did not anticipate that the encapsulated silica payload might affect the thermally-triggered morphological transition because the vesicles comprise the same $G_{58}H_{250}$ copolymer composition in all cases. However, both TEM images and DLS studies indicate that increasing the silica payload leads to qualitatively different thermoresponsive behaviour.

Both Derry et al.[14] and Förster and co-workers[15] have recently reported that time-resolved SAXS can be used to monitor changes in block copolymer morphology over time. Thus, in order to gain a better understanding of the silica release mechanism(s),

time-resolved SAXS studies were conducted on the $G_{58}H_{250}$ vesicles prepared *via* PISA at 10 % w/w copolymer in the presence of either 0, 5 or 30 % w/w silica nanoparticles. These dispersions were purified to remove excess silica via multiple centrifugation-redispersion cycles, then diluted to 1.0 % w/w copolymer and cooled to 0 ^{o}C for 30 min while recording SAXS patterns at 15 s intervals.

SAXS patterns obtained for the empty $G_{58}H_{250}$ vesicles suggest that they remained intact for up to 5 min at 0 ^{o}C. Selected SAXS patterns (recorded after 0, 2.5 and 5 min) were fitted using a vesicle model,[16] which provided satisfactory data fits (see Figure 5.2). The radius from the centre of the vesicle to the centre of the membrane, R_m, remained relatively constant, while the mean vesicle membrane thickness, T_m, was reduced from 15.9 ± 2.5 nm to 10.9 ± 3.6 nm over time at 0 ^{o}C. The volume fraction of water within the membrane, x_{sol}, increased from 0.16 to 0.69 after 5 min at 0 ^{o}C. This indicates greater hydration of the core-forming PHPMA block, as previously reported by Blanazs *et al*. for $G_{54}H_{140}$ worms at 4 °C.[17, 18]

After 5 min, the highly plasticised vesicles begin to dissociate: worms are formed after 8.75 min at 0 °C, as indicated by the gradient in the I(q) vs. q plot tending to negative unity at low q.[19] An established worm-like micelle model[20-22] provided a reasonably good fit to the corresponding scattering pattern (see Figure 5.2; data set recorded after 8.75 min). The worm cross-section radius, R_{sw}, was determined to be 9.0 ± 3.1 nm, with a mean worm contour length, L_w, of 349 nm and a worm Kuhn length, L_k, of 76.2 nm. The water volume fraction x_{sol} was determined to be 0.88 for the worms, which is significantly higher than that observed for the vesicles. Such vesicle-to-worm transitions are believed to be the result of surface plasticisation of the membrane, which leads to an increase in the effective stabiliser block DP and hence a reduction in the packing parameter.[5]

After 10 min at 0 ^{o}C, a spherical dimer model[4] produced a good fit to the SAXS pattern (Figure 5.2, 10 min), indicating worm dissociation according to the model proposed by Blanazs et al.[18] The sphere core radius, R_s, and x_{sol} were determined to be 11.2 ± 4.2 nm and 0.89, respectively. The low q gradient tends to zero for all SAXS patterns collected after 12.5 min, indicating the formation of approximately spherical particles.[19] Hence a spherical micelle model[20-23] was utilised to fit all SAXS

patterns recorded over longer time scales. Data fits were consistent with the formation of spheres with a R_s of 14.6 ± 4.3 nm and an x_{sol} of 0.87.

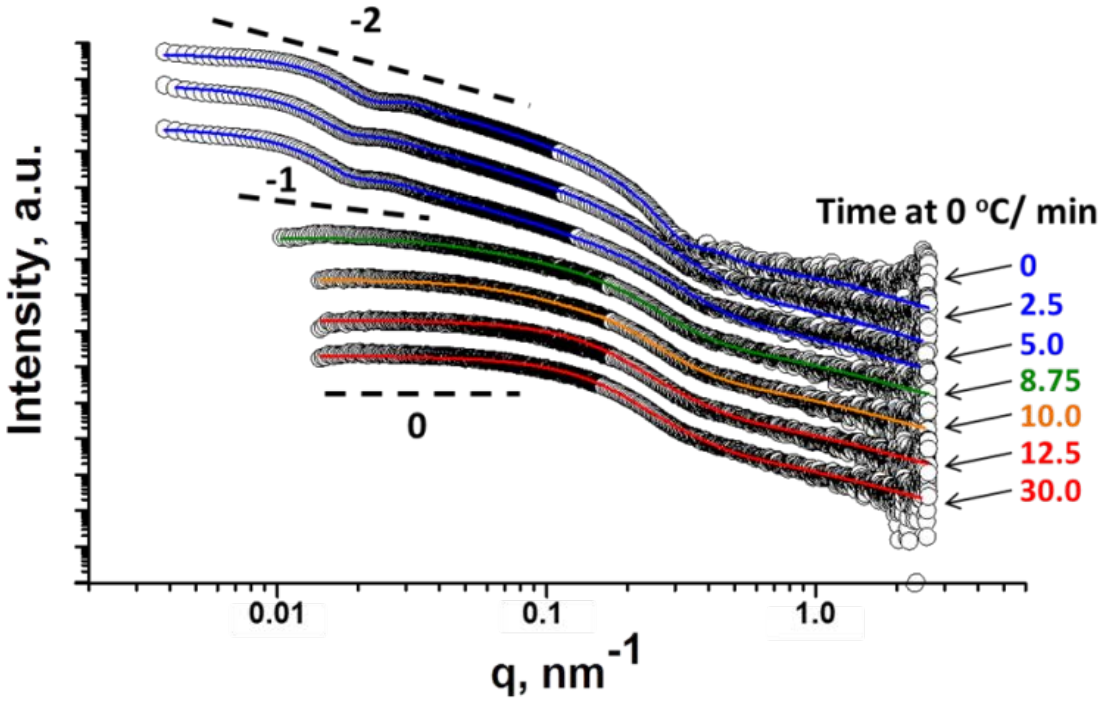

Figure 5.2. SAXS patterns obtained for 1.0 % w/w aqueous dispersions of $G_{58}H_{250}$ vesicles (originally prepared via PISA at 10 % w/w copolymer in the absence of 18.4 nm silica nanoparticles). The $G_{58}H_{250}$ vesicles were cooled to 0 °C for 30 min with scattering patterns being recorded at 15 s intervals. Selected SAXS patterns recorded after various times at 0 °C are shown (for clarity, these patterns are shifted vertically by an arbitrary scaling factor). Owing to the relatively high signal/noise ratio, patterns recorded from 8.75 min to 30 min were truncated at low *q*. Black open circles show the experimental data and data fits are indicated by solid lines. Vesicles are present at 0 °C for up to 5 min (blue fits) but subsequently undergo dissociation to form worm-like micelles after 8.75 min (green fit), followed by formation of spherical micelle dimers after 10 min (orange fit) and spheres after 12.5 min (red fits).

It is perhaps worth noting that the spherical dimers formed after 10 min have a significantly smaller R_s value compared to that obtained for the spheres formed after 12.5 min (11.2 ± 4.2 nm vs. 14.6 ± 4.3 nm, respectively). This significant increase in R_s when going from spherical dimers to spheres can be rationalised by considering the spatial redistribution of copolymer chains that occurs during this transition (see Figure 5.3). This explanation also applies to the preceding worm-to-dimer transition. In this latter case, the R_{sw} for the worms formed after 8.75 min at 0 ^{o}C is 9.0 ± 3.1 nm, which is significantly smaller than that for the dimers formed after 10 min.

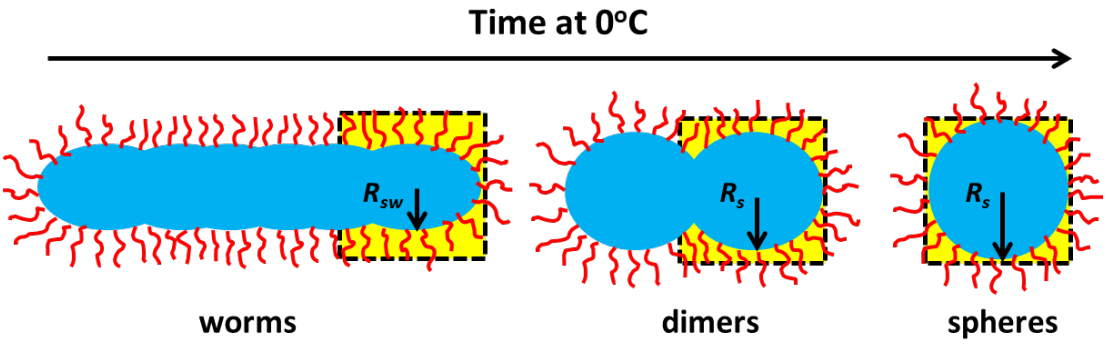

Figure 5.3. Schematic cartoon depicting the change in dimensions that occur when the $G_{58}H_{250}$ worms are converted into first spherical dimers and then spheres on cooling to 0 °C. There is a significant increase in the mean core radius on switching from worms to spherical dimers to spheres.

For the SAXS patterns recorded after 0, 8.75 and 30 min at 0 °C, data fits using appropriate models enabled the mean aggregation number (N_{agg}) for the vesicles, worms and spheres to be determined using the following three equations:

$$N_{agg}\ \text{vesicle} = (1-x_{sol})\frac{(V_{out}-V_{in})}{V_{co}} \quad (1)$$

$$N_{agg}\ \text{worm} = (1-x_{sol})\frac{\pi R_{sw}^{2} L_{w}}{V_{co}} \quad (2)$$

$$N_{agg}\ \text{sphere} = (1-x_{sol})\frac{{}^{4}/_{3}\pi R_{s}^{3}}{V_{co}} \quad (3)$$

where $V_{out} = \frac{4}{3}\pi(R_m + \frac{1}{2}T_m)^3$, $V_{in} = \frac{4}{3}\pi(R_m - \frac{1}{2}T_m)^3$ and V_{co} is the volume of the hydrophobic PHPMA core-forming block. Using the above three equations, we calculate approximately 49,900 copolymer chains per vesicle, 185 copolymer chains per worm and 29 copolymer chains per sphere. Assuming that the main source of uncertainty arises from the standard deviation in the sphere radius, a conservative estimate for the uncertainty in the associated N_{agg} is approximately 30 %. Significantly larger values are expected for the more polydisperse worms and vesicles. Nevertheless, the calculated N_{agg} values suggest that, on cooling to 0 °C, each vesicle dissociates to form 270 worms and, ultimately, 1750 spheres (thus each worm comprises approximately 7 spheres).

SAXS patterns recorded for $G_{58}H_{250}$ vesicles synthesised in the presence of 5.0 % w/w silica indicate that silica-loaded vesicles are initially present at 25 °C while spheres are formed after 30 min at 0 °C (see Figure 5.4). This vesicle-to-sphere transition is accompanied by release of the encapsulated silica nanoparticles as confirmed by TEM studies, see Figure 5.1.

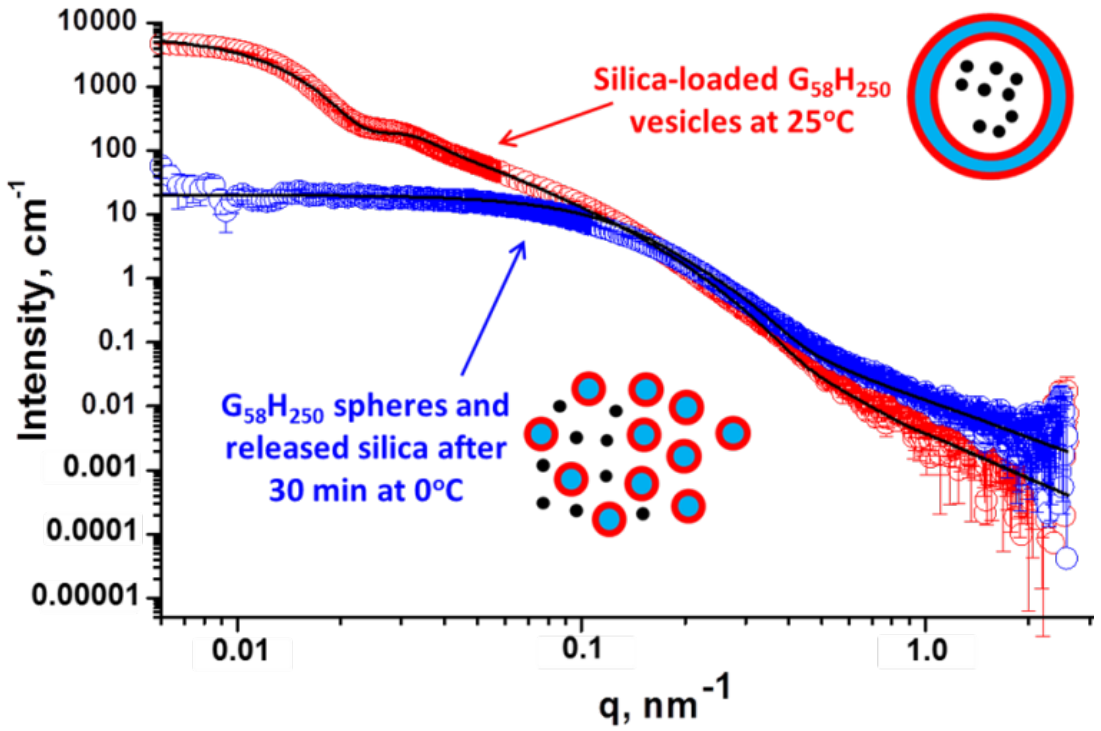

Figure 5.4. SAXS patterns obtained for a 1.0 % w/w aqueous dispersion of purified silica-loaded $G_{58}H_{250}$ vesicles (originally prepared via PISA at 10 % w/w copolymer in the presence of 5.0 % w/w silica nanoparticles) at 25 °C (red data) and after cooling the same vesicles to 0 °C for 30 min (blue data). Solid black lines represent data fits in each case using a two-population SAXS model (see main text for details).

Satisfactory fitting of the initial SAXS pattern recorded at 25 °C required a two-population 'vesicle plus sphere' model (see Appendix 7 for further details of this SAXS model).[1] The silica-loaded vesicles had a mean R_m of 127.8 ± 30.5 nm, a T_m of 15.4 ± 2.2 nm and an x_{sol} of 0.16. However, a two-population 'spherical micelle[20-23] plus sphere' model was required to obtain a reasonably good fit to the SAXS pattern observed after 30 min at 0 °C. Some deviation in the data fit was observed at around $q \sim 0.1$ nm^{-1}, which is ascribed to minor populations of dimers and trimers.[4] Such species can be observed in the TEM image shown in Figure 5.1. As expected,

the silica nanoparticles were unaffected by lowering the temperature because the R_s for this component remained constant at 9.2 ± 2.1 nm. The $G_{58}H_{250}$ spheres formed after 30 min at 0 °C exhibited an R_s of 14.6 ± 4.3 nm and an x_{sol} of 0.88, which are comparable values to those obtained after dissociation of the empty $G_{58}H_{250}$ vesicles. In summary, the thermally-triggered morphological transition observed for the silica-loaded $G_{58}H_{250}$ vesicles prepared in the presence of 5.0 % w/w silica nanoparticles is essentially identical to that found for the empty $G_{58}H_{250}$ vesicles.

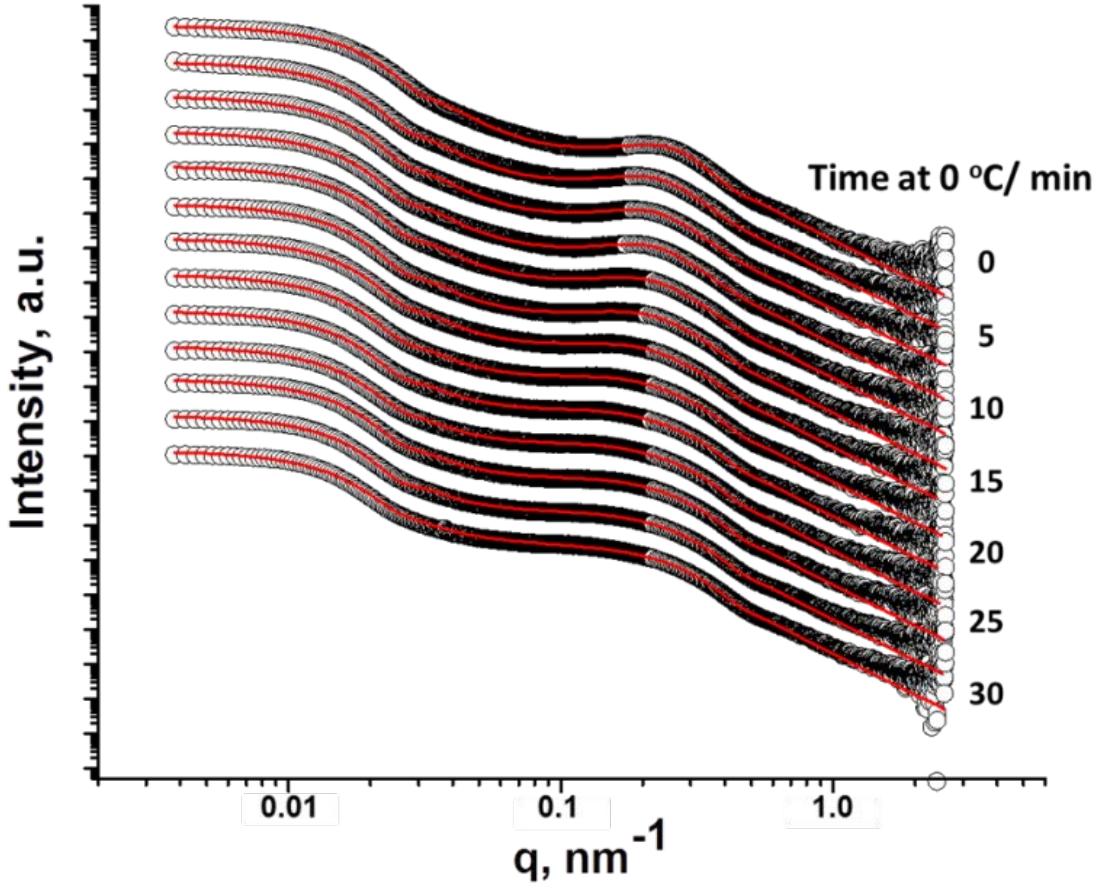

Figure 5.5. SAXS patterns obtained for a 1.0 % w/w aqueous dispersion of $G_{58}H_{250}$ vesicles (originally prepared via PISA at 10 % w/w copolymer in the presence of 30 % w/w silica nanoparticles). Excess non-encapsulated silica nanoparticles were removed via six centrifugation−redispersion cycles. The resulting purified silica-loaded $G_{58}H_{250}$ vesicles were cooled to 0 °C for 30 min while SAXS patterns were recorded at 15 s intervals. Only selected patterns recorded after various times at 0 °C are shown (for clarity, these patterns are shifted vertically by an arbitrary scaling factor). The experimental data are represented by black open circles while solid red lines show the data fits calculated using a two-population 'vesicle plus sphere' model.

In contrast, time-resolved SAXS patterns recorded for silica-loaded $G_{58}H_{250}$ vesicles prepared in the presence of 30 % w/w silica nanoparticles indicate that the original vesicles remained intact after cooling to 0 ^{o}C for 30 min (see Figure 5.5). These observations are also supported by TEM studies (see Figure 5.1). However, the structure factor peak at $q \sim 0.25$ nm^{-1} corresponding to the relatively high local concentration of encapsulated silica nanoparticles gradually disappears over time. This is consistent with release of the encapsulated nanoparticles, since this leads to a reduction in the effective silica concentration.

Fitting the corresponding SAXS patterns requires a sophisticated model that accounts for both the $G_{58}H_{250}$ vesicles and the spherical silica nanoparticles (see Appendix 7 for further information).[1] In order to study the extent of silica release under such conditions, this 'vesicle plus sphere' two-population model was modified to include two new fitting parameters. For the vesicle model, the effective scattering length density of the lumen, ξ_{lum}, was included as a fitting parameter in order to assess the rate of silica release from the vesicles at 0 ^{o}C. The scattering length density of pure amorphous silica, ξ_{SiO_2}, is 17.5 × 10^{10} cm^{-2} and that of water, ξ_{H_2O}, is 9.42 × 10^{10} cm^{-2}. At 25 °C, the vesicle lumen contains both silica nanoparticles and water. Fitting the SAXS pattern of the original silica-loaded vesicles indicates that ξ_{lum} is 11.75 × 10^{10} cm^{-2}. This value is intermediate between that of silica and water, as expected. The numerical value of ξ_{lum} is gradually reduced over time at 0 ^{o}C (see Figure 5.6a and Table 5.2). For example, the ξ_{lum} decreased to 10.99 × 10^{10} cm^{-2} after 15 min at 0 ^{o}C, and to 10.67 × 10^{10} cm^{-2} after a further 15 min. This reduction in x-ray contrast for the lumen confirms that the encapsulated silica nanoparticles are gradually released from the vesicles over time. Furthermore, these data suggest that initially the vesicle lumen contains approximately 29 vol. % silica (with the remaining volume being water), which is reduced to 15 vol. % silica after 30 min at 0 ^{o}C. This suggests that approximately 52 % of the encapsulated silica nanoparticles are released under these conditions. However, the ξ_{lum} is an average over the entire lumen. It assumes that the silica nanoparticles (and hence the electrons) are uniformly distributed throughout the vesicle lumen, but in practice this may not be the case.

For the sphere model, two sub-populations are used to model the silica component for the release kinetics: the silica nanoparticles released from the vesicles are

described by a spherical form factor while the silica nanoparticles remaining within the vesicle lumen are described by a sphere model with a structure factor for interacting hard spheres. The relative contributions made to the overall scattering by these two sub-populations were used to determine the fraction of encapsulated silica nanoparticles at any given time interval (see Appendix 7, Equation A7.10). The volume fraction of released silica, C_{rel}, was included as a fitting parameter.

C_{rel} increased from 3.19×10^{-5} at 0 °C and 0 min to 9.04×10^{-4} after 30 min at 0 °C (see Figure 5.6b and Table 5.2). As expected, the overall silica volume fraction in the dispersion, C_{SiO_2}, remains essentially constant, which validates this analytical approach (see Figure 5.6b and Table 5.2). SAXS analysis indicates that 68 % silica is released from the silica-loaded vesicles within 30 min at 0 °C. This is reasonably comparable to the release of 52 % silica estimated by fitting ξ_{lum} under the same conditions.

As discussed above, the ξ_{lum} is averaged over the entire vesicle lumen, so the value obtained from the measurements of C_{rel} is considered to be more accurate. Furthermore, the Percus-Yevick correlation radius for densely-packed spheres (R_{PY}) was 113 nm at 0 °C and 0 min and 251 nm after 30 min at 0 °C (see Table 5.2). This suggests that the released silica nanoparticles become well-dispersed in the aqueous continuous phase after vesicle dissociation occurs. Moreover, the Percus-Yevick effective volume fraction for packed spheres, f_{PY}, is reduced from 0.195 to 0.066 (see Table 5.2), thus confirming partial release of the silica nanoparticles from the vesicle lumen.

In summary, the silica nanoparticles are initially relatively densely-packed within the vesicles at 25 °C, which leads to a prominent structure factor, a high ξ_{lum}, a small C_{rel}, a short R_{PY} and a large f_{PY}. After 30 min at 0 °C, a substantial fraction of the encapsulated silica nanoparticles are released from the slowly dissociating vesicles, leading to loss of the original structure factor, a lower ξ_{lum}, a larger C_{rel}, a larger R_{PY} and a smaller f_{PY}.

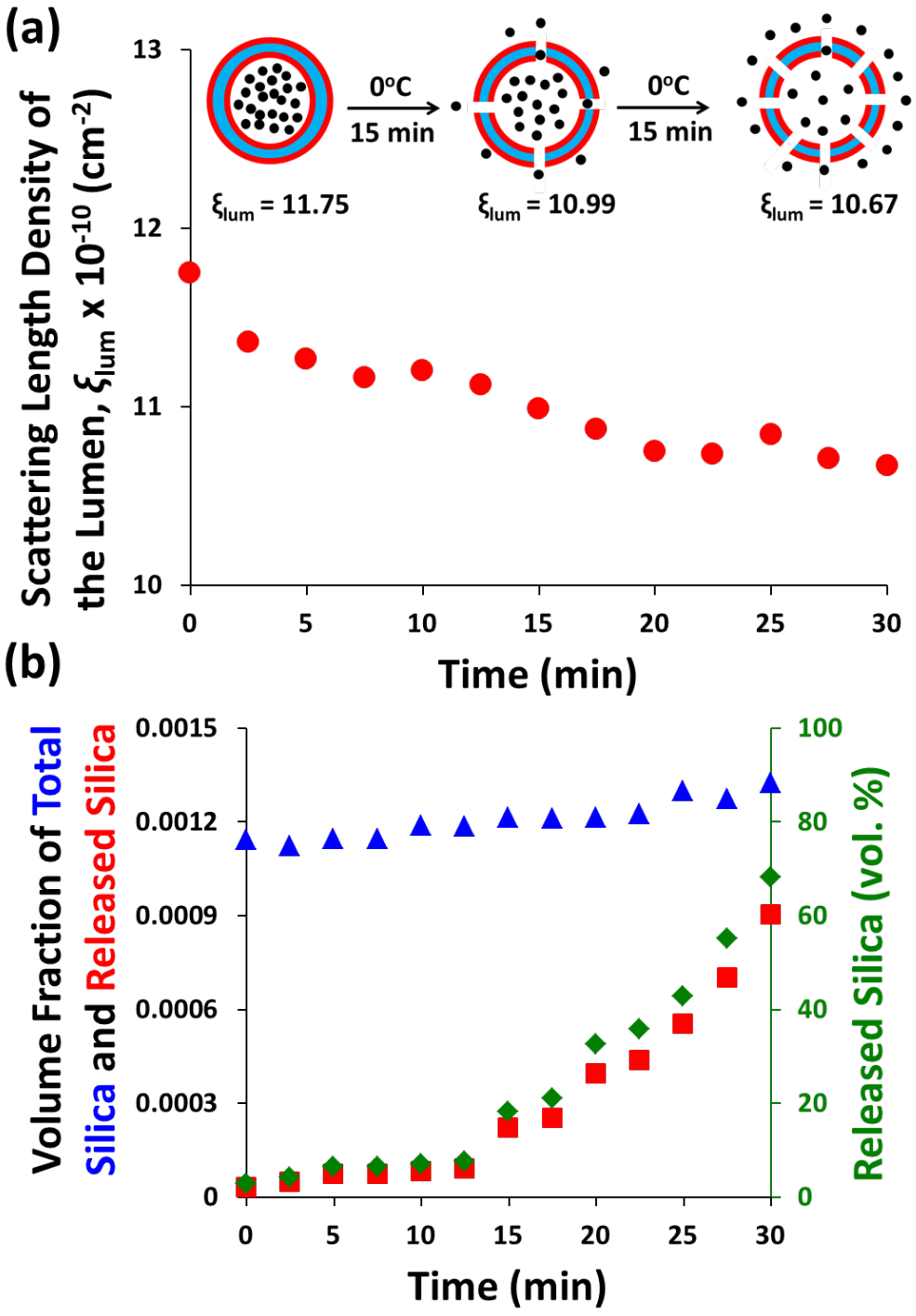

Figure 5.6. (a) Plot of the scattering length density of the $G_{58}H_{250}$ diblock copolymer vesicle lumen (ξ_{lum}) against time held at 0 °C (red circles). Inset: schematic cartoon illustrating how the release of silica nanoparticles from inside the vesicles changes the ξ_{lum} as the purified silica-loaded vesicles (originally prepared via PISA at 10 % w/w copolymer in the presence of 30 % w/w silica) are cooled to 0 °C for 30 min. (b) A plot of the total volume fraction of silica in the system (blue triangles corresponding to left y-axis), the volume fraction of released silica (red squares corresponding to left y-axis) and the percentage of released silica (green diamonds corresponding to right y-axis) against the time at which the purified silica-loaded $G_{58}H_{250}$ diblock copolymer vesicles (originally prepared with 30 % w/w silica) were cooled at 0 °C.

Table 5.2. Summary of SAXS structural parameters obtained for diluted 1.0 % w/w aqueous copolymer dispersions of purified $G_{58}H_{250}$ vesicles (originally prepared via PISA at 10 % w/w copolymer in the presence of 30 % w/w silica) when cooled to 0 °C for 30 min. Scattering patterns were recorded every 15 s. Selected SAXS patterns recorded after 2.5 min intervals at 0 °C were analysed using a two-population model comprising vesicles and spheres, with the latter component representing the silica nanoparticles. Vesicle parameters for population 1 are as follows: R_m is the mean radius from the centre of the vesicle to the centre of the membrane, σ_{Rm} is the associated standard deviation and ξ_{lum} is the scattering length density of the vesicle lumen. Sphere parameters for population 2 are as follows: C_{SiO_2} is the total volume fraction of silica nanoparticles in the aqueous dispersion, C_{rel} is the volume fraction of released silica nanoparticles, f_{PY} is the Percus-Yevick effective volume fraction of the packed silica spheres and R_{PY} is the Percus-Yevick correlation radius of the packed spheres.

Time /min	Population 1 (Vesicles)[a]		Population 2 (Silica nanoparticles)[b]			
	R_m (σ_{Rm}) / nm	ξ_{lum}	C_{SiO_2}	C_{rel}	f_{PY} /nm	R_{PY} /nm
0	141.0 (26.7)	11.75	0.00114	0.0000319	0.195	113
2.5	148.3 (33.3)	11.36	0.00112	0.0000477	0.175	127
5.0	149.9 (32.8)	11.26	0.00115	0.0000734	0.175	130
7.5	150.3 (32.7)	11.16	0.00115	0.0000736	0.177	132
10.0	150.9 (31.4)	11.20	0.00119	0.0000830	0.150	136
12.5	149.5 (31.7)	11.12	0.00119	0.0000908	0.131	134
15.0	149.1 (33.8)	10.99	0.00121	0.0002213	0.114	148
17.5	149.3 (34.0)	10.87	0.00121	0.0002547	0.086	158
20.0	149.8 (33.3)	10.75	0.00121	0.0003959	0.069	170
22.5	147.3 (36.2)	10.73	0.00123	0.0004388	0.063	181
25.0	149.0 (33.6)	10.85	0.00130	0.0005559	0.066	156
27.5	150.7 (33.3)	10.71	0.00127	0.0007022	0.048	161
30.0	146.7 (39.0)	10.67	0.00132	0.0009038	0.066	251

[a] The copolymer volume fraction in the dispersion ($C_{copolymer}$), the membrane thickness (T_m) and its associated standard deviation (σ_{Tm}) and the radius of gyration of the PGMA corona block (R_g) were each fixed at 0.001, 15.9 nm, 2.2 nm, and 2.3 nm, respectively.

[b] The core radius (R_{SiO_2}) and its associated standard deviation (σ_{RSiO_2}) were fixed at 9.2 nm and 2.1 nm, respectively.

Discussion

One important question that arises from this study is the following: how do the encapsulated silica nanoparticles get released if the vesicles sometimes apparently remain intact? In principle, one plausible explanation is that the smaller vesicles dissociate preferentially compared to the larger vesicles because the former species have a higher radius of curvature. If such size-dependent dissociation occurred, the mean vesicle diameter should increase with ageing time at 0^{o}C with a concomitant reduction in the vesicle number density. The latter parameter can be estimated using the x-ray scattering intensity at 0.01 nm^{-1} and does indeed decrease approximately two-fold (from ~16,000 cm^{-1} to ~7,000 cm^{-1}; see Figure 5.7). However, the mean vesicle radius, R_m, remains relatively constant at ~149 nm for the $G_{58}H_{250}$ vesicles, regardless of their ageing time at 0 ^{o}C (see Table 5.2). This suggests that vesicle dissociation is not in fact size-dependent.

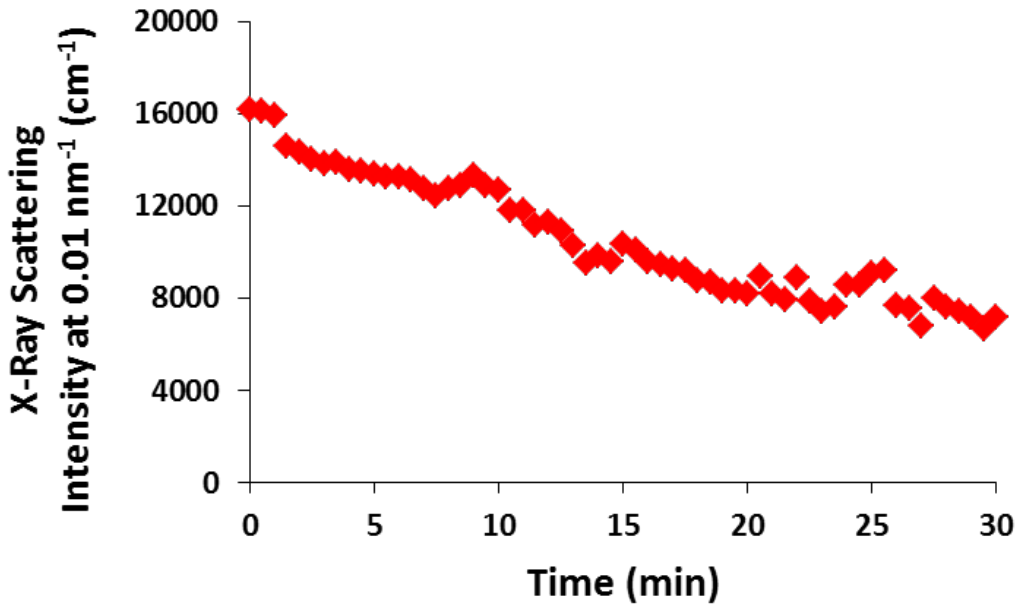

Figure 5.7. Time dependence of the x-ray scattering intensity at q = 0.01 nm^{-1} for purified silica-loaded $G_{58}H_{250}$ vesicles after cooling to 0 ^{o}C. In this example, the $G_{58}H_{250}$ vesicles were prepared in the presence of 30 % w/w silica nanoparticles.

An alternative explanation is that all vesicles, regardless of their size, eventually comprise perforated (and hence permeable) membranes while remaining intact, enabling silica nanoparticles to diffuse out through the increasingly porous

membrane. As discussed above, TEM images suggest that the vesicles do indeed remain intact and there is also good evidence for membrane perforation. Moreover, close inspection suggest that the pore dimensions are comparable to the number-average diameter of the silica nanoparticles (estimated to be 13 ± 3 nm by measuring 100 nanoparticles). Hence in principle the silica nanoparticles can escape from the vesicles if membrane perforation becomes extensive. However, this hypothesis does not explain the apparent reduction in vesicle number density indicated in the SAXS studies, unless this is actually an artefact related to membrane perforation.

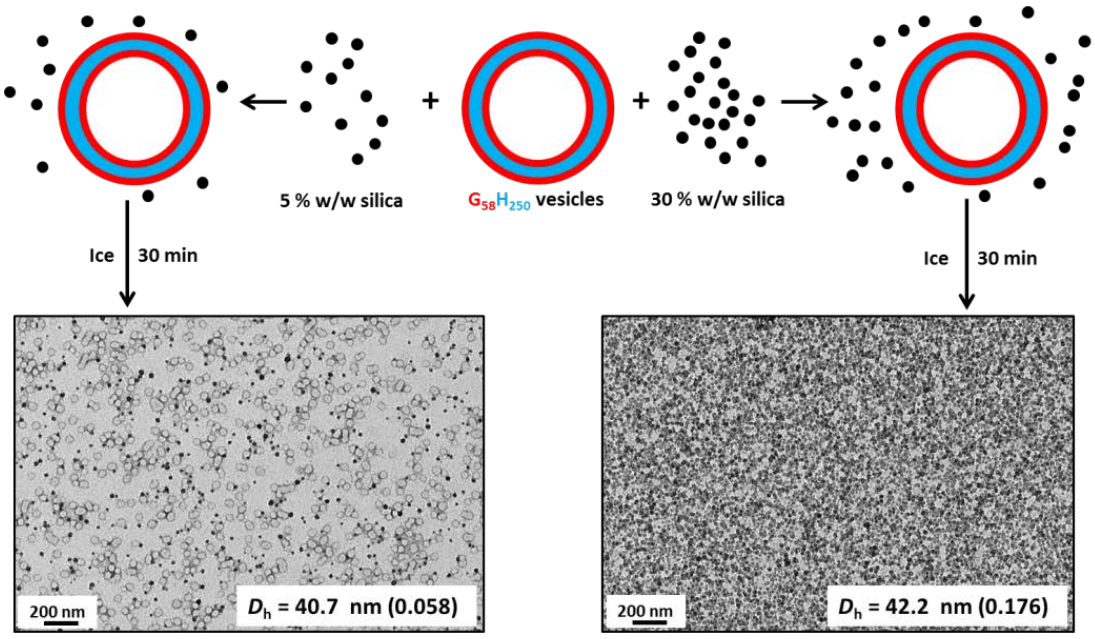

Figure 5.8. Schematic cartoon illustrating control experiments in which either a 5 % w/w or a 30% w/w aqueous dispersion of glycerol-functionalised silica nanoparticles was added to empty $G_{58}H_{250}$ diblock copolymer vesicles and subsequently cooled in ice for 30 min. TEM images and dynamic light scattering data (see inset text) indicate that $G_{58}H_{250}$ spheres were formed in both cases, regardless of the silica concentration.

Moreover, neither hypothesis explains why $G_{58}H_{250}$ vesicles readily dissociate to form spheres in the absence of any silica nanoparticles, yet do not apparently undergo dissociation at all if they contain relatively high silica loadings. Thus control experiments were performed to examine whether varying the silica nanoparticle concentration present in the continuous phase had any significant effect on the vesicle release kinetics or mechanism. Empty $G_{58}H_{250}$ vesicles prepared in the absence of any silica nanoparticles were added in turn to either a 5.0 % w/w or 30 %

w/w aqueous dispersion of silica nanoparticles. Each vesicle/silica binary mixture was then cooled to 0 °C for 30 min. TEM studies confirmed that the empty vesicles dissociated to form spheres, regardless of the background silica concentration (see Figure 5.8). Thus the presence of silica in the aqueous continuous phase clearly does not confer additional vesicle stabilisation.

According to a recent review article by Dimova, "*the bending rigidity of membranes is a sensitive indicator for the presence of inclusions or adsorbing species*".[24] Thus an intriguing question is whether the encapsulated silica nanoparticles can somehow reinforce the vesicle membrane. At first sight, this tentative explanation looks rather attractive, because the silica-loaded vesicles certainly become significantly more stable than empty vesicles when subjected to the same thermal trigger. Furthermore, higher silica loadings enhance the vesicle membrane stability with respect to the thermally-triggered release of such nanoparticles. In principle, the silica nanoparticles may physically adsorb to the inner surface of the vesicle lumen, which is likely to reinforce the vesicle morphology. However, there is no direct experimental evidence to support this hypothesis, either in the TEM images or in the SAXS data collected at 25^{o}C. [If silica nanoparticles did adsorb to the inner lumen, the most likely change in the SAXS pattern would be a more pronounced structure factor at intermediate *q*. Unfortunately, SAXS is not sufficiently sensitive to detect such local ordering].

The silica nanoparticle concentration within the vesicles also affects the characteristic time scale required for the observed morphological transitions. The x-ray scattering intensity at $q \sim 0.01$ nm^{-1} was analysed over time at 0 °C (see Figure 5.9). For the $G_{58}H_{250}$ vesicles prepared in the absence of any silica, the vesicle-to-sphere transition requires approximately 12 min for completion, whereas the same transition requires around 14 min for $G_{58}H_{250}$ vesicles prepared in the presence of 5.0 % w/w silica. For $G_{58}H_{250}$ vesicles prepared in the presence of 10 % w/w silica, the morphological transition from silica-loaded vesicles to worm clusters plus released silica requires approximately 16 min. For vesicles prepared in the presence of 20 or 30 % w/w silica, the morphological transition to perforated vesicles requires around 21 min and 23 min, respectively. These observations confirm that the silica nanoparticle loading achieved during the *in situ* PISA synthesis of these diblock

copolymer vesicles has a significant influence on the thermal stability of the vesicular morphology.

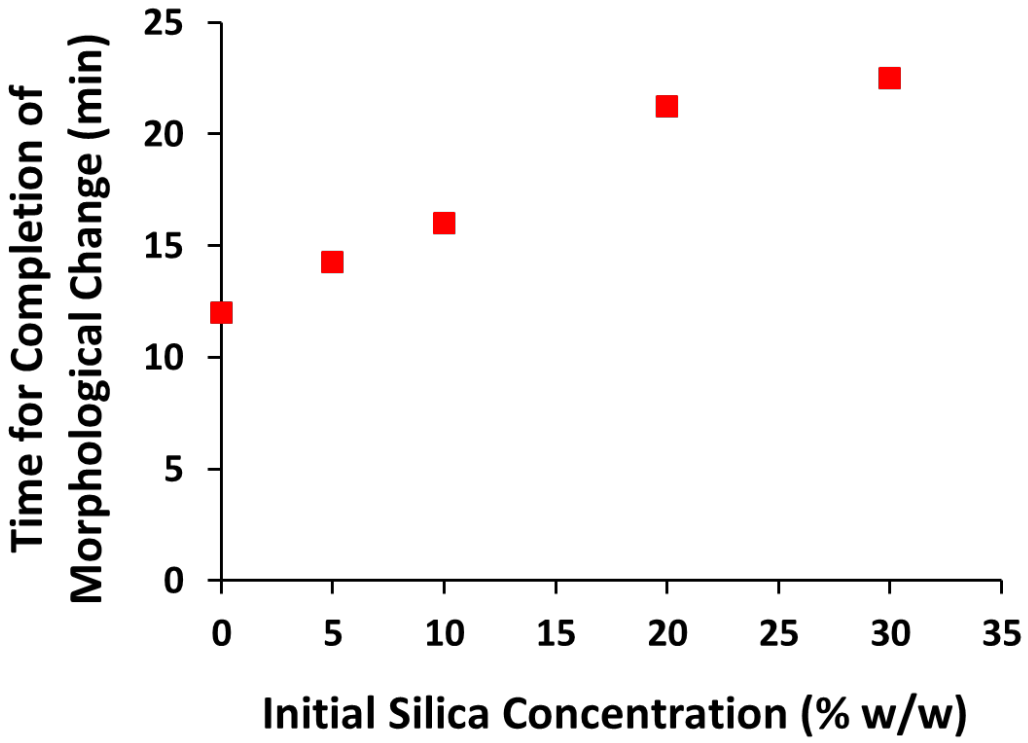

Figure 5.9. Relationship between the initial silica nanoparticle concentration against time required for completion of the morphological transition of the $G_{58}H_{250}$ diblock copolymer vesicles on cooling to 0 °C. The characteristic time taken for the morphological transition was estimated from the change in intensity of the SAXS patterns recorded at q = 0.01 nm^{-1}.

Conclusions

The thermally-triggered release of silica nanoparticles within $G_{58}H_{250}$ diblock copolymer vesicles has been studied. When silica-loaded vesicles are held at 0 °C for 30 min, TEM images suggest that the fundamental nature of the vesicle dissociation is profoundly affected by the concentration of silica nanoparticles within the lumen. For PISA syntheses conducted in the presence of either no silica or 5.0 % w/w silica, the expected vesicle-to-sphere transition is observed. When using 10 % w/w silica, the silica-loaded vesicles form aggregated worm clusters on cooling. For 20 or 30 % w/w silica, vesicle membranes gradually become perforated, with at least some vesicles remaining intact after 30 min at 0 °C. In all cases, the encapsulated silica

nanoparticles are released from the vesicles. Time-resolved SAXS experiments conducted at 0 °C allow the release kinetics to be examined. For empty $G_{58}H_{250}$ vesicles, the vesicles remain intact for 5 min, form worms after 8.75 min, spherical dimers after 10 min and finally spheres after 12.5 min. Fitting selected SAXS patterns using an appropriate model enables mean aggregation numbers to be calculated for each morphology, with each vesicle dissociating to afford approximately 1750 spheres. For $G_{58}H_{250}$ vesicles prepared in the presence of 30 % w/w silica, time-resolved SAXS experiments conducted at 0 °C suggest that most of the vesicles remain intact. However, the disappearance of the silica structure factor present in the original SAXS pattern indicates that the encapsulated silica is released, presumably through perforated vesicle membranes. Data fits for selected SAXS patterns revealed that the scattering length density of the vesicle lumen is reduced monotonically over time for silica-loaded vesicle dispersions held at 0 °C. More detailed analysis revealed that 68% of the encapsulated silica nanoparticles were released within 30 min under these conditions.

References

1. C. J. Mable, R. R. Gibson, S. Prevost, B. E. McKenzie, O. O. Mykhaylyk and S. P. Armes, *Journal Of The American Chemical Society*, 2015, **137**, 16098-16108.
2. S. Rose, A. Prevoteau, P. Elziere, D. Hourdet, A. Marcellan and L. Leibler, *Nature*, 2014, **505**, 382-385.
3. A. Sundararaman, T. Stephan and R. B. Grubbs, *Journal Of The American Chemical Society*, 2008, **130**, 12264-12265.
4. N. J. Warren, O. O. Mykhaylyk, D. Mahmood, A. J. Ryan and S. P. Armes, *Journal Of The American Chemical Society*, 2013, **136**, 1023-1033.
5. J. R. Lovett, N. J. Warren, S. P. Armes, M. J. Smallridge and R. B. Cracknell, *Macromolecules*, 2016, **49**, 1016-1025.
6. J.-M. Schumers, C.-A. Fustin and J.-F. Gohy, *Macromolecular Rapid Communications*, 2010, **31**, 1588-1607.
7. L. Zhang and A. Eisenberg, *Macromolecules*, 1996, **29**, 8805-8815.
8. K. Yu and A. Eisenberg, *Macromolecules*, 1998, **31**, 3509-3518.
9. C. Maiti, R. Banerjee, S. Maiti and D. Dhara, *Langmuir*, 2015, **31**, 32-41.
10. J. Du, Y. Tang, A. L. Lewis and S. P. Armes, *Journal Of The American Chemical Society*, 2005, **127**, 17982-17983.
11. J. Rodríguez-Hernández and S. Lecommandoux, *Journal Of The American Chemical Society*, 2005, **127**, 2026-2027.
12. M. Scherer, C. Kappel, N. Mohr, K. Fischer, P. Heller, R. Forst, F. Depoix, M. Bros and R. Zentel, *Biomacromolecules*, 2016, **17**, 3305-3317.
13. J. Ilavsky and P. R. Jemian, *Journal of Applied Crystallography*, 2009, **42**, 347-353.

14. M. J. Derry, L. A. Fielding, N. J. Warren, C. J. Mable, A. J. Smith, O. O. Mykhaylyk and S. P. Armes, *Chemical Science*, 2016, **7**, 5078-5090.
15. C. Fürst, P. Zhang, S. V. Roth, M. Drechsler and S. Förster, *Polymer*, 2016, **107**, 434-444.
16. J. Bang, S. Jain, Z. Li, T. P. Lodge, J. S. Pedersen, E. Kesselman and Y. Talmon, *Macromolecules*, 2006, **39**, 1199-1208.
17. J. Madsen, S. P. Armes and A. L. Lewis, *Macromolecules*, 2006, **39**, 7455-7457.
18. A. Blanazs, R. Verber, O. O. Mykhaylyk, A. J. Ryan, J. Z. Heath, C. W. I. Douglas and S. P. Armes, *Journal Of The American Chemical Society*, 2012, **134**, 9741–9748.
19. O. Glatter and O.Kratky, *Small-angle X-ray Scattering*, Academic Press, London, 1982.
20. J. S. Pedersen, *Journal of Applied Crystallography*, 2000, **33**, 637-640.
21. J. S. Pedersen and P. Schurtenberger, *Macromolecules*, 1996, **29**, 7602-7612.
22. V. J. Cunningham, L. P. D. Ratcliffe, A. Blanazs, N. J. Warren, A. J. Smith, O. O. Mykhaylyk and S. P. Armes, *Polymer Chemistry*, 2014, **5**, 6307-6317.
23. J. S. Pedersen and M. C. Gerstenberg, *Macromolecules*, 1996, **29**, 1363-1365.
24. R. Dimova, *Advances in Colloid and Interface Science*, 2014, **208**, 225-234.

Chapter Six - Conclusions and Future Work

Conclusions and Future Work

A range of block copolymer morphologies, such as spheres, worms and vesicles, can be accessed via PISA during RAFT aqueous dispersion polymerisation of HPMA. Generally speaking, the precise copolymer composition dictates the final copolymer morphology, although copolymer concentration can also be an important parameter. PGMA-PHPMA vesicles can be prepared in the form of concentrated dispersions *via* jellyfish intermediates. In principle, the 'open' nature of such jellyfish should allow *in situ* encapsulation. In practice, the encapsulation of water-soluble small molecules is problematic because of the permeability of the highly plasticised PHPMA membranes. However, silica nanoparticles (and globular proteins such as BSA[1]) can be encapsulated and retained within the vesicle lumen. Under optimised conditions, up to hundreds of silica nanoparticles can be encapsulated per vesicle. However, the time scale required for silica diffusion into the vesicle lumen is relatively long compared to that for complete fusion of the vesicle membrane. Hence the encapsulation efficiency of silica nanoparticles is relatively low at approximately 27 %. Controlled release of these silica nanoparticles has been demonstrated by cooling the thermosensitive PGMA-PHPMA vesicles to 0 - 10 ^{o}C. Surprisingly, the precise release mechanism depends on the initial silica concentration within the vesicle lumen. However, it is difficult to identify a real-world application where such low temperatures would be appropriate for triggered release.

Leibler and co-workers[2] have recently reported that silica nanoparticles enable the convenient repair of cleaved synthetic hydrogels or biological tissue (e.g. organs such as the liver). Hence silica nanoparticles may actually constitute a biomedically-relevant active species. In principle, the silica-loaded vesicles synthesised in Chapter Four could provide a 'self-healing' formulation for synthetic hydrogels, and perhaps also biological tissues. We have collaborated with Leibler's group to examine the glycerol-functionalised silica used herein for the attempted adhesion of gels and/or biological tissues. Unfortunately, these surface-treated silica nanoparticles were not successful in repairing cleaved hydrogels. Ideally, the specific silica sol (Ludox TM-50) used by Leibler and co-workers in their 2014 Nature paper should be utilised instead. However, our attempts to encapsulate such silica nanoparticles within

PGMA-PGPMA vesicles have been unsuccessful. However, another team has reported successful encapsulation of such non-functionalised anionic silica sols within poly(ethylene glycol)-poly(2-hydroxypropyl methacrylate) (PEG-PHPMA) diblock copolymer vesicles.[3] This synthetic protocol involved photo-initiated PISA at 20 °C. It is not clear whether such milder conditions are essential or whether the key difference involves switching from the steric stabiliser from PGMA to PEG. This aspect warrants further study and the collaboration with Leibler's team may be worth revisiting in the future.

In principle, diblock copolymer vesicles could be designed whereby the membrane-forming block exhibits UCST-like thermosensivity, rather than LCST-like behaviour. If successful, this would enable silica release to be triggered on heating rather than by cooling, which may open up new commercial applications. Moreover, various other functional nanoparticles could be encapsulated within vesicles. For example, quantum dots may be useful for fluorescence imaging while encapsulation of magnetite sols would confer magnetoresponsivity. In addition, gold sols can absorb near-infrared light which leads to localised heating that can destroy cancer cells.[4]

RAFT seeded emulsion polymerisation of a third water-immiscible monomer (BzMA) from PGMA-PHPMA precursor vesicles leads to the formation of PGMA-PHPMA-PBzMA triblock copolymer vesicles with a distinctive framboidal morphology. It has been shown that the ability to fine-tune the surface roughness of such vesicles is the key to optimising their performance as Pickering emulsifiers. Framboidal vesicles containing surface globules of 45 nm diameter exhibited an optimum Pickering emulsifier adsorption efficiency of 94 %. Moreover, literature precedent suggests that nanoparticles with pronounced surface topography undergo more efficient cell uptake.[5, 6] Thus such framboidal nanoparticles may also be of interest for fundamental studies of the effect of surface topology on cell uptake kinetics.[6] For example, it has been recently reported that the Dengue virus undergoes a temperature-driven conformational transition from a smooth to rough particle surface.[6] The smooth structure is present when the virus is non-infective within its mosquito host at 25 ^{o}C while the framboidal-like morphology is adopted when incubated at 37 ^{o}C.[7, 8] Since the latter temperature corresponds to human body

temperature, it is believed that this change in morphology is intimately associated with human infection by the Dengue virus. This conformational transition is remarkably similar to that reported in Chapter Two, whereby the smooth PGMA-PHPMA vesicles become framboidal when chain-extended with BzMA. Thus, these PGMA-PHPMA-PBzMA framboidal vesicles are an interesting new synthetic mimic for the infectious form of the Dengue virus. In general, viruses are the most efficient drug delivery systems found in Nature. Thus, if they could be designed to be stimulus-responsive, such framboidal vesicles may enable delivery of various protein-based drugs into cell nuclei, which has considerable therapeutic potential.

For RAFT dispersion polymerisation formulations, spheres, worms or vesicles can be normally obtained provided that the stabiliser block is not too long. However, with only a few notable exceptions, only kinetically-trapped spheres are obtained via RAFT aqueous emulsion polymerisation (e.g. for PGMA-PBzMA formulations[9]). In this thesis, it is shown that introducing an intermediate *water-soluble* PHPMA block enables access to well-defined worms for certain chemical compositions. Although vesicles cannot be obtained using this strategy, it would be interesting to examine alternative water-immiscible monomers such as methyl methacrylate, butyl methacrylate, 2,2,2-trifluoroethyl methacrylate or 2-(diisopropylamino)ethyl methacrylate could be used instead of BzMA.

PGMA-PHPMA diblock copolymer nano-objects are not stable when subjected to high shear, dissociating *in situ* to form diblock copolymer chains.[10] In order to stabilise such nanoparticles, chemical cross-linking has been utilised in the literature.[10] In contrast, the *linear* PGMA-PHPMA-PBzMA triblock copolymer worms and framboidal vesicles prepared in Chapters Two and Three are able to withstand the high-shear homogenisation conditions required for emulsification. This is attributed to the stronger inter-chain attractive forces associated with the more hydrophobic PBzMA block. Again, it would be interesting to evaluate whether methyl methacrylate, butyl methacrylate, 2,2,2-trifluoroethyl methacrylate or 2-(diisopropylamino)ethyl methacrylate can be used instead of BzMA in this context. Indeed, although not included in this thesis, I have used 2-(diisopropylamino)ethyl methacrylate to prepare *pH-responsive* framboidal vesicles; this study will be

reported elsewhere in due course. Thus, if all the main findings in this thesis were combined, protein-loaded pH-responsive framboidal vesicles could be designed for potential intracellular delivery applications.

During the course of this thesis, SAXS has been an invaluable characterisation technique for the analysis of block copolymer nano-objects. In Chapter Two, SAXS enabled a series of framboidal morphologies to be quantified in terms of the mean globule size, membrane thickness and overall vesicle diameter. In Chapter Three, SAXS provided the underpinning evidence to explain the counter-intuitive observation that vesicles could not be obtained from PGMA-PHPMA-PBzMA triblock copolymer worms. In Chapter Four, the structure factor observed by SAXS provided direct and irrefutable evidence for the encapsulation of silica nanoparticles within vesicles and then allowed calculation of the number of silica nanoparticles per vesicle. The time scale required for the release of such silica nanoparticles was then analysed in Chapter Five using *in situ* SAXS experiments. Finally, in the light of recent *in situ* SAXS studies by Derry and co-workers,[11] it would be fascinating to conduct similar SAXS experiments to monitor the evolution of the framboidal vesicle morphology during PISA.

References

1. C. J. Mable, R. R. Gibson, S. Prevost, B. E. McKenzie, O. O. Mykhaylyk and S. P. Armes, *Journal Of The American Chemical Society*, 2015, **137**, 16098-16108.
2. S. Rose, A. Prevoteau, P. Elziere, D. Hourdet, A. Marcellan and L. Leibler, *Nature*, 2014, **505**, 382-385.
3. J. Tan, H. Sun, M. Yu, B. S. Sumerlin and L. Zhang, *ACS Macro Letters*, 2015, **4**, 1249-1253.
4. X. H. Huang, I. H. El-Sayed, W. Qian and M. A. El-Sayed, *Journal Of The American Chemical Society*, 2006, **128**, 2115-2120.
5. B. J. Reynwar, G. Illya, V. A. Harmandaris, M. M. Muller, K. Kremer and M. Deserno, *Nature*, 2007, **447**, 461-464.
6. I. Canton and G. Battaglia, *Chemical Society Reviews*, 2012, **41**, 2718-2739.
7. X. Zhang, J. Sheng, P. Plevka, R. J. Kuhn, M. S. Diamond and M. G. Rossmann, *Proceedings of the National Academy of Sciences of the United States of America*, 2013, **110**, 6795-6799.
8. F. A. Rey, *Nature*, 2013, **497**, 443-444.
9. V. J. Cunningham, A. M. Alswieleh, K. L. Thompson, M. Williams, G. J. Leggett, S. P. Armes and O. M. Musa, *Macromolecules*, 2014, **47**, 5613-5623.
10. K. L. Thompson, P. Chambon, R. Verber and S. P. Armes, *Journal Of The American Chemical Society*, 2012, **134**, 12450-12453.
11. M. J. Derry, L. A. Fielding, N. J. Warren, C. J. Mable, A. J. Smith, O. O. Mykhaylyk and S. P. Armes, *Chemical Science*, 2016, **7**, 5078-5090.

Chapter Seven - Appendix

1. Structural models for framboidal particle SAXS analysis

Three distinctive copolymer morphologies could be identified by TEM studies (see Figure 2.2): (morphology 1, M1) vesicles with smooth featureless membranes, (morphology 2, M2) vesicles with pitted surfaces and (morphology 3, M3) vesicles with particulate membranes composed of an assembly of small micelle-like spheres (Figure 2.4). The latter morphology is comparable to core-shell nanocomposite particles (comprising polymer cores and particulate silica shells) reported by Balmer and co-workers[1-4], who demonstrated that the corresponding SAXS patterns could be fitted using a two-population model obtained by combining a core-shell model with a particulate shell.[1] A similar approach has been undertaken in this work. In the following description of the SAXS models, the hydrophobic component of the vesicle membrane (i.e., the PHPMA and PBzMA blocks) is called the membrane (or a membrane core) and the hydrophilic component of the vesicle membrane (i.e., the PGMA block) is called the corona.

In general, the scattering intensity of a system composed of n different (non-interacting) populations of polydisperse objects can be expressed as:

$$I(q) = \sum_{l=1}^{n} S_l(q) N_l \int_0^{\infty} \ldots \int_0^{\infty} F_l(q, r_{l1}, \ldots, r_{lk})^2 \Psi_l(r_{l1}, \ldots, r_{lk}) dr_{l1} \ldots dr_{lk} \qquad \textbf{A1.1}$$

where $F_l(q, r_{l1}, \ldots, r_{lk})$ is the form factor, $\Psi_l(r_{l1}, \ldots, r_{lk})$ is the distribution function, N_l is the number density per unit volume and $S_l(q)$ is the structure factor of the l^{th} population in the system. $r_{l1}, \ldots, r_{lk}$ is a set of k parameters describing the structural morphology of the l^{th} population. Based on our previous studies,[3, 4] it was assumed that the SAXS patterns can be represented as a sum of scattering signals generated by two populations (n = 2 in Equation A1.1): (i) vesicles (the first population, l = 1 in Equation A1.1) and (ii) spherical micelles forming the vesicle membrane (the second population, l = 2 in Equation A1.1). In the case of vesicles with smooth (or pitted) membranes, the second population can be simply removed from the model (n = 1 in Equation A1.1). The form factor for the first population, represented by vesicles, can be described as:[5]

$$F_1(q) = [A_{mc1}(q)]^2 + N_{agg1}\beta_c^2 F_c(qR_g) + N_{agg1}(N_{agg1} - 1)\beta_c^2 [A_{c1}(q)]^2 + 2N_{agg1}\beta_c A_{mc1}(q)A_{c1}(q) \quad \textbf{A1.2}$$

The amplitude of the membrane self-term in Equation A1.2 is:

$$A_{mc1}(q) = (1 - x_{sol})(\xi_{mc} - \xi_{sol})[V_{out}\Phi(qR_{mcout}) - V_{in}\Phi(qR_{mcin})]\exp\left(-\frac{q^2\sigma_{in}^2}{2}\right) \quad \textbf{A1.3}$$

where $R_{mcin} = R_{mc} - \frac{1}{2}T_{mc}$ is the inner radius of the membrane, $R_{mcout} = R_{mc} + \frac{1}{2}T_{mc}$ is the outer radius of the membrane, $V_{in} = \frac{4}{3}\pi R_{mcin}^3$ and $V_{out} = \frac{4}{3}\pi R_{mcout}^3$. R_{mc} is the radius from the centre of the vesicle to the middle of the membrane and T_{mc} is the membrane thickness (see Figure 2.4). $\Phi(x) = \frac{3[\sin(x) - x\cos(x)]}{(x)^3}$ is the form factor amplitude of a sphere. The exponent term represents a sigmoidal interface (width σ_{in}) that describes a decaying scattering length density between the PBzMA and PHPMA membrane-forming blocks and the PGMA corona. This parameter was fixed in the model at 0.25 nm. The vesicle aggregation number (i.e. the mean number of copolymer chains per vesicle) is given by $N_{agg1} = (1 - x_{sol})(V_{out} - V_{in})/V_{mc}$, where x_{sol} is the solvent fraction in the membrane and V_{mc} is the volume of the membrane block components (V_{mc} = $V_{PHPMA_{350}}$ + V_{PBzMA_z}). In this model it is assumed that the hydrophobic PHPMA and PBzMA blocks are uniformly distributed within the membrane. The corona block X-ray scattering length contrast is $\beta_c = V_c(\xi_c - \xi_{sol})$, where V_c is the corona block volume ($V_{PGMA_{63}}$). The block volumes are calculated from $V = \frac{M_n}{N_A\rho}$ using the number-average molecular weight, M_n, of the block components and the mass densities of the three blocks comprising the copolymer (ρ_{PHPMA} = 1.21 ± 0.01 g cm^{-3}, ρ_{PBzMA} = 1.15 ± 0.01 g cm^{-3} and ρ_{PGMA} = 1.31 ± 0.01 g cm^{-3}; these values were determined for the corresponding homopolymers using a helium pycnometer). ξ_{mc}, ξ_c, and ξ_{sol} are the X-ray scattering length densities of the membrane [ξ_{mc} = ($V_{PHPMA_{350}}\xi_{PHPMA}$ + $V_{PBzMA_z}\xi_{PBzMA}$)/V_{mc}, where ξ_{PHPMA} = 11.11 x 10^{10} cm^{-2} and ξ_{PBzMA} = 10.41 x 10^{10} cm^{-2}], the vesicle corona block (ξ_{PGMA} = 11.94 x 10^{10} cm^{-2}) and the solvent (ξ_{H_2O} = 9.42 x 10^{10} cm^{-2} for water or $\xi_{H_2O+sucrose}$ = 10.88 x 10^{10} cm^{-2} for the 40 % w/w aqueous sucrose solution assuming that scattering length

density of sucrose is 14.36 x 10^{10} cm^{-2} and mass density of water and sucrose is 1.0 g cm^{-3} and 1.59 g cm^{-3}, respectively). The self-correlation term of the corona block is given by the Debye function $F_c(qR_g) = \frac{2[\exp(-q^2R_g^2) - 1 + q^2R_g^2]}{q^4R_g^4}$, where R_g is the radius of gyration of the corona block. Assuming that there is no penetration of the corona blocks within the membrane, the amplitude of the corona self-term is expressed as:

$$A_{c1}(q) = \psi(qR_g)\frac{1}{2}\left[\frac{\sin[q(R_{mcout} + R_g)]}{q(R_{mcout} + R_g)} + \frac{\sin[q(R_{mcin} - R_g)]}{q(R_{mcin} - R_g)}\right] \qquad \textbf{A1.4}$$

where $\psi(qR_g) = \frac{1 - \exp(-qR_g)}{(qR_g)^2}$ is the factor amplitude of the corona chain. The polydispersities for two parameters (R_{mc} and T_{mc}), expressed as a Gaussian distribution, are considered for the first (vesicle) population:

$$\Psi_1(r_{11}, r_{12}) = \frac{1}{\sqrt{2\pi\sigma_{Rmc}^2}} e^{-\frac{(r_{11} - R_{mc})^2}{2\sigma_{Rmc}^2}} \frac{1}{\sqrt{2\pi\sigma_{Tmc}^2}} e^{-\frac{(r_{12} - T_{mc})^2}{2\sigma_{Tmc}^2}} \qquad \textbf{A1.5}$$

where σ_{Rmc} and σ_{Tmc} are the standard deviations for R_{mc} and T_{mc}, respectively. The number density per unit volume of the first population (l = 1 in Equation A1.1) is expressed as:

$$N_1 = \frac{c_1}{\int_0^\infty \int_0^\infty V_1(r_{11}, r_{12})\Psi_1(r_{11}, r_{12}) dr_{11} dr_{12}} \qquad \textbf{A1.6}$$

where c_1 is the total *volume fraction* of copolymer in the vesicles and $V_1(r_{11}, r_{12})$ is the total *volume* of copolymers in a vesicle [$V_1(r_{11},r_{12}) = (V_{mc}+V_c)N_{agg1}(r_{11},r_{12})$]. A dilute vesicle dispersion is assumed in the model, so the structure factor of the first population is set to unity [$S_1(q) = 1$]. The first population describes scattering from a continuous membrane (Figure 2.4, smooth vesicles). If the membrane has a particulate sub-structure, this generates an additional scattering signal that can be described by a second population (Figure 2.4, spherical micelles), l = 2 in Equation A1.1). The form factor of this population can be represented by a spherical micelle model:[5]

$$F_2(q) = [A_{mc2}(q)]^2 + N_{agg2}\beta_c^2 F_c(qR_g) + N_{agg2}(N_{agg2} - 1)\beta_c^2 [A_{c2}(q)]^2 + 2N_{agg2}\beta_c A_{mc2}(q) A_{c2}(q) \quad \textbf{A1.7}$$

If not stated otherwise, the parameters and functions in this micelle model are analogous to those of the vesicle model, Equation A1.2. The amplitude of the core self-term in Equation A1.7 is

$A_{mc2}(q) = (1 - x_{sol})(\xi_{mc} - \xi_{sol})\frac{4}{3}\pi R_s^3 \Phi(qR_s)\exp\left(-\frac{q^2\sigma_{in}^2}{2}\right)$, where R_s is the radius of the spherical micelle core (Figure 2.4). The form factor amplitude of the spherical micelle corona is $A_{c2}(q) = \psi(qR_g)\frac{\sin[q(R_s + R_g)]}{q(R_s + R_g)}$ where no penetration of the corona chains within the micelle cores was assumed. As for the vesicle model, β_c corresponds to the X-ray scattering length contrast of the corona block. The aggregation number, N_{agg2}, for the spherical micelles is given by $N_{agg2} = (1 - x_{sol})\frac{4\pi R_s^3}{3V_{mc}}$. The polydispersity for one parameter (R_s) can be expressed as a Gaussian distribution and is considered for the second population of spherical micelles:

$$\Psi_2(r_{21}) = \frac{1}{\sqrt{2\pi\sigma_{Rs}^2}} e^{\frac{(r_{21} - R_s)^2}{2\sigma_{Rs}^2}} \quad \textbf{A1.8}$$

where σ_{Rs} is the standard deviation for R_s. The number density per unit volume of the second population (l = 2 in Equation A1.1) is expressed as:

$$N_2 = \frac{c_2}{\int_0^\infty V_2(r_{21})\Psi_2(r_{21})dr_{21}} \quad \textbf{A1.9}$$

where c_2 is the total *volume fraction* of copolymer in the spherical micelles and $V_2(r_{21})$ is the total *volume* of copolymer in a spherical micelle [$V_2(r_{21}) = (V_{mc}+V_c)N_{agg2}(r_{21})$]. An effective structure factor expression previously proposed for interacting spherical micelles[6] is used for the second population in order to describe dense packing of the spherical micelles within the vesicle membrane:

$$S_2(q) = 1 + \frac{A_{mic}(q)^2[S_{PY}(q, R_{PY}, f_{PY}) - 1]}{F_2(q)} \quad \textbf{A1.10}$$

Herein the form factor of the average radial scattering length density distribution of micelles is $A_{\mathrm{mic}}(q) = A_{\mathrm{mc2}}(q) + N_{\mathrm{agg2}}\beta_{\mathrm{c}}A_{\mathrm{c2}}(q)$ and $S_{\mathrm{PY}}(q, R_{\mathrm{PY}}, f_{\mathrm{PY}})$ is a hard-sphere interaction structure factor based on the Percus-Yevick approximation[7], where R_{PY} is the interaction radius ($R_{\mathrm{PY}} = R_{\mathrm{s}} + \Delta R_{\mathrm{PY}}$, ΔR_{PY} is a fitting parameter) and f_{PY} is the hard-sphere volume fraction. A numerical integration was used for Equation A1.1, Equation A1.6 and Equation A1.9 during the fitting.

Nanoscale phase separation between the hydrophobic PBzMA and PHPMA blocks was also considered and a vesicle model with a three-layer membrane structure was developed for the corresponding SAXS analysis (see Figure 2.10 and Figure 2.11). In this model it is assumed that phase-separated blocks of PBzMA and PHPMA occupy both the central layer of the membrane and also an adjacent layer. Again, a two-population approach (n = 2 in Equation A1.1) was used and, by analogy to Equation A1.2, the vesicle form factor corresponding to the first population can be expressed as:

$$F_1(q) = [A^{3l}_{\mathrm{mc1}}(q)]^2 + N^{3l}_{\mathrm{agg1}}\beta_{\mathrm{c}}^2 F_{\mathrm{c}}(qR_{\mathrm{g}}) + N^{3\mathrm{l}}_{\mathrm{agg1}}(N^{3l}_{\mathrm{agg1}} - 1)\beta_{\mathrm{c}}^2[A_{\mathrm{c1}}(q)]^2 + 2N^{3l}_{\mathrm{agg1}}\beta_{\mathrm{c}}A^{3\mathrm{l}}_{\mathrm{mc1}}(q)A_{\mathrm{c1}}(q) \qquad \textbf{A1.11}$$

In this case the amplitude of the membrane self-term is

$$A^{3l}_{\mathrm{mc1}}(q) = \{(1 - x_{\mathrm{PHPMAsol}})(\xi_{\mathrm{PHPMA}} - \xi_{\mathrm{sol}})[V_{\mathrm{out}}\Phi(qR_{\mathrm{mcout}}) - V_{\mathrm{PBzMAout}}\Phi(qR_{\mathrm{PBzMAout}})] + (1 - x_{\mathrm{PBzMAsol}})(\xi_{\mathrm{PBzMA}} - \xi_{\mathrm{sol}})[V_{\mathrm{PBzMAout}}\Phi(qR_{\mathrm{PBzMAout}}) - V_{\mathrm{PBzMAin}}\Phi(qR_{\mathrm{PBzMAin}})] + (1 - x_{\mathrm{PHPMAsol}})(\xi_{\mathrm{PHPMA}} - \xi_{\mathrm{sol}})[V_{\mathrm{PBzMAin}}\Phi(qR_{\mathrm{PBzMAin}}) - V_{\mathrm{in}}\Phi(qR_{\mathrm{mcin}})]\}\exp\left(-\frac{q^2\sigma_{\mathrm{in}}^2}{2}\right) \qquad \textbf{A1.12}$$

where $R_{\mathrm{PBzMAin}} = R_{\mathrm{mc}} - \frac{1}{2}T_{\mathrm{PBzMA}}$ is the inner radius of the PBzMA layer of the membrane, $R_{\mathrm{PBzMAout}} = R_{\mathrm{mc}} + \frac{1}{2}T_{\mathrm{PBzMA}}$ is the outer radius of the PBzMA layer, $V_{\mathrm{PBzMAin}} = \frac{4}{3}\pi R^3_{\mathrm{PBzMAin}}$ and $V_{\mathrm{PBzMAout}} = \frac{4}{3}\pi R^3_{\mathrm{PBzMAout}}$. Because the number of PBzMA blocks and PHPMA blocks occupying the three-layer membrane must be the same and equal to the aggregation number, N^{3l}_{agg1}, then it follows that T_{PBzMA} is defined from the following relation:

$$\frac{4}{3}\pi[(R_{\mathrm{mc}}+\frac{1}{2}T_{\mathrm{PBzMA}})^3-(R_{\mathrm{mc}}-\frac{1}{2}T_{\mathrm{PBzMA}})^3]\frac{(1-x_{\mathrm{PBzMAsol}})}{V_{\mathrm{PBzMAy}}}=$$

$$\frac{4}{3}\pi[(R_{\mathrm{mc}}+\frac{1}{2}T_{\mathrm{mc}})^3-(R_{\mathrm{mc}}+\frac{1}{2}T_{\mathrm{PBzMA}})^3+(R_{\mathrm{mc}}-\frac{1}{2}T_{\mathrm{PBzMA}})^3-(R_{\mathrm{mc}}-\frac{1}{2}T_{\mathrm{mc}})^3]\frac{(1-x_{\mathrm{PHPMA}sol})}{V_{\mathrm{PHPMA}}}$$

A1.13

where x_{PBzMAsol} and x_{PHPMAsol} are the solvent fraction in the PBzMA layer and both PHPMA layers of the membrane, respectively. The vesicle aggregation number is given by: $N_{\mathrm{agg1}}^{3l}=(1-x_{\mathrm{PHPMAsol}})[V_{\mathrm{out}}-V_{\mathrm{in}}-(V_{\mathrm{PBzMAout}}-V_{\mathrm{PBzMAin}})]/V_{\mathrm{PHPMA350}}$. The other parameters utilised for this three-layer membrane vesicle model (Equation A1.11) have the same definitions as those used in the single-layer membrane vesicle model (Equation A1.2). The number density per unit volume of the first population (*l* = 1 in Equation A1.1) is expressed as:

$$N_1=\frac{c_1}{\int_0^\infty\int_0^\infty V_1^{3l}(r_{11},r_{12})\Psi_1(r_{11},r_{12})dr_{11}dr_{12}} \qquad \textbf{A1.14}$$

where c_1 is the total *volume fraction* of copolymer in population 1 and $V_1^{3l}(r_{11},r_{12})$ is the corresponding total *volume* of copolymer $[V_1^{3l}(r_{11},r_{12})=(V_{\mathrm{PBzMAz}}+V_{\mathrm{PHPMA350}}+V_{\mathrm{c}})N_{\mathrm{agg1}}^{3l}(r_{11},r_{12})]$. Polydispersities for two parameters (R_{mc} and T_{mc}) are introduced for the first population (Equation A1.5). A dilute vesicle dispersion is assumed, so the structure factor of the first population can be set to unity [$S_1(q)=1$].The form factor for the second population of particles associated with the particulate membrane structure, *l* = 2 in Equation A1.1, can be represented by a spherical micelle model where the core is represented by two components as a result of the nanoscale phase separation of the PHPMA and PBzMA blocks. By analogy to Equation A1.7, we have:

$$F_2(q)=[A_{\mathrm{mc2}}^{3l}(q)]^2+N_{\mathrm{agg2}}\beta_{\mathrm{c}}^2F_{\mathrm{c}}(qR_{\mathrm{g}})+N_{\mathrm{agg2}}(N_{\mathrm{agg2}}-1)\beta_{\mathrm{c}}^2[A_{\mathrm{c2}}(q)]^2+2N_{\mathrm{agg2}}\beta_{\mathrm{c}}A_{\mathrm{mc2}}^{3l}(q)A_{\mathrm{c2}}(q)$$

The amplitude of the core self-term is given by:

$$A_{\mathrm{mc2}}^{3l}(q)=[(1-x_{\mathrm{PHPMAsol}})(\xi_{\mathrm{PHPMA}}-\xi_{\mathrm{sol}})V_{\mathrm{s}}\Phi(qR_{\mathrm{s}})+$$
$$+(1-x_{\mathrm{PBzMAsol}})(\xi_{\mathrm{PBzMA}}-\xi_{\mathrm{PHPMA}})V_{\mathrm{sin}}\Phi(qR_{\mathrm{sin}})]\exp\left(-\frac{q^2\sigma_{\mathrm{in}}^2}{2}\right) \qquad \textbf{A1.15}$$

where R_{sin} is the inner radius of the PHPMA shell (i.e. the PBzMA core radius of the micelles) and R_s is the outer radius of the PHPMA shell, such that $V_{sin} = \frac{4}{3}\pi R_{sin}^3$ and $V_s = \frac{4}{3}\pi R_s^3$. If not stated otherwise, parameters and functions in this model are the same as those used in the vesicle model, Equation A1.12. The aggregation number for the spherical micelles is given by $N_{agg2}^{3l} = (1 - x_{PHPMAsol})(V_s - V_{sin})/V_{PHPMA350}$. Because the number of PBzMA blocks and PHPMA blocks occupying the micelle core must be the same and equal to the aggregation number, N_{agg2}^{3l}, R_{sin} is defined from the following relation:

$$\frac{4}{3}\pi R_{sin}^3 \frac{(1 - x_{PBzMAsol})}{V_{PBzMAz}} = \frac{4}{3}\pi (R_s^3 - R_{sin}^3) \frac{(1 - x_{PHPMAsol})}{V_{PHPMA}}$$

The other parameters used in this spherical micelle model with phase-separated micelle cores (Equation A1.14) have the same definition as those used in the spherical micelle model (Equation A1.7). The number density per unit volume of the second population is expressed as:

$$N_2 = \frac{c_2}{\int_0^\infty V_2^{3l}(r_{21}) \Psi_2(r_{21}) dr_{21}} \qquad \textbf{A1.16}$$

where c_2 is the total *volume fraction* of copolymer in population 2 and $V_2^{3l}(r_{21})$ is the corresponding total *volume* of copolymer $[V_2^{3l}(r_{21}) = (V_{PBzMAz} + V_{PHPMA350} + V_c) N_{agg2}^{3l}(r_{21})]$. The polydispersity for one parameter (R_s) is considered for the second population (Equation A1.8). An effective structure factor expression proposed for interacting spherical micelles[6] was used for the second population in order to describe the dense micelle packing within the vesicle membrane:

$$S_2(q) = 1 + \frac{A_{mic}^{3l}(q)^2 [S_{PY}(q, R_{PY}, f_{PY}) - 1]}{F_2(q)} \qquad \textbf{A1.17}$$

Herein the form factor of the average radial scattering length density distribution of the micelles is given by $A_{mic}^{3l}(q) = A_{mc2}^{3l}(q) + N_{agg2}^{3l} \beta_c A_{c2}(q)$. Numerical integration was used for Equation A1.14 and Equation A1.16 during the fitting.

2. Visible absorption spectra and calibration plot for $G_{63}H_{350}B_z$ copolymer vesicles (z = 25 to 400).

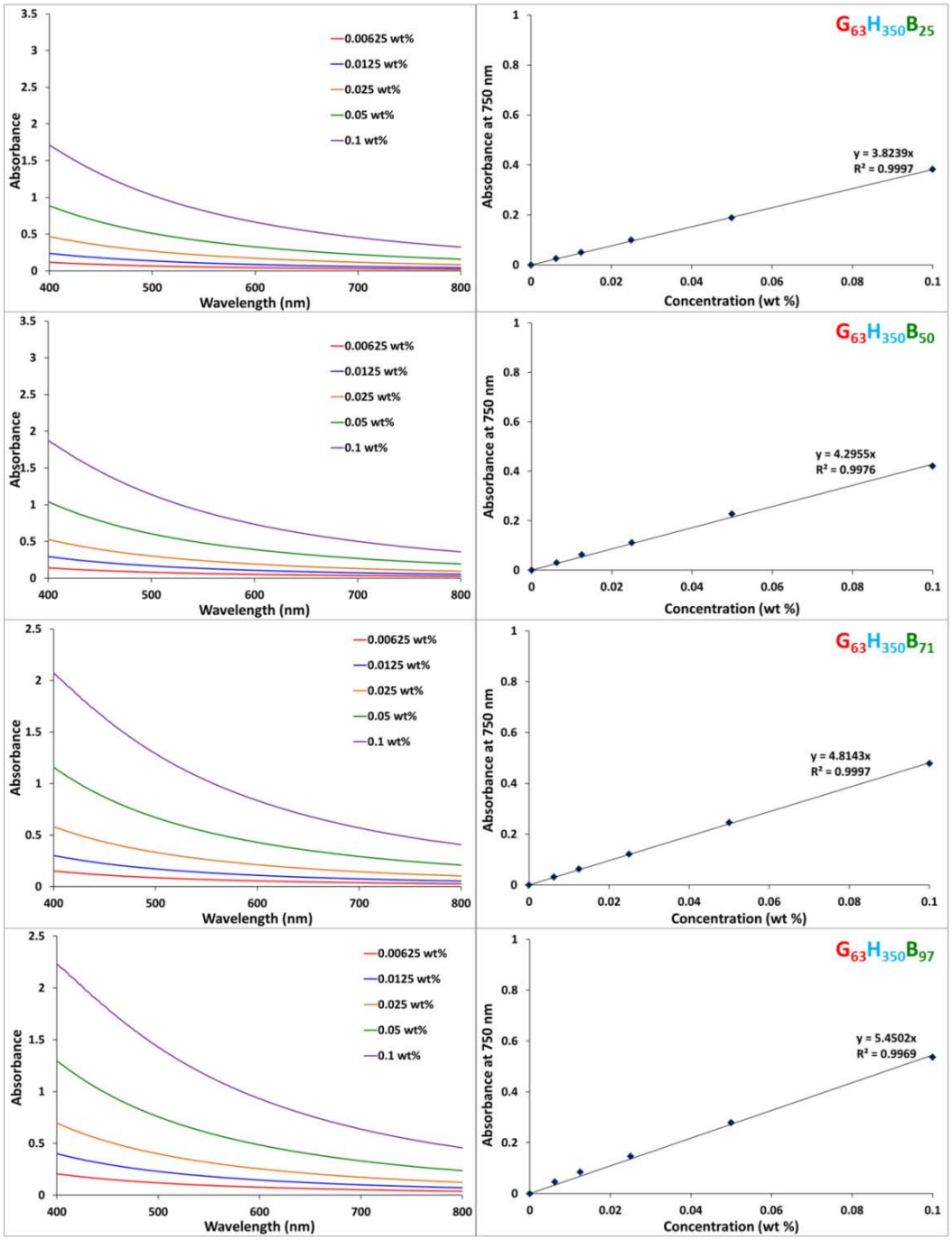

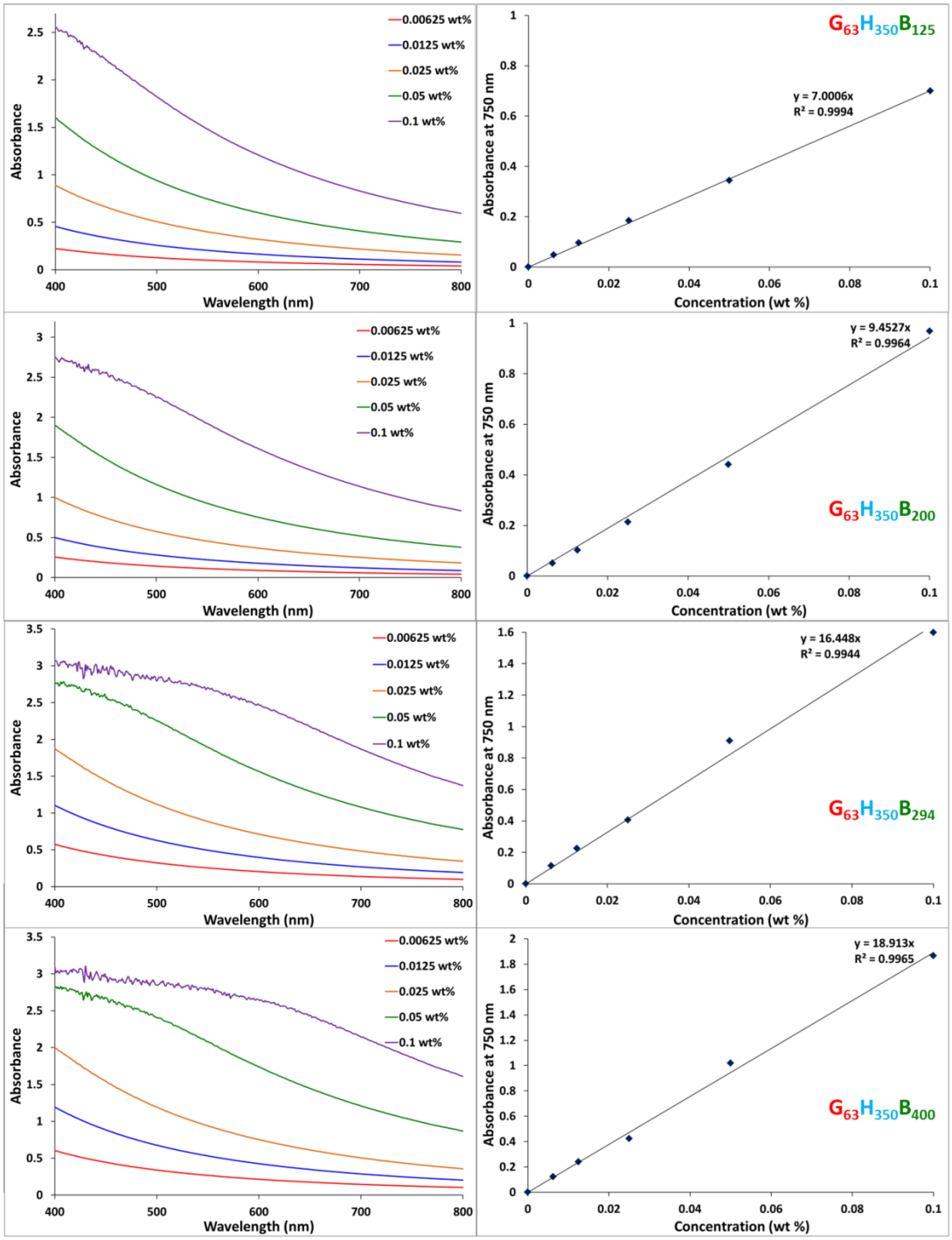

Visible absorption spectra (left) were recorded for a series of $G_{63}H_{350}B_z$ copolymer vesicles (where z ranges from 25 to 400) at various copolymer concentrations. An arbitrary wavelength (750 nm) was used to construct a linear calibration plot (right), which allows the concentration of non-adsorbed vesicles remaining in the aqueous phase after emulsification to be determined via turbidimetry.

3. Data to determine the adsorbed concentration of $G_{63}H_{350}B_z$ triblock copolymer vesicles (z = 0 to 400) in Pickering emulsions

Copolymer Composition	Initial Copolymer Concentration (% w/w)	Initial Copolymer Concentration (mM)	Copolymer Concentration in the Aqueous Phase (% w/w)*	Copolymer Concentration Adsorbed (% w/w)	Adsorption Efficiency (%)
$G_{58}H_{350}B_{25}$	0.5	0.08	0.28	0.22	44
	1.0	0.15	0.65	0.35	35
	1.5	0.23	0.97	0.53	36
	2.0	0.31	1.66	0.34	17
	2.5	0.39	2.26	0.24	10
	3.0	0.46	2.59	0.41	14
$G_{58}H_{350}B_{50}$	0.5	0.07	0.06	0.44	88
	1.0	0.15	0.35	0.65	65
	1.5	0.22	0.54	0.96	64
	2.0	0.29	1.23	0.77	38
	2.5	0.37	1.91	0.59	24
	3.0	0.44	2.51	0.49	16
$G_{58}H_{350}B_{71}$	0.5	0.07	0.16	0.34	67
	1.0	0.14	0.45	0.55	55
	1.5	0.21	0.58	0.92	61
	2.0	0.28	1.12	0.88	44
	2.5	0.35	1.43	1.07	43
	3.0	0.43	2.51	0.49	16
$G_{58}H_{350}B_{97}$	0.5	0.07	0.03	0.47	94
	1.0	0.13	0.31	0.69	69
	1.5	0.20	0.21	1.29	86
	2.0	0.26	0.63	1.37	69
	2.5	0.33	1.05	1.45	58
	3.0	0.40	2.11	0.89	30
$G_{58}H_{350}B_{125}$	0.5	0.06	0.00	0.50	100
	1.0	0.12	0.03	0.97	97
	1.5	0.18	0.08	1.42	94
	2.0	0.24	0.19	1.81	90
	2.5	0.30	0.23	2.27	91
	3.0	0.36	0.87	2.13	71
$G_{58}H_{350}B_{200}$	0.5	0.05	0.03	0.47	93
	1.0	0.11	0.06	0.94	94
	1.5	0.16	0.11	1.39	93
	2.0	0.21	0.22	1.78	89
	2.5	0.27	0.41	2.09	84
	3.0	0.32	0.94	2.06	69
$G_{58}H_{350}B_{294}$	0.5	0.05	0.01	0.49	99
	1.0	0.09	0.03	0.97	97
	1.5	0.14	0.07	1.43	95
	2.0	0.18	0.20	1.80	90
	2.5	0.23	0.41	2.09	83
	3.0	0.27	0.95	2.05	68
$G_{58}H_{350}B_{400}$	0.5	0.04	0.00	0.50	100
	1.0	0.08	0.02	0.98	98
	1.5	0.12	0.09	1.41	94
	2.0	0.16	0.21	1.79	90
	2.5	0.20	0.37	2.13	85
	3.0	0.24	0.81	2.19	73

*As determined by turbidimetry from a linear Beer-Lambert plot of absorbance (at an arbitrary fixed wavelength of 750 nm) against vesicle concentration.

4. Modified SAXS models for $G_{37}H_{60}B_z$ spherical micelles and worm-like micelles

In general, the X-ray intensity scattered by a dispersion of nano-objects [usually represented by the scattering cross section per unit sample volume, $\frac{d\Sigma}{d\Omega}(q)$] can be expressed as:

$$\frac{d\Sigma}{d\Omega}(q) = NS(q)\int_0^\infty \dots \int_0^\infty F\left(q, r_{1,} \dots, r_{\mathrm{k}}\right)^2 \Psi\left(r_{1,} \dots, r_{\mathrm{k}}\right) dr_1 \dots dr_{\mathrm{k}} \qquad \textbf{A4.2}$$

where $F(q, r_1, \dots, r_{\mathrm{k}})$ is their form factor, $r_1, \dots, r_{\mathrm{k}}$ is a set of *k* parameters describing the structural morphology, $\Psi\left(r_{1,} \dots, r_{\mathrm{k}}\right)$ is the probability function describing polydispersity of each parameter of the structure, S(q) is the structure factor and *N* is the nano-object number density per unit volume expressed as:

$$N = \frac{\varphi}{\int_0^\infty \dots \int_0^\infty V\left(r_{1,} \dots, r_{\mathrm{k}}\right) \Psi\left(r_{1,} \dots, r_{\mathrm{k}}\right) dr_1 \dots dr_{\mathrm{k}}} \qquad \textbf{A4.3}$$

where $V\left(r_{1,} \dots, r_{\mathrm{k}}\right)$ is volume of the nano-object and φ is their volume fraction in the dispersion.

Modified Spherical Micelle Model

The spherical micelle form factor for Equation A4.2 is given by:[8]

$$F_{\mathrm{s\_mic}}(q) = {N_{\mathrm{s}}}^2 {\beta_{\mathrm{s}}}^2 {A_{\mathrm{s}}}^2(q, R_{\mathrm{s}}) + N_{\mathrm{s}} {\beta_{\mathrm{c}}}^2 F_{\mathrm{c}}\left(q, R_{\mathrm{g}}\right) + N_{\mathrm{s}}(N_{\mathrm{s}} - 1){\beta_{\mathrm{c}}}^2 {A_{\mathrm{c}}}^2(q) + 2{N_{\mathrm{s}}}^2 \beta_{\mathrm{s}} \beta_{\mathrm{c}} A_{\mathrm{s}}(q, R_{\mathrm{s}}) A_{\mathrm{c}}(q) \qquad \textbf{A4.4}$$

where R_{s} is the radius of the hydrophobic spherical micelle core, R_{g} is the radius of gyration of the PGMA coronal block, the core block and the corona block X-ray scattering length contrast is given by $\beta_{\mathrm{s}} = V_{\mathrm{s}}(\xi_{\mathrm{s}} - \xi_{\mathrm{sol}})$ and $\beta_{\mathrm{c}} = V_{\mathrm{c}}(\xi_{\mathrm{c}} - \xi_{\mathrm{sol}})$, respectively. Here ξ_{s}, ξ_{c} and ξ_{sol} are the X-ray scattering length densities of the core block, corona block and the solvent (ξ_{sol} = 9.42 x 10^{10} cm^{-2}), respectively. Considering the amphiphilic properties of the PGMA-PHPMA-PBzMA triblock copolymers it is assumed in the model that PGMA block always locates in the coronal part of the micelles, PBzMA block is in the core part and PHPMA block could occupy intermediate position depending on composition of the triblock

copolymer. In order to describe the relative amounts of the PHPMA block existing within the core domain and within the corona, ξ_s is expressed as follows:

$$\xi_s = \frac{\xi_{PBzMA} V_{PBzMA} + \eta \xi_{PHPMA} V_{PHPMA}}{V_{PBzMA} + \eta V_{PHPMA}} \quad \textbf{A4.5}$$

and ξ_c is expressed as:

$$\xi_c = \frac{\xi_{PGMA} V_{PGMA} + (1-\eta) \xi_{PHPMA} V_{PHPMA}}{V_{PGMA} + (1-\eta) V_{PHPMA}} \quad \textbf{A4.6}$$

where ξ_{PBzMA} = 10.41 x 10^{10} cm^{-2}, ξ_{PHPMA} = 11.11 x 10^{10} cm^{-2} and ξ_{PGMA} = 11.94 x 10^{10} cm^{-2}. Here V_{PBzMA}, V_{PHPMA} and V_{PGMA} represent the volumes of each block and were obtained from $V = \frac{M_{n,pol}}{N_A \rho}$ using the solid-state homopolymer densities of PBzMA (ρ_{PBzMA} = 1.15 g cm^{-3}),[9] PHPMA (ρ_{PHPMA} = 1.21 g cm^{-3}) and PGMA (ρ_{PGMA} = 1.31 g cm^{-3}), where $M_{n,pol}$ corresponds to the number-average molecular weight of the polymer block determined by ^{1}H NMR spectroscopy. Similarly, the volume of the core, V_s is given by:

$$V_s = V_{PBzMA} + \eta V_{PHPMA} \quad \textbf{A4.7}$$

And the volume of the corona, V_c is given by:

$$V_c = V_{PGMA} + (1-\eta) V_{PHPMA} \quad \textbf{A4.8}$$

This alteration of the pre-existing model introduces η, which is the volume fraction of the PHPMA block which exists within the micelle core. Thus the product ηV_{PHPMA} gives the volume of PHPMA block that exists within the core domain, and (1-η)V_{PHPMA} gives the volume of the PHPMA block within the corona.

The sphere form factor amplitude is used for the amplitude of the core self-term:

$$A_c(q, R_s) = \Phi(qR_s) \exp\left(-\frac{q^2\sigma^2}{2}\right) \quad \textbf{A4.9}$$

where $\Phi(qR_s) = \frac{3[\sin(qR_s) - qR_s\cos(qR_s)]}{(qR_s)^3}$ and the exponential term describes a sigmoidal interface between the core and corona part of the micelles where the width σ accounting for a decaying or increasing scattering length density at the interface. This σ value was fixed at 2.5 during fitting.

The form factor amplitude of the spherical micelle corona is taken as:

$$A_{\mathrm{c}}(q) = \frac{\int_{R_{\mathrm{s}}}^{R_{\mathrm{s}}+2s} \mu_{\mathrm{c}}(r) \frac{\sin(qr)}{qr} r^2 dr}{\int_{R_{\mathrm{s}}}^{R_{\mathrm{s}}+2s} \mu_{\mathrm{c}}(r) r^2 dr} \exp\left(-\frac{q^2\sigma^2}{2}\right) \qquad \textbf{A4.10}$$

The radial profile, $\mu_{\mathrm{c}}(r)$, is represented by a linear combination of two cubic b splines, with two fitting parameters *s* and *a* corresponding to the width of the corona profile and the function weight coefficient, respectively. This information can be found elsewhere,[10, 11] as can the approximate integrated form of Equation A4.10.

The self-correlation term for the corona block is given by the Debye function:

$$F_{\mathrm{c}}(q, R_{\mathrm{g}}) = \frac{2\left[\exp\left(-q^2 {R_{\mathrm{g}}}^2\right) - 1 + q^2 {R_{\mathrm{g}}}^2\right]}{q^4 {R_{\mathrm{g}}}^4} \qquad \textbf{A4.11}$$

where R_{g} is the radius of gyration of the coronal block.

The aggregation number of the spherical micelle is:

$$N_{\mathrm{s}} = (1 - x_{\mathrm{sol}}) \frac{\frac{4}{3}\pi {R_{\mathrm{s}}}^3}{V_{\mathrm{s}}} \qquad \textbf{A4.12}$$

where x_{sol} is the volume fraction of solvent in the micelle core.

An effective structure factor expression proposed for interacting spherical micelles[6] has been used in Equation A4.2:

$$S_{\mathrm{s}}(q) = 1 + \frac{A^{\mathrm{av}}_{\mathrm{s\_mic}}(q)^2 [S_{\mathrm{PY}}(q, R_{\mathrm{PY}}, f_{\mathrm{PY}}) - 1]}{F_{\mathrm{s\_mic}}(q)} \qquad \textbf{A4.13}$$

Herein the form factor of the average radial scattering length density distribution of micelles is used as $A^{\mathrm{av}}_{\mathrm{s\_mic}}(q) = N_{\mathrm{s}}[\beta_{\mathrm{s}} A_{\mathrm{s}}(q, R_{\mathrm{s}}) + \beta_{\mathrm{c}} A_{\mathrm{c}}(q)]$ and $S_{\mathrm{PY}}(q, R_{\mathrm{PY}}, f_{\mathrm{PY}})$ is a hard-sphere interaction structure factor based on the Percus-Yevick approximation,[7] where R_{PY} is the interaction radius and f_{PY} is the hard-sphere effective volume fraction. A polydispersity of one parameter (R_{s}) is assumed for the micelle model which is described by a Gaussian distribution. Thus, the polydispersity function in Equation A4.2 can be represented as:

$$\Psi(r_1) = \frac{1}{\sqrt{2\pi {\sigma_{R\mathrm{s}}}^2}} \exp\left(-\frac{(r_1 - R_{\mathrm{s}})^2}{2{\sigma_{R\mathrm{s}}}^2}\right) \qquad \textbf{A4.14}$$

where σ_{Rs} is the standard deviation for R_s. In this respect R_s should be replaced by r_1 in Equations A4.3, A4.8, A4.9 and A4.11 for the modelling. In accordance with Equation A4.3 the number density per unit volume for the micelle model is expressed as:

$$N = \frac{\varphi}{\int_0^\infty V(r_1)\Psi(r_1)dr_1} \qquad \textbf{A4.15}$$

where φ is the total volume fraction of copolymer in the spherical micelles and $V(r_1)$ is the total *volume* of copolymer in a spherical micelle $[V(r_1) = (V_s + V_c)N_s(r_1)]$.

Modified Worm-Like Micelle Model

The worm-like micelle form factor for Equation A4.2 is given by:[8]

$$F_{w\_mic}(q) = N_w{}^2\beta_s{}^2F_{sw}(q) + N_w\beta_c{}^2F_c(q, R_g) + N_w(N_w - 1)\beta_c{}^2S_{cc}(q) + 2N_w{}^2\beta_s\beta_cS_{sc}(q) \qquad \textbf{A4.16}$$

where the core block and the corona block X-ray scattering length contrast is given by $\beta_s = V_s(\xi_s - \xi_{sol})$ and $\beta_c = V_c(\xi_c - \xi_{sol})$, respectively. The scattering length density of the core block (ξ_s) and the corona block (ξ_c) are determined as described in Equations A4.5 and A4.6, respectively, and the volume of core block (V_s) and the corona block (V_c) are determined as described in Equations A4.7 and A4.8, respectively.

The self-correlation term for the worm-like micelle core of radius R_{sw} is:

$$F_{sw}(q) = F_{worm}(q, L_w, b_w)A_{cs_{worm}}{}^2(q, R_{sw}) \qquad \textbf{A4.17}$$

which is a product of a core cross-section term:

$$F_{cs_{worm}}(q, R_g) = A_{cs_{worm}}{}^2(q, R_{sw}) = \left[2\frac{J_1(qR_{sw})}{qR_{sw}}\right]^2 \qquad \textbf{A4.18}$$

where J_1 is the first-order Bessel function of the first kind, and a form factor $F_{worm}(q, L_w, L_k)$ for self-avoiding semi-flexible chains represents the worm-like micelle, where L_k is the worm Kuhn length and L_w is the mean worm contour length. A complete expression for the chain form factor can be found elsewhere.[12] The self-correlation term for the corona block is given by the Debye function shown in Equation A4.11.

The interference cross-term between the worm micelle core and the corona chain is given by:

$$S_{\mathrm{sc}}(q) = \Psi^2(qR_{\mathrm{g}}){J_0}^2\left[q\left(R_{\mathrm{sw}} + R_{\mathrm{g}}\right)\right]F_{\mathrm{worm}}(q, L_{\mathrm{w}}, L_{\mathrm{k}}) \qquad \textbf{A4.19}$$

where $\Psi\left(qR_{\mathrm{g}}\right) = \frac{1-\exp\left(-q^2{R_{\mathrm{g}}}^2\right)}{\left(qR_{\mathrm{g}}\right)^2}$ is the form factor amplitude of the corona chain, R_{g} is the radius of gyration of the corona block and J_0 is the zero-order Bessel function of the first kind.

The interference term between the worm corona chains is:

$$S_{\mathrm{cc}}(q) = \Psi\left(qR_{\mathrm{g}}\right)A_{\mathrm{cs\_worm}}J_0\left[q\left(R_{\mathrm{sw}} + R_{\mathrm{g}}\right)\right]F_{\mathrm{worm}}(q, L_{\mathrm{w}}, L_{\mathrm{k}}) \qquad \textbf{A4.20}$$

The mean aggregation number of the worm-like micelle is given by:

$$N_{\mathrm{w}} = (1 - x_{\mathrm{sol}})\frac{\pi {R_{\mathrm{sw}}}^2 L_{\mathrm{w}}}{V_{\mathrm{s}}} \qquad \textbf{A4.21}$$

where x_{sol} is the volume fraction of solvent within the worm-like micelle core. Possible semi-spherical caps at the ends of each worm are not considered in this form factor. It is also assumed that $S(q) = 1$ at sufficiently low copolymer concentrations (e.g. 1.0% w/w).

A polydispersity of one parameter (R_{sw}) is assumed for the worm-like micelle model which is described by a Gaussian distribution. Thus, the polydispersity function in Equation A4.2 can be represented as:

$$\Psi(r_1) = \frac{1}{\sqrt{2\pi {\sigma_{R\mathrm{sw}}}^2}}\exp\left(-\frac{(r_1 - R_{\mathrm{sw}})^2}{2{\sigma_{R\mathrm{sw}}}^2}\right) \qquad \textbf{A4.21}$$

where σ_{Rsw} is the standard deviation for R_{sw}. In this respect R_{sw} should be replaced by r_1 in Equations A4.15-A4.20 for the modelling. In accordance with Equation A4.3 the number density per unit volume for the worm-like micelle model is expressed as:

$$N = \frac{\varphi}{\int_0^\infty V(r_1)\Psi(r_1)dr_1} \qquad \textbf{A4.22}$$

where φ is the total volume fraction of copolymer in the worm-like micelles and $V(r_1)$ is the total *volume* of copolymer in a worm-like micelle $[V(r_1) = (V_{\mathrm{s}} + V_{\mathrm{c}})N_{\mathrm{w}}(r_1)]$.

5. DCP calculations for silica-loaded $G_{58}H_{250}$ diblock copolymer vesicles

The volume of the vesicle, *V*, was calculated using Equation A5.1:

$$V = \frac{4}{3}\pi r^3 \qquad \textbf{A5.1}$$

where r is the mean vesicle radius. Using this *V*, together with the vesicle density, ρ, the vesicle mass, *m*, can be obtained using Equation A5.2:

$$m = V\rho \qquad \textbf{A5.2}$$

Equations A5.1 and A5.2 can be combined to give Equation A5.3:

$$m = \frac{4}{3}\pi r^3 \rho_{eff} \qquad \textbf{A5.3}$$

The effective density, ρ_{eff}, was obtained analytically from the DCP data by fixing the weight-average diameter at 291 nm. The ρ_{eff} value for empty vesicles (i.e. vesicles prepared in the *absence* of any silica nanoparticles) is 1.075 g cm^{-3} and this value increases from 1.076 to 1.141 g cm^{-3} when the $[\text{silica}]_0$ is increased from 5 to 35 % w/w, respectively (see Table 4.1). Using these values and Equation A5.3, the mass of the loaded vesicles, m_{l}, and the mass of the empty vesicles, m_{e}, can be calculated. The mass difference allows the encapsulated silica mass, m_{s}, to be calculated using:

$$m_{\text{s}} = m_{\text{l}} - m_{\text{e}} \qquad \textbf{A5.4}$$

The mass of one silica nanoparticle, $m_{1\text{s}}$, can be calculated using Equation A5.3, where the silica density, ρ, is 2.06(5) g cm^{-3} (as judged by helium pycnometry) and *r* is 9.2 nm (obtained from SAXS analysis). If the encapsulated silica mass, m_{s}, is

divided by the mass of one silica nanoparticle, m_{1s}, the mean number of silica nanoparticles per vesicle, N_{sv}, can be calculated using:

$$N_{sv} = \frac{m_s}{m_{1s}} \qquad \textbf{A5.5}$$

Subtracting the vesicle membrane thickness (15.9 nm) and four times the radius of gyration (2.3 nm) from the SAXS-derived mean vesicle radius of 145.5 nm, the volume of the vesicle lumen, V_l, can be calculated from Equation A5.1. The volume of encapsulated silica nanoparticles per vesicle, V_{sv}, can be calculated by multiplying the volume of one silica nanoparticle by N_{sv}. Subtracting the V_{sv} from the V_l allows the percentage of the vesicle lumen that is occupied by silica nanoparticles, V_{sl} to be calculated using:

$$V_{sl} = \left(\frac{V_{sv}}{V_l}\right) x\ 100 \qquad \textbf{A5.6}$$

The theoretical maximum number of encapsulated silica nanoparticles, can be calculated by multiplying the number of silica nanoparticles occupying 1.00 mL, N_s, which is based on the initial silica concentration, by V_l (see Equation A5.7):

$$\text{Theoretical } N_{sv} = N_s \times V_l \qquad \textbf{A5.7}$$

By dividing N_{sv} by the theoretical N_{sv}, the DCP-derived encapsulation efficiency, EE_{DCP}, can be calculated using:

$$EE_{DCP}\ (\%) = \left(\frac{\text{Actual } N_{sv}}{\text{Theoretical } N_{sv}}\right) \times 100 \qquad \textbf{A5.8}$$

It should be noted that calculation of the theoretical N_{sv} assumes that the silica nanoparticles have a mean diameter of 18.4 nm and that the Bindzil CC401 silica sol has a solids concentration of 40 % w/w. It also assumes that the silica concentration is constant both inside and outside the vesicle lumen and that there is no interaction between the silica nanoparticles and the vesicles.

6. TGA calculations for silica-loaded $G_{58}H_{250}$ diblock copolymer vesicles

The silica nanoparticles used in this work lose ~ 10.1 % mass on heating to 350 ^{o}C in air during TGA analysis. This is attributed to a combination of surface moisture and also pyrolysis of surface glycerol groups, which are present for this particular commercial grade. This mass loss must be taken into account when calculating the silica content of the vesicles. In order to account for this in each sample, the residual mass for each sample was divided by the silica weight remaining (10.1) divided by 100:

$$\text{silica content or } WR_c\ (\%) = \frac{WR}{(\text{silica } WR/100)} \qquad \textbf{A6.1}$$

Where *WR* is the weight remaining and WR_c is the corrected weight remaining. The silica content after centrifugation, determined using Equation A5.1, can be used to calculate the TGA-derived silica loading efficiency, LE_{TGA}:

$$LE_{TGA}\ (\%) = \left[\frac{\left\{\left(\frac{WR_c}{1 - WR_c}\right) \times 10\right\}}{[\text{silica}]_0}\right] \times 100 \qquad \textbf{A6.2}$$

7. SAXS models used for the analysis of silica-loaded vesicles

Silica-Loaded Vesicle Model

In order to analyse the synchrotron SAXS data obtained for these silica-loaded vesicles, it was necessary to develop an appropriate analytical model. Two types of particles are present in these dispersions: copolymer vesicles (morphology 1) and spherical silica nanoparticles (morphology 2). In general, the silica component scatters X-rays more strongly than the copolymer component. However, it is perhaps worth emphasising that the silica nanoparticles (morphology 2) dominate the scattering intensity at high *q*, whereas the much larger vesicles (morphology 1) dominate the scattering at low *q*. Drawing on our earlier structural characterisation of core-shell nanocomposite particles comprising copolymer cores and particulate silica shells[1], the scattering patterns associated with the silica-loaded copolymer vesicles can be satisfactorily described using a two-population model. In this case, population 1 corresponds to silica-loaded vesicles and population 2 describes the particulate nature of the corresponding vesicle lumen. Thus this two-population model includes a modified version of morphology 1, where the vesicle lumen is assumed to contain silica and hence can be described as a type of core-shell particle (where the X-ray contrast of the lumen core depends on the concentration of the encapsulated silica nanoparticles). In general, the scattering intensity of a system composed of *n* different (non-interacting) populations of polydisperse objects can be expressed as:

$$I(q) = \sum_{l=1}^{n} S_l(q) N_l \int_0^\infty \dots \int_0^\infty F_l(q, r_{l1}, \dots, r_{lk}) \Psi_l(r_{l1}, \dots, r_{lk}) dr_{l1} \dots dr_{lk}$$

(A7.1)

where $F_l(q, r_{l1}, \dots, r_{lk})$ is the form factor, $\Psi_l(r_{l1}, \dots, r_{lk})$ is the distribution function, N_l is the number density per unit volume and $S_l(q)$ is the structure factor of the l^{th} population in the system. r_{l1},...,r_{lk} is a set of *k* parameters describing the structural morphology of the l^{th} population. The two-population model can be derived from Equation A7.1 by taking $n = 2$ and assigning the silica-loaded copolymer vesicles to population 1 ($l = 1$) and the spherical silica nanoparticles within the vesicle lumen to population 2 ($l = 2$). The form factor for population 1 (vesicles) can be described as:[2]

$$F_1(q) = [A_{\mathrm{m1}}(q)]^2 + N_{\mathrm{agg}}\beta_{\mathrm{c}}^2 F_{\mathrm{c}}(qR_{\mathrm{g}}) + N_{\mathrm{agg}}(N_{\mathrm{agg}} - 1)\beta_{\mathrm{c}}^2[A_{\mathrm{c}}(q)]^2 + 2N_{\mathrm{agg}}\beta_{\mathrm{c}}A_{\mathrm{m1}}(q)A_{\mathrm{c}}(q) \quad \textbf{(A7.2)}$$

However, this expression requires modification to represent *silica-loaded* vesicles: the amplitude of the membrane self-term in Equation A7.2 must be replaced by an amplitude representing both the membrane (shell) and the silica-loaded lumen (core) expressed as the form factor amplitude for a core-shell spherical particle:[3]

$$A_{\mathrm{m1}}(q) = (1 - x_{\mathrm{sol}})(\xi_{\mathrm{m}} - \xi_{\mathrm{sol}})V_{\mathrm{out}}\phi(qR_{\mathrm{out}}) + [\xi_{\mathrm{lum}} - \xi_{\mathrm{sol}} - (1 - x_{\mathrm{sol}})(\xi_{\mathrm{m}} - \xi_{\mathrm{sol}})]V_{\mathrm{in}}\phi(qR_{\mathrm{in}}) \quad \textbf{(A7.3)}$$

where $R_{\mathrm{in}} = R_{\mathrm{m}} - \frac{1}{2}T_{\mathrm{m}}$ is the inner radius of the hydrophobic membrane (or the lumen), $R_{\mathrm{out}} = R_{\mathrm{m}} + \frac{1}{2}T_{\mathrm{m}}$ is the outer radius of the hydrophobic membrane, $V_{\mathrm{in}} = \frac{4}{3}\pi {R_{\mathrm{in}}}^3$ is the volume of the vesicle lumen and $\mathrm{V_{out}} = \frac{4}{3}\pi {R_{\mathrm{out}}}^3$ is the volume of the vesicle defined by the boundary of the hydrophobic membrane. R_{m} is the radius from the center of the vesicle to the middle of the membrane, T_{m} is the hydrophobic membrane thickness and $\phi(x) = \frac{3[\sin(x) - x\cos(x)]}{(x)^3}$ is the form factor amplitude of a homogeneous sphere. The vesicle aggregation number (i.e. the mean number of copolymer chains per vesicle) is given by $N_{\mathrm{agg}} = (1 - x_{\mathrm{sol}})(V_{\mathrm{out}} - V_{\mathrm{in}})/V_{\mathrm{m}}$ where x_{sol} is the solvent fraction in the hydrophobic membrane and V_{m} is the volume of the membrane-forming hydrophobic PHPMA block ($V_{\mathrm{m}} = V_{\mathrm{PHPMA250}}$). The X-ray scattering length contrast for the membrane and corona block is $\beta_{\mathrm{m}} = V_{\mathrm{m}}(\xi_{\mathrm{m}} - \xi_{\mathrm{sol}})$ and $\beta_{\mathrm{c}} = V_{\mathrm{c}}(\xi_{\mathrm{c}} - \xi_{\mathrm{sol}})$, respectively, where V_{c} is the corona block volume (V_{PGMA58}). The block volumes are calculated from $V = \frac{M_{\mathrm{w}}}{\rho N_A}$ using the weight-average molecular weight, M_{w}, of the block components and the mass densities of the three blocks comprising the copolymer (ρ_{PHPMA} = 1.21 ± 0.01 g cm^{-3} and ρ_{PGMA} = 1.31 ± 0.01 g cm^{-3}; these solid-state values were determined for the corresponding homopolymers using helium pycnometry). ξ_{sol}, ξ_{m}, ξ_{c}, and ξ_{lum} are the X-ray scattering length densities of the surrounding solvent (ξ_{H2O} = 9.42 x 10^{10} cm^{-2}), the membrane-forming hydrophobic block (ξ_{PHPMA} = 11.11 x 10^{10} cm^{-2}), the vesicle corona block (ξ_{PGMA} = 11.94 x 10^{10} cm^{-2}) and the vesicle lumen [$\xi_{\mathrm{lum}} = (1 - V_{\mathrm{SiO_2}}/V_{\mathrm{in}})\xi_{\mathrm{H_2O}} + (V_{\mathrm{SiO_2}}/V_{\mathrm{in}})\xi_{\mathrm{SiO_2}}$, where $\xi_{\mathrm{SiO_2}}$ = 17.5 × 10^{10} cm^{-2}, and $V_{\mathrm{SiO_2}}$ is the volume occupied by the silica nanoparticles within the vesicle lumen], respectively. It should be noted that the $(\beta_{\mathrm{c}}/\beta_{\mathrm{m}})^2$ ratio is approximately 0.08, which

suggests that the profile of the electron density distribution within the corona might need to be included in the model. However, recent modeling of experimental data for a similar system has demonstrated that incorporation of a profile function in the model has a negligible effect on the derived structural parameters.[4] The self-correlation term for the corona block in Equation A7.2 is given by the Debye function, $F_c(qR_g) = \frac{2[\exp(-q^2R_g^2)-1+q^2R_g^2]}{q^4R_g^4}$, where R_g is the radius of gyration of the corona block. Assuming that there is no penetration of the corona blocks within the membrane, the amplitude of the corona self-term is expressed as:

$$A_c(q) = \Psi(qR_g)\frac{1}{2}\left[\frac{sin[q(R_{out}+R_g)]}{q(R_{out}+R_g)} + \frac{sin[q(R_{in}-R_g]}{q(R_{in}-R_g)}\right] \quad \textbf{(A7.4)}$$

where $\Psi(qR_g) = \frac{1-\exp(-qR_g)}{(qR_g)^2}$ is the form factor amplitude of the corona chain. The polydispersities for two parameters (R_m and T_m), expressed as a Gaussian distribution, are considered for the first population of silica-loaded vesicles:

$$\Psi_1(r_{11}, r_{12}) = \frac{1}{\sqrt{2\pi\sigma_{Rm}^2}} e^{-\frac{(r_{11}-R_m)^2}{2\sigma_{Rm}^2}} \frac{1}{\sqrt{2\pi\sigma_{Tm}^2}} e^{-\frac{(r_{12}-T_m)^2}{2\sigma_{Tm}^2}} \quad \textbf{(A7.5)}$$

where σ_{Rm} and σ_{Tm} are the standard deviations for R_m and T_m, respectively. The number density per unit volume of population 1 (l = 1 in Equation A7.1) is expressed as:

$$N_1 = \frac{c_1}{\int_0^\infty \int_0^\infty V_1(r_{11},r_{12})\Psi_1(r_{11},r_{12})dr_{11}dr_{12}} \quad \textbf{(A7.6)}$$

where c_1 is the total *volume fraction* of copolymer vesicles and $V_1(r_{11}, r_{12})$ is the total *volume* of copolymer chains within a vesicle [$V_1(r_{11}, r_{12}) = (V_m + V_c)N_{agg}(r_{11}, r_{12})$]. It is assumed that the copolymer vesicle dispersions are sufficiently dilute to enable the structure factor for population 1 to be set to unity [$S_1(q) = 1$]. Population 1 describes scattering from a vesicle assuming a homogeneous lumen with an effective scattering length density, ξ_{lum}. However, the lumen actually has a particulate structure arising from the encapsulated silica nanoparticles. This generates an *additional* scattering signal that can be described by population 2 (sphere model), for which l = 2 in Equation A7.1.

Modified Model for Silica Release

The form factor for this population is simply that for a homogeneous sphere:

$$F_2(q) = \left(\xi_{\mathrm{SiO_2}} - \xi_{\mathrm{sol}}\right)^2 \phi^2(qR_{\mathrm{SiO_2}}) \qquad \textbf{(A7.7)}$$

where $R_{\mathrm{SiO_2}}$ is the mean radius of the silica nanoparticles. All other parameters and functions in the model for population 2 are analogous to those for population 1 (Equation A7.2). The polydispersity of one parameter ($R_{\mathrm{SiO_2}}$), expressed as a Gaussian distribution, is considered for population 2:

$$\Psi_2(r_{21}) = \frac{1}{\sqrt{2\pi\sigma^2_{R_{\mathrm{SiO_2}}}}} e^{-\frac{\left(r_{21}-R_{\mathrm{SiO_2}}\right)^2}{2\sigma^2_{R_{\mathrm{SiO_2}}}}} \qquad \textbf{(A7.8)}$$

where $\sigma_{R_{SiO_2}}$ is the standard deviation for $R_{\mathrm{SiO_2}}$. The number density per unit volume of population 2 is expressed as:

$$N_2 = \frac{c_{\mathrm{SiO2}}}{\int_0^\infty V_2(r_{21})\Psi_2(r_{21})dr_{21}} \qquad \textbf{(A7.9)}$$

where c_2 is the total *volume fraction* of silica particles in the sample and $V_2(r_{21}) = \frac{4}{3}\pi r_{21}^3$ is the *volume* of a single spherical silica nanoparticle. Since inter-particle interactions are expected for silica nanoparticles occupying the vesicle lumen, a structure factor $S_2(q)$ should be incorporated into the SAXS analysis using Equation A7.1. According to its manufacturer (AkzoNobel), approximately 50% of the surface silanol groups on the CC401 silica nanoparticles are glycerol-functionalised, hence such nanoparticles should exhibit significantly lower anionic surface charge compared to conventional aqueous silica sols.[5,6] Thus, depending upon the surface charge density and background salt, it might be necessary to account for electrostatic interactions between silica nanoparticles when modelling the SAXS data. In principle, this correction requires a suitable Hayter-Penfold structure factor for charged particles.[13] However, the well-known Percus-Yevick approximation[7] for hard spheres might be applicable for this system. In order to validate this hypothesis, SAXS patterns recorded for various concentrations of aqueous silica dispersions were fitted using Equation A7.1 for a single population using a spherical particle form factor, a particle size distribution and a number density per unit volume as described by Equations A7.7, A7.8 and A7.9, respectively. The Percus-Yevick approximation[7] has a structure factor $S_{\mathrm{PY}}(q, R_{\mathrm{PY}}, f_{\mathrm{PY}})$, where the interaction radius

R_{PY} and effective hard-sphere volume fraction f_{PY} were used as fitting parameters. This approach produced satisfactory fits to the data (see Figure A7.1).

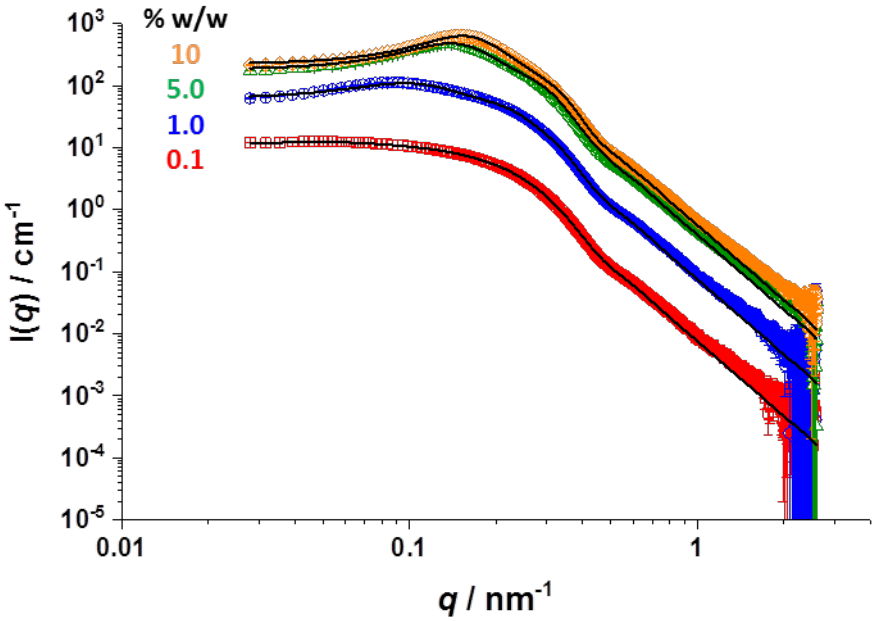

Figure A7.1. SAXS patterns recorded for 0.1% w/w (red squares), 1.0 % w/w (blue circles), 5.0 % w/w (green triangles) and 10 % w/w (orange diamonds) aqueous dispersions of glycerol-functionalised silica nanoparticles. Data were fitted using an established sphere model incorporating a Percus-Yevick 'hard sphere' structure factor.

This suggests that this relatively simple approximation returns reliable silica volume fractions and hence is suitable for analysis of the rate of release of the silica nanoparticles from the silica-loaded vesicles. Moreover, there is a good correlation between the mass of silica nanoparticles calculated from SAXS fittings ($C_{SiO2mass}$ x 100%) and the actual silica masses used to prepare these aqueous dispersions (Table A7.1).

Given that two types of silica nanoparticles can be present in the dispersion simultaneously (e.g. packed silica encapsulated within the vesicle lumen with an associated structure factor, plus freely diffusing silica released from the vesicle lumen with no corresponding structure factor), the structure factor term for population 2 (silica nanoparticles) in Equation A7.1 is expressed as:

$$S_2(q) = \frac{1}{c_{SiO2}}[S_{PY}(q, R_{PY}, f_{PY}) \times (c_{SiO2} - c_{rel}) + c_{rel}] \qquad \textbf{(A7.10)}$$

where C_{rel} is the volume fraction of the released silica nanoparticles. The volume fraction of encapsulated silica nanoparticles can be obtained from $C_{enc} = C_{SiO_2} - C_{rel}$. This refined model was incorporated into Irena SAS macros for Igor Pro software[8]

and numerical integration of Equations A7.1, A7.6 and A7.9 was used for data fitting.

Table A7.1. Summary of parameters (particle volume fraction in the dispersions C_{SiO2}, particle mass fraction in the dispersion $C_{SiO2mass}$ calculated from C_{SiO2} assuming that the mass densities of silica and water are 2.19 g cm^{-3} and 1.00 g cm^{-3}, respectively, particle radius R_{SiO2}, standard deviation of the particle radius σ_{RSiO2}, inter-particle distance R_{PY} and effective volume fraction f_{PY}) as a result of fitting SAXS data for 0.1, 1.0, 5.0 and 10 % w/w aqueous dispersions of glycerol-functionalised silica nanoparticles using a Percus-Yevick 'hard sphere' structure factor.

Silica concentration	0.1 % w/w	1.0 % w/w	5.0 % w/w	10 % w/w
C_{SiO2}	4.11×10^{-4}	4.07×10^{-3}	2.13×10^{-2}	3.04×10^{-2}
$C_{SiO2mass}$	9.00×10^{-4}	8.87×10^{-3}	4.54×10^{-2}	6.42×10^{-2}
R_{SiO_2} / nm	9.22	9.19	9.13	9.13
$\sigma_{R_{SiO_2}}$ / nm	2.14	2.13	2.08	2.07
R_{PY} / nm	43.6	29.0	19.5	17.8
f_{PY}	0.018	0.094	0.165	0.184

References

1. J. A. Balmer, O. O. Mykhaylyk, J. P. A. Fairclough, A. J. Ryan, S. P. Armes, M. W. Murray, K. A. Murray and N. S. J. Williams, *Journal Of The American Chemical Society*, 2010, **132**, 2166-2168.
2. J. A. Balmer, O. O. Mykhaylyk, A. Schmid, S. P. Armes, J. P. A. Fairclough and A. J. Ryan, *Langmuir*, 2011, **27**, 8075-8089.
3. L. A. Fielding, O. O. Mykhaylyk, S. P. Armes, P. W. Fowler, V. Mittal and S. Fitzpatrick, *Langmuir*, 2012, **28**, 2536-2544.
4. L. A. Fielding, O. O. Mykhaylyk, A. Schmid, D. Pontoni, S. P. Armes and P. W. Fowler, *Chemistry of Materials*, 2014, **26**, 1270-1277.
5. J. Bang, S. Jain, Z. Li, T. P. Lodge, J. S. Pedersen, E. Kesselman and Y. Talmon, *Macromolecules*, 2006, **39**, 1199-1208.
6. J. S. Pedersen, *Journal of Chemical Physics*, 2001, **114**, 2839-2846.
7. D. J. Kinning and E. L. Thomas, *Macromolecules*, 1984, **17**, 1712-1718.
8. J. S. Pedersen, *Journal of Applied Crystallography*, 2000, **33**, 637-640.
9. L. A. Fielding, J. A. Lane, M. J. Derry, O. O. Mykhaylyk and S. P. Armes, *Journal Of The American Chemical Society*, 2014, **136**, 5790-5798.
10. J. S. Pedersen and M. C. Gerstenberg, *Colloids and Surfaces a-Physicochemical and Engineering Aspects*, 2003, **213**, 175-187.
11. J. S. Pedersen, C. Svaneborg, K. Almdal, I. W. Hamley and R. N. Young, *Macromolecules*, 2003, **36**, 416-433.
12. J. S. Pedersen and P. Schurtenberger, *Macromolecules*, 1996, **29**, 7602-7612.
13. J. B. Hayter and J. Penfold, *Molecular Physics*, 1981, **42**, 109-118.